Analysis of fluctuations and correlations in kinetic Monte Carlo methods

Théophile Bonnet

université
PARIS-SACLAY

Analysis of Fluctuations and Correlations in Kinetic Monte Carlo Methods

Analyse des fluctuations et des corrélations dans les méthodes Monte-Carlo cinétiques

Thèse de doctorat de l'université Paris-Saclay

École doctorale n°576, particules, hadrons, énergie et noyau : instrumentation, imagerie, cosmos et simulation (PHENIICS)
Spécialité de doctorat : Sciences de l'énergie nucléaire
Graduate School : Physique. Référent : Faculté des sciences d'Orsay

Thèse préparée dans l'unité de recherche
Service d'Études des Réacteurs et de Mathématiques Appliquées
(Université Paris-Saclay, CEA)
sous la direction d'**Andrea ZOIA**, Ingénieur-Chercheur
et le co-encadrement de **Davide MANCUSI**, Ingénieur-Chercheur

Thèse soutenue à Paris-Saclay, le 17 novembre 2023, par

Théophile BONNET

Composition du jury
Membres du jury avec voix délibérative

Cheikh DIOP Directeur de Recherche, CEA, Université Paris-Saclay	Président
Gaël POETTE Ingénieur-Chercheur (HDR), CEA, Université de Bordeaux	Rapporteur et examinateur
Eugene SHWAGERAUS Professeur, Cambridge University (Royaume-Uni)	Rapporteur et examinateur
Sandra DULLA Professeure, Politecnico di Torino (Italie)	Examinatrice
Eric DUMONTEIL Directeur de Recherche, CEA, Université Paris-Saclay	Examinateur
Alberto ROSSO Directeur de Recherche, Université Paris-Saclay	Examinateur

THESE DE DOCTORAT
NNT : 2023UPASP153

université PARIS-SACLAY

ÉCOLE DOCTORALE
Particules, hadrons, énergie et noyau : instrumentation, imagerie, cosmos et simulation (PHENIICS)

Titre : Analyse des Fluctuations et Corrélations dans les Méthodes Monte-Carlo Cinétiques
Mots clés : Monte-Carlo, transport de particules, cinétique, corrélations, fluctuations

Résumé :

Les outils de calcul scientifique jouent un rôle déterminant dans la modélisation du comportement des réacteurs nucléaires. La simulation numérique permet de pallier la pénurie de résultats expérimentaux, en particulier en régime non stationnaire (ou cinétique). Traditionnellement, la caractérisation du comportement des cœurs de réacteurs nucléaires s'appuie sur l'utilisation d'outils de simulation déterministes. Ces codes se fondent sur la résolution numérique de systèmes d'équations discrétisées. Ils permettent d'obtenir rapidement des résultats approchés, dont la validité doit être établie en les comparant à des résultats de référence. La simulation Monte-Carlo, quant à elle, n'introduit quasiment aucune erreur de modélisation et joue ainsi le rôle de méthode de référence.

Une simulation Monte-Carlo consiste à échantillonner un grand nombre de trajectoires aléatoires de neutrons dans le réacteur, suivant des lois de probabilité qui dépendent des lois physiques sous-jacentes. La méthode de Monte-Carlo permet un traitement exact, mais « lent » du système étudié, car l'incertitude statistique sur les résultats est inversement proportionnelle à la racine carrée du nombre d'histoires simulées. L'incertitude peut être réduite en modifiant les lois d'échantillonnage, de manière à en préserver le comportement moyen tout en modifiant la variance. On parle alors de méthodes de réduction de variance.

Jusqu'à très récemment, la simulation Monte-Carlo était appliquée uniquement aux problèmes stationnaires, à cause du coût numérique de son application à la cinétique. En effet, la séparation entre l'échelle de temps des neutrons, dont la durée de vie est très courte, et celle des précurseurs (produits de fission qui peuvent émettre des neutrons par décroissance), pose un défi considérable. De récentes avancées techniques et algorithmiques permettent cependant d'étendre l'utilisation des simulations Monte-Carlo au domaine des calculs cinétiques.

Les méthodes de réduction de variance affectent tous les moments statistiques d'ordre supérieur ou égal à deux. De récents travaux ont mis en avant différents phénomènes apparaissant dans les simulations cinétiques et trouvant leur origine dans les corrélations spatio-temporelles qui existent entre neutrons appartenant à la même chaîne de fission. Par exemple, le phénomène du « clustering » décrit l'existence de collections de neutrons spatialement corrélées formant des « amas spontanés » à courte distance.

L'objectif de ce travail de thèse est de caractériser l'interaction entre les méthodes de réduction de variance et les corrélations spatio-temporelles, et l'effet de cette interaction sur la fiabilité des incertitudes des simulations Monte-Carlo cinétiques.

Pour ce faire, cette thèse est articulée suivant deux axes. Dans une première partie, nous considérons un modèle simplifié de réacteur nucléaire, décrit à l'aide de la théorie de la diffusion. Nous obtenons une caractérisation analytique de la fonction de corrélations à deux points, décrivant les corrélations entre paires de particules, mais également d'autres observables d'intérêt, telles que la distribution des « familles » des neutrons dans les chaînes de fission. Notre étude couvre à la fois le cas de l'évolution de la population neutronique sans contrainte extérieure, et celui de l'évolution sous contrainte, qui représente un modèle simplifié de contrôle de la population sur la cinétique des neutrons.

Dans un second temps, nous sortons du cadre de la théorie de la diffusion. Un nouveau modèle, représentatif du comportement des simulations Monte-Carlo cinétiques telles que réalisées dans le code de référence TRIPOLI-4®, développé au CEA, permet d'évaluer l'impact de différents algorithmes Monte-Carlo sur les corrélations entre neutrons, dans l'optique de faciliter la détermination d'une stratégie de simulation optimale au sens de la réduction des corrélations, autant dans le cas cinétique que stationnaire.

université PARIS-SACLAY

ÉCOLE DOCTORALE
Particules, hadrons, énergie et noyau : instrumentation, imagerie, cosmos et simulation (PHENIICS)

Title: Analysis of Fluctuations and Correlations in Kinetic Monte-Carlo Methods
Keywords: Monte Carlo, particle transport, kinetics, correlations, fluctuations

Abstract:

Numerical simulation tools play a crucial role in modelling the behaviour of nuclear reactors. Numerical simulations mitigate the lack of experimental data, in particular in non-stationary (or kinetic) regime. The characterization of the behaviour of nuclear reactors customarily relies on deterministic simulation tools. These codes numerically solve systems of discretized equations. Approximate results can be rapidly obtained, but their validity must be verified against reference calculations. Monte Carlo simulations, on the other hand, introduce almost no modelling errors, and thus play the role of references.

Monte Carlo simulations consist in sampling a large number of random trajectories of neutrons following probability laws derived from the underlying physical laws. Monte Carlo methods are "exact" but slow, because the statistical uncertainty is inversely proportional to the square root of the number of simulated histories. The statistical uncertainties can be reduced by modifying the sampling laws so that the average behaviour is preserved while the variance is modified. We thus speak of variance-reduction methods. Until recently, Monte Carlo simulations have only been applied only to stationary problems, due to their extremely high computational cost for non-stationary problems. In fact, the time-scale separation between the neutron lifetime (which is very short) and the precursor decay time (leading to further neutrons that are crucial for the reactor dynamics) represents a hard challenge for numerical simulation. However, recent technical and algorithmic advances have changed the status quo, enabling the use of Monte Carlo simulation for kinetics.

Variance-reduction methods affect all higher order statistical moments. Recent work has highlighted peculiar phenomena in kinetic simulations, originating from space-time correlations between neutrons belonging to the same fission chain. For instance, the "clustering" phenomenon describes the emergence of spontaneous "neutron aggregation" mechanisms, which are ultimately responsible for the appearance of a wild patchiness in the spatial neutron density.

In this thesis, we characterize the interaction between variance reduction methods and space-time correlations in kinetic Monte Carlo methods, as well as the effects of this interaction on the reliability of uncertainty estimation for this class of simulations.

For this purpose, this thesis is divided in two parts. First, we consider a simplified model of a nuclear reactor, described by diffusion theory. We obtain analytical solutions for the pair correlation function describing correlations between pairs of particles, as well as for other observables of interest, such as the distribution of neutron "families" within fission chains. Our investigation covers both the case of the free evolution of the neutron population, and the case of the evolution under constraint, which mimics the effect of population control on the neutron and precursor dynamics.

In the second part of the manuscript, we introduce a more realistic model, representative of the behaviour of kinetic Monte Carlo simulations realized in reference particle-transport codes such as TRIPOLI-4®, developed at CEA. This investigation helps to evaluate the effects of several Monte Carlo variance-reduction and population-control algorithms on neutron correlations, with the aim of devising an optimal simulation strategy for quenching correlations, in stationary and non-stationary simulations.

Acknowledgements

Une fois arrivé à la fin de la thèse (et surtout, à la fin du manuscrit), il est tout de même satisfaisant de regarder derrière soi, et de pouvoir prendre dans les mains ce manuscrit tant craint, si plein d'imperfections, et dont on finit tout de même par être fier. Ces trois années ont été parfois difficiles, parfois grisantes, et surtout extrêmement remplies. Dans tous les cas, je n'aurais pas pu les affronter sans le soutien inconditionel de tant de gens, tant au SERMA que dans ma vie personnelle, et que j'aimerais remercier ici.

First, I would like to thank the members of my committee, Cheikh Diop, Sandra Dulla, Eric Dumonteil, and Alberto Rosso for taking time from their busy schedule to attend my viva in person. In particular, I would like to thank Eugene Shwageraus and Gaël Poette, who additionally took the time to proof-read my manuscript and provided detailed comments on my work.

J'aimerais aussi remercier Andrea et Davide, pour leur encadrement sans faille, leur direction éclairée, et leur soutien tout au long de ma thèse, mais particulièrement dans les dernières semaines de rédaction. Merci encore pour vos soirées et weekends quelque peu écourtés par les relectures.

Merci aussi à mes collègues et amis du SERMA de manière générale. En particulier, j'aimerais remercier Hunter, Emeline et Coline, pour les pauses cafés, les jeux de rôle, les longues discussions sur la déliquescence du monde, et puis aussi les gros délires sur divers sujets...

Merci à mes collocs, particulièrement Guillaume et Germain, les vieux de la vieille. On a fait beaucoup de parties de MarioKart, on s'est beaucoup plaint (soyons français), et on a pas assez mangé de raclettes. Guillaume, bon courage pour ta thèse !

Enfin, merci à mes amis de licence et de master, désolé vous êtes trop nombreux pour que je cite tout vos noms ! Pour toutes les soirées jeux, séries, les jeux de rôle (encore), les bars, les discussions, et beaucoup, beaucoup de plaintes (encore) !

Merci aussi à Arnaud, que j'ai malheureusement peu vu ces derniers temps, mais qui reste encore et toujours un de mes plus grands amis.

Ensuite, j'aimerai remercier ma famille. Je n'ai pas de mots suffisamment forts pour vous remercier de tout ce que vous avez fait pour moi, de votre soutien, de votre joie et de votre persévérance dans les moments sombres, qui ont été nombreux ces dernières années. J'ai la meilleure famille dont on puisse rêver, et je n'en changerais pour rien au monde.

Quentin, Audrey, je vous remercie pour vos nombreux conseils que je n'ai pas suivi pour la plupart, mais que j'aurais souvent dû suivre. J'espère pouvoir continuer a vous réjouir par mes histoires encore de nombreuses années !

Bien sûr, merci à toi Amélie, pour toutes ces danses, ces longues soirées, ces (très) nombreuses bouteilles d'alcool vidées, tes très bons cocktails (aux conséquences parfois imprévisibles) et ton soutien. C'était une merveilleuse respiration lors des derniers mois de la thèse. Malgré toutes tes dénégations, tu es une super partenaire de danse, et j'ai adoré pouvoir autant danser avec toi !

Un grand merci aussi à Raphaël pour ton amitié sans faille, ta serviabilité et ta gentillesse. Depuis le lycée, ça commence à remonter ! La population d'aliens est en chute libre depuis quelques mois, ce qui était de plus en plus satisfaisant au fur et à mesure que la thèse avançait. J'espère pouvoir conserver cette amitié jusqu'à la tombe.

Table des matières

Table des figures

Liste des tableaux

1 -Introduction

In the context of nuclear reactor safety, the development of predictive, reliable and fast simulation tools for multi-physics simulations coupling neutron flux solvers with thermal-hydraulics and thermo-mechanics codes, under stationary and transient conditions, is the subject of very extensive research programs in several leading institutions[1].

The neutron density, i.e. the average number of particles in phase space[2], obeys the Boltzmann equation [2]. Analytical solutions for this equation are beyond reach, except for highly simplified configurations; numerical simulations are thus mandatory. Thanks to the linearity of the Boltzmann equation and to the intermediate dimension of the phase space (neither too high nor too low), deterministic and Monte Carlo methods can be both successfully used to obtain numerical solutions, each presenting specific advantages and drawbacks.

The Boltzmann equation in non-stationary conditions is traditionally solved using *deterministic methods*, which rely on the discretization of the phase space. Because of the extremely large number of unknowns (of the order of $\sim 10^{14}$) that would result from a reasonably fine discretization of space, direction and time variables, most state-of-the-art deterministic simulation codes adopt the so-called two-step approach, whereupon the results of a finely-discretized calculation at the scale of a fuel assembly (or a collection of fuel assemblies) in stationary conditions is used to prepare the homogenized and condensed nuclear data that are then injected into time-dependent simplified transport solvers with coarse energy discretization for simulations at the full-core scale [3–5]. Often, a factorization of the phase space is introduced, separating time with respect to the classical phase-space variables [4, 6, 7].

Deterministic solvers are computationally fast, but they achieve their speed at the expense of introducing discretization biases and reactor-dependent models (e.g., self-shielding) that call for the validation of this class of numerical tools against high-fidelity simulations and experimental measurements [8]. Experimental data concerning nuclear reactors in the stationary state are generally available, although somewhat scarce since in most cases they belong to plant operators and are thus not directly accessible. In this respect, remarkable initiatives aimed at establishing international benchmarks for code validation (including depletion and multi-physics coupling) have been recently promoted, such as VERA (Virtual Environment for Reactor Applications)[3], BEAVRS (Benchmark for Evaluation And Validation of Reactor Simulations)[4], and Watts Bar (TVA Watts Bar Unit 1 Multi-Physics Benchmark)[5]. The situation is definitely worse for data pertaining to non-stationary regimes, such as operational transients following the insertion of control rods, or experimental campaigns aimed at probing the reactor behaviour under external solicitations, which are seldom available. Extreme cases, such as accidental transients which might lead to fuel degradation, are dangerous and not directly accessible by experimental means, in spite of their relevance for the validation of simulation codes [9].

In view of these considerations, *Monte Carlo* simulations play a special role, in that they do not suffer from discretization errors [10] and can thus provide a high-fidelity 'golden standard' for the validation of deterministic solvers; furthermore, they become *de facto* mandatory to assess the biases of deterministic solvers in non-stationary reactor regimes.

[1] See for instance the initiatives promoted in the USA, such as the CESAR project (`cesar.mcs.anl.gov`) or the CASL consortium (`www.casl.gov`), and the European projects FP7 HPMC and McSAFE (`cordis.europa.eu/projects`).

[2] The (classical) phase space includes position (three variables) and velocity (three variables). Velocity can be equivalently expressed using direction (two variables) and energy (one variable).

[3] `https://world-nuclear-news.org/Articles/Federal-funding-for-reactor-modelling-initiative`.

[4] `http://crpg.mit.edu/sites/default/files/css_injector_images_image/BEAVRS_2.0.2_spec.pdf`.

[5] `https://www.oecd-nea.org/jcms/pl_32202/tva-watts-bar-unit-1-multi-physics-benchmark`.

1.1 . Monte Carlo simulations : from stationary to time-dependent

Monte Carlo simulations for particle transport problems are based on the random sampling of the particles' trajectories in the phase space. For the applications of interest in reactor physics, particles are primarily neutrons, delayed-neutron precursors and photons. In this thesis, we will focus on neutrons and precursors. Their random interactions with the surrounding media are sampled in accordance with the probability laws given in the nuclear data libraries ; particle tracking is determined by computing the intersections of their flights between collisions with the cells of the geometrical model. Trajectories are followed until particles disappear, either by capture events or by leaking from the boundaries of the system. Along each trajectory, physical observables such as reaction rates are estimated by setting appropriate 'tallies' and collecting statistics (mean and variance) over a sufficiently large ensemble of sampled trajectories. The sample average over particle histories yields *unbiased* estimates of the expected value of the sought observables, from the law of large numbers ; the sample variance yields the associated statistical uncertainty of the sample average, from the central limit theorem [10]. The variance of the sample average is inversely proportional to the number of sampled histories, which makes Monte Carlo simulations typically (much) slower than deterministic solvers. However, this limitation is compensated by the unbiasedness of the obtained estimates : deterministic and Monte Carlo codes complement each other and are equally necessary.

Mainly due to considerations related to the required simulation time, combined with limited computer power, in reactor physics Monte Carlo codes have been long applied almost exclusively to the solution of stationary problems in isothermal conditions. Recent advances in both algorithms and computer power have however paved the way towards a whole range of new applications for Monte Carlo simulations, specifically aimed at extending the perimeter of applicability of these methods to multi-physics problems. Enormous progress has been achieved e.g. in the field of depletion calculations, where the behaviour of the neutron density is coupled to the transmutation of the media under irradiation, whose evolution is ruled by the generalized Bateman equations : Monte Carlo codes have been efficiently coupled with (deterministic) solvers for the Bateman equations, and the stability of the resulting simulation schemes has been thoroughly investigated [11–16].

Over the last ten years, there has been a growing interest in the development of a novel class of Monte Carlo methods devoted to kinetic (i.e., time-dependent) simulations, whose computing time was prohibitively high until quite recently. Prompted by the pioneering work by Sjenitzer and Hoogenboom [17, 18], ingenuous variance-reduction and population-control methods targeted at efficiently handling time-dependent problems have been first tested on simplified configurations, and then successfully extended to realistic reactor models with thermal-hydraulics feedback effects [19–26].

1.2 . Correlations and fluctuations in kinetic Monte Carlo simulations

Due to the still relatively recent appearance of these breakthroughs, a comprehensive framework for the investigation of time-dependent Monte Carlo simulations for reactor physics applications is yet to be established, despite many promising early investigations. The accuracy and precision of Monte Carlo methods is crucial, because they are intended as a golden standard with respect to which simplified approaches are to be compared. In particular, the reliability of the sought results is only as good as the one of the associated confidence intervals, which are customarily estimated by inference techniques, i.e. collecting the sample variance over Monte Carlo histories. The sample variance captures the fluctuations in the tallies due to the inherently stochastic nature of particle histories. If the particle histories are independent, and the fluctuations are well-behaved, then the quantification of the sample variance is straightforward. However, kinetic simulations pose peculiar challenges in this respect.

To begin with, the initial neutron and precursor source for kinetic problems often corresponds to the *equilibrium* (stationary) reactor condition, which means that the particles beginning the time-dependent simulation inherit the correlations that are known to affect the eigenvalue calculations needed to sample

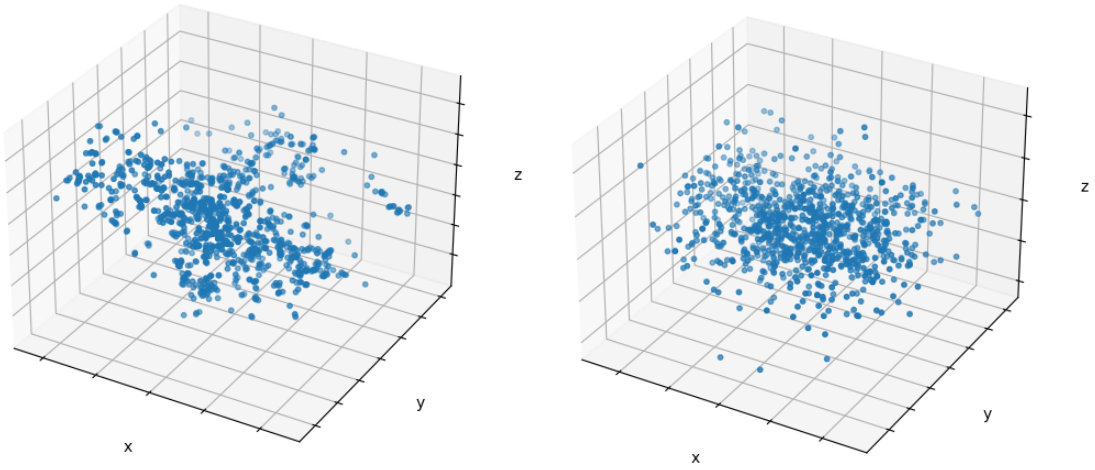

Figure 1.1 : Snapshots of the spatial positions of neutrons at equilibrium in eigenvalue Monte Carlo simulations. Left : correlations are strong, and neutrons are clustered ; right : correlations are weak, and neutrons are uniformly distributed in space.

the equilibrium particle configuration [10]. When the number of simulated particles is low, these correlations are enhanced, and manifest themselves in the form of spontaneous aggregation of particles ('*clustering*'), resulting in patchy spatial distributions [27] such as those illustrated in Fig. 1.1. Furthermore, kinetic Monte Carlo simulations come with their own sets of problems : particle histories may 'branch' because of fission events inducing secondary neutrons, which increases the overall variance and is responsible for correlations in time and in space, even when the reactor is critical. These effects might in some extreme cases lead to an unbounded growth of the variance over time, dubbed *critical catastrophe* [28].

In the following, we provide a concise overview of the state-of-the-art knowledge on these issues, the key open questions and their relevance for applications.

1.2.1 . Correlations in eigenvalue Monte Carlo simulations

As illustrated in the following chapters, the equilibrium neutron and precursor population can be sampled by Monte Carlo methods simulating fission chains over several *generations* (a generation being defined as the neutron history between birth by fission and death by leakage or absorption), until the stationary regime is attained [10]. At each generation, the genealogy of any neutron can be thus traced back to an ancestor, and the set of neutrons sharing a common ancestor forms a *family* : events pertaining to the same family will be correlated. Such correlations affect both the statistics of a tally over generations at a given spatial cell, and the statistics of tallies at distinct spatial cells within a generation : these two points of view are intimately related.

The assessment of *generational* correlations is a long-lasting problem. In eigenvalue Monte Carlo simulations, the average and the variance are typically estimated over successive generations by assuming that tallies collected in each generation are identically and independently distributed. This corresponds to an *ergodic averaging* procedure, by analogy with the ergodic assumption in equilibrium statistical physics. While the tallies are indeed identically distributed (after convergence has been reached), they are also correlated, in view of the previous considerations, and this affects the estimation of their uncertainty.

Brissenden and Garlick first noted that neglecting generational correlations when estimating the variance using ergodic averaging leads to an underestimation of the variance of the tallies [29] : one has thus to distinguish between the (underestimated) *apparent* variance obtained through ergodic averaging and the *true* variance that would have been obtained through *ensemble averaging* over a set of fully

independent replicas[6]. Ueki et al. [30] showed that the discrepancy between apparent and true variance may be significant for local (i.e., spatially distributed) tallies. They also showed that the convergence rate of the apparent variance with respect to the number of simulated particles deviated from the scaling expected for independent histories, although later Herman demonstrated that the usual scaling is asymptotically recovered for large population sizes [31]. Min-Jae et al. found that the ratio of the apparent-to-true variance is not uniform in space [32].

Methods aiming at predicting the true variance based on the apparent variance have been proposed, most often relying on simplifying assumptions : Yamamoto et al. modelled the underestimation of the variance of local tallies and its dependency on space and tallying bin size [33]. Sutton applied a discretized phase-space approach to understand the spatial non-uniformity of the apparent-to-true variance ratio [34]. Miao et al. computed the auto-correlation coefficients between spatial tallies to analyse the behaviour of generational correlations [35–37].

The impact of *spatial* correlations in eigenvalue Monte Carlo simulations was recently highlighted by Dumonteil et al., who first pointed out the emergence of neutron clustering [27] ; diagnostic tools to detect spatial correlations were later developed by Nowak et al. [38] building upon previous findings [28]. Although such spatial correlations are not supposed to alter the average tallies, Cosgrove et al. have shown that a potentially more problematic situation arises when Monte Carlo simulations are coupled to a fuel depletion solver, which might amplify existing numerical instabilities [12, 39] and induce biases on the average observables [40]. Sutton has proposed to relate the behaviour of neutron clustering to the statistics of the families, observing that a smaller number of independent families (or a larger family size) induces stronger correlations [41, 42]. This research field is still unsettled, and somewhat contradictory statements may be found in the literature. Some authors have suggested that clustering might have an impact also on the average tallies, beside affecting the estimation of the variance [43, 44]. In stark contrast, other authors have suggested that spatial correlations have no effect on the estimation of statistical uncertainty [45].

1.2.2 . Correlations in time-dependent Monte Carlo simulations

Time-dependent Monte Carlo simulations for reactor physics applications have only recently been introduced, which explains why the analysis of the behaviour of correlations in this class of problems is still in its infancy. Furthermore, despite effective advances in variance-reduction methods, the computing cost of kinetic problems is still very high, so that the investigation of correlations is most often carried out in simplified models with varying degrees of approximations.

Dumonteil et al. initially assessed spatial correlations at a given observation time by disregarding the contributions of precursors and assuming unbounded media [27]. The effects of bounded media on space-time correlations were later taken into account [46, 47], leading to the development of a more refined model where the neutron population is kept constant to mimic the impact of population-control methods [28]. An interesting feature of these models is that most of their findings carry over also to generation-based eigenvalue problems, if one replaces time by the discrete generation index [38] : this also means that the open questions concerning the latter translate into open questions concerning the former. Unsurprisingly, the main finding is that clustering occurs due to fission events, similarly as in the case of eigenvalue problems. If no population control is applied, the variance of a critical system will grow unbounded, eventually leading to an abnormal termination of the kinetic simulations (critical catastrophe) ; population control averts the critical catastrophe. The impact of precursors (in unbounded media, and in the absence of population control) has been examined by Houchmandzadeh et al. [48], who have shown that the amplitude of the correlations was dramatically quenched and their evolution in time considerably slowed down for systems close to criticality.

[6]There is no formal restriction preventing from using independent replicas in the context of power iteration. The main reason that led Monte Carlo practitioners to rely on ergodic averaging stems from considerations of computational cost : independent replicas would involve a total cost much higher than ergodic averaging, and this was prohibitive in the early history of Monte Carlo methods.

All these investigations are restricted to spatially homogeneous media and simplified transport models, which hinders the immediate applicability of these findings to more realistic applications, although some relevant general tendencies can be successfully extracted. An even more serious limitation is that the models mentioned above rely on the hypotheses of *analog* Monte Carlo simulations, excluding variance-reduction techniques. In view of its utmost importance for production Monte Carlo codes, the interference between non-analog Monte Carlo methods, variance-reduction and population-control techniques and the behaviour of correlations in kinetic problems calls for a deeper understanding, as witnessed by recent contributions [49].

1.3 . Goal and structure of the thesis

Based on these considerations, in this thesis we set out to establish a *unified and coherent framework* for the analysis of *fluctuations and correlations in kinetic Monte Carlo simulations*, with the goal of ensuring the reliability of the statistical uncertainty estimates in such calculations. In particular, we will focus on the non-trivial interplay between the behaviour of fluctuations and correlations and the application of variance-reduction and population-control techniques, as well as sampling strategies used for non-analog Monte Carlo simulations. Our investigation will cover both algorithms devoted specifically to time-dependent problems and algorithms devoted to (stationary) eigenvalue problems, by virtue of their central role for the sampling of the equilibrium neutron and precursor population. The results of our analysis and the novel approaches that we have chosen in order to achieve our goals will be presented in details in the remainder of this manuscript.

This work is structured as follows :

- First, in Chapter 2, we present the general background on Monte Carlo simulations in reactor physics, with special emphasis on the methods used for kinetic problems.
- In Part I (Chapters 3 and 4), we shall present our results in a simplified diffusion-based analog kinetic Monte Carlo simulation, where a population of neutrons and precursors evolves in time following a Branching Brownian Motion. We will characterize fission-induced correlations in such a system and derive characteristic quantities in order to facilitate the analysis of more realistic simulations. A focus on the effects of an idealized population-control mechanism in analog simulations will be introduced.
- In Part II (Chapters 5 and 6), we shall present our results regarding non-analog kinetic Monte Carlo simulations, making use of a broad range of variance-reduction and population-control techniques. We will propose suitable estimators for the analysis of correlations in such systems, and we will discuss the effects of variance-reduction and population-control methods on fluctuations and correlations.

In Chapter 2 we will briefly recall the main concepts of neutron transport in reactor physics, in a general time-dependent setting of the Boltzmann equation, including the contributions of the delayed-neutron precursors. Simplified formulations of the Boltzmann equations, encompassing the multi-group and diffusion approximations, will be illustrated. Next, we will introduce the basic principles of Monte Carlo simulations, both analog and non-analog, to estimate the solution of the time-dependent Boltzmann equation ; we will in particular discuss the most important variance-reduction and population-control techniques that will be used in the remainder of the manuscript. Special cases of Monte Carlo algorithms to solve the multi-group and diffusion versions of the Boltzmann equations will be detailed.

Chapter 3 will introduce a diffusion-based simplified kinetic Monte Carlo simulation scheme based on Branching Brownian Motion that includes delayed events in order to account for precursors. We will analyze fission-induced spatial correlations between particles using the space-dependent moment equations, based on the Pál-Bell backward formalism. Within the framework of this simplified transport

model, we will derive exact expressions for the typical length and time scales of the correlations in this class of simulations.

A step toward the characterization of population-control algorithms will be provided in Chapter 4 by enforcing idealized constraints on neutrons and precursors, still within the framework of diffusion-based simplified kinetic Monte Carlo simulations. Relying on the forward formulation of the master equation, we will establish moment equations whenever possible for the particle statistics, and derive analytical (or semi-analytical) expressions for the key observables. Such quantities will be compared to Monte Carlo simulations, used as a reference, and to the results obtained without population control. In addition, we shall complement the analysis of the moment equations by a discussion on the statistical behaviour of neutron 'families' defined over fission chains.

In Chapter 5, we will turn to the more realistic case of non-analog Monte Carlo simulations in the framework of the multi-group Boltzmann equation. The first step of our analysis will consist in examining the initial particle source corresponding to a critical reactor, which is often required in time-dependent problems. This source depends on a preliminary stationary Monte Carlo simulation to solve the k-eigenvalue problem and access the fundamental eigenstate. The power iteration algorithm used to converge towards the fundamental mode is itself prone to non-trivial effects due to inter-generation and intra-generation correlations, which we will investigate extensively in view of their impact on the source for kinetic simulations. For this purpose, we will use a few benchmark configurations including spatially homogeneous and heterogeneous systems. We will assess the impact of various variance-reduction and population-control techniques on correlations in stationary Monte Carlo methods, relying on usual and novel tallies.

In Chapter 6, we will finally examine the case of non-analog kinetic Monte Carlo simulations, still within the framework of the multi-group Boltzmann equation. We will first consider a simplified benchmark configuration that will allow extracting the key tendencies of correlations : in particular, we will examine the impact of precursors, which will be shown to play a key role in determining the amplitude and the spatial behaviour of the correlations. Then, we will revisit the more realistic benchmark configurations introduced in Chapter 5. We will assess the correlations of the equilibrium neutron and precursor populations, as determined by running the power iteration described in the previous chapter, and then analyze time-dependent simulations. Three different regimes will be explored : critical, subcritical and supercritical.

Conclusions will be finally drawn in Chapter 7, where we will also present the main perspectives for future work.

1.4 . Published works

Part of the material presented in this thesis has previously appeared in the following publications :

- T. Bonnet, D. Mancusi, and A. Zoia, "Space and time correlations for diffusion models with prompt and delayed birth-and-death events", Phys. Rev. E, vol. 105, no. 6, p. 064105, Jun. 2022.[Online]. Available : `https://link.aps.org/doi/10.1103/PhysRevE.105.064105`

- T. Bonnet, D. Mancusi, and A. Zoia, "The Statistics of Family Histories in Kinetic Monte Carlo Simulations," in Proceedings of M&C 2023 International Conference on Mathematics and Computational Methods Applied to Nuclear Science and Engineering, Niagara Falls, Canada, Aug. 13-17th, 2023.

- H. Belanger, T. Bonnet, D. Mancusi, and A. Zoia, "The Effects of Branchless Collisions on Neutron Clustering" in Proceedings of M&C 2023 International Conference on Mathematics and Computational Methods Applied to Nuclear Science and Engineering, Niagara Falls, Canada, Aug. 13-17th, 2023.

- T. Bonnet, H. Belanger, D. Mancusi, and A. Zoia, "The effect of branchless collisions and population control on correlations in Monte Carlo power iteration", submitted to Nuclear Science and Engineering. Preprint avalaible : `https://arxiv.org/abs/2309.03767`

Furthermore, some of the results have been or will be presented (oral talks) at the following international conferences and workshops :

- International Conference on Transport Theory (ICTT), Bertinoro, Italy, Jul. 10-16th, 2022.
- M&C 2023 International Conference on Mathematics and Computational Methods Applied to Nuclear Science and Engineering, Niagara Falls, Canada, Aug. 13-17th, 2023.
- Fourth annual workshop "Mathématiques pour la neutronique", GdR MaNu, INSTN/Saclay, France, Dec. 7th, 2022.
- Invited talk at the Inaugural meeting, GdR Branchement, Institut de Mathématiques de Toulouse, France, Nov. 8-10th, 2023.

2 - Time-dependent Monte Carlo simulation for reactor physics applications

In this chapter, we introduce the question of correlations in time-dependent neutron-transport Monte Carlo simulations. We start by recalling the basic features of the time-dependent Boltzmann equation, which governs neutron transport in the kinetic regime, and introducing notations and concepts that will be useful in the following. Then, we illustrate how Monte Carlo methods can be used in order to solve the time-dependent Boltzmann equation, and briefly review the key variance-reduction and population-control strategies that have been recently proposed to cope with the distinct challenges of kinetic Monte Carlo simulations.

2.1 . A brief introduction to neutron-transport problems

2.1.1 . Neutron-matter interactions

Neutrons are neutral particles that interact with matter only through collisions with the surrounding nuclei, and otherwise stream freely. Although the neutron is unstable, and spontaneously decays to a proton, the typical decay time in void is of the order of ten minutes, a timescale which is much longer than the typical neutron life-time within nuclear systems, i.e., shorter than 10^{-2} s for the longest-lived particles. For this reason, the spontaneous decay can be safely neglected for the applications to reactor physics that we will examine in the following. Since the energy range of interest for reactor physics is conventionally assumed to lie between 20 MeV and 10^{-5} eV, relativistic effects at high energy can be neglected in most applications. Neutron-matter interactions should in principle be described using quantum mechanics, since the de Broglie wavelength of the neutron ranges between 10^{-13} cm for neutrons at high energy (say at 20 MeV) and 10^{-8} cm for neutrons that are in thermal equilibrium with the traversed medium (say at 0.025 meV) : these scales are comparable, respectively, with the typical radius of nuclei and with the typical distance over which molecular bonds develop. However, the common practice in reactor physics is that the quantum-physics aspects required for collision events are pre-computed by nuclear physics specialists and condensed in tabulated data that can be accessed and interpolated as needed, including interaction probabilities and the probability of selecting a specific reaction channel (e.g., elastic or inelastic scattering, capture or fission), energy-angle distributions for the outgoing neutrons, and the associated yields. Thus, it can be safely assumed that neutrons evolve in a classical phase space with coordinates $P = \{\mathbf{r}, \mathbf{\Omega}, E, t\}$, where $\mathbf{r}$ is the position vector, $\mathbf{\Omega}$ is the direction vector, E is the energy, and t is time.

Within this framework, the probability that an incident neutron interacts with a nucleus i in the medium via reaction channel k is assigned by introducing the notion of partial *microscopic* cross sections $\sigma_{i,k}(E)$, that carry units of an area (and are usually measured in units of barns, where 1 b $= 10^{-24}$ cm^2). The microscopic cross sections have a highly intricate dependence on the energy E, which basically stems from the fact that they condense all the complex quantum-physics interaction laws, as mentioned earlier. The sum over all the reaction channels k yields the total microscopic cross section for a given nuclide, namely,

$$\sigma_{i,t}(E) = \sum_k \sigma_{i,k}(E), \tag{2.1}$$

so that $p_{i,k}(E) = \sigma_{i,k}(E)/\sigma_{i,t}(E)$ expresses the probability of choosing the reaction channel k, conditioned on the event of having a collision with the nuclide i.

The allowed reactions channels are often grouped into three categories : scattering, sterile absorption, and fission [2] :

- Scattering can be either elastic or inelastic, and most often leads to a unit yield ; reactions of the class (n, xn), with $x = 2, 3$ or even 4 are possible, albeit rarer in the energy range of interest

for reactor physics. The energy-angle spectrum of the emerging neutrons is in most cases rather involved, and strongly depends on the nature of the collided nuclide. In the remainder of the manuscript, we will mainly focus on the simple case of isotropic scattering with unit yield.

- A neutron undergoing a capture (i.e., sterile absorption) stays within the collided nuclide and thus disappears with respect to the transport process : the neutron history is terminated. Other particles might be emitted, such as photons or charged particles, but here we will exclusively focus on neutrons, and such events will be neglected.

- Upon fission, the incident neutron is absorbed and splits the target nucleus into (most often) two 'fragments'. Contrary to sterile absorption, fission leads to the emission of secondary neutrons. The number of emitted neutrons is random. On average, ν_p so-called 'prompt' neutrons of high energy (e.g. around 2 MeV for Uranium 235) are emitted almost immediately after the fission event. It is reasonable to assume that the angular distribution of the prompt neutrons is isotropic. The shape of the energy spectrum $\chi_p(E)$ can be approximated with simple analytical forms, such as the one proposed by Watt [50]. The fission fragments are left in excited states, which generally de-excite via β^- decay. In some cases, additional neutrons may be emitted along the decay chain : since these neutrons are emitted over the timescale of β^- decay (1–10 s for Uranium 235), they are dubbed 'delayed neutrons'. Correspondingly, due to their role, such excited states take the name of *delayed-neutron precursors*. The number of created precursors per fission event is random, with average ν_d. The fission fragments are heavy and lose almost all their kinetic energy within microns with respect to the fission event : for this reason, it is assumed that delayed neutrons are emitted at the same location as the prompt neutrons originating from the same fission event. The energy spectrum $\chi_d(E)$ of delayed neutrons has a shape that is qualitatively similar to the one of prompt neutrons, but with a sensibly smaller average energy, of the order of 400 keV for Uranium 235. The angular distribution can again be taken as isotropic. The total number of possible precursors is about 300 : for the sake of simplicity, in nuclear data libraries they have been grouped into a small number of 'families' (6 or 8), each family j having spectrum $\chi_d^j(E)$, decay constant λ_j and yield ν_d^j, with $\nu_d = \sum_j \nu_d^j$. The ratio $\beta = \nu_d/(\nu_p + \nu_d)$ is small, of the order of 0.6% for Uranium 235.

In general, a medium is composed of many different nuclides, each having a total microscopic cross section $\sigma_{i,t}(E)$ and a concentration $N_i(\mathbf{r})$ (usually in units of nuclides per cubic centimeter). The probability of selecting a given nuclide upon a collision at $\mathbf{r}$ induced by a neutron of energy E is thus given by

$$p_i(\mathbf{r}, E) = \frac{N_i(\mathbf{r})\sigma_{i,t}(E)}{\sum_j N_j(\mathbf{r})\sigma_{j,t}(E)}. \tag{2.2}$$

The interaction probability with the medium per unit flight length for a reaction k is then given by the partial *macroscopic* cross section Σ_k, carrying units of inverse length (usually, cm^{-1}), i.e.,

$$\Sigma_k(\mathbf{r}, E) = \sum_i N_i(\mathbf{r})\sigma_{i,k}(E). \tag{2.3}$$

Finally, the total interaction probability per unit flight length within a medium is given by the total macroscopic cross section

$$\Sigma_t(\mathbf{r}, E) = \sum_k \Sigma_k(\mathbf{r}, E). \tag{2.4}$$

It is assumed that the media of interest for reactor physics applications are sufficiently isotropic at the spatial scales seen by the neutrons, so that in practice the cross sections do not depend on the direction of flight $\mathbf{\Omega}$.

Since neutrons freely stream within the medium and only interact with nuclides upon collision, with Poisson probability $\Sigma_t(\mathbf{r}, E)ds$ for a flight of infinitesimal length ds at position $\mathbf{r}$, in direction $\mathbf{\Omega}$ and

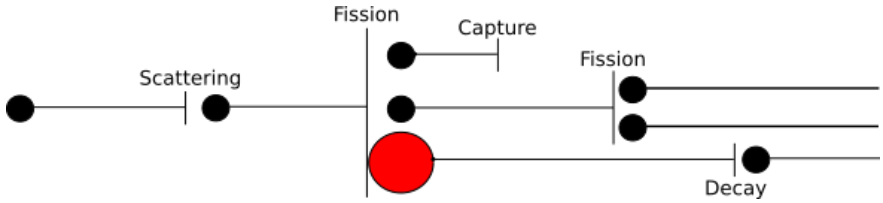

Figure 2.1 : Example of a fission chain as a succession of scattering, capture and fission events, including the precursor decay and the emission of delayed neutrons. The chain is renewed at each fission event, upon which a new branch of the chain is created. Black dots denote neutrons, red dots denote precursors, and connecting lines denote particle flights between collision events.

with energy E, it follows that the flight lengths s between collision events are distributed according to a non-homogeneous exponential probability density $f(s)$ with parameter $\Sigma_t(\mathbf{r}, E)$, namely,

$$f(s) = \Sigma_t(\mathbf{r} + s\mathbf{\Omega}, E) e^{-\int_0^s \Sigma_t(\mathbf{r} + s'\mathbf{\Omega}, E) ds'}. \tag{2.5}$$

When the material properties of the medium are spatially homogeneous, Eq. (2.5) becomes a simple exponential probability density function.

The overall picture of the physical mechanisms recalled here shows that the succession of flights and collisions forms a chain of stochastic events, with fission playing a special role in that new 'branches' might appear. For illustration, the stochastic dynamics of a representative fission chain is provided in Fig. 2.1. The evolution of the fission chains depends on the balance between the loss and production events, which is quantified using the multiplication factor

$$k = \frac{\text{production}}{\text{absorption} + \text{leakage}}. \tag{2.6}$$

If $k > 1$ the system is said to be supercritical and the average number of neutrons will grow in time; if $k < 1$ the system is said to be subcritical and the average number of neutrons will decrease in time; finally, if $k = 1$ the system is said to be critical and the average number of neutrons will be stationary in time.

2.1.2 . The time-dependent Boltzmann equation

In order to characterize the stochastic evolution of the fission chains, equations can be established for the statistical moments of neutron and precursor populations. In particular, the conservation law (expressing the net change as the balance between creations and losses) for the neutron density $n(\mathbf{r}, \mathbf{\Omega}, E, t)$, i.e., the average number of neutrons in an elementary volume in phase space, and the precursor density $c^j(\mathbf{r}, t)$ for each family $j = 1, 2, \cdots, M_f$, M_f being the number of families, leads to the time-dependent Boltzmann equation. The product of $n(\mathbf{r}, \mathbf{\Omega}, E, t)$ with the neutron speed v, which often occurs in the equation, is called *angular flux* and is denoted by

$$\varphi(\mathbf{r}, \mathbf{\Omega}, E, t) = v n(\mathbf{r}, \mathbf{\Omega}, E, t). \tag{2.7}$$

The Boltzmann equation, expressed as a function of the angular flux, reads

$$\frac{1}{v}\frac{\partial}{\partial t}\varphi(\mathbf{r}, \mathbf{\Omega}, E, t) + \mathbb{L}\varphi(\mathbf{r}, \mathbf{\Omega}, E, t) = \mathbb{F}_p\varphi(\mathbf{r}, \mathbf{\Omega}, E, t) + \sum_j \frac{\chi_d^j(\mathbf{r}, E)}{4\pi}\lambda_j c_j(\mathbf{r}, t) + \mathcal{S}(\mathbf{r}, \mathbf{\Omega}, E, t), \tag{2.8}$$

where we have introduced the net disappearance operator

$$\mathbb{L}\varphi = \mathbf{\Omega}\cdot\nabla\varphi + \Sigma_t(\mathbf{r}, E)\varphi - \iint \nu_s(\mathbf{r}, E')\Sigma_s(\mathbf{r}, \mathbf{\Omega}' \to \mathbf{\Omega}, E' \to E)\varphi(\mathbf{r}, \mathbf{\Omega}', E', t) dE' d\mathbf{\Omega}', \tag{2.9}$$

and the prompt fission operator

$$\mathbb{F}_p\varphi = \frac{\chi_p(\mathbf{r},E)}{4\pi}\iint \nu_p(\mathbf{r},E')\Sigma_f(\mathbf{r},E')\varphi(\mathbf{r},\mathbf{\Omega}',E',t)dE'd\mathbf{\Omega}'. \tag{2.10}$$

Here Σ_t is the total macroscopic cross section, Σ_f is the macroscopic fission cross section, Σ_s is the differential scattering cross section, χ_p is the prompt fission emission energy spectrum, χ_d^j is the delayed emission energy spectrum for precursor family j, ν_p is the average prompt fission yield, ν_d^j is the average delayed neutron yield for precursor family j, λ_j is the exponential decay constant for family j, and $\nu_s(\mathbf{r},E')$ is the particle yield due to scattering. The term $\mathcal{S}$ denotes an external source [2].

The net disappearance operator is the sum of the streaming term $\mathbf{\Omega}\cdot\nabla\varphi$, expressing the flow out of the elementary volume in the phase space, the collision rate $\Sigma_t\varphi$, describing the loss of neutrons by interaction with the medium, minus the scattering term $\nu_s(\mathbf{r},E')\Sigma_s(\mathbf{r},\mathbf{\Omega}'\to\mathbf{\Omega},E'\to E)\varphi(\mathbf{r},\mathbf{\Omega}',E',t)$, describing the rate of transfer of neutrons with energy E' and direction $\mathbf{\Omega}'$ to neutrons with energy E and direction $\mathbf{\Omega}$. The prompt fission operator $\mathbb{F}_p\varphi$ denotes the production rate of prompt neutrons.

Equation (2.8) is coupled to the evolution equations for the precursor densities c_j, which read

$$\frac{\partial c_j(\mathbf{r},t)}{\partial t} = \iint \nu_d^j(\mathbf{r},E')\Sigma_f(\mathbf{r},E')\varphi(\mathbf{r},\mathbf{\Omega}',E',t)\,dE'\,d\mathbf{\Omega}' - \lambda_j c_j(\mathbf{r},t), \tag{2.11}$$

The term $\nu_d^j(\mathbf{r},E')\Sigma_f(\mathbf{r},E')\varphi(\mathbf{r},\mathbf{\Omega}',E',t)$ expresses the production rate of precursors due to fission events. On physical grounds, we can neglect any external precursor source.

The system of Eqs. (2.8) and (2.11) is closed by applying initial and boundary conditions to φ and the c_j's. The solution of Eqs. (2.8) and (2.11) fully characterizes the time evolution of the average neutron density and the average precursor density in the phase space.

2.1.3 . Timescale separation between neutrons and precursors

It is important to note that the typical timescales of neutrons and precursors in nuclear reactors are vastly different. The average *neutron generation time* Λ, i.e., the average time between the birth of a neutron by fission and its disappearance by the subsequent fission event, is about $\Lambda \simeq 0.1$ µs for fast reactors, and $\Lambda \simeq 20$ µs for light-water-moderated reactors. The delayed neutron fraction is $\beta \simeq 0.003$ for fast reactors, and $\beta \simeq 0.006$ for light-water-moderated reactors. The family-averaged precursor decay time is about $\lambda^{-1} \simeq 10$ s for both systems. Thus, fission chains at equilibrium (i.e., for a critical reactor) generally take the form of short outbursts of prompt neutrons that die out rapidly, over a few Λ (the system is subcritical without the contribution of the delayed neutrons); at each fission event, a small fraction of the fission neutrons is produced in the form of precursors, which much later emit additional delayed neutrons that are responsible for the chain to be critical and thus stationary. Due to the values of the physical constants involved, the number of neutrons circulating in the reactor at equilibrium is much smaller than the number of precursors : this can be quantified by the dimensionless parameter $\theta = (\lambda\Lambda/\beta)$, which expresses the ratio between the population sizes of neutrons and precursors. For fast reactors, $\theta \sim 10^{-6}$, and for light-water-moderated reactors $\theta \sim 10^{-4}$.

The unbalance between the two timescales is actually highly beneficial for reactor control : thanks to the presence of the delayed neutrons, the kinetics of the neutron population is slowed down by a factor θ compared to the case where precursors are neglected. However, on the computational side, this also means that the system of Eqs. (2.8) and (2.11) is stiff, which poses distinct challenges to both deterministic and Monte Carlo solvers, calling for specific numerical methods and clever modifications of the algorithms conceived for stationary problems. In particular, the strategies required for kinetic Monte Carlo simulation will be illustrated in Sec. 2.3.

2.1.4 . Determination of the equilibrium source

Most often, the initial condition for the system of Eqs. (2.8) and (2.11) corresponds to the reactor being critical. The stationary initial state of the neutron and precursor density is then determined by formulating an eigenvalue problem for the Boltzmann equation and solving for the associated fundamental eigenmode. More precisely, this condition is obtained by setting the time derivatives to zero in Eqs. (2.8) and (2.11), neglecting the external source, and then plugging the resulting stationary Eqs. (2.11) for the precursor population into the stationary Boltzmann Eq. (2.8). This leads to

$$\mathbb{L}\varphi(\mathbf{r},\mathbf{\Omega},E) = \mathbb{F}\varphi(\mathbf{r},\mathbf{\Omega},E), \tag{2.12}$$

where $\mathbb{F}$ is the stationary fission operator defined by

$$\mathbb{F}\varphi(\mathbf{r},\mathbf{\Omega},E) = \mathbb{F}_p\varphi(\mathbf{r},\mathbf{\Omega},E) + \sum_j \frac{\chi_d^j(\mathbf{r},E)}{4\pi} \iint \nu_d^j(\mathbf{r},E')\Sigma_f(\mathbf{r},E')\varphi(\mathbf{r},\mathbf{\Omega}',E')dE'd\mathbf{\Omega}' \tag{2.13}$$

and $\varphi(\mathbf{r},\mathbf{\Omega},E)$ is the stationary neutron angular flux.

In general, Eq. (2.12) does not necessarily admit a non-null solution $\varphi(\mathbf{r},\mathbf{\Omega},E)$. To ensure the existence of a stationary state, the fission terms are rescaled by suitable constants k_i, yielding an eigenvalue problem for the discrete spectrum of eigenpairs $\{k_i,\varphi_{k_i}\}$:

$$\mathbb{L}\varphi_{k_i}(\mathbf{r},\mathbf{\Omega},E) = \frac{1}{k_i}\mathbb{F}\varphi_{k_i}(\mathbf{r},\mathbf{\Omega},E), \tag{2.14}$$

where φ_{k_i} are the eigenstates associated to the k_i-eigenvalues [2]. It is assumed that the eigenvalues k_i can be ordered, with $\cdots \leq k_i \leq k_{i-1} \leq \cdots \leq k_2 \leq k_1 < k_0$, where $k_0 > 0$ is the fundamental eigenvalue, with multiplicity one. The question of the completeness of the spectrum of k-eigenfunctions as a basis to expand the stationary angular flux $\varphi(\mathbf{r},\mathbf{\Omega},E)$ is non-trivial and problem-dependent [2]. Among these eigenpairs, the fundamental eigenstate $\varphi_{k_0} \geq 0$ is associated to the largest eigenvalue k_0 and is the only eigenstate that is everywhere non-negative. It is endowed with special interest as it corresponds to the equilibrium state of the reactor. The parameter $R = k_1/k_0 < 1$, i.e. the ratio between the eigenvalue k_1 associated with the first excited eigenstate and the fundamental eigenvalue k_0, takes the name of dominance ratio and characterizes the relaxation of higher-order eigenmodes towards the fundamental eigenmode [2]. The fundamental eigenvalue is sometimes noted k_{eff}, and physically corresponds to the multiplication factor, i.e. the ratio of the size of two successive fission generations.

Once the fundamental eigenstate of the angular flux is known, the distribution of neutrons at $t = t_0$ corresponding to a critical reactor is obtained from [18]

$$n^{\text{eq}}(\mathbf{r},\mathbf{\Omega},E,t=t_0) = \frac{\varphi_{k_0}(\mathbf{r},\mathbf{\Omega},E)}{v}. \tag{2.15}$$

Observe that the neutron source includes contributions from all kinds of collisions, and not just fission events. The initial distribution of precursors can be correspondingly deduced from Eq. 2.11 in the steady state, yielding

$$c_j^{\text{eq}}(\mathbf{r},t=t_0) = \frac{1}{\lambda_j} \iint \nu_d^j(\mathbf{r},E')\Sigma_f(\mathbf{r},E')\varphi_{k_0}(\mathbf{r},\mathbf{\Omega}',E')d\mathbf{\Omega}'dE'. \tag{2.16}$$

Equations (2.15) and (2.16) define the *equilibrium source* for kinetic problems.

2.2 . A review of Monte Carlo methods for particle-transport problems

In this section, we present an overview of general Monte Carlo methods for particle-transport problems, before addressing the special case of time-dependent transport problems obeying the system of Eqs. (2.8) and (2.11).

Monte Carlo simulations rely on the stochastic sampling of particle histories : for the applications considered here, particles can be either neutrons or precursors. Sampling is based on pseudo-random number generators, which generate sequences of numbers 'behaving as they were random' using deterministic algorithms starting from an initial 'seed'. By definition, such sequences are not truly random, and after a given period they repeat themselves ; furthermore, the numbers of the series are correlated. While sophisticated statistical tests and theorems from number theory can provide a sound basis for choosing an appropriate generator for Monte Carlo simulations, in practice the goodness of the pseudo-random number generators must be judged by the quality of the obtained results. Modern pseudo-random generators have very large periods (e.g. $\sim 2^{128}$ for the PCG64 random generator [51], or $\sim 2^{19937}$ for the Mersenne Twister [52]) and sufficiently weak correlations ; we shall thus assume that the samples of the generators behave as if they were independently and identically distributed.

There exist two main families of Monte Carlo methods : in *analog* simulations, the rules of the Monte Carlo game follow closely the physical laws of the underlying transport process ; on the contrary, in *non-analog* simulations the sampling rules are suitably modified in order to achieve a smaller statistical uncertainty on the estimated observables. In the latter case, the average of the observables is preserved by correspondingly modifying the statistical weight of the particles : this ensures that the non-analog game will yield a fair (unbiased) result with respect to the analog game. The choice of the non-analog games should be guided by considerations related to reducing the statistical uncertainty for a given amount of computer cost involved in the sampling procedure : the arsenal of non-analog sampling techniques goes under the name of *variance-reduction methods*.

The statistical weights encode the fact that, in non-analog games, particles do not contribute equally to the estimation of the statistical moments of the simulated population. To fix the ideas, consider a very simple example : a neutron with initial statistical weight of $w = 1$ undergoes a collision event ; upon collision, the absorption probability is p_a and the survival probability $p_s = 1 - p_a$. The analog simulation of this process would be to sample $\xi \sim \mathcal{U}[0, 1[$, i.e. ξ is sampled uniformly in $[0, 1[$, and to kill the neutron if $\xi < p_a$: either the neutron survives the collision event, or it dies ; with this algorithm, the statistical weight of the neutron is preserved. An equivalent non-analog scheme is to enforce the survival of the neutron by modifying the statistical weight w of the neutron exiting the collision ; the neutron always survives and its statistical weight is multiplied by the survival probability p_s at each collision. In both situations, the average statistical weight of the surviving neutrons after k collisions is $\mathbb{E}[w] = p_s^k$. The variance of the number of surviving neutrons after k collisions in the analog game will be $\mathrm{Var}[w] = k p_s (1 - p_s)$, while it will be 0 for the non-analog game.

Often, variance-reduction methods are used in combination with *population-control* methods, whose aim is to prevent the population (or the statistical weights) from shrinking or exploding. These issues will be discussed extensively in the following.

2.2.1 . Tallying in Monte Carlo simulations

The ultimate goal of Monte Carlo simulations is to provide an unbiased estimate of the average value of the observables of interest, such as the flux, reaction rates, particle current, etc. The Monte Carlo estimation of the sought physical observable is called a *score* or *tally*, which is in general a functional of the random walks of the sampled particle histories. Since the evolution of the particle histories is a stochastic process, the tallies are random variables, with unknown distributions. For each history, each sampled event in the Monte Carlo simulation has a (possibly zero) contribution to the score, and the average is computed by taking the sample mean over all the related contributions brought by all particle histories. Contributions to the Monte Carlo score are gathered using *estimators*. To fix the idea, let

$$\varphi_{V,\Delta E} = \int_V \int_{E_m}^{E_M} \int \varphi(\mathbf{r}, \mathbf{\Omega}, E) d\mathbf{\Omega} dE d\mathbf{r} \tag{2.17}$$

be the stationary scalar neutron flux integrated over a volume V and over the energy interval $\Delta E = [E_m, E_M]$. It is assumed that the material properties are constant in the region V. It can be shown that the corresponding Monte Carlo score can be estimated using the collision estimator

$$h(\mathbf{r}, E, w) = \frac{w}{\Sigma_t^V(E)}, \tag{2.18}$$

with $h(\mathbf{r}, E, w) = 0$ for $\mathbf{r} \notin V$ or $E \notin \Delta E$. Here w is the statistical weight of the incident neutron, $\Sigma_t^V(E)$ is the total cross section value within the region V, and E is the energy of the incident neutron. The estimator h is a deterministic function evaluated at the random collision points with the random coordinates of the incident neutron, and is non-vanishing only when the collision coordinates fall within the integration region V and ΔE. For each neutron, upon collision h is added to the Monte Carlo score, and the mean value of the score is computed over a large ensemble of Monte Carlo histories :

$$\mu[h(\mathbf{r}, E)] = \sum_i \sum_j h(\mathbf{r}_{i,j}, E_{i,j}, w_{i,j}), \tag{2.19}$$

where i is the index over histories, and j the index over collisions for a given history.

Each simulated history yields an estimate of the sought observables, and is called a *replica*. Confidence intervals for the mean value of the scores can be obtained relying on the Central Limit Theorem by estimating the variance of the scores. Ideally, samples are assumed to be statistically independent, in which case estimating the variance is straightforward. In literature, the variance associated to the ensemble average defines the *true* variance [29]. In some situations (as discussed in Sec. 1.2.1), independence is not verified and more complex inference techniques are necessary. A thorough and rigorous introduction to estimators and tallies can be found in Ref. 10.

2.2.2 . Example of a typical analog Monte Carlo simulation

In the simplest analog framework, neutron histories are simulated by closely following the elementary physical laws that describe neutron-matter interactions, which can be retrieved from the nuclear data libraries. For instance, a neutron moving in a homogeneous medium would sample flight lengths from an exponential distribution of parameter $\Sigma_t(E)$, once the emission direction $\mathbf{\Omega}$ and energy E are known :

$$f(s) = \Sigma_t(E) e^{-\Sigma_t(E) s}. \tag{2.20}$$

Using the inverse transform method, the flight length can be sampled from

$$s = -\frac{1}{\Sigma_t(E)} \ln(1 - \xi), \tag{2.21}$$

where $\xi \sim \mathcal{U}[0, 1[$.

If the spatial position of the particle after the flight falls within the system (i.e., if the particle is not lost upon leaving the boundaries), the particle will undergo a collision event. The collided nuclide is

selected by drawing $\xi \sim \mathcal{U}[0,1[$ and comparing ξ to the probability $p_i(E)$ defined in Eq. (2.2). Once the nuclide is sampled, the reaction channel k is determined by drawing again $\xi \sim \mathcal{U}[0,1[$ and comparing ξ to the probability $p_{i,k}(E)$ defined by

$$p_{i,k} = \frac{\sigma_{i,k}(E)}{\sigma_{i,t}(E)}, \tag{2.22}$$

with $\sum_k p_{i,k} = 1$.

If the event is scattering or fission, the number and features of the secondary particles are sampled according respectively to the yield and energy-angle distribution of the chosen reaction channel. For instance, for isotropic elastic scattering (with unit yield $\nu_s = 1$) one would first sample the scattering cosine μ_C in the center-of-mass frame, uniformly in the interval $-1 \leq \mu_C \leq 1$, and the outgoing energy E' would be determined by the collision kinematics as

$$E' = E\frac{A^2 + 2\mu_C A + 1}{(A+1)^2} \leq E, \tag{2.23}$$

where A is the ratio of the mass of the collided nuclide with respect to the mass of the neutron, and E is the energy of the incident neutron. Since μ_C is random, E' is also random, and is correlated to μ_C. The azimuthal angle is taken to be uniformly distributed in $[0, 2\pi]$. For fission, the energy of the secondary neutrons would be sampled from the fission spectra $\chi_p(E)$ and $\chi_d^j(E)$, which are in most cases only weakly dependent on the energy of the incident neutron. In order to sample the number n_f of secondary neutrons, one would need the full distribution $p(n_f)$ of the fission yield : in practice, it turns out that in most nuclear data libraries the full distribution is not provided, and the only available piece of information is the average prompt and delayed neutron yield. Thus, a full analog sampling of the number n_f of secondary neutrons is not possible, and for historical reasons the most commonly adopted choice for Monte Carlo neutron-transport codes is to sample the integer numbers surrounding the value of the average yield ; the probability of drawing either one is determined so that the average number of sampled neutrons is precisely equal to the average fission yield. For the prompt neutrons, for instance, we have

$$n_f = \lfloor \xi + \nu_p \rfloor, \tag{2.24}$$

with $\xi \sim \mathcal{U}[0,1[$. Note that, for the purpose of solving for the average neutron density or neutron flux, as described by the Boltzmann equation, only the average fission yields are required, and the sampling procedure for the multiplicity only affects the variance of the tallies.

2.2.3 . Overview of basic non-analog methods

The simple example discussed in Sec. 2.2 shows that introducing *non-analog* sampling strategies can be effective in reducing the variance associated to the scores. In this section, we provide a brief overview of the most common variance-reduction and population-control techniques that will be used throughout this work. For the sake of conciseness, we only sketch their basic features, and implementation details are left for discussion when they are used in specific applications.

Implicit capture and forced fission

Implicit capture is perhaps one of the best-known non-analog collision sampling strategies. First, we assume a non-fissile medium, so that neutrons undergo either sterile absorption or scattering. To prevent neutron histories from being terminated by sterile capture without contributing to scores, one can resort to *implicit capture* : upon collision, the neutron is forced to survive (i.e., to undergo scattering), and its statistical weight is multiplied by the survival probability

$$w' = w\frac{\Sigma_s}{\Sigma_t}, \tag{2.25}$$

where w' is the weight of the outgoing neutron and w is the weight of the incident neutron. The ratio of scattering to total cross section is evaluated at the incident neutron coordinates. With implicit capture, neutron histories can only be terminated by leakage, which suggests that the use of Russian roulette (see

Sec. 2.2.3) can be beneficial to remove particles whose statistical weight has become insignificant for the simulation.

When fission is taken into account, implicit capture can be combined with *forced fission*, whose aim is to promote the birth of secondary neutrons and thus the sampling of additional fission chains. In this case, at each collision site the incident neutron is forced to undergo scattering, as above. The statistical weight of the emitted neutron is corrected as in Eq. (2.25). Furthermore, provided that the collided nuclide is fissile, a fission event is systematically sampled, and the prompt and delayed fission yields are adjusted as $\nu_p\Sigma_f/\Sigma_t$ or $\nu_d\Sigma_f/\Sigma_t$, respectively, in order to ensure a fair game. This means that $n_{p,f}$ prompt fission neutrons are sampled following

$$n_{p,f} = \left\lfloor \xi + \frac{\nu_p \Sigma_f}{\Sigma_t} \right\rfloor, \tag{2.26}$$

where $\xi \sim \mathcal{U}[0,1[$, and are assigned the statistical weight w of their parent neutron. Furthermore, $\nu_{d,f}$ delayed neutrons (or, in the case of kinetic simulations, precursors : see Sec. 2.3) are also sampled following

$$n_{d,f} = \left\lfloor \xi + \frac{\nu_d \Sigma_f}{\Sigma_t} \right\rfloor, \tag{2.27}$$

and are assigned the statistical weight of their parent neutron. This is the technique used e.g. in the Monte Carlo code TRIPOLI-4®, developed at CEA [53]. Other implementations of the forced fission algorithm exist [10, 54], but they will not be discussed here.

Branchless collisions

Branchless collisions have been popularized by Lux and Koblinger [10] and applied with success first to fixed source stationary simulations in Ref. 55, and then to kinetic simulations [18, 56]. The main idea of branchless collisions is that each collision leads to a single outgoing particle that is assigned the same statistical weight multiplier, regardless of the chosen reaction channel :

$$w' = w\frac{\sum \nu_k \Sigma_k}{\Sigma_t}, \tag{2.28}$$

where ν_k is the yield associated to reaction channel k. For instance, if k is the scattering reaction as defined in Sec. 2.1.1, its yield is ν_s. If it is the prompt fission channel, then $\nu_k = \nu_p$, and if it is the delayed fission channel, then $\nu_k = \nu_d$, and so on. The reaction channel k is sampled with probability

$$P_k = \frac{\nu_k \Sigma_k}{\sum \nu_k \Sigma_k}, \tag{2.29}$$

and the corresponding interaction leads to the production of exactly one particle for the sampled channel. The features (direction, energy, etc.) of the outgoing particle are sampled as in Sec. 2.2.2. Note that, in time-dependent Monte Carlo simulations, choosing the delayed fission channel leads to the 'replacement' of the incoming neutron by a precursor particle, as discussed later. Branchless collisions are actually a generalization of implicit capture, and reduce to implicit capture in non-multiplying media. Note in particular that neutron histories can only be terminated by leakage, encouraging the use of additional population-control algorithms.

Russian roulette and splitting

When particles are assigned statistical weights, it is legitimate to consider the trade-off between increased calculation time and the statistical significance of simulated particles. It may be then advisable to control the distribution of the statistical weights to avoid needlessly spending calculation time on particles that do no matter much for the estimation of scores. Such 'population control' methods must be unbiased in order to preserve the average scores.

Russian roulette is one the simplest ways to ensure that the statistical weight do not become too low [10]. When the statistical weight w of a particle falls below a threshold w_R, the particle plays Russian

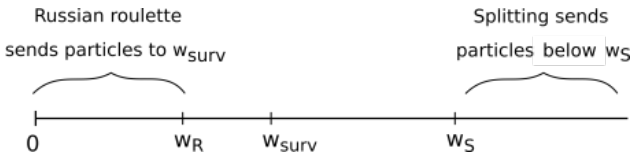

Figure 2.2 : Diagram illustrating the effects of Russian roulette and splitting

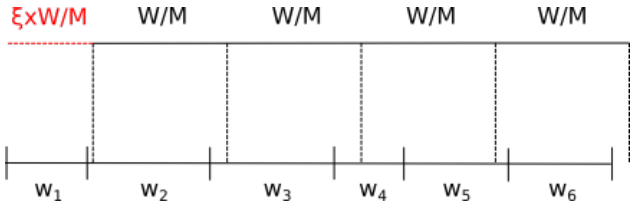

Figure 2.3 : Example of use of weight combing for an initial population of $N = 6$ particles combed to $M = 4$; particles $2, 3, 4, 5$ are copied once, and particle 1 and 6 are ignored. The final tooth falls outside the particle bank.

roulette ; its weight is updated in the following way :

$$\begin{cases} w' = w_{\text{surv}} & \text{with probability } w/w_{\text{surv}} \\ w' = 0 & \text{otherwise,} \end{cases} \tag{2.30}$$

i.e. the particle is either assigned the *survival weight* $w_{\text{surv}} > w_R$, or killed (and thus removed from the Monte Carlo simulation). Note that the particle weight is conserved on average.

Another common variance reduction technique is *splitting*. When the statistical weight w of the particle becomes higher than a threshold w_S, the particle is split in $n_s = \lfloor w/w_S \rfloor$ identical copies, and each copy is assigned a statistical weight $w' = w/n_s$. Again, the particle weight is conserved on average.

One should note that these two algorithms can be applied at any stage of the simulation ; in particular, they can be applied after collisions or before collisions. The effects of the combination of Russian roulette and splitting is illustrated in Fig. 2.2.

Weight combing

Assume a population of N particles of total statistical weight $W = \sum_n w_n$, where the w_n might have a large statistical dispersion. We want to *comb* this population into a new population of M particles sharing the same weight $w_{\text{av}} = W/M$ and having the same total weight $M \times (W/M) = W$ as the initial population. Furthermore, we require combing to be unbiased, in the sense that the average weight of individual particles should be preserved [57].

The combing procedure is better explained by a scheme, and one can refer to Fig. 2.3 for illustration. Essentially, each 'tooth' of the comb corresponds to a copy of a particle in the initial population : if the weight of a particle is large and several teeth fall on the same particle, it will be copied several times and each copy will be assigned the statistical weight w_{av}. Conversely, if the weight of a particle is small, then so is the probability that a tooth falls on it and the particle might not be copied at all. It can be shown that the unbiasedness of the combing scheme is ensured by selecting the first tooth randomly, at position $\xi \times W/M$, with $\xi \sim \mathcal{U}[0, 1]$; the subsequent teeth are identically spaced by W/M.

Several variants of combing exist, as summarized by Variansyah and McLarren in Ref. 49, such as importance-based combing and uniform combing. Nonetheless, weight combing is more commonly used than these variants.

2.3 . Monte Carlo methods for kinetic simulations

The Monte Carlo simulation of time-dependent particle transport is relatively straightforward in principle, and is guided by the idea that each particle is assigned a time label, which is updated based on the ratio of the travelled length over the particle speed. In practice, based on the considerations mentioned in Sec. 2.1.3 concerning the separation of the timescales of neutrons and precursors, and in Sec. 2.1.4 concerning the necessity of estimating the fundamental eigenmode of the Boltzmann equation in order to sample the initial condition for reactors in a critical configuration, the Monte Carlo simulation of reactor physics problems in the kinetic regime poses distinct challenges. The separation of timescales calls for special variance-reduction techniques capable of simultaneously dealing with the fast timescale of neutrons and the long timescale of precursors ; furthermore, the size of the precursor population is expected to be much larger than the size of the neutron population, but only neutrons contribute directly to tallies. Finally, in most applications, the fundamental eigenmode $\varphi_{k_0}(\mathbf{r}, \mathbf{\Omega}, E)$ must be sampled before being able to run a kinetic simulation.

Although time-dependent transport problems have been among the very first Monte Carlo calculations run on computers[1], the challenges recalled here have *de facto* hindered the use of time-dependent Monte Carlo methods for reactor physics applications, where the role of precursors cannot be neglected, until the pioneering work of Sjenitzer and Hoogenboom [17, 18, 58]. These authors have paved the way towards an efficient implementation of kinetic Monte Carlo schemes fully taking into account precursors. Although their results stem from a great amount of ingenuity in conceiving and refining algorithms, it must be also acknowledged that these methodological advances have greatly benefited from the considerable increase in available computer power over the last ten years.

One of the key point of the scheme proposed by Sjenitzer and Hoogenboom is the use of *ad hoc* variance-reduction methods targeting the time variable. The introduction of a collapsed precursor particle, coupled with a forced decay scheme, allows considerably reducing the statistical dispersion due to the timescale of precursors, while preserving the unbiasedness of the scores [59]. The introduction of branchless collisions, including a special modification to account for precursors, allows mitigating the statistical dispersion due to the appearance of branches in neutron histories at each fission event [18]. The introduction of population-control mechanisms such as Russian roulette, splitting and weight combing ensures that the population size does not diverge nor vanish in the course of the kinetic simulation [17, 18].

The strategy of Sjenitzer and Hoogenboom has been implemented over the last few years in several production-level Monte Carlo codes, sometimes with algorithmic improvements, variants and modifications [23, 60–62]. Intense research efforts have been devoted to kinetic Monte Carlo methods, as witnessed by the European H2020 McSAFE project (2017-2020), which was devoted to the industrialization of such methods in view of enhancing their reliability and ease of use for real-world applications [63]. Within this framework, kinetic Monte Carlo simulations have been validated against the experimental data of the reactivity insertion accident (RIA) test campaign carried out in the 1960s on the SPERT III E-core [25, 64]. Extensive verification based on code-to-code comparisons on reactor benchmarks has allowed singling out possible performance issues and identifying future research paths concerning algorithmic and implementation improvements [21, 22]. Among current research trends concerning kinetic Monte Carlo methods, a special role is played by GUARDYAN, the only production-level Monte Carlo code designed specifically for time-dependent Monte Carlo simulations and entirely based on GPUs [56]. The GPU architecture implies massive changes in the way Monte Carlo simulation is performed, but has shown potential for excellent performances [26].

In the next section, we review the most frequently used Monte Carlo methods for kinetic Monte Carlo simulations, including the sampling of the equilibrium source distribution. The general concepts are recalled here, whereas the details of the more complex algorithms are introduced in Chapters 5-6, where they are specifically needed. The overall simulation scheme is illustrated in Algorithm 1 and will

[1] In these simulations, precursors were neglected.

Algorithm 1: Kinetic Monte Carlo scheme

```
Choose tentative source Q;
for each replica m do
    Inject Q into power iteration calculation;
    Iterate until convergence to the stationary state;
    Sample the kinetic source S_m;
    Normalize S_m to desired total weight;
    for each time-step do
        Transport particles;
        Apply population control;
        Save surviving particles for next time-step;
        Accumulate statistics;
```

be detailed in the following.

2.4 . Determining the fundamental eigenpair : the power iteration method

Often, the source for time-dependent problems corresponds to the reactor being in a critical state, which amounts to being able to sample from Eqs. (2.15) and (2.16) at equilibrium. As such, it is necessary to determine the dominant eigenpair $\{k_0, \varphi_{k_0}\}$ of Eq. (2.14), which can be estimated by Monte Carlo methods using the well-known power iteration method [10]. Starting from an arbitrary tentative fission source Q, a 'neutron generation' is sampled : each history of the initial particle population consists of a succession of flights and collisions, whereupon neutrons undergo scattering, fission, or capture. The neutrons are followed until they are absorbed (by fission or capture) or leak out of the system. Upon fission, on average, ν descendant neutrons are sampled and stored in a 'fission bank' (using for instance forced fission), and are not further followed during the current generation. When all the histories of a given generation have been sampled, the neutrons in the fission bank are tested (if required) for population control, and neutrons surviving population control are promoted to source neutrons for the next generation. In addition, before starting the next generation, the weight of each neutron is divided by the generation-wise estimate of the multiplication factor, so that all generations start with the same total weight. It can be shown that, after a sufficiently large number of generations, the fission source distribution reaches a statistical equilibrium, and subsequent generations will be identically *but not independently* distributed. The lack of independence is due to the fact that successive generations are by construction correlated, the fission source for a given generation stemming from the fission sites of the previous generation. The fission source converges towards its fundamental eigenmode, and the ratio between the statistical weights of two successive fission sources converges towards the fundamental eigenvalue k_0. The rate of convergence of the power iteration from an arbitrary initial condition to the stationary state is primarily driven by the *dominance ratio* R, i.e. the ratio k_1/k_0 [30]. The generations that are needed to reach equilibrium are usually called inactive, and are discarded for the purpose of collecting tally statistics, since during this phase of the power iteration the particle distribution has not yet reached its asymptotic stationary behaviour.

For historical reasons, mainly motivated by considerations of computation cost, the sought averages are estimated by running the power iteration for a sufficient number of generations after convergence has been reached, and collecting the required statistics over these so-called *active* generations. Thus, the approach used by Monte Carlo practitioners for power iteration is basically an *ergodic* average, in analogy with equilibrium statistical mechanics. This is to be compared with the standard approach that one would apply to estimate ensemble averages over independent replicas, in which case a collection of power iteration simulations would be needed, each starting from a tentative fission source and having

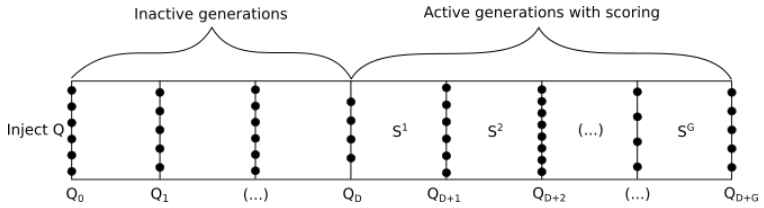

Figure 2.4 : Power iteration scheme when using ergodic average, with D inactive generations and G scoring generations

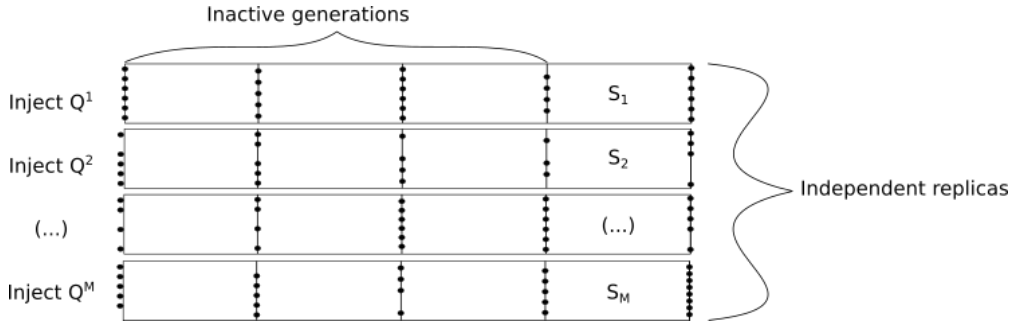

Figure 2.5 : Power iteration scheme when using ensemble average, with D inactive generations and 1 scoring generations.

a sufficient number of inactive generations until convergence, plus a final generation to collect tallies. The ergodic approach to power iteration has been preferred because the involved computer cost is much lower, although this comes at the expense of introducing correlations in the estimated observables. In the literature, the variance obtained using ergodic averages is dubbed 'apparent', in contrast with the true variance that would be obtained running independent replicas [29]. The ergodic and ensemble average approaches for power iteration are illustrated Fig. 2.4 and 2.5, respectively.

2.4.1 . Sampling the stationary source for kinetic problems

Let us assume that the neutron population is distributed according to the fundamental eigenmode $\varphi_{k_0}(\mathbf{r}, \mathbf{\Omega}, E)$: we have recalled in Sec. 2.2.1 that an unbiased estimator for the angular flux consists in tallying the quantity $w/\Sigma_t(\mathbf{r}, E)$ at each collision. Based on Eq. (2.15), the estimator for the initial neutron density at position $\mathbf{r}$ and energy E is thus

$$h_n = \frac{w}{v\Sigma_t(\mathbf{r}, E)}. \tag{2.31}$$

The precursor density for a family j can be simultaneously sampled, provided that the current material is fissile, using the estimator

$$h_c^j = \frac{w\,\nu_d^j}{\lambda_j}\frac{\Sigma_f(\mathbf{r}, E)}{\Sigma_t(\mathbf{r}, E)}.$$

The statistical dispersion due to the large variation of the decay constants λ_j can be considerably reduced by introducing the combined (or collapsed) precursor particle, as defined by Sjenitzer and Hoogenboom [17], a representative particle whose statistical weight depends on the decay rate for each family. The combined precursor density at equilibrium can be estimated using

$$h_c = \frac{w\nu_d}{\bar{\lambda}}\frac{\Sigma_f(\mathbf{r}, E)}{\Sigma_t(\mathbf{r}, E)}, \tag{2.32}$$

where

$$\bar{\lambda} = \frac{\beta}{\sum_j \frac{\beta_j}{\lambda_j}}$$

is the family-averaged decay rate of the combined precursor. It is important to stress that the collapsed precursor sampling scheme is unbiased.

Because the number of collisions, their positions, etc. are random variables, the total statistical weight of the kinetic source is a random variable, which has to be normalized to a known value at the start of the kinetic simulation. It is customary to start the time-dependent simulations with the same total weight as in the calculation leading to the estimation of the fundamental eigenmode $\varphi_{k_0}(\mathbf{r}, \mathbf{\Omega}, E)$ (see Sec. 2.4), although it is possible to choose a different value. In addition, population control can be applied on the kinetic source.

2.4.2 . Sampling the time-dependent process

Let us assume now that the neutron and precursor source needed for time-dependent transport has been sampled, e.g. following the procedure in Sec. 2.4.1. Starting from the source, particle histories are followed through time as described in Algorithm 1. Particles beginning their life at $t = t_0$ are assigned a time label, in addition to the space, direction and energy coordinates that are required for stationary problems.

The tracking of particles over time $[t_0, T]$ is decomposed in discrete (and not necessarily evenly spaced) time intervals $[t_i, t_{i+1}]$: particles are simulated until the end of each time-step, whereupon a population control algorithm such as combing, Russian roulette, and splitting is possibly applied to neutrons and precursors, in order to control the dispersion of statistical weights as well as to keep the total number of simulated particles within acceptable limits. Since neutron and precursor transport is a Markov process, particles can be stopped at arbitrary times without incurring any bias. Thus, the time mesh for kinetic Monte Carlo simulations has to be contrasted with the time mesh used in deterministic calculations, which effectively induces discretization errors in the obtained results.

In addition, a time-grid has to be defined to allow scoring time-dependent tallies. This time-grid does not need to coincide with the time-grid for population control, although it is often the case. Some tallies are based on snapshots of the neutron and/or precursor population at the end of the time bin ; however, most tallies, such as neutron flux or reaction rates, are integrated over each time-window, which means that all contributions falling within the current time bin are summed in the estimator. This procedure is again unbiased.

The life of a neutron during a time-step is simulated as described in Sec. 2.2.2. At each travelled flight length l at speed v is associated a displacement in time by the amount $\delta t = l/v$. The neutron is followed until it undergoes a termination event (leakage, capture in the case of analog simulations, Russian roulette, etc.) or it reaches the end of the current time-step. If the flight duration takes the neutron after the end of the time-step, the neutron is transported until the end of the time-step, and then added to the bank of neutrons that collectively undergo population control before beginning the following time-step. Secondary neutrons and precursors originating from fission events within a time step are stored in a bank of secondary particles whose histories are simulated once the history of the primary particle has been terminated. Due to fission, the typical history will have 'branches', which generally increase both the statistical dispersion and the computer time. Observe in particular that the presence of branches induces non-trivial correlations between particles being present at distinct sites and distinct times, since they might stem from a common ancestor. To cope with the increased variance and computational cost inherent to kinetic simulations, the collision sampling strategy is generally non-analog and encompasses techniques such as branchless collisions (see Sec. 2.2.3).

In an analog decay strategy, precursors are sampled at fission events and emit delayed neutrons following their exponential decay law with parameter λ_j. The analog emission time of the delayed neutron is sampled as

$$\tau = t_b - \frac{1}{\lambda_j} \ln(1 - \xi), \tag{2.33}$$

where t_b is the birth time of the precursor and $\xi \sim \mathcal{U}[0, 1[$. Upon emission, the delayed neutron behaves as any other neutron would.

However, due to the large separation between the timescale of neutrons and the one of precursors, as mentioned earlier, the number of neutrons at a given time is much smaller than the number of precursors when using analog sampling, which motivated the introduction of the 'forced precursor decay' strategy [18, 59]. The idea is to introduce a third time-grid for the simulation, which generally coincides with the tallying time-grid, and enforce precursor decay in each time-step : a fraction of the precursor's statistical weight always survives, related to the probability that the precursor does *not* decay during the time-step. The forced decay time is generally chosen uniformly in each time-step, and precursors are not eliminated upon decay.

After the decay time is sampled, the statistical weight for precursors and for the subsequent delayed neutrons is determined as follows. For a precursor originating from the equilibrium source distribution, the statistical weight reads

$$\mathcal{W}_c^{\mathsf{eq}}(t|t_0) = w_c \sum_j \frac{\bar{\lambda}}{\lambda_j}\frac{\beta_j}{\beta} e^{-\lambda_j(t-t_0)}, \tag{2.34}$$

where w_c it the precursor weight at production time and t_0 is the initial time of the equilibrium source. The remaining fraction of statistical weight leads to the production of a delayed neutron at time t with adjusted statistical weight. Correspondingly, the statistical weight of the delayed neutron is

$$\mathcal{W}_{\mathsf{delayed}}^{\mathsf{eq}}(t|t_0) = w_c(t_{i+1}-t_i) \sum_j \bar{\lambda}\frac{\beta_j}{\beta} e^{-\lambda_j(t-t_0)}, \tag{2.35}$$

where w_c is the parent precursor weight *at the production time of the parent precursor*.

The statistical weight for a precursor produced in the course of the kinetic simulation reads

$$\mathcal{W}_c(t|t_0) = w_c \sum_j \frac{\beta_j}{\beta} e^{-\lambda_j(t-t_0)}, \tag{2.36}$$

where here t_0 denotes the production time (i.e., the time of the fission event) and w_c the associated statistical weight. The corresponding statistical weight of the delayed neutron reads

$$\mathcal{W}_{\mathsf{delayed}}(t|t_0) = w_c(t_{i+1}-t_i) \sum_j \lambda_j\frac{\beta_j}{\beta} e^{-\lambda_j(t-t_0)}. \tag{2.37}$$

Upon decay, the actual family of the combined precursor has to be sampled in order to determine the energy of the delayed neutron. The probability for the delayed neutron to originate from family j is given by

$$p(j,t|t_0) = \frac{\lambda_j \frac{\beta_j}{\beta} e^{-\lambda_j(t-t_0)}}{\sum_k \lambda_k \frac{\beta_k}{\beta} e^{-\lambda_k(t-t_0)}}. \tag{2.38}$$

When using this sampling strategy, the population size of precursors can only increase : precursors are not eliminated by decay anymore, and their number increases due to fission. This suggests the use of population control algorithms to keep the population size manageable. For a thorough discussion, see e.g. Ref. 62.

2.5 . Simplified formulations of the transport equations

The system of Eqs. (2.8) and (2.11) provides a complete description of reactor kinetics. For some applications, if one is interested in trading accuracy for computer time, these equations can be simplified introducing suitable hypotheses. The main interest of such strategy is for deterministic solvers, which in any case must rely on a discretized, and thus approximated, version of the Boltzmann and precursor equations. Nonetheless, simplified formulations of Eqs. (2.8) and (2.11) may also be interesting to obtain closed-form solutions to be compared with Monte Carlo simulation results, or to considerably reduce the computation cost of Monte Carlo simulations. In the following we will briefly examine some of these approaches, detail the resulting equations, and for each propose a Monte Carlo counterpart.

2.5.1 . The multi-group approximation

The multi-group formulation of the transport equation consists in integrating the continuous energy variable E over a finite number G of energy intervals $[E_g, E_{g-1}]$, $g = 1, \cdots, G$, which are called *groups*. Correspondingly, the multi-group angular flux is defined by

$$\varphi_g(\mathbf{r}, \mathbf{\Omega}, t) = \int_{E_g}^{E_{g-1}} \varphi(\mathbf{r}, \mathbf{\Omega}, E, t) dE. \tag{2.39}$$

Integrating Eqs. (2.8) and (2.11) over the energy intervals $[E_g, E_{g-1}]$ yields the system of discretized equations

$$\frac{1}{v_g}\frac{\partial}{\partial t}\varphi_g + \mathbb{L}^G\varphi_g = \mathbb{F}_p^G\varphi_g + \sum_j \frac{\chi_{d,g}^j}{4\pi}\lambda_j c_j(\mathbf{r}, t) + \mathcal{S}_g, \tag{2.40}$$

and

$$\frac{\partial c_j(\mathbf{r}, t)}{\partial t} = \sum_{g'} \int \nu_{d,g'}^j \Sigma_{f,g}\varphi_{g'}(\mathbf{r}, \mathbf{\Omega}', t)\, d\mathbf{\Omega}' - \lambda_j c_j(\mathbf{r}, t). \tag{2.41}$$

The stationary formulation can be expressed similarly. In order to establish Eqs. (2.40) and (2.41), We have made use of the following definitions : the multi-group net loss operator reads

$$\mathbb{L}^G\varphi_g = \mathbf{\Omega}\cdot\nabla\varphi_g + \Sigma_{t,g}\varphi_g - \sum_{g'}\int \nu_{s,g'}\Sigma_{s,g'\to g}(\mathbf{r}, \mathbf{\Omega}' \to \mathbf{\Omega})\varphi_{g'}(\mathbf{r}, \mathbf{\Omega}', t) d\mathbf{\Omega}', \tag{2.42}$$

and the multi-group prompt fission operator reads

$$\mathbb{F}_p^G\varphi_g = \frac{\chi_{p,g}}{4\pi}\sum_{g'}\int \nu_{p,g'}(\mathbf{r})\Sigma_{f,g'}\varphi(\mathbf{r}, \mathbf{\Omega}', t) d\mathbf{\Omega}'. \tag{2.43}$$

By inspection, it is apparent that the multi-group constants (cross sections, spectra, etc.) that occur in Eqs. (2.40) and (2.41) must be of the form

$$\Sigma_{k,g}(\mathbf{r}, \mathbf{\Omega}) = \frac{\int_{E_g}^{E_{g-1}} \Sigma_k(\mathbf{r}, E)\varphi(\mathbf{r}, \mathbf{\Omega}, E, t) dE}{\varphi_g(\mathbf{r}, \mathbf{\Omega}, t)} \tag{2.44}$$

for the cross sections of reaction k, and

$$\Sigma_{s,g'\to g}(\mathbf{r}, \mathbf{\Omega}) = \frac{\int_{E_g}^{E_{g-1}}\int_{E_{g'}}^{E_{g'-1}} \Sigma_s(\mathbf{r}, \mathbf{\Omega}' \to \mathbf{\Omega}, E' \to E)\varphi(\mathbf{r}, \mathbf{\Omega}, E, t) dE\, dE'}{\varphi_{g'}(\mathbf{r}, \mathbf{\Omega}', t)}, \tag{2.45}$$

for the scattering differential cross section. The other constants of the multi-group equations have similar angular-flux-weighted expressions.

Observe that the weighting factor appearing in the multi-group constants is precisely the angular flux $\varphi(\mathbf{r}, \mathbf{\Omega}, E, t)$, which is the unknown solution of the original system of Eqs. (2.8) and (2.11). Therefore, in order to achieve a rigorous derivation of the parameters of the multi-group equations one should have already solved the continuous-energy problem, which is what we wanted to avoid in the first place. Furthermore, observe that now the multi-group cross sections depend also on the particle direction $\mathbf{\Omega}$, contrary to the regular continuous-energy cross section, due to the dependence on $\varphi(\mathbf{r}, \mathbf{\Omega}, E, t)$. The problem of computing reliable multi-group constants has attracted enormous research efforts, since the beginning of the era of computational methods for reactor physics problems, and goes well beyond the scope of this manuscript. In the context of the numerical methods developed for deterministic solvers, it is common practice to inject into the definitions of the multi-group constants a tentative flux shape, derived by carefully taking into account self-shielding effects using state-of-the-art models (see e.g. [65–69]). More recently, Monte Carlo codes have been successfully used in order to estimate the multi-group constants [70–73].

The analysis of fluctuations and correlations in kinetic Monte Carlo problems carried out in Chapter 6 will be based on Eqs. (2.40) and (2.41), in order to keep the computation cost within reasonable limits. For the benchmark calculations performed in this context, the multi-group constants are given in the literature. This means that the Monte Carlo sampling procedures outlined in Sec. 2.2 and in Sec. 2.3 for continuous-energy particle transport can be immediately transposed to the multi-group case. Each particle is assigned an index g for the group, instead of the continuous energy variable E. The particle speed is also replaced by the group speed v_g. Cross sections are dealt with exactly as in the continuous-energy case ; the scattering transfer kernel is now a matrix, and the outgoing group g' can be straightforwardly sampled (conditioned to the incident energy group g) once the matrix elements have been properly normalized. Position and direction are not discretized.

2.5.2 . The diffusion approximation

In Chapter 3-4, we will derive analytical results for the statistical moments of the fluctuations and correlations in kinetic Monte Carlo methods, which will pave the way towards a sound and reliable framework for the interpretation of the simulation results. For this purpose, we will need closed-form expressions for the first few moments (and other related observables) of the neutron and precursor populations. The multi-group Eqs. (2.40) and (2.41) are in general not amenable to exact solutions, which is why we will further simplify the underlying equations by introducing the diffusion approximation.

There exist several ways of introducing the diffusion equation based on the Boltzmann equation [2]. In one approach, the derivation of the diffusion equation relies on the so-called P_N expansion : the Boltzmann equation is integrated over the direction $\mathbf{\Omega}$ and one tries to single out terms depending on the scalar flux

$$\varphi(\mathbf{r}, E, t) = \int \varphi(\mathbf{r}, \mathbf{\Omega}, E, t) d\mathbf{\Omega} \tag{2.46}$$

alone. Usually, the derivation is done by neglecting energy, and then rephrasing the resulting equation into a multi-group formalism. The key idea is that the equation for $\varphi(\mathbf{r}, t)$ obtained integrating the Boltzmann equation over the direction is not closed, since it depends on the current

$$\mathbf{J}(\mathbf{r}, t) = \int \mathbf{\Omega} \varphi(\mathbf{r}, \mathbf{\Omega}, t) d\mathbf{\Omega}. \tag{2.47}$$

The P_0 equation reads

$$\frac{1}{v}\frac{\partial \varphi}{\partial t} + \nabla \cdot \mathbf{J} + \Sigma_a(\mathbf{r})\varphi = \nu_p \Sigma_f(\mathbf{r})\varphi + \sum_j \lambda_j c_j(\mathbf{r}) + Q \tag{2.48}$$

and is basically a conservation law, with $\Sigma_a(\mathbf{r}) = \Sigma_t(\mathbf{r}) - \Sigma_s(\mathbf{r})$ and Q the angle-integrated external source. The equations for the precursor concentrations $c_j(\mathbf{r}, t)$ follow from

$$\frac{\partial c_j}{\partial t} = \nu_d^j \Sigma_f(\mathbf{r})\varphi - \lambda_j c_j(\mathbf{r}). \tag{2.49}$$

Observe that no approximations have been introduced so far : the P_0 Eqs. (2.48) and (2.49) are exact (in a single-speed framework), albeit not closed, since Eq. (2.48) depends on the unknown quantity $\mathbf{J}(\mathbf{r}, t)$, whose equation must be determined.

The P_1 equation for $\mathbf{J}(\mathbf{r}, t)$ can be then written down multiplying the Boltzmann equation by $\mathbf{\Omega}$ and integrating again over directions, in order to single out terms depending on $\mathbf{J}(\mathbf{r}, t)$ and on $\varphi(\mathbf{r}, t)$ alone. It turns out that the equation for $\mathbf{J}(\mathbf{r}, t)$ is not closed either, since it involves higher-order moments. We obtain a hierarchy of P_N equations, each being exact (up to the fact that we have neglected the energy dependence) but not solvable, as the hierarchy is infinite.

The diffusion approximation is obtained by truncating the hierarchy at the order P_1, assuming that the current and the scalar flux are related by

$$\mathbf{J}(\mathbf{r}, t) = -\mathcal{D}(\mathbf{r}) \nabla \varphi(\mathbf{r}, t), \tag{2.50}$$

which takes the name of Fick's law, by analogy with the similar relation occurring in the equation describing the transport of mass. In Eq. (2.50), the quantity

$$\mathcal{D}(\mathbf{r}) = \frac{1}{3\Sigma_{tr}(\mathbf{r})} \tag{2.51}$$

is the diffusion coefficient, with $\Sigma_{tr}(\mathbf{r}) = \Sigma_t(\mathbf{r}) - \bar{\mu}\Sigma_s(\mathbf{r})$ the so-called transport cross section, and $\bar{\mu}$ the average scattering angle. For isotropic scattering, for example, $\bar{\mu} = 0$. Injecting Fick's law into the P_0 equation, we finally obtain the *diffusion equation* for single-speed particles, namely,

$$\frac{1}{v}\frac{\partial \varphi}{\partial t} - \nabla \cdot (\mathcal{D}(\mathbf{r})\nabla\varphi) + \Sigma_a(\mathbf{r})\varphi = \nu_p\Sigma_f(\mathbf{r})\varphi + \sum_j \lambda_j c_j(\mathbf{r}) + Q(\mathbf{r}), \tag{2.52}$$

to be coupled with the precursor Eq. (2.49). We have assumed that the source is isotropic.

For the special case where the material properties are spatially homogeneous, we have $\nabla\cdot\mathcal{D}\nabla = \mathcal{D}\nabla^2$, and the diffusion equation takes the form

$$\frac{1}{v}\frac{\partial \varphi}{\partial t} - \mathcal{D}\nabla^2\varphi + \Sigma_a(\mathbf{r})\varphi = \nu_p\Sigma_f(\mathbf{r})\varphi + \sum_j \lambda_j c_j(\mathbf{r}) + Q(\mathbf{r}), \tag{2.53}$$

Once the single-speed diffusion equation has been introduced, a multi-group version can be obtained based on the analogy with the multi-group formalism for the Boltzmann equation, although a rigorous derivation is much more involved than in the single-speed case. This would read

$$\frac{1}{v_g}\frac{\partial \varphi_g}{\partial t} - \nabla \cdot (\mathcal{D}_g\nabla\varphi_g) + \Sigma_{t,g}\varphi_g = \sum_{g'} \Sigma_{s,g'\to g}\varphi_{g'} + \chi_{p,g}\sum_{g'}\nu_{p,g'}\Sigma_{f,g'}\varphi_{g'} + \sum_j \lambda_j c_j + Q_g, \tag{2.54}$$

coupled with

$$\frac{\partial c_j}{\partial t} = \chi^j_{d,g}\sum_{g'}\nu^j_{d,g'}\Sigma_{f,g'}\varphi_{g'} - \lambda_j c_j. \tag{2.55}$$

The diffusion equation can be solved using Monte Carlo simulation (assuming again that all the constants occurring in the equation are known). However, contrary to the multi-group version of the Boltzmann equation, the diffusion equation calls for an entirely different distribution for the particle displacements. The diffusion equation for neutrons has the same functional form as the well-known diffusion equation related to e.g. the heat equation, for which a rigorous mapping based on the Feynman-Kac formalism allows phrasing the solution of the equation in terms of a Wiener stochastic process, better known as Brownian motion [74]. For the case of the neutron diffusion equation, the fission term (which has no analogue in the heat equation) can be dealt with by endowing the Brownian motion with the possibility of branching [75].

For the sake of conciseness, we will detail here the simpler case of the single-speed diffusion equation in homogeneous materials, with a single precursor family. Suppose that, at a given time, $N(t)$ neutrons and $M(t)$ precursors are present in the system. Neutrons undergo regular Brownian motion with diffusion coefficient $\mathcal{D}$, until an event occurs. For each neutron, the fission rate is $v\Sigma_f$, and the capture rate is $v\Sigma_c$: the distribution of these events being exponential in time, the time to the first neutron interaction is sampled as

$$\delta t_i = -\frac{1}{v(\Sigma_c + \Sigma_f)N(t)}\log(1-\xi), \tag{2.56}$$

with $\xi \sim \mathcal{U}[0,1[$. For precursors, the only event is decay, which happens at rate λ : the time to the first precursor decay is sampled as

$$\delta t_d = -\frac{1}{\lambda M(t)}\log(1-\xi), \tag{2.57}$$

with $\xi \sim \mathcal{U}[0,1[$. We take then the time increment to the next event as $\delta t = \min(\delta t_d, \delta t_i)$. The motion of individual neutrons is sampled from

$$\delta x \sim \mathcal{N}(0, 2d\,\mathcal{D}\,\delta t), \tag{2.58}$$

where $\mathcal{N}(\mu, \sigma^2)$ is the normal law of mean μ and variance σ^2, and d is the dimension. If required, boundary conditions are applied. When all new neutron positions have been sampled, the stopping event is treated : upon fission, ν_p prompt neutrons and ν_d precursors are produced on average, as customary ; upon capture, the neutron is removed from the simulation ; and upon decay a precursor is transformed into a delayed neutron. If δt is larger than the duration of the time interval that is used for tallying the physical observables of interest, the population is stopped at the end of the time step and then restarted without memory, which does not introduce any bias because of the Markov nature of the underlying stochastic process.

2.6 . Beyond the average : fluctuations and correlations

Throughout this Chapter, we have been concerned with establishing the neutron and precursor transport equations in the kinetic regime, either in their exact formulation or under some simplifying hypotheses, and we have shown how these equations can be solved by Monte Carlo methods sampling the random walks of neutrons and precursors in the phase space.

Thanks to the increasing computer power, it becomes possible today to address non-stationary problems by Monte Carlo simulation, which allows for an 'exact' treatment of the geometry and of the physics of the simulated system, introducing virtually no approximations nor discretization effects. Monte Carlo simulations therefore produce unbiased estimates of the first moments of the sought observables, which are precisely the solutions of the kinetic equations.

However, as detailed in the previous sections and in Chapter 1, such estimates come with a statistical uncertainty that is (asymptotically) inversely proportional to the square root of the number of sampled histories. The almost complete absence of approximations is thus thwarted by the very high calculation cost required to achieve the target accuracy, especially in kinetic simulations. Furthermore, the behaviour of the statistical uncertainty is made more complex by the fact that the simulated particle histories are correlated, the correlations stemming ultimately from fission events.

Since in most cases Monte Carlo simulations involve some forms of variance-reduction and population-control techniques, the behaviour of fluctuations and correlations in kinetic Monte Carlo simulations depends on the non-trivial interplay between the way the sampling strategies are conceived, and the effects inherent to the physics-inspired underlying stochastic processes. In the following Chapters, we will attempt at establishing a rigorous framework that enables to quantify such fluctuations and correlations, and thus enhance the reliability of the uncertainty estimation in kinetic Monte Carlo simulation.

2.7 . Simulation tools developed for this work

The investigation of correlations occurring in Monte Carlo methods, either in stationary problems over generations or in time-dependent problems over time, could hardly be carried out entirely based on a theoretical framework, and the support of simulations is of course compulsory, especially in the case of complex systems including energy effects and spatial heterogeneity. On the other hand, it turns out that the use of production-level Monte Carlo codes is not an appropriate choice, since correlation functions and related quantities are typically very expensive to compute ; the memory footprint is especially large. On top of that, for our investigation we often need to extensively modify the traditional sampling strategies and implement unusual scores (as discussed in the following chapters), which is in most cases cumbersome due to the complexity of production-level codes.

For these reasons, we have decided to develop our own simulations codes from scratch.

First, we focused on correlations in time-dependent branching Brownian motion, a convenient stochastic representation for diffusion-based models. For this purpose, we developed *JOFFREY*, a Monte Carlo mini-app performing analog simulations of time-dependent branching Brownian motion of a population of neutrons and precursors in a one-dimensional homogeneous, multiplicative medium.

Next, as we focused on more realistic systems, we implemented *COYOTE*, a Monte Carlo simulation

mini-app coupling a traditional power iteration module with a time-dependent transport module, in a multi-group framework. Coyote supports slab geometries, with an arbitrary number of slabs associated to possibly different materials. Each material is defined by its energy-dependent macroscopic cross-sections and kinetic parameters. The boundary conditions can be periodic, reflection, or vacuum. Coyote comes with a set of variance-reduction methods that can be freely and independently activated : Russian roulette and splitting, several versions of branchless collisions, forced fission, implicit capture, forced decay of precursors, combined precursor, and importance ratios. Population control can be enforced by weight combing and sampling without replacement (in the power iteration module). The tallies are numerous and range from usual flux-based quantities to correlation functions, pair distance functions, Feynman moments of the fission sites distribution, etc., as detailed in the following. Ensemble or ergodic averages can be computed, which is particularly useful for the analysis of correlations.

Première partie

Correlations in time-dependent diffusion problems solved by analog Monte Carlo methods

3 -Space-time correlations in simplified kinetic simulations with neutrons and precursors

Kinetic Monte Carlo simulation lends itself quite naturally to the investigation of the statistical behaviour of stochastic neutron and precursor populations around their average. However, in order to establish a clear framework for our investigations, it is convenient to start our analysis from a model that is simple enough to obtain exact results, and yet sufficiently non-trivial to retain all the basic ingredients of realistic multiplying systems. This allows extracting the main trends, the scaling laws and the key guidelines that will be used in the following chapter for the interpretation of more complex time-dependent Monte Carlo simulations, including some elementary population-control mechanisms.

The aim of this chapter is thus to characterize the behaviour of space-time correlations and fluctuations in a simplified model of nuclear reactor. For this purpose, instead of considering the (generally non-analog) Monte Carlo solution of the Boltzmann equation, we will introduce a diffusion-based set of stochastic rules mimicking the neutron and precursors dynamics that can be sampled by analog Monte Carlo methods. The well known Galton-Watson birth-and-death stochastic process will be modified to account for precursors, which yields a two-species model with different transition rates for each species [76]. The modified Galton-Watson stochastic process will be coupled with a model of random spatial displacements within the diffusion approximation, which under suitable assumptions can be derived from the exact neutron transport theory, as mentioned in Sec. 2.5.2. The combination of these two stochastic processes results in a Branching Brownian Motion (BBM), whose statistical moments will be shown to be attainable by analytical means. This is to be contrasted with the stochastic process underlying the Boltzmann equation, which is seldom amenable to closed-form solutions for its statistical moments. In the diffusion framework, and relying mainly on the Pál-Bell backward formalism, we will be able to derive exact expressions for the characteristic quantities describing the behaviour of space-time correlations of neutrons and precursors in a nuclear reactor, and we will compare them to analog Monte Carlo simulation results obtained by directly sampling the BBM model, which will be used as a reference.

While our focus here is on the investigation of neutron fluctuations in kinetic simulations, the use of analog Monte Carlo methods (where the sampling laws are directly inspired by the underlying physical process occurring in multiplying systems) allows immediately transposing the results obtained in this Chapter to the analysis of neutron fluctuations occurring in the real systems, up to a scaling factor due to the fact that the number of sampled particles in Monte Carlo simulations is usually much lower than the number of particles that are present in a nuclear reactor[1].

Most of the material presented in this chapter is taken from our published work in Ref. 77.

3.1 . A simple stochastic model for nuclear reactor physics

In the simplest incarnation of our nuclear reactor model [48], we represent the random movement of neutrons as a Brownian motion with a diffusion coefficient $\mathcal{D}$, and we use a Galton-Watson birth-death process to describe fission and capture. Each neutron undergoes sterile capture at a rate $\gamma = 1/v\Sigma_c$ and fission events at a rate $\beta = 1/v\Sigma_f$. Captured neutrons are simply killed. When fission occurs, a random number of new neutrons are emitted at the position of the incident neutron, which is killed [78]. The probability to emit instantaneously k *prompt* neutrons is denoted as p_k. *Delayed* neutrons may further appear at the spatial site of a fission event after a random, exponentially distributed time with rate λ, corresponding to the decay of the *delayed neutron precursors* [78]. We denote by q_k the probability that k delayed neutron precursors are created at a fission event. For illustration, some representative neutron and precursor histories are shown in Fig. 3.1. In nuclear reactors, the average precursor decay time $1/\lambda$ is

[1] With the only possible exception of start-up or shut-down regimes, where the reactor is operated at very low power.

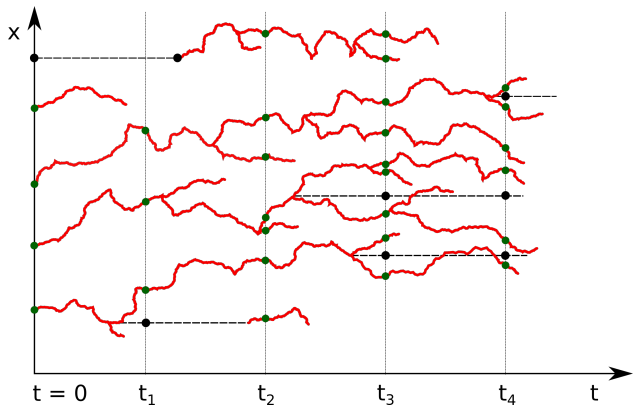

Figure 3.1 : Schematic illustration of the evolution of neutrons and precursors in the simplest model (anarchic model). At time $t = 0$, 4 neutrons and 1 precursor are present. Neutrons (red solid lines) diffuse and undergo fission and capture; precursors (dashed black lines) do not diffuse. When they decay, they are replaced by a neutron at the same position. Because of the birth-death process, the total number of neutrons and the total number of precursors fluctuate.

typically much larger than the average neutron lifetime $1/(\gamma+\beta)$. Furthermore, denoting respectively by $\nu_{p,1} = \sum_k k p_k$ and $\nu_{d,1} = \sum_k k q_k$ the average number of prompt and delayed neutrons resulting from fission, we typically have $\nu_{p,1} \gg \nu_{d,1}$ [78]. For reasons that will become clear in the following, we are using the notation $\nu_{p,l}$ and $\nu_{d,l}$ to indicate the l-th falling factorial moments of the number of neutrons and precursors produced from fission, respectively, with

$$\nu_{p,l} = \sum_{k=0}^{\infty} k(k-1)\dots(k-l+1)\, p_k \tag{3.1}$$

and

$$\nu_{d,l} = \sum_{k=0}^{\infty} k(k-1)\dots(k-l+1)\, q_k. \tag{3.2}$$

For the sake of simplicity, our model neglects the energy dependence of the neutron-matter interaction rates. Furthermore, the spatial structure of the reactor core will be simplified by assuming that all the material properties (diffusion coefficient, fission and capture rates) are homogeneous. All the physical parameters are taken to be uniform in space and constant in time. Contrary to Ref. 48, which considered unbounded systems, here the reactor will be modeled as a finite-size box with reflection (Neumann) boundary conditions, mimicking the fact that in nuclear reactors neutron leakage from the core is deliberately kept small. To simplify matters even further, we will focus on one-dimensional systems, which are more easily amenable to analytical solutions : in what follows, we will thus consider a one-dimensional reactor of half-size L, i.e. the $[-L, L]$ segment. This model captures the key physical mechanisms that are responsible for the fluctuations of the fission chains.

Throughout this chapter, we will use the parameter values given in Tab. 3.1, whose units are arbitrary.

3.1.1 . The critical regime

Nuclear reactors are operated at the critical regime, where the equilibrium between births by fission and deaths by capture allows the neutron population and hence the heat production to be stationary on average [78]. In our model, criticality is imposed by requiring that

$$\beta(\nu_{p,1} + \nu_{d,1} - 1) = \gamma, \tag{3.3}$$

which is equivalent to equating the production and disappearance rates. The criticality condition does not depend on the number of neutrons present in the system : indeed, nuclear reactors can be operated at

	$\theta = 1$	$\theta = 10^{-1}$	$\theta = 10^{-3}$
N	10^2	10^2	10^2
M	10^2	10^3	10^5
L	1	1	1
$\mathcal{D}$	10^{-2}	10^{-2}	10^{-2}
β	0.2	0.2	0.2
γ	0.3	0.3	0.3
λ	10^{-1}	10^{-2}	10^{-4}
$\nu_{p,1}$	2	2	2
$\nu_{d,1}$	0.5	0.5	0.5
$\nu_{p,2}$	2	2	2
$\nu_{d,2}$	0	0	0

Table 3.1 : Different sets of parameters used in this work. Here N is the initial (average) number of neutrons, M is the initial (average) number of precursors, L is the box half-size, $\mathcal{D}$ is the diffusion coefficient, β is the fission rate, γ is the capture rate, λ is the decay rate of precursors, $\nu_{p,l}$ and $\nu_{d,l}$ are the l-th falling factorial moments of the number of neutrons and precursors produced from fission, respectively, and $\theta = \lambda/(\beta\nu_{d,1})$. Units are arbitrary.

steady-state at virtually any power level, the power being proportional to the average number of neutrons in the core. Due to its inherently stochastic nature, the neutron population density at a spatial site will display fluctuations (often dubbed 'neutron noise' [78]) because of random displacements in and out the spatial cell and because of random changes in the number of particles following fission and capture events within the cell.

3.1.2 . Observables of interest

Fluctuations are characterized by the statistical moments of the neutron and precursor population as a function of position and time. Let V_1 and V_2 be two non-overlapping 'detectors'[2] located within the reactor. We are interested in computing the average number of neutrons $\mathbb{E}[n_i](t_i)$ and precursors $\mathbb{E}[m_i](t_i)$ present at time t_i in detector $i \in \{1, 2\}$, and the two-point correlations between particles detected in V_1 at time t_1 and particles detected in V_2 at time t_2, which stem from the cross-moments $\mathbb{E}[n_1 n_2](t_1, t_2)$, $\mathbb{E}[n_1 m_2](t_1, t_2)$, and $\mathbb{E}[m_1 m_2](t_1, t_2)$. Often, it is preferable to work with continuous observables : we therefore define the neutron and precursor densities by taking the limits

$$n(x_i, t_i) = \lim_{V_i \to 0} \frac{\mathbb{E}[n_i](t_i)}{V_i} \tag{3.4}$$

$$m(x_i, t_i) = \lim_{V_i \to 0} \frac{\mathbb{E}[m_i](t_i)}{V_i}, \tag{3.5}$$

where x_i is the center of the detector location, $i \in \{1, 2\}$. The average population sizes are then obtained by integrating the particle densities over the entire system :

$$n(t) = \int n(x, t)\, dx \tag{3.6}$$

$$m(t) = \int m(x, t)\, dx. \tag{3.7}$$

[2]We assume for the sake of simplicity a perfect detection process : in our model, all the neutrons falling within a given region V_i, $i \in \{1, 2\}$, are counted.

Similarly, we define the pair correlation functions by taking the limits

$$u(x_1,t_1,x_2,t_2) = \lim_{V_1,V_2\to 0} \frac{\mathbb{E}[n_1 n_2](t_1,t_2)}{V_1 V_2} \tag{3.8a}$$

$$v(x_1,t_1,x_2,t_2) = \lim_{V_1,V_2\to 0} \frac{\mathbb{E}[n_1 m_2](t_1,t_2)}{V_1 V_2} \tag{3.8b}$$

$$w(x_1,t_1,x_2,t_2) = \lim_{V_1,V_2\to 0} \frac{\mathbb{E}[m_1 m_2](t_1,t_2)}{V_1 V_2}. \tag{3.8c}$$

The function $u(x_1,t_1,x_2,t_2)$ fully characterizes the behavior of fluctuations and correlations of the neutron population, and in this respect is key to the investigation of neutron noise. Similarly as for the case of the average densities, integral quantities can be obtained by integrating the previous equations over the whole spatial domain : for the two-point neutron correlation function, e.g., we would have

$$u(t_1,t_2) = \iint u(x,t_1,y,t_2)\,dx\,dy. \tag{3.9}$$

The information content of the two-point correlation function can be conveniently condensed in the *mean-squared neutron pair distance* $\langle r^2\rangle(t)$, which is defined as

$$\langle r^2\rangle(t) = \frac{\iint (x_1-x_2)^2 u(x_1,t,x_2,t)\,dx_1\,dx_2}{u(t,t)}, \tag{3.10}$$

which is also helpful in assessing the behaviour of neutron noise [28, 79].

3.2 . A theoretical framework for correlations analysis in the anarchic model

We begin our analysis by assuming that the neutron and precursor populations are free to evolve according to the stochastic rules described in Sec. 3.1, without any constraint. This system, which we will call the *anarchic* model (for illustration, see Fig. 3.1), is representative of an analog kinetic Monte Carlo simulation where no population control is imposed on the particle histories. The equations for the particle density and for the two-point correlation functions can be conveniently established using the backward master equation approach proposed by Pál and Bell (which is a special case of the Feynman-Kac backward formalism) [78, 80]. The idea is to first derive the equations for the moments $n'_i(x_0,t_0) = n(x_i,t_i|x_0,t_0)$, with $i\in\{1,2\}$, and $u'_{1,2}(x_0,t_0) = u(x_1,t_1,x_2,t_2|x_0,t_0)$, conditioned to having *a single initial neutron* starting from position x_0 at time t_0, treating x_1, x_2, t_1 and t_2 as parameters, and x_0 and t_0 as variables. While the method is general, the derivation proposed below is original.

3.2.1 . Derivation of the (backward) moment equations for a single initial particle

Let $\mathcal{P}(n_1,t_1,n_2,t_2|x_0,t_0)$ be the probability to find n_1 particles at time t_1 in detector V_1 and n_2 particles at time t_2 in detector V_2, for a single particle starting in x_0 at time t_0, with $t_2 > t_1$; the results for $t_2 < t_1$ are recovered by arguments of symmetry. Pál and Bell have independently derived a backward formalism yielding the (adjoint) master equation for $\mathcal{P}$. The manipulation of the resulting equation is rather cumbersome, and in most cases neutron noise can be characterized using the lowest-order moments of n_1 and n_2. We will be in particular interested in the average number of neutrons in detector V_1 at time t_1, namely,

$$\mathbb{E}[n_1](t_1|x_0,t_0) = \sum_{n_1,n_2} n_1 \mathcal{P}(n_1,t_1,n_2,t_2|x_0,t_0) \tag{3.11}$$

and in the two-point correlation function between particles detected in V_1 at time t_1 and particles detected in V_2 at time t_2, namely,

$$\mathbb{E}[n_1 n_2](t_1,t_2|x_0,t_0) = \sum_{n_1,n_2} n_1\, n_2\, \mathcal{P}(n_1,t_1,n_2,t_2|x_0,t_0). \tag{3.12}$$

By virtue of these considerations, it is therefore more convenient to introduce the probability-generating function associated to $\mathcal{P}$, namely,

$$W(z_1, z_2, x_0, t_0) = \sum_{n_1} \sum_{n_2} z_1^{n_1} z_2^{n_2} P(n_1, n_2, t_1, t_2 | x_0, t_0), \tag{3.13}$$

where z_i is the conjugate variable of n_i, $i \in \{1, 2\}$, and hence derive the equations for the (falling factorial) moments, which follow from

$$\mathbb{E}[n_1(n_1-1)\dots(n_1-k+1)n_2(n_2-1)\dots(n_2-l+1)](t_1, t_2|x_0, t_0) = \frac{\partial^{k+l}}{\partial z_1^k \partial z_2^l} W(z_1, z_2, x_0, t_0)|_{z_1=1, z_2=1}, \tag{3.14}$$

with $k, l \geq 0$ and the normalization $W(1, 1, x_0, t_0) = 1$. It can be shown that $W(z_1, z_2, x_0, t_0)$ satisfies the non-linear backward evolution equation

$$-\frac{\partial}{\partial t_0} W = \mathcal{D}\nabla_{x_0}^2 W - (\gamma + \beta)W + \beta G_p(W) G_d(W_d) + \gamma, \tag{3.15}$$

where $G_p(z) = \sum_k z^k p_k$ is the probability-generating function associated to the prompt fission probability distribution p_k and $G_d(z) = \sum_k z^k q_k$ is the probability-generating function for the precursor probability distribution q_k [80]. The quantity W_d in Eq. (3.15) is the probability-generating function associated to the creation of a precursor at (x_0, t_0), namely,

$$W_d(z_1, z_2|x_0, t_0) = \lambda \int_{t_0}^{\infty} e^{-\lambda(t'-t_0)} W(z_1, z_2|x_0, t') dt'. \tag{3.16}$$

Taking the derivative of Eq. (3.15) once with respect to z_1 and using the definition in Eq. (3.14), we obtain the evolution equation for the average neutron number in V_1, for a single starting particle in (x_0, t_0) :

$$\mathcal{L}^\dagger \mathbb{E}[n_1](t_1|x_0, t_0) = 0, \tag{3.17}$$

where $\mathcal{L}^\dagger$ is a backward linear operator defined by

$$\mathcal{L}^\dagger f(x_0, t_0) = \frac{\partial f}{\partial t_0} + \mathcal{D}\nabla_{x_0}^2 f + \alpha_p f + \beta \nu_{d,1} \lambda \int_{t_0}^{\infty} f(x_0, t') e^{-\lambda(t'-t_0)} dt', \tag{3.18}$$

with the shorthand

$$\alpha_p = \beta(\nu_{p,1} - 1) - \gamma. \tag{3.19}$$

Equation (3.17) is to be solved with the final condition

$$\mathbb{E}[n_1](t_1|x_0, t_0 = t_1) = \begin{cases} 1 & \text{if } x_0 \in V_1 \\ 0 & \text{otherwise.} \end{cases} \tag{3.20}$$

Letting $\mathcal{G}(x, t, x_0, t_0)$ be the Green's function associated to the operator $\mathcal{L}^\dagger$, the solution to Eq. (3.17) reads

$$\mathbb{E}[n_1](t_1|x_0, t_0) = \int dx' \chi_{V_1}(x') \mathcal{G}(x', t_1, x_0, t_0), \tag{3.21}$$

where $\chi_V(x)$ is the characteristic function of a domain V.

Taking the mixed derivative of Eq. (3.15) with respect to z_1 and z_2, and using again the definition in Eq. (3.14), we obtain the evolution equation for the two-point correlation function, for a single particle starting in (x_0, t_0) :

$$\mathcal{L}^\dagger \mathbb{E}[n_1 n_2](t_1, t_2|x_0, t_0) = -f_{\text{corr}}(t_1, t_2|x_0, t_0), \tag{3.22}$$

where we have defined

$$f_{\text{corr}}(t_1,t_2|x_0,t_0) = \beta\nu_{p,2}\mathbb{E}[n_1]\mathbb{E}[n_2] + \beta\nu_{p,1}\nu_{d,1}\mathbb{E}[n_1]\lambda\int_{t_0}^{t_2} e^{-\lambda(t'-t_0)}\mathbb{E}[n_2](t')dt' + \beta\nu_{p,1}\nu_{d,1}\mathbb{E}[n_2]\lambda\int_{t_0}^{t_1} e^{-\lambda(t'-t_0)}\mathbb{E}[n_1](t')dt' + \beta\nu_{d,2}\lambda^2\int_{t_0}^{t_1} e^{-\lambda(t'-t_0)}\mathbb{E}[n_1](t')dt'\int_{t_0}^{t_2} e^{-\lambda(t'-t_0)}\mathbb{E}[n_2](t')dt' \quad (3.23)$$

with the shorthand notation $\mathbb{E}[n_i] = \mathbb{E}[n_i](t_1|x_0,t_0)$, $i \in \{1,2\}$. Equation (3.22) is to be solved with the final condition

$$\mathbb{E}[n_1n_2](t_0=t_1) = \begin{cases} \mathbb{E}[n_2](t_2|x_0,t_0=t_1) & \text{if } x_0 \in V_1 \\ 0 & \text{otherwise.} \end{cases} \quad (3.24)$$

Using the Green's function associated to the operator $\mathcal{L}^\dagger$, the solution to Eq. (3.22) can be expressed as

$$\mathbb{E}[n_1n_2](t_1,t_2|x_0,t_0) = \int dx'\chi_{V_1}(x')\mathbb{E}[n_2](t_2|x',t_1)\mathcal{G}(x',t_1,x_0,t_0) + \int_{t_0}^{t_1} dt'\int dx' f_{\text{corr}}(t_1,t_2|x',t')\mathcal{G}(x',t',x_0,t_0). \quad (3.25)$$

The continuous version of Eqs. (3.21) and (3.25) can be obtained by centering the detector regions V_1 and V_2 around x_1 and x_2, respectively, defining

$$n(x_1,t_1|x_0,t_0) = \lim_{V_1\to 0}\frac{\mathbb{E}[n_1](t_1|x_0,t_0)}{V_1}$$
$$u(x_1,t_1,x_2,t_2|x_0,t_0) = \lim_{V_1,V_2\to 0}\frac{\mathbb{E}[n_1n_2](t_1,t_2|x_0,t_0)}{V_1V_2}$$

and letting the detector sizes shrink to zero.

3.2.2 . Analysis of the Green's function of $\mathcal{L}^\dagger$

By separation of variables, the Green's function $\mathcal{G}(x,t|x_0,t_0)$ associated to $\mathcal{L}^\dagger$ can be expressed as

$$\mathcal{G}(x,t,x_0,t_0) = \sum_{k=0}^{+\infty}\varphi_k(x)\varphi_k^\dagger(x_0)T_k(t|t_0), \quad (3.26)$$

where the time-eigenfunctions $T_k(t|t_0)$ read

$$T_k(t|t_0) = \left(\omega_k^+ - \omega_k^-\right)^{-1} \times \left[e^{\omega_k^+(t-t_0)}(\omega_k^+ + \lambda) - e^{\omega_k^-(t-t_0)}(\omega_k^- + \lambda)\right], \quad (3.27)$$

with two associated families of eigenvalues

$$\omega_k^\pm = \frac{\alpha_k + \alpha_p - \lambda \pm \sqrt{(\alpha_k+\alpha_p+\lambda)^2 + 4\lambda\beta\nu_{d,1}}}{2}. \quad (3.28)$$

The quantities α_k are the eigenvalues associated to operator $\mathcal{D}\nabla_x^2$, with the corresponding eigenfunctions $\varphi_k(x)$. For reflection boundary conditions, we have $\alpha_k = -\mathcal{D}(k\pi/2L)^2$ and

$$\varphi_k(x) = \cos\left(\frac{k\pi x}{2L}\right) \quad (3.29)$$

for $k \geq 0$. The functions $\varphi_k^\dagger(x_0)$ are obtained from the orthonormality condition of the eigenfunctions, and for reflection boundary conditions read

$$\varphi_k^\dagger(x_0) = \begin{cases} \dfrac{1}{2L} & \text{if } k = 0 \\ \dfrac{1}{L}\cos\left(\dfrac{k\pi x_0}{2L}\right) & \text{if } k \geq 1. \end{cases} \quad (3.30)$$

In nuclear reactors, the two families $\omega_k^\pm$ are widely separated because of the typical values of λ, α_p and $\beta\nu_{d,1}$. Loosely speaking, the ω_k^+ family is associated to the dynamics of precursors, while ω_k^- describes prompt neutron dynamics.

3.2.3 . Generalization to a collection of particles

Once the single-particle moments are known, it is then straightforward to generalize the framework to describe a collection of $\mathcal{N}$ *independent and identically distributed* neutrons whose initial coordinates are distributed according to a given source $\mathcal{Q}(x_0, t_0)$. Observe that the resulting probability-generating function $W_{\mathcal{Q}}(z_1, z_2)$ is related to the single-particle probability-generating function $W(z_1, z_2, , x_0, t_0)$ by

$$W_{\mathcal{Q}^{\mathcal{N}}}(z_1, z_2) = \left[\int_{-\infty}^{t_1} dt_0 \int dx_0\, W(z_1, z_2, x_0, t_0)\mathcal{Q}(x_0, t_0)\right]^{\mathcal{N}}. \tag{3.31}$$

Then, by taking the derivative of Eq. (3.31) once with respect to z_1 we obtain the average number of particles in V_1 for a collection of $\mathcal{N}$ source particles :

$$\mathbb{E}[n_1](t_1|\mathcal{Q}_{\mathcal{N}}) = \mathcal{N}\int_{-\infty}^{t_1} dt_0 \int dx_0 \mathbb{E}[n_1](t_1|x_0, t_0)\mathcal{Q}(x_0, t_0). \tag{3.32}$$

Similarly, by taking the mixed derivative of Eq. (3.31) with respect to z_1 and z_2 we obtain the pair correlation between detector V_1 and V_2 for a collection of $\mathcal{N}$ source particles :

$$\begin{aligned}\mathbb{E}[n_1 n_2](t_1, t_2|\mathcal{Q}_{\mathcal{N}}) = &\frac{(\mathcal{N}-1)}{\mathcal{N}}\mathbb{E}[n_1](t_1|\mathcal{Q}_{\mathcal{N}})\mathbb{E}[n_2](t_2|\mathcal{Q}_{\mathcal{N}}) \\ &+ \mathcal{N}\int_{-\infty}^{t_1} dt_0 \int dx_0 \mathbb{E}[n_1 n_2](t_1, t_2|x_0, t_0)\mathcal{Q}(x_0, t_0).\end{aligned} \tag{3.33}$$

In particular, if we denote the single-particle source distribution as $\mathcal{Q}(x_0, t_0)$, the density $n(x, t)$ reads

$$n(x, t) = \mathcal{N}\iint_{-\infty}^{t} \mathcal{Q}(x_0, t_0)\mathcal{G}(x, t|x_0, t_0)\, dx_0\, dt_0, \tag{3.34}$$

which expresses a linear superposition principle. The pair correlation function can be also explicitly computed based on the Green's function, and reads

$$\begin{aligned}u(x_1, t_1, x_2, t_2) = &\frac{\mathcal{N}-1}{\mathcal{N}} n(x_a, t_a)\, n(x_b, t_b) + \mathcal{G}(x_b, t_b|x_a, t_a)\, n(x_a, t_a) \\ &+ \beta\nu_{p,2}\int_0^{t_a}\int \mathcal{G}(x_a, t_a|x, t)\, \mathcal{G}(x_b, t_b|x, t)\, n(x, t)\, dx\, dt \\ &+ \beta\nu_{p,1}\nu_{d,1}\int_0^{t_a}\int \mathcal{G}(x_a, t_a|x, t)\, c(x_b, t_b|x, t)\, n(x, t)\, dx\, dt \\ &+ \beta\nu_{p,1}\nu_{d,1}\int_0^{t_a}\int \mathcal{G}(x_b, t_b|x, t)\, c(x_a, t_a|x, t)\, n(x, t)\, dx\, dt \\ &+ \beta\nu_{d,2}\int_0^{t_a}\int c(x_a, t_a|x, t)\, c(x_b, t_b|x, t) n(x, t)\, dx\, dt,\end{aligned} \tag{3.35}$$

where $t_a = \min\{t_1, t_2\}$, $t_b = \max\{t_1, t_2\}$,

$$x_a = \begin{cases} x_1 & \text{if } t_a = t_1 \\ x_2 & \text{if } t_a = t_2 \end{cases}, \tag{3.36}$$

and

$$x_b = \begin{cases} x_1 & \text{if } t_b = t_1 \\ x_2 & \text{if } t_b = t_2 \end{cases}. \tag{3.37}$$

The quantity

$$c(x_a, t_a|x, t) = \lambda\int_t^{t_a} \mathcal{G}(x_a, t_a|x, t')e^{-\lambda(t'-t_a)}\, dt' \tag{3.38}$$

represents the expected number of neutrons detected at (x_a, t_a) produced by a precursor at (x, t), with $t_a > t$.

The terms appearing in the correlation function in Eq. (3.35) can be given a physical interpretation. The first term describes the contribution of the detection of uncorrelated particles, i.e. particles that do not share any common ancestor. The second term describes self-correlations, i.e. the detection of the same particle history at (x_a, t_a) and later at (x_b, t_b). The four remaining terms represent the possible contributions due to fission events : the first one corresponds to the correlations induced by detection at (x_a, t_a) and (x_b, t_b) of neutrons stemming from different prompt neutrons produced by a common fission event at (x, t) ; the following two terms are symmetrical and correspond to correlations induced by detection at (x_a, t_a) and (x_b, t_b) of neutrons stemming from a prompt neutron and a precursor produced by a common fission event at (x, t) ; finally, the remaining term corresponds to correlations induced by detection at (x_a, t_a) and (x_b, t_b) of neutrons stemming from different precursors produced by a common fission event at (x, t).

3.2.4 . The source corresponding to the critical regime

If the reactor is assumed to be in the critical regime, it is then possible to choose the single-particle source $\mathcal{Q}(x_0, t_0)$ so that the average neutron density $n(x, t)$ is stationary at any time $t > 0$: this is for instance achieved by taking $\mathcal{Q}(x_0, t_0) = \mathcal{Q}_c(x_0, t_0)$, with

$$\mathcal{Q}_c(x_0, t_0) = \frac{1}{2L}\left[\frac{\theta}{1+\theta}\delta(t_0) + \frac{1}{1+\theta}\lambda \exp(-\lambda t_0)\right], \tag{3.39}$$

where $t_0 > 0$ and $\theta = \lambda/(\beta\nu_{d,1})$. This particular choice of $\mathcal{Q}(x_0, t_0)$ will be called the *critical source*. The first term in Eq. (3.39) corresponds to neutrons appearing at $t_0 = 0$ with probability $\theta/(1+\theta)$, while the second term corresponds to delayed neutrons appearing at exponentially distributed times from the decay of the precursors initially present at $t_0 = 0$, with complementary probability $1/(1+\theta)$. For our simple homogeneous one-dimensional reactor with reflection boundary conditions, the spatial distribution $1/(2L)$ is flat over the domain (Eq. (3.29)).

3.2.5 . Further generalizations of the Pál and Bell backward formalism

The Pál and Bell backward formalism lends itself to many possible generalizations. For instance, if we were to start our system with a collection of (independently distributed) N prompt neutrons, each having a source distribution $\mathcal{Q}_n(x_0, t_0)$, and M delayed neutrons, each having a source distribution $\mathcal{Q}_m(x_0, t_0)$, then Eq. (3.31) would be replaced by

$$\begin{aligned} W_{\mathcal{Q}_{n+m}}(z_1, z_2) = &\left[\int_{-\infty}^{t_1} dt_0 \int dx_0\, W(z_1, z_2, x_0, t_0)\mathcal{Q}_n(x_0, t_0)\right]^N \\ &\times \left[\int_{-\infty}^{t_1} dt_0 \int dx_0\, W(z_1, z_2, x_0, t_0)\mathcal{Q}_m(x_0, t_0)\right]^M . \end{aligned} \tag{3.40}$$

Correspondingly, setting $\mathcal{N} = N + M$ and denoting

$$\mathcal{Q}_{n+m}(x_0, t_0) = \frac{N}{N+M}\mathcal{Q}_n(x_0, t_0) + \frac{M}{N+M}\mathcal{Q}_m(x_0, t_0), \tag{3.41}$$

for the average number of particles we would have

$$\mathbb{E}[n_1](t_1|\mathcal{Q}_{n+m}) = \mathcal{N}\int_{-\infty}^{t_1} dt_0 \int dx_0\, \mathbb{E}[n_1](t_1|x_0, t_0)\mathcal{Q}_{n+m}(x_0, t_0), \tag{3.42}$$

and for the pair correlation we would have

$$\begin{aligned} \mathbb{E}[n_1 n_2](t_1, t_2|\mathcal{Q}_{n+m}) = &\mathcal{N}^2\mathbb{E}[n_1](t_1|\mathcal{Q}_{n+m})\mathbb{E}[n_2](t_2|\mathcal{Q}_{n+m}) \\ &- N\mathbb{E}[n_1](t_1|\mathcal{Q}_n)\mathbb{E}[n_2](t_2|\mathcal{Q}_n) - M\mathbb{E}[n_1](t_1|\mathcal{Q}_m)\mathbb{E}[n_2](t_2|\mathcal{Q}_m) \\ &+ \mathcal{N}\int_{-\infty}^{t_1} dt_0 \int dx_0 \mathbb{E}[n_1 n_2](t_1, t_2|x_0, t_0)\mathcal{Q}_{n+m}(x_0, t_0). \end{aligned} \tag{3.43}$$

Furthermore, the Pál and Bell backward formalism can be easily extended to include more general detectors (for instance, an array $\mathbf{V} = (V_1, \ldots, V_K)$ of K non-overlapping regions), and to more general sources (for instance, N and M can be themselves random variables with Poisson distributions).

3.2.6 . Exact solutions for the anarchic model with a critical source

For the critical anarchic model with a critical source, the solution of the pair correlation function in Eq. (3.35) can be derived explicitly. For $t_1 < t_2$, the pair correlation function $u(x_1, t_1, x_2, t_2)$ can be decomposed as follows :

$$u(x_1,t_1,x_2,t_2) = \frac{\mathcal{N}(\mathcal{N}-1)\theta^2}{4L^2(1+\theta)^2} + \frac{\mathcal{N}\theta}{2L(1+\theta)}\mathcal{G}(x_2,t_2,x_1,t_1) + \frac{\mathcal{N}\theta}{2L(1+\theta)}\left[u_{pp}(x_1,t_1,x_2,t_2) + u_{pd}(x_1,t_1,x_2,t_2) + u_{dp}(x_1,t_1,x_2,t_2) + u_{dd}(x_1,t_1,x_2,t_2)\right]. \tag{3.44}$$

Each component is defined in terms of the respective eigenmode expansion, namely,

$$u_{pp} = \sum_k \varphi_k(x_1)\varphi_k^\dagger(x_2)u_{pp}^k \tag{3.45}$$

$$u_{pd} = \sum_k \varphi_k(x_1)\varphi_k^\dagger(x_2)u_{pd}^k \tag{3.46}$$

$$u_{dp} = \sum_k \varphi_k(x_1)\varphi_k^\dagger(x_2)u_{dp}^k \tag{3.47}$$

$$u_{dd} = \sum_k \varphi_k(x_1)\varphi_k^\dagger(x_2)u_{dd}^k. \tag{3.48}$$

For the prompt-prompt component u_{pp}^k we have :

$$u_{pp}^0(t_1,t_2) = \frac{\beta\nu_{p,2}}{(1+\theta)^2}\left[\theta^2 t_1 + \theta\left(\frac{e^{\omega_d t_1}-1}{\omega_d} + \frac{e^{\omega_d t_2} - e^{\omega_d(t_2-t_1)}}{\omega_d}\right) + \frac{e^{\omega_d(t_1+t_2)} - e^{\omega_d(t_2-t_1)}}{2\omega_d}\right], \tag{3.49}$$

where we have introduced $\omega_d = -\tau_2^{-1} = -\beta\nu_{d,1} - \lambda$, and

$$u_{pp}^k(t_1,t_2) = \frac{\beta\nu_{p,2}}{(\omega_k^+ - \omega_k^-)^2}\left[\frac{(\omega_k^+ + \lambda)^2}{2\omega_k^+}\left(e^{\omega_k^+(t_1+t_2)} - e^{\omega_k^+(t_2-t_1)}\right) + \frac{(\omega_k^- + \lambda)^2}{2\omega_k^-}\left(e^{\omega_k^-(t_1+t_2)} - e^{\omega_k^-(t_2-t_1)}\right) + \frac{(\omega_k^+ + \lambda)(\omega_k^- + \lambda)}{\omega_k^+ + \omega_k^-}\left(e^{\omega_k^+(t_2-t_1)} + e^{\omega_k^-(t_2-t_1)} - (e^{\omega_k^+ t_1 + \omega_k^- t_2} + e^{\omega_k^+ t_2 + \omega_k^- t_1})\right)\right],$$

for $k \geq 1$. For the prompt-delayed component u_{pd}^k we have

$$u_{pd}^0(t_1,t_2) = \frac{\beta\nu_{d,1}\nu_{p,1}\theta}{(1+\theta)^2}\left[\theta t_1 + \frac{e^{\omega_d t_1}-1}{\omega_d} + \frac{\theta(e^{\omega_d(t_2-t_1)} - e^{\omega_d t_2})}{\omega_d} + \frac{e^{\omega_d(t_2-t_1)} - e^{\omega_d(t_1+t_2)}}{2\omega_d}\right] \tag{3.50}$$

and

$$u_{pd}^k(t_1,t_2) = \frac{\beta\lambda\nu_{d,1}\nu_{p,1}}{(\omega_k^+ - \omega_k^-)^2}\left[(\omega_k^+ + \lambda)\left(\frac{e^{\omega_k^+(t_1+t_2)} - e^{\omega_k^+(t_2-t_1)}}{2\omega_k^+} + \frac{e^{\omega_k^-(t_2-t_1)} - e^{\omega_k^+ t_1 + \omega_k^- t_2}}{\omega_k^+ + \omega_k^-}\right) + (\omega_k^- + \lambda)\left(\frac{e^{\omega_k^+(t_2-t_1)} - e^{\omega_k^+ t_2 + \omega_k^- t_1}}{\omega_k^+ + \omega_k^-} + \frac{e^{\omega_k^-(t_1+t_2)} - e^{\omega_k^-(t_2-t_1)}}{2\omega_k^-}\right)\right] \tag{3.51}$$

for $k \geq 1$. For the delayed-prompt component u_{dp}^k we have

$$u_{dp}^0(t_1,t_2) = \frac{\beta\nu_{d,1}\nu_{p,1}\theta}{(1+\theta)^2}\left[\theta t_1 + \theta\left(\frac{1-e^{\omega_d t_1}}{\omega_d}\right) + \frac{e^{\omega_d t_2} - e^{\omega_d(t_2-t_1)}}{\omega_d} + \frac{e^{\omega_d(t_1-t_2)} - e^{\omega_d(t_2+t_1)}}{2\omega_d}\right] \tag{3.52}$$

and

$$u_{dp}^{k}(t_1,t_2)=\frac{\beta\lambda\nu_{d,1}\nu_{p,1}}{(\omega_k^+-\omega_k^-)^2}\left[(\omega_k^++\lambda)\left(\frac{e^{\omega_k^+(t_1+t_2)}-e^{\omega_k^+(t_2-t_1)}}{2\omega_k^+}+\frac{e^{\omega_k^+(t_2-t_1)}-e^{\omega_k^+t_2+\omega_k^-t_1}}{\omega_k^++\omega_k^-}\right)\right.$$
$$\left.+(\omega_k^-+\lambda)\left(\frac{e^{\omega_k^-(t_2-t_1)}-e^{\omega_k^+t_1+\omega_k^-t_2}}{\omega_k^++\omega_k^-}+\frac{e^{\omega_k^-(t_1+t_2)}-e^{\omega_k^-(t_2-t_1)}}{2\omega_k^-}\right)\right] \tag{3.53}$$

for $k\geq 1$. Finally, for the delayed-delayed component u_{dd}^k we have

$$u_{dd}^{0}(t_1,t_2)=\frac{\beta\nu_{d,2}\theta^2}{(1+\theta)^2}\left[t_1+\frac{1+e^{\omega_d(t_1-t_2)}-e^{\omega_dt_1}-e^{\omega_dt_2}}{\omega_d}+\frac{e^{\omega_d(t_1+t_2)}-e^{\omega_d(t_2-t_1)}}{2\omega_d}\right] \tag{3.54}$$

and

$$u_{dd}^{k}(t_1,t_2)=\frac{\beta\lambda^2\nu_{d,2}}{(\omega_k^+-\omega_k^-)^2}\left[\frac{e^{\omega_k^+(t_1+t_2)}-e^{\omega_k^+(t_2-t_1)}}{2\omega_k^+}+\frac{e^{\omega_k^-(t_1+t_2)}-e^{\omega_k^-(t_2-t_1)}}{2\omega_k^-}\right.$$
$$\left.+\frac{e^{\omega_k^+(t_2-t_1)}+e^{\omega_k^-(t_2-t_1)}-e^{\omega_k^+t_1+\omega_k^-t_2}-e^{\omega_k^-t_1+\omega_k^+t_2}}{\omega_k^++\omega_k^-}\right] \tag{3.55}$$

for $k\geq 1$. Note that Eq. (3.35), which is applicable to generic values of t_1 and t_2, is recovered by operating the substitutions $t_1\to\min\{t_1,t_2\}$ and $t_2\to\max\{t_1,t_2\}$ in Eq. (3.44).

Taking $t_1=t_2=t$, we can obtain an expression for the mean-squared pair distance $\langle r^2\rangle(t)$. For our case (reflection boundary conditions, $\nu_{d,2}=0$), the expression reads :

$$\begin{aligned}\langle r^2\rangle(t)&=\frac{\iint(x-y)^2u(x,y,t)\,dx\,dy}{u(t,t)}\\&=\frac{2L^2}{3}\left(1-\frac{1}{N+u_0^{pp}(t)+u_0^{dp}(t)+u_{pd}^0(t)}\right)\\&\quad-\frac{64L^2}{N+u_{pp}^0(t)+u_{dp}^0(t)+u_{pd}^0(t)}\sum_{\substack{k=1\\k\text{ odd}}}^{+\infty}\frac{u_{pp}^k(t)+u_{dp}^k(t)+u_{pd}^k(t)}{(k\pi)^4}\end{aligned} \tag{3.56}$$

3.3 . Analysis of the pair correlation function

Inspection of Eq. (3.34) shows that the average neutron density in a critical reactor starting form the critical source in Eq. (3.39) is trivially constant, as expected, and reads $n(x,t)=N/(2L)$. This value depends on the number N of neutrons emitted from the source and on the reactor size $2L$. Correspondingly, the average total number of neutrons $n(t)$ will be constant and equal to N, and it can be shown that the average total number of precursors $m(t)$ will be also constant and equal to $M=N/\theta$.

The correlation function in Eq. (3.35), on the contrary, is not stationary for a critical system. While Eq. (3.35) is exact, the evaluation of $\mathcal{G}$ requires the numerical computation of an infinite series. In the following, the semi-analytical solution is henceforth obtained using Eqs. (3.44-3.54) by summing the series up to order $k=1000$. The resulting correlation function has been carefully verified against Monte Carlo simulations, as shown in Figs. 3.2a and 3.2b. It is more convenient to plot the *corrected pair correlation function* $\tilde{u}(x_1,t_1,x_2,t_2)=u(x_1,t_1,x_2,t_2)-\delta(x_1-x_2)\,n(x_1,t_1)$, which is equivalent to ignoring the singular term $\delta(x_1-x_2)$ due to the self-correlations occurring in the system at $t_1=t_2$. Note that this does not remove all of the self-correlation contributions, as self-correlations also include contributions from points $x_1\neq x_2$. By abuse of language, and when it does not impede understanding, in the following we shall call $\tilde{u}$ the 'pair correlation function' nonetheless. Since the function has four

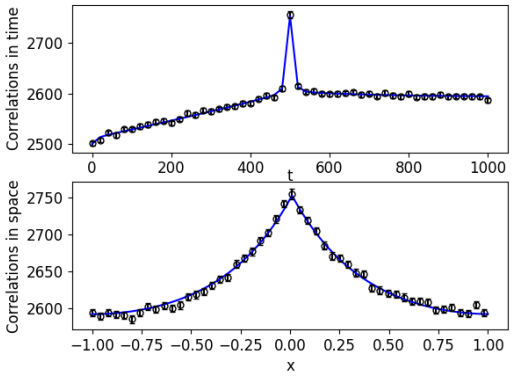

(a) On the graph we plot $u(x_1, t_1, x_2, t)$ for $x_1 = x_2 = 0$ and $t_1 = T/2$. The bottom graph shows $u(x_1, t_1, x, t_2)$ the spatial shape when $t_1 = t_2 = T/2$ and $x_1 = 0$.

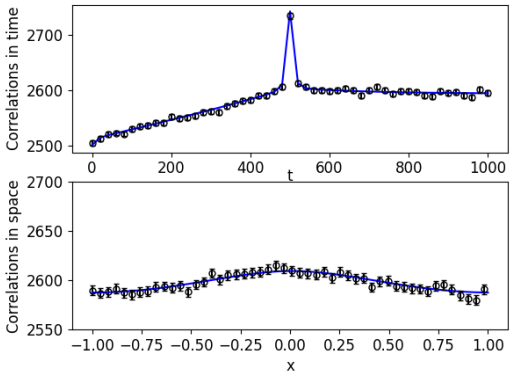

(b) Same as Fig. 3.2a, except that the top graph gives the time dependency for $x_1 = 0$ and $x_2 = -0.02$. The bottom graph shows spatial correlations with $t_1 = T/2 = 500$ and $t_2 = 490$.

Figure 3.2 : Pair correlation function for a critical population starting with, on average, $N = 100$ prompt neutrons and $M = 10^3$ precursors, for a deterministic total population size $\mathcal{N} = N + M$. Parameters are taken as in Table 3.1 for $\theta = 10^{-1}$. Blue solid line : analytical results from Eq. (3.35). Black circles : Monte Carlo simulations result with 10^6 replicas.

independent variables, for the sake of simplicity we present one-dimensional cuts for fixed values of the other variables.

Figure 3.2a shows the time shape of the correlation function when particles are detected at the same spatial position $x_1 = x_2$ (top panel), and the spatial shape when the detection times $t_1 = t_2$ are the same (bottom panel). The detection positions chosen for Fig. 3.2a are far from the boundaries of the reactor. Figure 3.2b illustrates the time shape of the correlation function for two different detection positions (top), and its spatial shape for two different detection times (bottom).

Figures 3.2a (top panel) and 3.2b (top panel) show that, after an initial transient, $t \lesssim 50$, the time profile of the pair correlation function exhibits a linear build-up. For $t_1 > t_2$, correlations saturate. Indeed, the linear build-up describes fissions happening at time t_1 that may contribute to further fissions occurring at a fixed t_2, meaning that obviously fissions occurring at $t_1 > t_2$ cannot contribute.

The analysis of $u(x_1, t_1, x_2, t_2)$ shows that the correlation function displays several typical time scales. First, the spatial boundedness of the system introduces timescales that are related to diffusion. The prompt time scales accumulate around and are asymptotically dominated by the mixing time, which is related to the time a neutron needs in order to explore the whole configuration space [46]. With the introduction of precursors, additional remarkable timescales appear. As shown in Eq. (3.35), the two-point, two-time correlation function involves products of the Green's function, Eq. (3.26), which has the structure of an infinite sum of exponential modes with characteristic time constants ω_k^+ and ω_k^-. The correlation function can then be expressed as an infinite sum of exponential modes with characteristic time constants $2\omega_k^+$, $2\omega_k^-$, $\omega_k^+ + \omega_k^-$ and $\omega_k^+ - \omega_k^-$ (see Sec. 3.2.2 for details). If we restrict our attention to the one-time, two-point correlation function, $u(x_1, x_2, t) = u(x_1, t, x_2, t)$, then the $\omega_k^+ - \omega_k^-$ modes disappear. The first few characteristic time constants for each family are represented in Fig. 3.3. We can identify four different interesting timescales :

- the separation of the first two characteristic time constants of the $\omega_k^+ + \omega_k^-$ family is given by $(\omega_0^+ + \omega_0^-) - (\omega_1^+ + \omega_1^-) = -\alpha_1 = 4L^2/\mathcal{D}\pi^2 = \tau_D^{-1}$. This is exactly the inverse of the mixing time for a system without delayed neutrons, as studied in Ref. 46. For the parameter values of Figs. 3.2a and 3.2b, the prompt mixing time would be $\tau_D \simeq 41$.

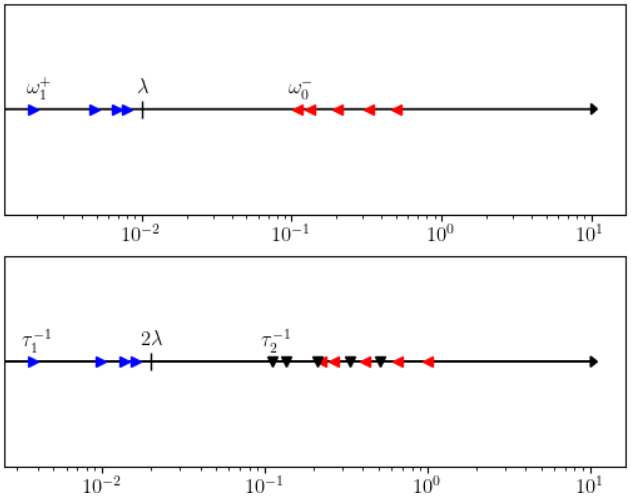

Figure 3.3 : Scatter plot of the characteristic time constants of the Green's function (top) and of the one-time, two-point correlation function (bottom), for the anarchic system, up to order $k = 5$. Top : blue right-pointing triangles represent $|\omega_k^+|$; red left-pointing triangles represent $|\omega_k^-|$. Bottom : blue right-pointing triangles represent $|2\omega_k^+|$; black down-pointing triangles represent $|\omega_k^+ + \omega_k^-|$; red left-pointing triangles represent $|2\omega_k^-|$. Note that $\omega_0^- = 0$ and $2\omega_0^- = 0$ cannot be represented in either plot (the system is critical). The dominant mode for each family ($k = 0$) is the leftmost one. The parameter values are the same as in Fig. 3.2a.

- on a timescale of the order of $\tau_2 = |\omega_0^+ + \omega_0^-|^{-1} = (\beta\nu_{d,1} + \lambda)^{-1}$, the correlation function reaches a quasi-stationary regime, after prompt dynamics has stabilized but before delayed dynamics comes into play. Note that the expression of τ_2 is independent of the spatial characteristics of the system, such as its spatial extent or the diffusion coefficient. Therefore, this time scale corresponds to a collective behaviour. For times of the order of a few τ_2, the prompt modes contribute a time-independent term to the correlation function. The delayed modes, on the other hand, have timescales that are much longer than τ_2 ; therefore, the remaining exponentials terms $\exp(2\omega_k^+ t)$ can be replaced with their first-order Maclaurin development, yielding a linear dependency on time. This explains the presence of linear build-up regimes in Figs. 3.2a and 3.2b. For the parameters of these figures, we have $\tau_2 \simeq 9$.

- on a timescale of the order of $\tau_1 = |2\omega_1^+|^{-1}$, the correlation function acquires its asymptotic spatial shape. In this sense, this timescale is analogous to the mixing time of prompt systems ; however, given the expression of Eq. (3.28), it involves the precursor decay constant λ and is therefore generally much longer than the prompt mixing time, which is given by τ_D. For the parameter values of Figs. 3.2a and 3.2b, we have $\tau_1 \simeq 269$.

- for times much longer than τ_1, all the exponential terms in the correlation function have died out. The spatial shape of the correlation function is frozen, but the overall scale factor increases linearly with t. It has been previously shown by Houchmandzadeh et al. [48] (and our calculations confirm this) that the slope of this eventual linear regime is τ_E^{-1}, where

$$\tau_E = \frac{N(1+\theta)^2}{\beta\nu_2\theta^2}, \tag{3.57}$$

where

$$\nu_2 = \nu_{p,2} + 2\nu_{d,1}\nu_{p,1} + \nu_{d,2},$$

and $N = \mathcal{N}\theta/(1+\theta)$ is the average number of neutrons in the system. After a time of the order of τ_E, the standard deviation of the total population size becomes equal to the mean population

size. This is the regime of the critical catastrophe : because of the unbounded fluctuations, the population will almost surely go eventually extinct, despite the fact that the average population size is constant [78, 80]. This apparently paradoxical behaviour is a well-known characteristic of critical birth-and-death processes. The quantity τ_E thus physically represents the typical *extinction time* of the system. For the parameter values of Figs. 3.2a and 3.2b, the extinction time is $\tau_E \simeq 1.5 \times 10^4$; therefore, this regime is not observable in the figures above.

The space profile of the correlation function, shown in Fig. 3.2a (bottom panel), has the tent-like shape that is typical of clustering behaviour. Despite the fact that the mean population density is uniform and constant, specific histories can exhibit strong patchiness (clusters) where pairs of particles will tend to be located at short distances from each other. This is coherent with previous findings for a reactor model neglecting delayed neutrons [27, 46, 47]. Figure 3.2b (bottom) suggests a relaxation toward a flat distribution for t_1 and t_2 sufficiently far from each another. Further analyses (not shown here for conciseness) confirm this conjecture.

It is tempting to characterize the importance of neutron clustering by defining a dimensionless parameter $\eta = \tau_1/\tau_E$, i.e. the ratio of the two longest timescales in the system. When $\eta \gg 1$, clustering will relax slowly over a time of the order of the extinction time, and therefore it will be observable over the whole lifetime of the system. It is interesting to consider how the dimensionless parameter η scales with θ for small θ, which is the regime of interest for nuclear reactors. By replacing $\lambda = \theta\beta\nu_{d,1}$ in Eq. (3.28) and developing in Maclaurin series in θ, we obtain

$$\omega_1^+ \simeq \frac{\theta}{\alpha_1^{-1} + \alpha_p^{-1}}. \tag{3.58}$$

Hence,

$$\tau_1 \simeq \frac{\alpha_1^{-1} + \alpha_p^{-1}}{2\theta}. \tag{3.59}$$

This should be contrasted with the mixing time for a system without delayed neutrons, which is $\tau_D = 1/\alpha_1$. Even in the regime where diffusion dominates ($\alpha_1 \ll \alpha_p$), we can see that the presence of delayed neutrons slows down mixing by a factor of $1/\theta$. Unsurprisingly, this is the factor that is introduced by delayed neutrons in the characteristic response times of the *mean* reactor populations around criticality [48]. Thus, mixing is essentially a phenomenon that characterizes the behaviour of the average neutron and precursor densities.

When Eq. (3.59) is replaced in the definition of the clustering parameter η, we find

$$\eta = \frac{\tau_1}{\tau_E} \simeq \frac{\alpha_1^{-1} + \alpha_p^{-1}}{2N}\beta\nu_2\theta. \tag{3.60}$$

This goes to show that the presence of delayed neutrons is very effective in quenching clustering, because of the different scaling of τ_1 and τ_E with θ. It is worth remarking in passing that the fact that the extinction time scales as θ^{-2} for small values of θ is not a coincidence, but it is due to the fact that τ_E is a purely stochastic quantity, which can only be defined in terms of the second-order moments of the populations.

3.4 . Analysis of the mean-squared pair distance

The quantity $\langle r^2 \rangle(t)$ yields the average square distance between pairs of particles (observed at the same time), and in this respect provides information on their tendency toward clustering [28, 79]. At time $t_0 = 0$, we have

$$\langle r^2 \rangle(0) = \langle r^2 \rangle_{iid} = \frac{2L^2}{3}, \tag{3.61}$$

since the neutrons are independently and uniformly distributed within the reactor. At later times, neutrons exhibit correlations induced by fission events and correspondingly $\langle r^2 \rangle(t) < \langle r^2 \rangle_{iid}$, which is a signature of the spatial clustering regime. For the anarchic model, we can obtain semi-analytical formulas for $\langle r^2 \rangle(t)$

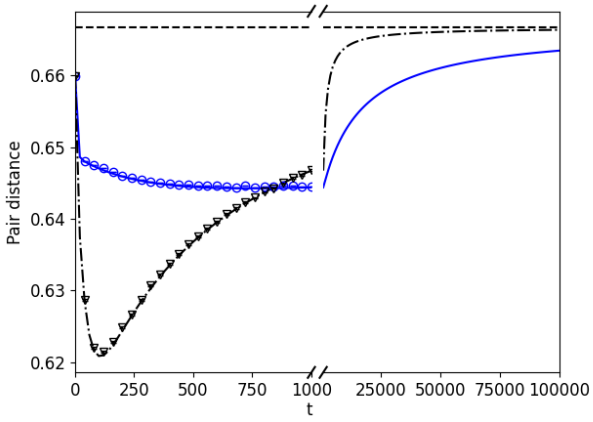

Figure 3.4 : Mean-squared pair distance in a one-dimensional box $[-L, L]$ for critical populations using two sets of parameters taken from Table 3.1. Blue (gray) circles for Monte Carlo simulation with $\theta = 10^{-2}$; blue (gray) solid line for analytical integration of Eq. (3.35); black triangles for Monte Carlo simulation with $\theta = 1$; black pointed-line for the analytical integration of Eq. (3.10). Error bars are shown but are barely visible.

in the form of a series, whose expression can be found in Eq. (3.56), generalizing previous findings for the model without delayed neutrons [28].

Figure 3.4 shows the time evolution of the mean-squared pair distance for a choice of model parameters. The formula from Eq. (3.56) is compared to the result of the Monte Carlo simulation. Pair distance in Monte Carlo is estimated by taking the ensemble average of the squared distances of all the neutron pairs present in the system at a given time, normalized by the ensemble average of the square of the number of particles at a given time. For times of the order of the extinction time, the quantity $\langle r^2 \rangle(t)$ asymptotically reverts to the uncorrelated value $\langle r^2 \rangle_{iid}$, with a convergence speed that depends on the model parameters. This is explained by the fact that for $t \gg \tau_E$ the population in a critical regime almost certainly dies out and correlations become spatially flat over the entire reactor. This result is again coherent with previous findings for the case where precursors were neglected [28].

3.5 . Conclusions

We considered a simplified one-dimensional stochastic model of a nuclear reactor including neutrons and precursors. We derived the moment equations characterizing the time and space correlations of the particles present in the system.

Our main tool was the two-point, two-time neutron-neutron second-order moment (the pair correlation function), which characterizes the joint observation of neutrons at (x_1, t_1) and at (x_2, t_2). By using the Pál-Bell backward formalism, we derived the exact pair correlation function for the anarchic model, where all the populations are left free to evolve, starting from a distributed source composed of a collection of initial particles (neutrons, precursors or both).

We identified two typical timescales, namely the time τ_2 necessary for the prompt correlation dynamics to relax, and the time τ_1 necessary for correlations to achieve their asymptotic spatial shape. The latter generalizes the concept of mixing time (initially introduced for purely prompt stochastic models, without precursors) to a system with delayed neutrons. For typical values of the physical parameters, τ_1 is actually much longer than the mixing time of a critical system without delayed neutrons.

The system is further characterized by its extinction time τ_E, which represents the typical time required to observe catastrophic fluctuations of the total population size. Similarly to the mixing time, the extinction time for a system with delayed neutrons is much longer than the extinction time for a critical system without delayed neutrons, for typical values of the physical parameters.

This framework sets the bases to fully characterize the stochastic evolution of a collection of neutron and precursors when no external constraints are imposed. In the next chapter, we will focus on the space and time correlations in the presence of idealized population control algorithms.

4 -Space-Time Correlations in simplified kinetic simulations with idealized population control

So far, we have considered the case of kinetic simulations using freely evolving particle populations. In practice, some forms of population control will be generally used, in order to prevent fatal numerical instabilities such as the 'critical catastrophe' discussed in the previous chapter.

In the following, we will introduce and thoroughly examine a class of stochastic models coupling the branching Brownian model presented in Chapter 3 with an idealized mechanism of population control that mimics more realistic strategies, but is simple enough to allow for analytical solutions for the observables of interest.

For this purpose, we will suitably generalize an approach originally conceived for the case where precursors are neglected [28]. For this model, a control mechanism has been introduced as follows : whenever a neutron is created by fission, another neutron is randomly chosen and eliminated [28, 47]. This sampling strategy was inspired by heuristic arguments proposed in the context of theoretical ecology [79, 81] : it preserves exactly the total number of individuals in the system and has a deep impact on the behaviour of the correlations. In particular, it has been shown to induce an upper bound on the amplitude of neutron noise and thus prevent the occurrence of the critical catastrophe [28, 47].

The enforcement of control mechanisms, which correlate birth and death events, breaks the independence of particle histories, so that the backward formalism can no longer be used [82]. We will resort to a forward master equation approach instead, which is slightly more involved. Thus, for the sake of simplicity we will focus exclusively on the case of binary fission and on the production of at most one delayed neutron precursor, although our findings can be straightforwardly extended to general neutron and precursor production distributions, at the expense of more cumbersome formulas. For the same reason, contrary to Chapter 3, we shall only consider spatial correlations with both particles observed at the same time.

The analysis of spatial moments will be complemented by the investigation of the statistical behaviour of *neutron genealogical trees*. The main idea behind this approach is that fission progeny originating from the same fission event are correlated and share a common ancestor. Neutrons sharing at least one common ancestor form a genealogical tree of correlated particles, which we call *family* by analogy with population dynamics. We will show that, in the course of the stochastic evolution of the population dynamics obeying the rules of the Galton-Watson birth-and-death process with population control, all the families but one will eventually become extinct [83]. The relationship between the evolution of the statistics of the neutron families and spatial correlations is encoded in the competition between birth, death, and diffusion. In this chapter, we will provide a formal framework to derive analytically the moments of the distribution of the extinction time for all the families but one, for a collection of neutrons and precursors evolving in time under different population control mechanisms.

Population control has a clear physical counterpart in real systems. In nuclear reactors, various feedback mechanisms act against the excursions of the neutron population. An example of utmost importance is provided by the Doppler effect. The probability of neutron-matter interaction depends on the temperature of the medium ; in nominal conditions, the probability of sterile absorption increases with increasing temperature [2]. Since the temperature of the reactor is driven by the number of neutrons in the system, the overall result of the Doppler effect is that deviations from the mean in the number of neutrons in the reactor tend to be quenched. The typical timescale of the Doppler effect is shorter than the neutron lifetime, so that the feedback acts almost instantaneously on the behaviour of the fission chains [2]. In this respect, the analysis of analog kinetic Monte Carlo simulations with population control can be transposed to the analysis of neutron fluctuations occurring in the real systems when feedback mechanisms are taken into account.

Most of the work presented in this chapter has been previously published in Ref. 77 and Ref. 84.

4.1 . Application of population control to a collection of neutrons alone

An extensive characterization of the correlations for a collection of diffusing and multiplying particles where the number of individuals is kept exactly constant has been derived in the literature [28], building upon previous results from theoretical ecology [79]. In these works, precursors were neglected. Moreover, the approach presented in Ref. 28 does not lend itself to a straightforward generalization to the broader case of a collection of neutrons and precursors.

To overcome this issue, we introduce here a novel strategy that allows deriving a rigorous analytical framework based on *forward master equations*. For pedagogical reasons, we begin our investigation by considering the simpler case of a collection of neutrons alone, where our approach recovers the results of Ref. 28, albeit in a more general setting that can be then extended to take into account the presence of precursors. This new model will be discussed in Sec. 4.2 and following.

If precursors are neglected, a stochastic model with a population control constraint that preserves exactly the number of neutrons in the system can be obtained by setting the rules defined in Ref. 28. Each neutron induces fission with rate β, producing exactly two prompt neutrons. Capture is conditioned to fission : upon fission, another neutron randomly chosen in the remaining population is eliminated. Between fission events, neutrons undergo diffusion. This ensures that the number of neutrons N is constant, which corresponds to a critical reactor with strict population control.

4.1.1 . Derivation of the space-dependent master equation

We assume again that the viable space is the one-dimensional domain $[-L, L]$. Following the strategy introduced in Ref. 48, we derive the forward space-dependent master equation by partitioning the domain into a set of K segments of equal length $\delta x = 2L/K$, which we denote as V_k with $k \in \{1, \dots, K\}$. Correspondingly, we write $\mathbf{n} = (n_1, \dots, n_K)$. Let $\mathcal{P}(\mathbf{n}, t)$ be the joint probability observing n_k neutrons in each of the K detectors, with $k \in \{1, \dots, K\}$, given an initial condition at $t_0 = 0$ of N neutrons uniformly distributed in space. We have $\sum_i n_i = N$. In addition, for conceptual ease, diffusion will be first modelled as a discrete random walk by defining the rate ξ at which a neutron jumps from V_k to $V_{k\pm1}$. The evolution equations for $\mathcal{P}(\mathbf{n}, t)$ can be written more concisely introducing the annihilation a_k and creation $a_k^\dagger$ operators, whose action on a state vector $\mathbf{v} = (v_1, \dots, v_K)$ is defined by

$$a_k \mathbf{v} = (\dots, v_{k-1}, v_k - 1, v_{k+1}, \dots)$$
$$a_k^\dagger \mathbf{v} = (\dots, v_{k-1}, v_k + 1, v_{k+1}, \dots).$$

The stochastic rules allow for the following transitions

- a transition $\mathbf{n} \to a_i a_{i\pm1}^\dagger \mathbf{n}$ with rate per neutron ξ, corresponding to diffusion from site i to neighbouring sites.
- a transition $\mathbf{n} \to a_i^\dagger a_j \mathbf{n}$ with rate per neutron β and probability

$$p = \frac{n_i - 1}{N} \frac{n_j + 1}{N - 1}, \tag{4.1}$$

  corresponding to fission in bin i and capture in bin j.

Based on these rules, the discrete master equation reads

$$\frac{\partial}{\partial t}\mathcal{P}(\mathbf{n}, t) = \sum_i \Bigg[\xi(n_{i+1} + 1)\mathcal{P}(a_{i+1}^\dagger a_i \mathbf{n}, t) + \xi(n_{i-1} + 1)\mathcal{P}(a_{i-1}^\dagger a_i \mathbf{n}, t) - 2\xi n_i \mathcal{P}(\mathbf{n}, t)$$
$$+ \beta N \sum_{j \neq i} \left(\frac{n_i + 1}{N} \frac{n_j - 1}{N - 1} \mathcal{P}(a_i^\dagger a_j \mathbf{n}, t) - \frac{n_i}{N} \frac{n_j}{N - 1} \mathcal{P}(\mathbf{n}, t) \right) \Bigg]. \tag{4.2}$$

Equation (4.2) is hardly amenable to analytical solutions, but insights about the statistical behaviour of the neutron population can nonetheless be gained by investigating the statistical moments of the neutron population.

4.1.2 . Derivation of the spatial moments

Equation (4.31) describes the evolution of the discrete occupation probability. Correspondingly, we can derive the average number of neutrons in V_i at time t from

$$\mathbb{E}[n_i](t) = \sum_{\mathbf{n}} n_i \mathcal{P}(\mathbf{n}, t). \tag{4.3}$$

The two-point correlation between neutrons detected in V_i and neutrons detected in V_j at time t is similarly derived from

$$\mathbb{E}[n_i n_j](t) = \sum_{\mathbf{n}} n_i n_j \mathcal{P}(\mathbf{n}, t). \tag{4.4}$$

The equation for the spatial moment of order l can be obtained by multiplying Eq. (4.2) by n_k^l and summing over all possible states. For the first moment, this procedure yields

$$\frac{\partial}{\partial t}\mathbb{E}[n_k](t) = \gamma \Delta_k \mathbb{E}[n_k](t), \tag{4.5}$$

where Δ_k denotes the discrete Laplace operator, such that $\Delta_k f_k = f_{k+1} - 2f_k + f_{k-1}$. Taking the limit $V_i \to 0$ leads to the one-dimensional diffusion equation

$$\frac{\partial}{\partial t} n(x,t) = \mathcal{D}\nabla^2 n(x,t), \tag{4.6}$$

with V_i centered around x. The diffusion rate ξ is assumed to scale as $1/\sqrt{\delta x}$, so that the diffusion coefficient is recovered as

$$\lim_{\delta x \to 0} \xi \delta x^2 = \mathcal{D}. \tag{4.7}$$

With reflection boundary conditions, the solution of Eq. (4.6) is simply the spatially uniform density

$$n(x,t) = \frac{N}{2L}. \tag{4.8}$$

Similarly, for the second moment we obtain

$$\begin{aligned}\frac{\partial}{\partial t}\mathbf{E}[n_k n_l](t) = \gamma\left(\Delta_l \mathbf{E}[n_k n_l](t) + \Delta_k \mathbb{E}[n_l n_k](t)\right) - \frac{2\beta}{N_0 - 1}\mathbb{E}[n_k n_l](t) + \delta_{k,l}\frac{2N_0\beta}{N_0-1}\mathbb{E}[n_k](t) \\ + \delta_{i,j}\xi\left(\mathbb{E}[n_{i+1}](t) + \mathbb{E}[n_{i-1}](t) + 2\mathbb{E}[n_i](t)\right) - \delta_{i+1,j}\xi\left(\mathbb{E}[n_{i+1}](t) + \mathbb{E}[n_i](t)\right) \\ - \delta_{i-1,j}\xi\left(\mathbb{E}[n_i](t) + \mathbb{E}[n_{i-1}](t)\right),\end{aligned} \tag{4.9}$$

where $\delta_{i,j}$ denotes the Kronecker symbol. Taking again the limit $V_i \to 0$ leads to

$$\frac{\partial}{\partial t}\tilde{u}(x,y,t) = \mathcal{D}(\nabla_x^2 + \nabla_y^2)\tilde{u}(x,y,t) - \frac{2\beta}{N-1}\tilde{u}(x,y,t) + 2\beta n(x,t)\delta(x-y), \tag{4.10}$$

where, for the sake of conciseness, we have introduced the modified pair correlation function $\tilde{u}(x,y,t) = u(x,y,t) - \delta(x-y)n(x,t)$. Here δ denotes the Dirac distribution. The detectors V_i and V_j are centered around x and y, respectively. Finally, we assume

$$\lim_{V_i, V_j \to 0} \delta_{i,j} = \delta(x-y). \tag{4.11}$$

When taking the limit $V_i \to 0$, the last two lines of Eq. (4.9) lead to higher-order derivatives of the Dirac distribution, that disappear when using $\tilde{u}$ instead of u.

Equation (4.10) is a linear equation that can be solved in terms of the Green's function

$$\mathcal{G}(x,y,t|x',y',t') = G(x,t|x',t')G(y,t|y',t')e^{-\frac{2\beta}{N-1}(t-t')}, \tag{4.12}$$

where G is the Green's function associated to Eq. (4.6), i.e. the Gaussian propagator, which read

$$G(x,t|x',t') = \frac{1}{\sqrt{4\pi\mathcal{D}(t-t')}} e^{\frac{(x-x')^2}{4\mathcal{D}(t-t')}}. \tag{4.13}$$

The formal solution of Eq. (4.10) then reads

$$\begin{aligned}\tilde{u}(x,y,t) = 2\beta \iint dx'dt' G(x,t|x',t')G(y,t|x',t')e^{-\frac{2\beta}{N-1}(t-t')}n(x',t') \\ + \frac{N(N-1)}{N^2} n(x,t)n(y,t)e^{-\frac{2\beta}{N-1}t}.\end{aligned} \tag{4.14}$$

The exponential term in Eq. (4.14) indicates that correlations saturate exponentially fast, with a typical timescale $\tau_M = (N-1)/2\beta$, instead of diverging linearly as in the anarchic model, and the critical catastrophe is consequently averted. Spatial clustering is therefore mitigated because correlations now admit a maximum value. These results are consistent with the findings previously derived using the heuristic arguments of Ref. 28 (see also Ref. 47). In addition, contrary to the backward formalism which relies on the assumption of statistical independence between particles, the forward formalism developed here can take into account the particle correlations arising due to mass conservation.

4.1.3 . Analysis of the statistics of neutron families

The two-point function $\tilde{u}(x,y,t)$ encodes the spatial correlations of a collection of neutrons, under the constraint that the total population N is kept constant. A complementary investigation of the statistical behaviour of the individuals in birth-and-death models can be carried out by determining the distribution of the number of neutron 'families' as a function of time : this approach has been first suggested in the context of theoretical biology [81, 85–87], then applied to reactor physics by de Mulatier et al. [28], and further investigated by Sutton and Mittal for the analysis of clustering phenomena in Monte Carlo simulations [41, 42].

Consider again the time-dependent Galton-Watson birth-and-death process in which neutrons reproduce upon fission, and die upon capture, in the one-dimensional reflected system introduced in the previous section.

Source neutrons are assigned an identifier in $\{1,\dots,F\}$, which they transmit to their descendants. Let n_i be the number of neutrons with identifier i. Neutrons sharing the same identifier form a *family*. The simulation starts with F initial families. The size of a family increases by one when one of its members induces fission ; it decreases by one when a neutron is the family is killed by capture. A family becomes extinct when the last of its members is captured. Some families will thus disappear over time, while others will proliferate, inducing a large number of descendants. If no additional families are introduced, which in reactor physics is equivalent to the absence of either an external source or spontaneous fission, all the families but one will eventually become extinct, leading to the *fixation* of the neutron population [83]. The time to fixation is called *fixation time* : we will show that this quantity may be related to the timescale driving the growth and saturation of correlations. The fixation time in mass-preserving models somehow plays the role of the *extinction* time in the anarchic model, with a significant difference : the moments of the extinction time are not finite, whereas those of the fixation time are finite, and will be investigated in the remainder of this section.

In order to shed light on the evolution of neutron families, we will derive the equations governing the first few moments of the family statistics. Here, we present the derivation of the fixation time for a population of prompt neutrons in a homogeneous medium, in a continuous-time context and neglecting precursors, and show that we can obtain closed-form expressions for these quantities.

First, we remark that, for a homogeneous medium with mass preserving boundary conditions, each neutron has an equal probability of fathering the surviving family, implying a fixation probability of $f(n) = n/N$ for a family of size n in a total population of N neutrons. To compute the *fixation time* τ_p of the population, we first examine the family-wise conditional fixation time. Let A be a family identifier ; the other families are ignored. We denote by $\mathbb{E}[\tau_p|A](n)$ the average fixation time *conditioned to the*

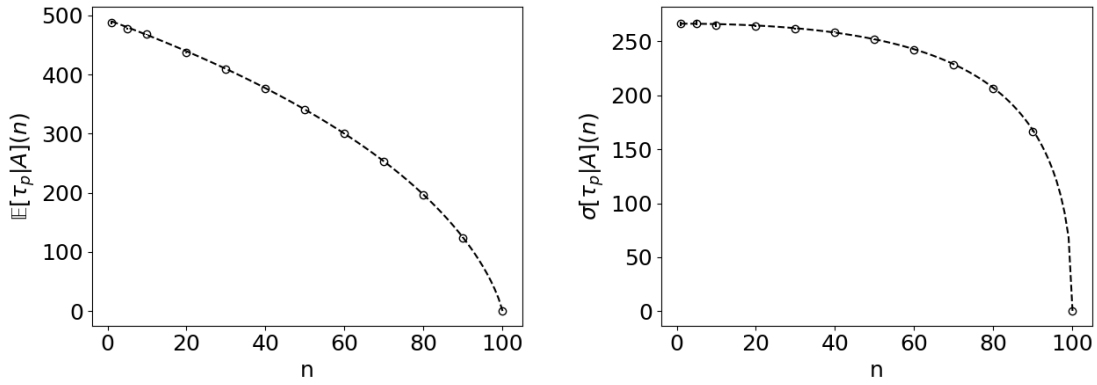

Figure 4.1 : Average fixation time $\mathbb{E}[\tau_p|A](n)$ (left) and standard deviation $\sigma[\tau_p|A](n)$ of the fixation time (right) for $N = 100$ and $\beta = 0.2$ in the prompt case. Dashed lines : analytical solution ; circles : Monte Carlo. The Monte Carlo estimates are within 3σ of the analytical results

event that family A achieves fixation. From the law of total expectation [88], we can deduce a recurrence relation for $\mathbb{E}[\tau_p|A](n)$ as follows

$$\begin{aligned} f_p(n)\mathbb{E}\left[\tau_p|A\right](n) = \quad & p_+ f_p(n+1)\mathbb{E}\left[(\tau_p + \delta\tau(n))|A\right](n+1) \\ & + p_- f_p(n-1)\mathbb{E}\left[(\tau_p + \delta\tau(n))|A\right](n-1), \end{aligned} \tag{4.15}$$

where $p_\pm$ are the probabilities that transition $n \to n \pm 1$ happens. In this context, we simply have $p_+ = p_- = 1/2$, while $\delta\tau(n) = (N-1)/(\beta n(N-n))$ is the inverse of the total rate of 'useful' transitions, i.e., transitions that change the number of neutrons in A.

Equation (4.15) can be recast in a concise form by defining $\tilde{\tau}_{p,1}(n) = n\mathbb{E}[\tau_p|A](n)$ if $n > 0$ and $\tilde{\tau}_{p,1}(0) = 0$, yielding

$$\tilde{\tau}_{p,1}(n+1) - 2\tilde{\tau}_{p,1}(n) + \tilde{\tau}_{p,1}(n-1) = -\frac{N-1}{\beta(N-n)}, \tag{4.16}$$

which is to be solved with the boundary condition $\tilde{\tau}_{p,1}(N) = 0$ (i.e., the population is already fixed if $n = N$), and $\tilde{\tau}_{p,1}(0) = 0$ by construction. We obtain the explicit solution

$$\mathbb{E}[\tau_p|A](n) = \frac{N-1}{\beta n}[1 - n + (N-n)(H_{N-1} - H_{N-n})] + \frac{(N-1)^2}{\beta N}, \tag{4.17}$$

where H_n is the n-th harmonic number. We find that, taking $N \gg 1$, $\mathbb{E}[\tau_p|A](1) \sim N/\beta$. Comparison with Monte Carlo simulations shows perfect statistical agreement, as shown in Fig. 4.1.

The expression for $\mathbb{E}[\tau_p|A](n)$ yields the conditional average fixation time for a family of initial size n. We define then $\tau_p(n_1, \ldots, n_F)$ as the average fixation time for a population consisting of competing families with initial sizes $n_1, \ldots, n_F$, which is given by the average of the family-wise conditional fixation time :

$$\tau_p(n_1, \ldots, n_F) = \sum_{i=1,\ldots,F} f(n_i)\mathbb{E}[\tau_p|A](n_i). \tag{4.18}$$

In particular, when $N = F$ and $n_i = 1 \ \ \forall i$, then $\tau_p(1, \ldots, 1) = \mathbb{E}[\tau_p|A](1) = (N-1)^2/(\beta N)$.

Let us now examine the variance of the fixation time, using the law of total expectation on $\mathbb{E}[\tau_p^2|A](n)$. After defining $\tilde{\tau}_{p,2}(n) = n\mathbb{E}[\tau_p^2|A](n)$ for $n > 0$ and $\tilde{\tau}_{p,2}(0) = 0$, we find that $\tilde{\tau}_{p,2}(n)$ satisfies the equation

$$\tilde{\tau}_{p,2}(n+1) - 2\tilde{\tau}_{p,2}(n) + \tilde{\tau}_{p,2}(n-1) = \frac{(N-1)}{\beta(N-n)}\left(\frac{1}{\beta N} - 2\mathbb{E}[\tau_p|A](n)\right), \tag{4.19}$$

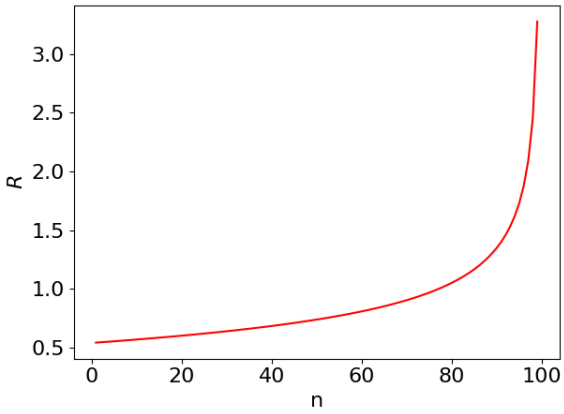

Figure 4.2 : Ratio $R = \sigma[\tau_p](n)/\mathbb{E}[\tau_p](n)$ of the standard deviation to the average of the fixation time, as a function of the family size, in the prompt case, with $\beta = 0.2$ and $N = 100$.

Applying boundary conditions $\tilde{\tau}_{p,2}(N) = 0$ and using again $\tilde{\tau}_{p,2}(0) = 0$ by construction, we can explicitly solve Eq. (4.19), which yields the second moment of the family-wise conditional fixation time

$$\mathbb{E}[\tau_p^2|A](n) = \tau_{p,2}^S(n) - \mathbb{E}[\tau_p|A](n) + C_N, \tag{4.20}$$

where $\tau_2^S(n)$ and C_N are given by

$$\tau_{p,2}^S(n) = 2N\left(\frac{N-1}{\beta N}\right)^2\left(\frac{N}{n}\sum_{j=1}^{n-1}\frac{H_{N-j}(n-j)}{j} - [1+NH_{N-1}]\,(H_n-1)\right)$$

$$C_N = \left(\frac{N-1}{\beta N}\right)^2\left\{2N\left[(H_N-1)(1+NH_{N-1}) - \sum_{j=1}^{N-1}\frac{H_{N-j}(N-j)}{j}\right] - 1\right\}.$$

It is worth noting that the standard deviation $\sigma[\tau_p](n) = \sqrt{\mathrm{Var}[\tau_p|A]}$ of the fixation time is of the same order of magnitude as the average fixation time : in some cases, fixation might happen relatively early in the simulation. In particular, the ratio of $\sigma[\tau_p](n)$ over $\mathbb{E}[\tau_p](n)$ in Fig. 4.2 shows that the latter is of the same order of magnitude as the former, even for $n \ll N$.

It is interesting to remark that, due to our choice of mass-preserving boundary conditions, the statistics of families for the bounded box reactor is insensitive to spatial effects : the moments of the fixation time do not depend on the typical spatial scale of the problem at hand. This is in stark contrast with the two-point correlation function for the same system, and thus with the squared pair distance $\langle r^2(t)\rangle$. For the case of particles evolving with population control in *unbounded* homogeneous media, Meyer et al. showed that $\langle r^2(t)\rangle$ reads

$$\langle r^2(t)\rangle = 4\mathcal{D}\tau_{R,p}\left(1 - e^{-\frac{t}{\tau_{R,p}}}\right), \tag{4.21}$$

indicating that the saturation occurs over a characteristic timescale $\tau_{R,p} = (N-1)/(2\beta)$ [79]. It follows that for $N \gg 1$ we have $\tau_{R,p} \sim \mathbb{E}[\tau_p|A](1)/2$, i.e., the average fixation time is equal to twice the renewal time, which suggests a close relation between the statistical behaviour of families and the one of spatial clustering [79]. However, for particles evolving with population control in *bounded* homogeneous media having reflective boundary conditions, the exponential relaxation of $\langle r^2(t)\rangle$ towards an asymptotic value does depend on the spatial scale of the system (i.e. the mixing time) [28], whereas the moments of the fixation time do not, as shown here. The identification of fixation and clustering timescales appears thus to be fully meaningful for infinite and homogeneous media alone. Indeed, the emergence of clustering in confined geometries results from the competition between fixation and spatial mixing due to diffusion [46] : the fixation time cannot be identified with the clustering timescale anymore.

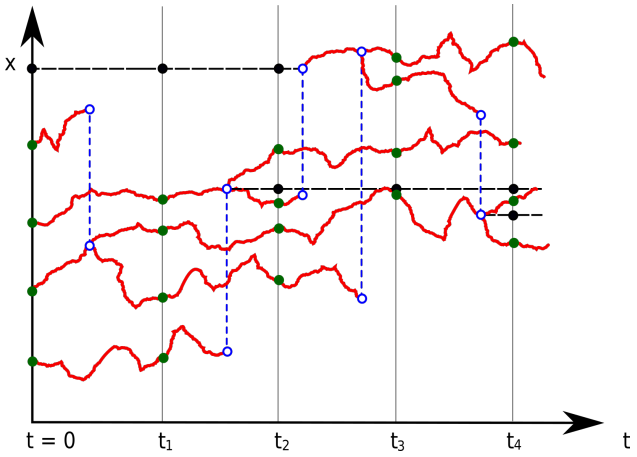

Figure 4.3 : A typical history for a system of 4 neutrons and 1 precursor in the N-control model. Neutrons diffuse (in red line) until they branch or are destroyed by another neutron being produced in the system (these correlated event are shown in vertical blue dashed lines), and precursor lifetime is shown by horizontal black dashed lines.

4.2 . Control of neutrons in a system of neutrons and precursors

We will now revisit the stochastic model introduced in Sec. 4.1 by introducing precursors : we will show that the effects of population control become more cumbersome to take into account ; nonetheless, we will be able to derive a class of models that allow for analytical or semi-analytical solutions that can be benchmarked against Monte Carlo simulations.

Let us consider a population of neutrons and precursors, evolving based on the stochastic rules described in Sec. 3.2. Since neutrons are responsible for the Monte Carlo tallies, it seems natural to enforce population control *on neutrons alone*, which can be achieved as follows.

Each neutron induces fission with a rate of β ; the fission event produces exactly two prompt neutrons (with probability $p_2 = 1$). Additionally, fission events produce a precursor with probability q_1, and no precursor with the complementary probability $q_0 = 1 - q_1$. Upon decay, with rate λ, the precursor yields a delayed neutron. In this specific case, we have $q_1 = \nu_{d,1}$, which is not true in general. In order to ensure a constant number N of neutrons in the system, whenever a neutron is produced, either from fission or from a decaying precursor, another neutron is randomly chosen and eliminated (for illustration, see Fig. 4.3). Observe that the total number of precursors is left free to fluctuate. We will call this scheme the N-*control* algorithm.

4.2.1 . Analysis of the moments of the total populations

We begin our analysis by addressing the behaviour of the population sizes. First, we denote by N and M the (arbitrary) initial number of neutrons and precursors. The master equation for the total population sizes is easily derived, and because of population control it has a dependency on n only through the initial condition. It reads

$$\frac{\partial}{\partial t}\mathcal{P}(n,m,t) = \beta N \nu_{d,1}\mathcal{P}(n,m-1,t) - \beta N \nu_{d,1}\mathcal{P}(n,m,t) + (m+1)\lambda\mathcal{P}(n,m+1,t) - m\lambda\mathcal{P}(n,m,t). \tag{4.22}$$

We deduce the equation for the precursor population sizes by multiplying Eq. (4.22) by m (resp m) and summing over all possible realizations, which leads to

$$\frac{\partial}{\partial t}n(t) = 0 \tag{4.23a}$$

$$\frac{\partial}{\partial t}m(t) = \beta\nu_{d,1}N - \lambda m(t). \tag{4.23b}$$

These equations can be readily solved, together with the initial conditions, and yield

$$n(t) = N$$
$$m(t) = \frac{\beta\nu_{d,1}}{\lambda} N \left(1 - e^{-\lambda t}\right) + Me^{-\lambda t}.$$

For the *N-control* model, the average total precursor number $m(t)$ exponentially relaxes to the same equilibrium solution as for the anarchic model, i.e., $m_\infty = N\,\beta\nu_{d,1}/\lambda = N/\theta$. If the initial condition satisfies $N = M\theta$, we simply obtain $m(t) = M$ for any t. The equations for the second-order moments of the total population can be also derived, and read

$$\frac{\partial}{\partial t} u(t) = 0 \tag{4.24a}$$
$$\frac{\partial}{\partial t} v(t) = \beta\nu_{d,1}\, u(t) - \lambda\, v(t) \tag{4.24b}$$
$$\frac{\partial}{\partial t} w(t) = \beta\nu_{d,1} N\,(2m(t) + 1) - \lambda(2w(t) - m(t)). \tag{4.24c}$$

The solutions to these equations are

$$u(t) = N^2 \tag{4.25}$$
$$v(t) = Nm(t) \tag{4.26}$$
$$w(t) = m(t)^2 + m(t) - Me^{-2\lambda t}, \tag{4.27}$$

where u, v, and w are as defined in Sec. 3.1.2. In the *N-control* model, the variance of the neutron population size is zero, as expected, which means in particular that the critical catastrophe is averted. The variance of the precursor population size converges exponentially to m_∞. It is actually easy to show that if the distribution of the precursor population size is Poissonian at the initial time, then it is Poissonian at all times. First we remind the shape of the Poisson distribution

$$\mathsf{Poiss}_\mu(m) = \frac{\mu^m}{m!} e^{-\mu}, \tag{4.28}$$

where μ is a function of time. We make the following ansatz :

$$\mathcal{P}(n, m, t) = \delta_{nN} \mathsf{Poiss}_{\mu(t)}(m). \tag{4.29}$$

Plugging this into Eq. (4.22) and simplifying leads to

$$\frac{\partial}{\partial t}\mu = \lambda(m_\infty - \mu). \tag{4.30}$$

Since this equation holds for any m, we can conclude that $\mathcal{P}(n, m, t)$ has the assumed shape provided that the ansatz also holds at $t = 0$ and that $\mu(0) = m_\infty$

4.2.2 . Derivation of the spatial master equation

In order to derive equations for the spatial moments of the neutron and precursor densities, we use again the strategy proposed in Ref. 48 : we partition the viable one-dimensional domain into a set of K equal segments of length $\delta x = 2L/K$, which we denote as V_k, with $k \in \{1, \ldots, K\}$. Correspondingly, we write $\mathbf{n} = (n_1, \ldots, n_K)$, $\mathbf{m} = (m_1, \ldots, m_K)$, and we denote by $\mathcal{P}(\mathbf{n}, \mathbf{m}, t)$ the joint probability of observing n_k neutrons and m_k precursors in each of the K detectors at time t, for $1 \leq k \leq K$, given an initial condition with N neutrons and M precursors at time $t_0 = 0$, independently and uniformly distributed in space. The stochastic rules are those defined in Sec. 4.2 and the transition rates are specified below.

In addition to diffusion, which applies only to neutrons and thus behaves the same as in a reactor without precursors, the system has the following transitions :

- A fission in bin i and a capture in a different bin j ($i \neq j$), without precursor production. The corresponding transition is $(a_i^\dagger a_j \mathbf{n}, \mathbf{m}) \to (\mathbf{n}, \mathbf{m})$, with rate

$$\beta_1 = \beta \frac{(n_i+1)(n_j-1)(1-\nu_{d,1})}{N(N-1)}.$$

- A fission and capture in the same bin but with production of one additional precursor. The corresponding transition is $(\mathbf{n}, a_i \mathbf{m}) \to (\mathbf{n}, \mathbf{m})$ with rate

$$\beta_2 = \beta \frac{n_i(n_i-1)\nu_{d,1}}{N(N-1)}$$

- A capture in bin i and a fission in a different bin j ($i \neq j$) with precursor production. The corresponding transition is $(a_i^\dagger a_j \mathbf{n}, a_j \mathbf{m}) \to (\mathbf{n}, \mathbf{m})$ with rate

$$\beta_3 = \beta \frac{(n_i+1)(n_j-1)\nu_{d,1}}{N(N-1)}$$

- A precursor decay in bin i and neutron capture in bin j ($i \neq j$). The corresponding transition is $(a_i a_j^\dagger \mathbf{n}, a_i^\dagger \mathbf{m}) \to (\mathbf{n}, \mathbf{m})$ with rate

$$\beta_4 = \lambda \frac{(m_i+1)(n_j+1)}{mN}$$

- A precursor decay and neutron capture in the same bin. The corresponding transition is $(\mathbf{n}, a_i^\dagger \mathbf{m}) \to (\mathbf{n}, \mathbf{m})$ with rate

$$\beta_5 = \lambda \frac{(m_i+1)n_i}{mN}$$

Other transitions are possible, but they do not modify the state of the system, and as such do not appear in the master equation (for example, fission and capture in the same bin i, without precursor production).

Probability balance then yields the master equation

$$\begin{aligned}
\frac{\partial}{\partial t}\mathcal{P}(\mathbf{n},\mathbf{m},t) = \sum_i \Big[& \xi(n_{i+1}+1)\mathcal{P}(a_{i+1}^\dagger a_i \mathbf{n},\mathbf{m},t) + \xi(n_{i-1}+1)\mathcal{P}(a_{i-1}^\dagger a_i \mathbf{n},\mathbf{m},t) - 2\xi n_i \mathcal{P}(\mathbf{n},\mathbf{m},t) \Big] \\
& + \beta(1-\nu_{d,1})N \sum_{i,j\neq i} \left(\frac{n_i+1}{N}\frac{n_j-1}{N-1}\mathcal{P}(a_i^\dagger a_j \mathbf{n},\mathbf{m},t) - \frac{n_i}{N}\frac{n_j}{N-1}\mathcal{P}(\mathbf{n},\mathbf{m},t) \right) \\
& + \beta\nu_{d,1}N \sum_{i,j\neq i} \left(\frac{n_i+1}{N}\frac{n_j-1}{N-1}\mathcal{P}(a_i^\dagger a_j \mathbf{n}, a_j\mathbf{m},t) - \frac{n_i}{N}\frac{n_j}{N-1}\mathcal{P}(\mathbf{n},\mathbf{m},t) \right) \\
& + \beta\nu_{d,1}N \sum_{i} \left(\frac{n_i}{N}\frac{n_i-1}{N-1}\mathcal{P}(\mathbf{n}, a_i\mathbf{m},t) - \frac{n_i}{N}\frac{n_i-1}{N-1}\mathcal{P}(\mathbf{n},\mathbf{m},t) \right) \\
& + \lambda m \sum_{i,j\neq i} \left(\frac{m_i+1}{m}\frac{n_j+1}{N}\mathcal{P}(a_i a_j^\dagger \mathbf{n}, a_i^\dagger \mathbf{m},t) - \frac{m_i}{m}\frac{n_j}{N}\mathcal{P}(\mathbf{n},\mathbf{m},t) \right) \\
& + \lambda m \sum_{i} \left(\frac{m_i+1}{m}\frac{n_i}{N}\mathcal{P}(\mathbf{n}, a_i^\dagger \mathbf{m},t) - \frac{m_i}{m}\frac{n_i}{N}\mathcal{P}(\mathbf{n},\mathbf{m},t) \right).
\end{aligned} \tag{4.31}$$

where ξ is the diffusion rate of a neutron from a site to a neighbouring one, $m = \sum_i m_i$ is the total number of precursors, and the total number of neutrons is $n = \sum_i n_i = N$ because of population control. Once we have the space-dependent master equation, we can derive the equations for the spatial moments.

4.2.3 . Derivation and analysis of the spatial moments

We define the discrete spatial moments of the neutron and precursor populations by

$$\mathbb{E}[n_i](t) = \sum_{\mathbf{n},\mathbf{m}} n_i \, \mathcal{P}(\mathbf{n},\mathbf{m},t) \tag{4.32a}$$

$$\mathbb{E}[m_i](t) = \sum_{\mathbf{n},\mathbf{m}} m_i \, \mathcal{P}(\mathbf{n},\mathbf{m},t), \tag{4.32b}$$

for $i \in \{1,\dots,K\}$. The two-point correlations between particles detected in V_i and particles detected in V_j at time t are similarly obtained from

$$\mathbb{E}[n_i n_j](t) = \sum_{\mathbf{n},\mathbf{m}} n_i \, n_j \, \mathcal{P}(\mathbf{n},\mathbf{m},t) \tag{4.33a}$$

$$\mathbb{E}[n_i m_j](t) = \sum_{\mathbf{n},\mathbf{m}} n_i \, m_j \, \mathcal{P}(\mathbf{n},\mathbf{m},t) \tag{4.33b}$$

$$\mathbb{E}[m_i m_j](t) = \sum_{\mathbf{n},\mathbf{m}} m_i \, m_j \, \mathcal{P}(\mathbf{n},\mathbf{m},t), \tag{4.33c}$$

for $i,j \in \{1,\dots,K\}$. The associated moment equations can be obtained from Eq. (4.31) by summation over all possible states, and for the average they read

$$\frac{\partial}{\partial t}\mathbb{E}[n_i](t) = \xi \Delta_i \mathbb{E}[n_i](t) + \lambda \left(\mathbb{E}[m_i](t) - \frac{\mathbb{E}[n_i m](t)}{N} \right) \tag{4.34a}$$

$$\frac{\partial}{\partial t}\mathbb{E}[m_i](t) = \beta \nu_{d,1} \mathbb{E}[n_i](t) - \lambda \mathbb{E}[m_i](t), \tag{4.34b}$$

where $\Delta_i f_i = f_{i+1} - 2f_i + f_{i-1}$ is the discrete Laplace operator. Taking the continuous limit $V_i \to 0$ yields

$$\frac{\partial}{\partial t} n(x,t) = \mathcal{D} \nabla_x^2 n(x,t) + \lambda \left(m(x,t) - \frac{1}{N} H^n(x,t) \right) \tag{4.35a}$$

$$\frac{\partial}{\partial t} m(x,t) = \beta \nu_{d,1} \, n(x,t) - \lambda \, m(x,t), \tag{4.35b}$$

where we have defined the cross-moment

$$H^n(x,t) = \lim_{V_i \to 0} \frac{1}{V_i} \mathbb{E}[n_i(t) m(t)], \tag{4.36}$$

with V_i centered around x, and the diffusion coefficient

$$\mathcal{D} = \lim_{\delta x \to 0} (\xi \, \delta x^2). \tag{4.37}$$

A somewhat surprising fact is that the term $H^n(x,t)$ appearing in the equation for the average is actually a second-order moment : this means that unfortunately the hierarchy of the spatial moment equations *is not closed*, and analytical solutions are therefore out of reach for this model. This is to be contrasted with the case of the moments of the integral quantities, Eqs. (4.23) and (4.24), which are closed. On the other hand, Monte Carlo simulations heuristically indicate that, taking $M = N/\theta$ and a uniform spatial distribution, the first moments seem to verify

$$n(x,t) = \frac{N}{2L} \tag{4.38}$$

$$m(x,t) = \frac{M}{2L}, \tag{4.39}$$

which coincides with the solutions of the case without population control.

Similarly, the equations for the discrete pair correlation functions read

$$\begin{aligned}\frac{\partial}{\partial t}\mathbb{E}[n_i n_j](t) &= \xi\left(\mathbb{E}[\Delta_i n_i n_j](t) + \mathbb{E}[\Delta_j n_i n_j](t)\right) - \frac{2\beta}{N_0-1}\mathbb{E}[n_i n_j](t) + \lambda C_N\left(\mathbb{E}[n_i m_j](t) + \mathbb{E}[m_i n_j](t)\right) \\ &- \frac{2\lambda}{N}\mathbb{E}[n_i n_j m](t) + \frac{2\beta}{N_0-1}\delta_{i,j}N_0\mathbb{E}[n_i](t) + \lambda\delta_{i,j}\left(\mathbb{E}[m_i](t) + \frac{\mathbb{E}[n_i m](t)}{N}\right) \\ &+ \delta_{i,j}\xi\left(\mathbb{E}[n_{i+1}](t) + \mathbb{E}[n_{i-1}](t) + 2\mathbb{E}[n_i](t)\right) - \delta_{i+1,j}\xi\left(\mathbb{E}[n_{i+1}](t) + \mathbb{E}[n_i](t)\right) \\ &- \delta_{i-1,j}\xi\left(\mathbb{E}[n_i](t) + \mathbb{E}[n_{i-1}](t)\right) \end{aligned} \tag{4.40}$$

$$\begin{aligned}\frac{\partial}{\partial t}\mathbb{E}[n_i m_j](t) &= \xi\mathbb{E}[\Delta_i n_i m_j](t) - \lambda\frac{N-1}{N}\mathbb{E}[n_i m_j](t) - \lambda\frac{\mathbb{E}[n_i m_j m](t)}{N} \\ &+ \beta\nu_{d,1}C_{N-1}\mathbb{E}[n_i n_j](t) + \lambda\mathbb{E}[m_i m_j](t) + \delta_{i,j}\left(\frac{\beta\nu_{d,1}N}{N-1}\mathbb{E}[n_i](t) - \lambda\mathbb{E}[m_i](t)\right)\end{aligned} \tag{4.41}$$

$$\frac{\partial}{\partial t}\mathbb{E}[m_i m_j](t) = \beta\nu_{d,1}\left(\mathbb{E}[m_i n_j](t) + \mathbb{E}[n_i m_j](t)\right) - 2\lambda\mathbb{E}[m_i m_j](t) + \delta_{i,j}\left(\beta\nu_{d,1}\mathbb{E}[n_i](t) + \lambda\mathbb{E}[m_i](t)\right). \tag{4.42}$$

When taking the continuous limit it is easier to write the equations for the modified pair correlations functions

$$\tilde{u}(x,y,t) = u(x,t,y,t) - n(x,t)\delta(x-y) \tag{4.43}$$

$$v(x,y,t) = v(x,t,y,t) \tag{4.44}$$

$$\tilde{w}(x,y,t) = w(x,t,y,t) - m(x,t)\delta(x-y), \tag{4.45}$$

which involve third-order moments :

$$\begin{aligned}\frac{\partial}{\partial t}\tilde{u}(x,y,t) &= \mathcal{D}\left(\nabla_x^2 + \nabla_y^2\right)\tilde{u}(x,y,t) - \frac{2\beta}{N-1}\tilde{u}(x,y,t) + \lambda C_N\left(v(x,y,t) + v(y,x,t)\right) - \frac{2\lambda}{N}H^{nn}(x,y,t) \\ &+ \delta(x-y)\left(2\beta n(x,t) + \frac{2\lambda}{N}H^n(x,t)\right)\end{aligned} \tag{4.46a}$$

$$\begin{aligned}\frac{\partial}{\partial t}v(x,y,t) &= \mathcal{D}\nabla_x^2 v(x,y,t) - \lambda C_N v(x,y,t) - \frac{\lambda}{N}H^{nm}(x,y,t) + \beta\nu_{d,1}C_{N-1}\tilde{u}(x,y,t) + \lambda\tilde{w}(x,y,t) \\ &+ \delta(x-y)\frac{\beta\nu_{d,1}N}{N-1}n(x,t)\end{aligned} \tag{4.46b}$$

$$\frac{\partial}{\partial t}\tilde{w}(x,y,t) = \beta\nu_{d,1}\left(v(x,y,t) + v(y,x,t)\right) - 2\lambda\tilde{w}(x,y,t). \tag{4.46c}$$

For the sake of conciseness, we have defined the two third-order cross-moments

$$H^{nn}(x,y,t) = \lim_{V_i,V_j\to 0}\frac{1}{V_i V_j}\mathbb{E}[n_i(t)n_j(t)m(t)] \tag{4.47}$$

$$H^{nm}(x,y,t) = \lim_{V_i,V_j\to 0}\frac{1}{V_i V_j}\mathbb{E}[n_i(t)m_j(t)m(t)]. \tag{4.48}$$

and the shorthand $C_N = (N-1)/N$. The detection volumes V_i and V_j are assumed to be centered around x and y, respectively. It is interesting to note that we can recognize in Eq. (4.46a) the *renewal time* (or, equivalently, the fixation time [41]) $\tau_{R,0} = (N-1)/(2\beta)$ for a population of prompt neutrons under population control without precursors [79]. Although this definition can be extended to a population of neutrons and precursors, we obviously expect the associated renewal time to differ from $\tau_{R,0}$.

On a side note, Monte Carlo simulations of the N-control model for $\theta \ll 1$ seem to show that the relative spatial dependence of the pair correlation function is almost exactly the same as in the anarchic model for $t_1 = t_2$. This is illustrated in Fig. 4.4, where we plot the shape of the correlation function for

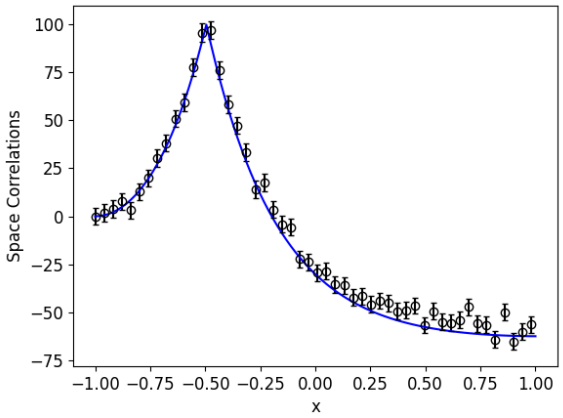

Figure 4.4 : Spatial dependence of the difference between the pair correlation function evaluated in $(x, y = -0.5)$ and $(x = -L = -1, y = -0.5)$. Black circles : Monte Carlo simulation of the N-control scheme; blue solid line : analytical solution of the anarchic model. Here, $\theta = 10^{-3}$. Parameters are taken from Table 3.1.

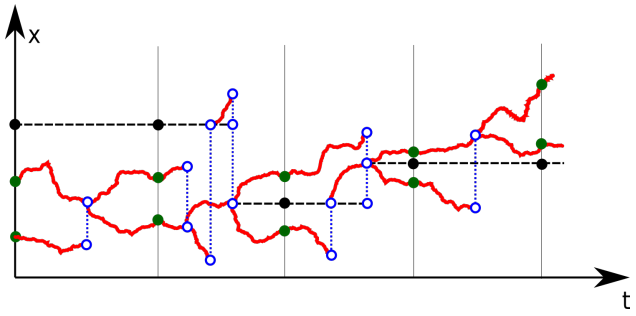

Figure 4.5 : A typical history for a system of 2 neutrons and 1 precursor in the NM-control model. Neutrons diffuse (in red solid lines) until they branch or are destroyed by another neutron being produced in the system (these correlated event are shown in vertical blue dashed lines), and precursor lifetime is shown by horizontal black dashed-lines.

both models, for a fixed value of $y = -0.5$ and relative to its value in $x = -L = -1$. This remark does not hold true for $\theta \sim 1$.

Note that, although the hierarchy of the moment equations is not closed, the underlying stochastic process can be straightforwardly simulated using the Monte Carlo method. In the following, we shall make extensive use of this fact to compare the N-control model, which plays the role of a reference for population control, with other models enforcing similar constraints on the population. Indeed, the occurrence of $H^{nn}(x, y, t)$ and $H^{nm}(x, y, t)$ suggests that the lack of closure originates from the fact that the N-control model correlates the size of the precursor population with the local neutron and precursor densities. It is tempting to suggest the use of the approximation

$$H^{n}(x, t) \simeq n(x, t)m(t) \tag{4.49}$$

in order to close Eqs. (4.35), and of similar approximations for $H^{nn}(x, y, t)$ and $H^{nm}(x, y, t)$. Doing so in the general case yields equations with time-dependent coefficients in the moment equations. However, we do not know how to construct a Monte Carlo game associated to these approximate moment equations. This effectively prevents us from validating the analytical results by comparing them with an equivalent Monte Carlo simulation, but the goodness of the approximation could be assessed by comparing the analytical results against the Monte Carlo simulations for the N-control model.

Another way to close the hierarchy of moment equations is to apply population control to both populations, so that the size of the precursor population is not a random variable. By doing so, we

sacrifice some physical relevance of the N-control model, but we gain the ability to derive analytical solutions. We henceforth propose two alternative models, and we discuss under which conditions they may approximate the N-control model.

4.3 . Control of neutrons and precursors

The first alternative model consist in considering a process in which the total number of neutrons N *and* the total number of precursors M are kept under constraint. Conservation of N is enforced as previously described. Conservation of M is enforced as follows : when a neutron undergoes fission and produces a precursor, another randomly chosen precursor is destroyed. When a precursor emits a delayed neutron, the precursor is *not* destroyed. In this way, we ensure that N and M are kept constant at any time (see Fig. 4.5). We call this algorithm the NM*-control* scheme. For the total population statistics, NM-control trivially yields one possible state, given by the initial condition (N, M), with vanishing variance.

4.3.1 . Derivation of the spatial master equation

The spatial behaviour of the neutron and precursor populations is nonetheless non-trivial. The possible transitions (in addition to diffusion) are listed below :

- A neutron capture in bin i and fission in a different bin j $(i \neq j)$ without precursor production. The corresponding transition is $(a_i^\dagger a_j \mathbf{n}, \mathbf{m}) \to (\mathbf{n}, \mathbf{m})$ with rate

$$\beta_1 = \beta \frac{(n_i + 1)(n_j - 1)(1 - \nu_{d,1})}{N(N-1)},$$

- A neutron capture in bin i, fission in bin j with precursor production, and destruction of another precursor in bin k, where $i \neq j \neq k$. The corresponding transition is $(a_i^\dagger a_j \mathbf{n}, a_j a_k^\dagger \mathbf{m}) \to (\mathbf{n}, \mathbf{m})$ with rate

$$\beta_2 = \beta \frac{\nu_{d,1}(n_i + 1)(n_j - 1)(m_k + 1)}{N(N-1)M},$$

- A fission with precursor production and a neutron capture in bin i, and precursor destruction in bin k $(i \neq k)$. The corresponding transition is $(\mathbf{n}, a_i a_k^\dagger \mathbf{m}) \to (\mathbf{n}, \mathbf{m})$ with rate

$$\beta_3 = \beta \frac{n_i(n_i - 1)(m_k + 1)\nu_{d,1}}{N(N-1)M},$$

- A neutron capture and precursor destruction in bin i, and a fission with precursor production in bin j $(i \neq j)$. The corresponding transition is $(a_i^\dagger a_j \mathbf{n}, a_i^\dagger a_j \mathbf{m}) \to (\mathbf{n}, \mathbf{m})$ with rate

$$\beta_4 = \beta \frac{(n_i + 1)(n_j - 1)(m_i + 1)\nu_{d,1}}{N(N-1)M},$$

- A neutron capture in bin i, a fission with precursor production and a precursor destruction in bin j $(i \neq j)$. The corresponding transition is $(a_i^\dagger a_j \mathbf{n}, \mathbf{m}) \to (\mathbf{n}, \mathbf{m})$ with rate

$$\beta_5 = \beta \frac{(n_i + 1)(n_j - 1)m_j\nu_{d,1}}{N(N-1)M},$$

- A precursor decay in bin i and a neutron capture in a different bin j $(i \neq j)$. The corresponding transition is $(a_i a_j^\dagger \mathbf{n}, \mathbf{m}) \to (\mathbf{n}, \mathbf{m})$ with rate

$$\beta_6 = \lambda \frac{m_i(n_j + 1)}{NM},$$

By using the definitions in Section 4.2.2, we use probability balance to write the master equation

$$\begin{aligned}
\frac{\partial}{\partial t}\mathcal{P}(\mathbf{n},\mathbf{m},t) = \sum_i \Bigg[& \xi(n_{i+1}+1)\mathcal{P}(a_{i+1}^\dagger a_i \mathbf{n},\mathbf{m},t) + \xi(n_{i-1}+1)\mathcal{P}(a_{i-1}^\dagger a_i \mathbf{n},\mathbf{m},t) - 2\xi n_i \mathcal{P}(\mathbf{n},\mathbf{m},t) \\
& + \sum_{j\neq i}\left(\frac{\beta(1-\nu_{d,1})}{N-1}(n_i+1)(n_j-1)\mathcal{P}(a_i^\dagger a_j\mathbf{n},\mathbf{m},t) - \frac{\beta(1-\nu_{d,1})}{N-1}n_i n_j \mathcal{P}(\mathbf{n},\mathbf{m},t)\right)\Bigg] \\
+\frac{\beta\nu_{d,1}}{(N-1)M}\Bigg[& \sum_{\substack{i,j,k\\ i\neq j\neq k}}\Big((n_i+1)(n_j-1)(m_k+1)\mathcal{P}(a_i^\dagger a_j\mathbf{n}, a_j a_k^\dagger \mathbf{m},t) - n_i n_j m_k \mathcal{P}(\mathbf{n},\mathbf{m},t)\Big) \\
& \sum_{\substack{i,k\\ i\neq k}}\Big(n_i(n_i-1)(m_k+1)\mathcal{P}(\mathbf{n}, a_i a_k^\dagger\mathbf{m},t) - n_i(n_i-1)m_k\mathcal{P}(\mathbf{n},\mathbf{m},t)\Big) \\
& \sum_{\substack{i,j\\ i\neq j}}\Big((n_i+1)(n_j-1)(m_i+1)\mathcal{P}(a_i^\dagger a_j\mathbf{n}, a_i^\dagger a_j\mathbf{m},t) - n_i n_j m_i\mathcal{P}(\mathbf{n},\mathbf{m},t)\Big) \\
& \sum_{\substack{i,j\\ i\neq j}}\Big((n_i+1)(n_j-1)m_j\mathcal{P}(a_i^\dagger a_j\mathbf{n},\mathbf{m},t) - n_i n_j m_j\mathcal{P}(\mathbf{n},\mathbf{m},t)\Big)\Bigg] \\
+\frac{\lambda}{N}\sum_{\substack{i,j\\ i\neq j}}\Big(m_i(n_j+1)\mathcal{P}(a_i a_j^\dagger\mathbf{n},\mathbf{m},t) - m_i n_j\mathcal{P}(\mathbf{n},\mathbf{m},t)\Big), &
\end{aligned} \tag{4.50}$$

where $n = N$ and $m = M$ at all times.

4.3.2 . Derivation and analysis of the spatial moments

By multiplying by n_i (resp m_i) the neutron (resp precursor) population in spatial cell i and summation over all possible states, the equations for the first spatial moments are given by

$$\frac{\partial}{\partial t}\mathbb{E}[n_i](t) = \xi\Delta_i\mathbb{E}[n_i](t) + \lambda\left(\mathbb{E}[m_i](t) - \mathbb{E}[n_i](t)\frac{M}{N}\right) \tag{4.51}$$

$$\frac{\partial}{\partial t}\mathbb{E}[m_i](t) = \beta\nu_{d,1}\left(\mathbb{E}[n_i](t) - \mathbb{E}[m_i](t)\frac{N}{M}\right), \tag{4.52}$$

showing that the constraint of fixed (N, M) indeed sidesteps the closure issues of the N-control model. The equations for the first-order moments are now closed and, taking the continuous limit, they read :

$$\frac{\partial}{\partial t}n(x,t) = \mathcal{D}\nabla_x^2 n(x,t) + \lambda\left(m(x,t) - n(x,t)\frac{M}{N}\right) \tag{4.53a}$$

$$\frac{\partial}{\partial t}m(x,t) = \beta\nu_{d,1}\left(n(x,t) - m(x,t)\frac{N}{M}\right). \tag{4.53b}$$

If N and M are in the equilibrium ratio $N/M = \theta = \lambda/(\beta\nu_{d,1})$, then Eqs. (4.53) reduce to the usual forward equations for the first moments of freely evolving populations of neutrons and precursors [48]. This has two consequences. First, we can conclude that the mixing time for the NM-control model is the same as for the anarchic model, τ_1. Second, Eqs. (4.53) admit uniform and constant asymptotic solutions

$$n(x,t) \to n_\infty(x) = \frac{N}{2L} \tag{4.54a}$$

$$m(x,t) \to m_\infty(x) = \frac{M}{2L}. \tag{4.54b}$$

For the second-order moments we obtain once again a closed system of equations, first in its discrete formulation :

$$\begin{aligned}\frac{\partial}{\partial t}\mathbb{E}[n_i n_j](t) &= \xi\left(\mathbb{E}[\Delta_i n_i n_j](t) + \mathbb{E}[\Delta_j n_i n_j](t)\right)\\ &\quad - \left(\frac{2\beta}{N-1} + \frac{2\lambda M}{N}\right)\mathbb{E}[n_i n_j](t) + \lambda C_N(\mathbb{E}[m_i n_j](t) + \mathbb{E}[n_i m_j](t))\\ &\quad + \frac{2N\beta}{N-1}\delta_{i,j}\mathbb{E}[n_i](t) + \lambda\delta_{i,j}\left(\mathbb{E}[m_i](t) + \mathbb{E}[n_i](t)\frac{M}{N}\right)\\ &\quad + \delta_{i,j}\xi\left(\mathbb{E}[n_{i+1}](t) + \mathbb{E}[n_{i-1}](t) + 2\mathbb{E}[n_i](t)\right) - \delta_{i+1,j}\xi\left(\mathbb{E}[n_{i+1}](t) + \mathbb{E}[n_i](t)\right)\\ &\quad - \delta_{i-1,j}\xi\left(\mathbb{E}[n_i](t) + \mathbb{E}[n_{i-1}](t)\right) \qquad (4.55)\\ \frac{\partial}{\partial t}\mathbb{E}[n_i m_j](t) &= \xi\mathbb{E}[\Delta_i n_i m_j](t) - \left(\frac{\beta\nu_{d,1}N}{M} + \lambda\frac{M}{N}\right)\mathbb{E}[n_i m_j](t) + \beta\nu_{d,1}\frac{N-2}{N-1}\mathbb{E}[n_i n_j](t)\\ &\quad + \lambda\mathbb{E}[m_i m_j](t) + \frac{\beta\nu_{d,1}N}{(N-1)}\delta_{i,j}\mathbb{E}[n_i](t) \qquad (4.56)\\ \frac{\partial}{\partial t}\mathbb{E}[m_i m_j](t) &= \beta\nu_{d,1}C_M\left(\mathbb{E}[m_i n_j](t) + \mathbb{E}[n_i m_j](t)\right) \qquad (4.57)\\ &\quad - \frac{2\beta\nu_{d,1}N}{M}\mathbb{E}[m_i m_j](t) + \beta\nu_{d,1}\delta_{i,j}\left(\mathbb{E}[n_i](t) + \mathbb{E}[m_i](t)\frac{N}{M}\right).\end{aligned}$$

Taking the continuous limit, we have then :

$$\begin{aligned}\frac{\partial}{\partial t}\tilde{u}(x,y,t) &= \mathcal{D}\left(\nabla_x^2 + \nabla_y^2\right)\tilde{u}(x,y,t) - \tau_n^{-1}\tilde{u}(x,y,t) + \lambda C_N\left(v(x,y,t) + v(y,x,t)\right)\\ &\quad + 2\beta\delta(x-y)n(x,t) \qquad (4.58a)\\ \frac{\partial}{\partial t}v(x,y,t) &= \mathcal{D}\nabla_x^2 v(x,y,t) - \tau_c^{-1}v(x,y,t) + \beta\nu_{d,1}C_{N-1}\tilde{u}(x,y,t) + \lambda\tilde{w}(x,y,t)\\ &\quad + \delta(x-y)\left(2\beta\nu_{d,1}n(x,t) + \lambda m(x,t)\right) \qquad (4.58b)\\ \frac{\partial}{\partial t}\tilde{w}(x,y,t) &= \beta\nu_{d,1}C_M(v(x,y,t) + v(y,x,t)) - \tau_p^{-1}\tilde{w}(x,y,t), \qquad (4.58c)\end{aligned}$$

with $C_M = (M-1)/M$ and where we defined the time constants

$$\tau_n = \left(\frac{2\beta}{N-1} + \frac{2\lambda M}{N}\right)^{-1} \qquad (4.59a)$$

$$\tau_c = \left(\frac{\beta\nu_{d,1}N}{M} + \lambda\frac{M}{N}\right)^{-1} \qquad (4.59b)$$

$$\tau_p = \frac{M}{2\beta\nu_{d,1}N}, \qquad (4.59c)$$

Equations (4.58) are a linear system of equations for $(\tilde{u}, v, \tilde{w})$. Following the heuristic arguments of Zhang et al. [81], we should expect the renewal time for our system to be determined by the dominant time constant of the correlation functions. In the NM-control model, the collective modes of the correlation functions are associated to the eigenvalues of the matrix of the coefficients of $(\tilde{u}, v, \tilde{w})$ in Eqs. (4.58), which reads

$$R = \begin{pmatrix} -\tau_n^{-1} & 2\lambda C_N & 0\\ \beta\nu_{d,1}C_{N-1} & -\tau_c^{-1} & \lambda\\ 0 & 2\beta\nu_{d,1}C_M & -\tau_p^{-1}\end{pmatrix}. \qquad (4.60)$$

Assuming that N and M are chosen in the equilibrium ratio $N = \theta M$ and that N is large, we can extract the scaling behaviour of the eigenvalues of R with respect to θ, for small θ. The eigenvalues $\{r_1, r_2, r_3\}$

read

$$r_1 \simeq -2\beta\nu_{d,1} \tag{4.61}$$

$$r_2 \simeq -\beta\nu_{d,1} \tag{4.62}$$

$$r_3 \simeq -\frac{2\beta\theta^2(1+3\nu_{d,1})}{N(1+\theta)^2}, \tag{4.63}$$

with $r_1 < r_2 < r_3$. The time constant associated to the dominant eigenvalue, r_3, is the renewal time for the NM-control model, and reads

$$\tau_R^{NM} \simeq \frac{N(1+\theta)^2}{2\beta\theta^2(1+3\nu_{d,1})}. \tag{4.64}$$

This expression is very similar to the extinction time for the anarchic scheme, Eq. (3.57). However, the renewal time τ_R^{NM} is not related to the extinction time for the system, because no critical catastrophe is possible in the NM-control model.

Similarly to how we did for the anarchic scheme, we can then define a dimensionless clustering parameter $\eta^{NM} = \tau_1/\tau_R^{NM}$. However, given that the mixing time of the NM-control scheme is the same as the mixing time of the anarchic scheme, and that the renewal time τ_R^{NM} is very similar to the extinction time of the anarchic scheme, the clustering parameter also results in a $1/\theta$ scaling for small θ, and the remarks made about the anarchic scheme apply verbatim to the NM-control scheme.

The full solution for Eqs. (4.58) is cumbersome. However, we can obtain asymptotic solutions in the form of Fourier series. Let $\tilde{u}_\infty(x,y)$, $v_\infty(x,y)$ and $\tilde{w}_\infty(x,y)$ be the asymptotic shapes of the correlation functions for long times :

$$\tilde{u}_\infty(x,y) = \lim_{t\to\infty} \tilde{u}(x,y,t) \tag{4.65}$$

$$v_\infty(x,y) = \lim_{t\to\infty} v(x,y,t) \tag{4.66}$$

$$\tilde{w}_\infty(x,y) = \lim_{t\to\infty} \tilde{w}(x,y,t). \tag{4.67}$$

We use the following Fourier decomposition :

$$f(x,y) = \sum_{k_x,k_y=-\infty}^{+\infty} f_{k_x,k_y} \exp\left(i\kappa_{k_x}(L-x)\right) \exp\left(i\kappa_{k_y}(L-y)\right). \tag{4.68}$$

Here $\kappa_k = k\pi/(2L)$ are the characteristic wave numbers for reflection boundary conditions and $f(x,y)$ stands for any of $\tilde{u}_\infty(x,y)$, $v_\infty(x,y)$ or $\tilde{w}_\infty(x,y)$. The coefficients satisfy the relation

$$f_{k_x,k_y} = \frac{1}{2\pi} \iint \exp\left(-i\kappa_{k_x}(L-x)\right) \exp\left(-i\kappa_{k_y}(L-y)\right) f(x,y)\, dx\, dy. \tag{4.69}$$

The linear system of equations solved by the Fourier coefficients can be obtained from Eqs. (4.58) by setting the time derivative terms to zero, multiplying by $\exp(-i\kappa_{k_x})\exp(-i\kappa_{k_y}y)/(2\pi)$, integrating over $dx\,dy$ and using Eq. (4.69) and Eqs. (4.53). Using the Neumann boundary conditions on f_∞, the Fourier decomposition then reduces to

$$f_\infty = \sum_{k=-\infty}^{+\infty} f_{k,k} \cos\left(\frac{k\pi}{2L}(L-x)\right) \cos\left(\frac{k\pi}{2L}(L-y)\right). \tag{4.70}$$

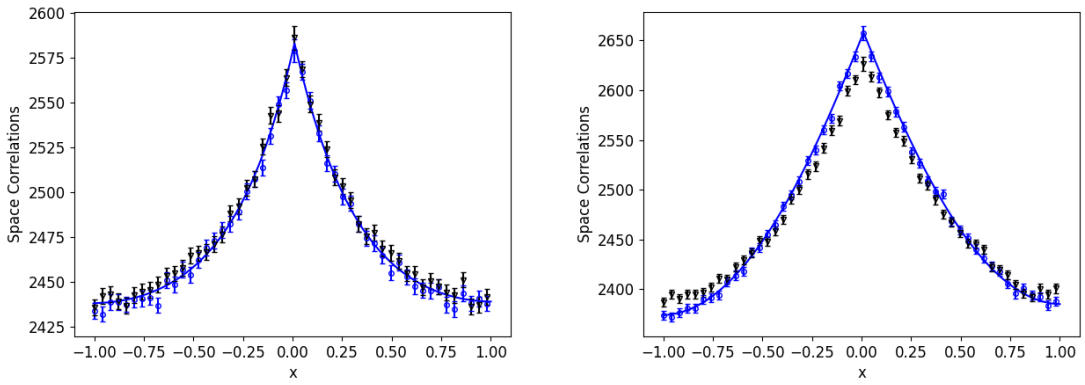

(a) Asymptotic pair correlation function for $\theta = 10^{-3}$ and $y = 0$.

(b) Asymptotic pair correlation function for $\theta = 1$ and $y = 0$.

Figure 4.6 : Asymptotic pair distance for different value of θ. The parameters are taken from Table 3.1. Black triangles : Monte Carlo simulations for the N-control scheme. Blue circles : Monte Carlo simulations of the NM-control scheme, both with 10^6 replicas. Blue solid line : analytical solution of the NM-control scheme Eqs. (4.58).

Indeed, in this case all the coefficients with $k_x \neq k_y$ are zero. The terms $f_{k,k}$ thus read

$$\tilde{u}_{k,k} = \frac{m(N-1)\lambda^2 + n\beta\left(N(\alpha_1 + \tilde{k}^2 D) + 2(N-1)\nu_{d,1}\lambda\right)}{LN\left(\alpha_1 + \tilde{k}^2 D\right)\left(\tau_n + 2\tilde{k}^2 D\right) - 2L(N-2)\beta\nu_{d,1}\lambda} \tag{4.71}$$

$$v_{k,k} = \frac{2nN\beta\left((N-1)\tau_n + (N-2)\beta + 2\tilde{k}^2(N-1)D\right)\nu_{d,1} + m(N-1)N\left(\tau_n + 2\tilde{k}^2 D\right)\lambda}{2L(N-1)\left(N(\alpha_1 + \tilde{k}^2 D)(\tau_n + 2\tilde{k}^2 D\right) - 2(N-2)\beta\nu_{d,1}\lambda)} \tag{4.72}$$

$$\tilde{w}_{k,k} = \frac{M-1}{N}\tilde{v}_{k,-k} \tag{4.73}$$

where τ_n, τ_c are given by Eqs. (4.59), and n, m and $\tilde{k}$ are respectively given by

$$n = \frac{N}{2L}, \qquad m = \frac{M}{2L}, \qquad \tilde{k} = \frac{k\pi}{2L}.$$

The asymptotic two-point neutron-neutron correlation function for the NM-control model was numerically computed by truncating the Fourier series after 1000 terms. It is compared with Monte Carlo simulations for the N-control and the NM-control scheme, for two sets of physical parameters, in Figs. 4.6a and 4.6b.

For $\theta = 0.001$ (Fig. 4.6a), the NM-control scheme provides a good approximation of the N-control scheme, and all the curves representing neutron correlations are very similar. This means that, when $\theta \ll 1$, which is the case in nuclear reactors, a system where neutrons and precursors are both kept under control has similar correlation functions as a system where population control acts on neutrons alone. On the other hand, when $\theta = 1$ (Fig. 4.6b), the N-control and NM-control models yield similar, but different correlation functions. Indeed, we observe that the NM-control scheme results in stronger spatial short-range correlations compared to the N-control scheme, while long-range correlations are weaker in the NM-control scheme. This can be easily explained : in the N-control scheme, when a precursor decays, it is destroyed and replaced by a neutron that immediately starts diffusing. This mechanism can be seen as a kind of delayed diffusion ; when a neutron induces a fission event and produces a precursor, it effectively suspends diffusion for a time of the order of $1/\lambda$. On the other hand, in the NM-control model, a precursor does not die when it decays, and thus plays the role of a source at a fixed position until it is replaced by another precursor. The precursor density can then undergo significant local fluctuations

favouring short-range correlations by inducing overproduction of neutrons in a small volume, at the expense of long-range correlations.

Some insight about the similarity between the N-control and NM-control schemes for $\theta \ll 1$ can be gained by comparing Eqs. (4.46) and Eqs. (4.58). Indeed, remember that $\theta \ll 1$ means that the number of precursors is much larger than the number of neutrons. If $m(t)$ is sufficiently large, which is the case here, its fluctuations will be negligible compared to its mean value. This allows us to consider $m(t)$ as a deterministic observable. If we then assume that

$$\mathbb{E}[n_i(t)n_j(t)m(t)] \simeq \mathbb{E}[n_i(t)n_j(t)]\mathbb{E}[m(t)],$$

then Eq. (4.46a) reduces to Eq. (4.58a). Thus, in this limit, neutron-neutron correlations follow the same dynamics in both schemes. It is worth remarking however that, under the same approximation, the equations for v and $\tilde{w}$ in the N-control model do not reduce to the corresponding equations in the NM-control model. Similarly to the prompt system, we can complement the analysis of spatial moments by investigating the statistical behaviour of neutron families.

4.3.3 . Analysis of the statistics of neutron families

The analysis of the time and space correlations of the NM-control can be usefully complemented by the investigation of the statistics of neutron families, which relies on a generalization of the approach discussed in Sec. 4.1.3 for the simpler case of the constrained model without precursors.

For the NM-control model, both source neutrons and precursors are assigned an identifier (an integer in $\{1, \dots, F\}$), which they transmit to their descendants. Let n_i (m_i) be the number of neutrons (precursors) with identifier i. Particles sharing the same identifier form a *family*, so that the simulation starts with F initial families. The size of a family increases by one when one of its members induces fission without precursor production, and by two if it is a fission with precursor production. The size decreases by one when a neutron or precursor is killed.

To the best of our knowledge, the effect of introducing delayed events in a time-dependent Galton-Watson process has not been investigated in the context of family fixation. We focus on the case where the number of neutrons and precursors satisfies the ratio $M = N/\theta$, with $\theta = \lambda/\beta\nu_d$, which corresponds to the equilibrium initial condition.

To write the recurrence equations describing the conditional moments of the fixation time τ we need to consider all the 'useful' transitions, i.e. those that change the number of neutrons or precursors in family A, and the corresponding rates and probabilities. There are 6 such transitions that can be deduced from Section 4.3 :

- $(n, m) \to (n+1, m)$ with rate $\beta_{(+1,0)} = \frac{\beta(N-n)n}{N-1}\left[(1-\nu_d) + \frac{\nu_d m}{M}\right] + \frac{\lambda}{N}m(N-n)$.
- $(n, m) \to (n-1, m)$ with rate $\beta_{(-1,0)} = \frac{\beta(N-n)n}{N-1}\left[(1-\nu_d) + \frac{\nu_d(M-m)}{M}\right] + \frac{\lambda}{N}n(M-m)$.
- $(n, m) \to (n, m+1)$ with rate $\beta_{(0,+1)} = \frac{\beta\nu_d}{(N-1)M}n(n-1)(M-m)$.
- $(n, m) \to (n, m-1)$ with rate $\beta_{(0,-1)} = \frac{\beta\nu_d}{(N-1)M}(N-n)(N-n-1)m$.
- $(n, m) \to (n+1, m+1)$ with rate $\beta_{(+1,+1)} = \frac{\beta\nu_d}{(N-1)M}n(N-n)(M-m)$.
- $(n, m) \to (n-1, m-1)$ with rate $\beta_{(-1,-1)} = \frac{\beta\nu_d}{(N-1)M}(N-n)nm$.

We also define the rate of useful transitions

$$\beta_u(n, m) = \sum_{\mathbf{v}\in T} \beta_{\mathbf{v}}(n, m),$$

where $T = \{(\pm 1, 0), (0, \pm 1), \pm(1, 1)\}$. Observe that $\beta_u \leq \beta_t$, where $\beta_t = \beta N + \lambda M$ represents the total transition rate, since not all transitions contribute to fixation. Subsequently, one can define the probability

that a transition $\mathbf{v}$ happens, conditioned to the fact that the transition is useful : $p_{\mathbf{v}}(n,m) = \beta_{\mathbf{v}}/\beta_t(n,m)$. One might equivalently consider all transitions (instead of only useful transitions), in which case β_u and β_t coincide, and the transition $(n,m) \to (n,m)$ should be explicitly taken into account.

Fixation probability

In this situation, we do not know *a priori* the fixation probability $f(n,m)$. However, from the law of total expectation we write

$$f(n,m) = \sum_{\mathbf{v}\in T} p_{\mathbf{v}}(n,m) f(n+v_1, m+v_2), \tag{4.74}$$

with boundary conditions $f(N,M) = 1$ and $f(0,0) = 0$. Equation (4.74) admits the solution

$$f(n,m) = \frac{Nn + M\theta m}{N^2 + \theta M^2}. \tag{4.75}$$

For $M = N/\theta$, Eq. (4.75) reduces to $(n+m)/(N+M)$: regardless of their nature, all individuals have the same probability of fathering the fixating family. Moreover, the linearity of the fixation probability f suggests that neutrons and precursors behave like two independent populations with respect to fixation. The solution in Eq. (4.75) has been carefully verified against Monte Carlo simulations (not shown here for conciseness). Knowledge of f will now allow us to apply our methodology to the problem of the fixation time.

Moments of the fixation time

We investigate the statistical moments of the fixation time. Let us first consider the average (conditional) fixation time $\mathbb{E}[\tau|A](n,m)$. Using the law of total expectation and defining an intermediary function $g_1(n,m) = f(n,m)\mathbb{E}[\tau|A](n,m)$ for $(n,m) \neq (0,0)$ and $g_1(0,0) = 0$, we obtain

$$\sum_{\mathbf{v}\in T} p_{\mathbf{v}}(n,m) g_1(n+v_1, m+v_2) - g_1(n,m) = -\sum_{\mathbf{v}\in T} \frac{p_{\mathbf{v}}(n,m) f(n+v_1, m+v_2)}{\beta_t(n,m)}. \tag{4.76}$$

The presence of non-constant coefficients and the shape of the source term make Eq. (4.76) harder to solve analytically. However, Eq. (4.76) is formally a multi-dimensional difference equation ; it can be thus solved numerically by regarding it as a system of non-homogeneous linear equations for the $(N+1)(M+1)$ unknowns $g(n,m)$, with ($0 \leq n \leq N$, $0 \leq m \leq M$). The equations provided by Eq. (4.76) are complemented with equations stemming from boundary conditions imposing that $g_1(n,m) = 0$ outside of the domain. The linear system is then solved numerically, and results are successfully compared to Monte Carlo simulations in Fig. 4.7.

The variance of the fixation time can be obtained from the second moment, which, after using the law of total expectation and defining an intermediate function $g_2(n,m) = f(n,m)\mathbb{E}[\tau^2](n,m)$ for $(n,m) \neq (0,0)$ and $\mathbb{E}[\tau^2](0,0) = 0$, is determined by

$$\sum_{\mathbf{v}\in T} p_{\mathbf{v}}(n,m) g_2(n+v_1, m+v_2) - g_2(n,m) = \sum_{\mathbf{v}\in T} \left[\frac{2p_{\mathbf{v}}(n,m) g_1(n+v_1, m+v_2)}{\beta_u(n,m)} + \frac{p_{\mathbf{v}}(n,m) f(n+v_1, m+v_2)}{\beta_u(n,m)^2} \right]. \tag{4.77}$$

Again, Eq. (4.77) is solved numerically by using the boundary condition $g_2(N,M) = 0$. Results are verified against Monte Carlo simulation in Fig. 4.7, with good agreement. Remark also that there is very little difference between the average fixation time for a family initially starting with one precursor or with one neutron, as expected from the shape of f.

The standard deviation $\sigma[\tau](n,m) = \sqrt{\mathrm{Var}[\tau](n,m)}$ can be shown to behave similarly to the prompt case, in the sense that it has the same order of magnitude as the average fixation time : this means that fixation can happen early in the simulation, compared to the average fixation time.

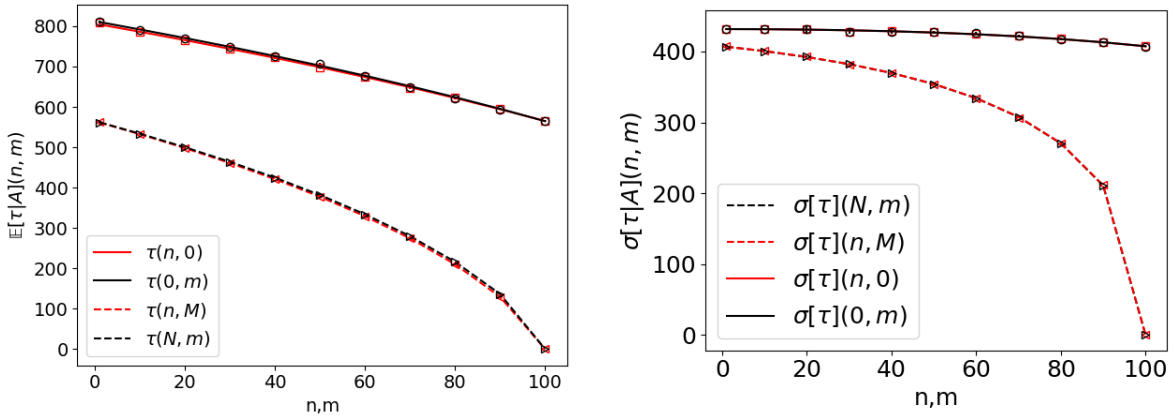

Figure 4.7 : One-dimensional slices of the average fixation time $\mathbb{E}[\tau|A](n,m)$ (left) and of the standard deviation of the fixation time $\sigma[\tau|A](n,m)$ (right), for $N = 100$, $M = 100$, $\beta = 0.2$, $\nu_d = 0.5$, and $\lambda = 0.1$. Solid and dashed lines : numerical results obtained by solving Eqs.(4.76)-(4.77); markers : Monte Carlo results are within 3σ of the deterministic solution.

We conclude by revisiting the relation between family statistics and spatial clustering. Again, due to the choice of mass-preserving boundary conditions, the statistics of families is insensitive to spatial effects. Due to the numerical nature of our solution, we can only provide empirical scaling relations for the fixation time $\tau_1 = \mathbb{E}[1,0]$ (or equivalently $\mathbb{E}[0,1]$). Assuming $N \gg 1$, we can show that $\tau_1 \sim N/\beta\nu_d\theta^2$ when $\theta \ll 1$ (numerical investigations not detailed here for conciseness); conversely, $\tau_1 \sim N/\beta\nu_d$ when $\theta \gg 1$). Given that the equilibrium ratio $M = N/\theta$ is enforced, M does not appear explicitly in this expression. For the case of particles evolving in *unbounded* homogeneous systems, the time evolution of $\langle r^2(t)\rangle$ is characterized by a single timescale, i.e, the renewal time τ_R, whose leading-order term reads

$$\tau_R \sim \frac{N(1+\theta)^2}{2\beta\theta^2(1+3\nu_d)}, \tag{4.78}$$

provided that N is large. Thus, the fixation time and the renewal time have a very similar scaling, similarly as in the prompt case. For an illustration of the relation between fixation and clustering, Fig. 4.8 displays the pair distance $\langle r^2(t)\rangle$ and the number of surviving families; the fixation time and the renewal time are also represented. The time evolution of the number of families and that of the pair distance are of the same order of magnitude. As explained in Sec. 4.1.3, the identification between the fixation time and the clustering timescale only holds for unbounded systems.

4.4 . Immigration model

We have observed that the precursor population exhibits only weak fluctuations in the $\theta \ll 1$ limit. This suggests another alternative model where precursors are modeled as a fixed external source, with the aim of obtaining a time-dependent solution that, in this limit, successfully approximates the N-control model. Thus, we model the system as a collection of neutrons under population control, with an external, time-independent source term modelling precursor decay. Formally, this model is equivalent to an *immigration model* with a time-independent, Poissonian immigration source describing the asymptotic precursor decay density, given by

$$\mathcal{Q}_I(x) = \lambda m_\infty(x) = \frac{\lambda}{\theta} n_\infty(x), \tag{4.79}$$

where θ is the parameter of the equivalent NM-control scheme. Population control is enforced by requiring that each time a new neutron enters the system, whether by fission or from the external source, we destroy another randomly chosen neutron, as illustrated in Fig. 4.9.

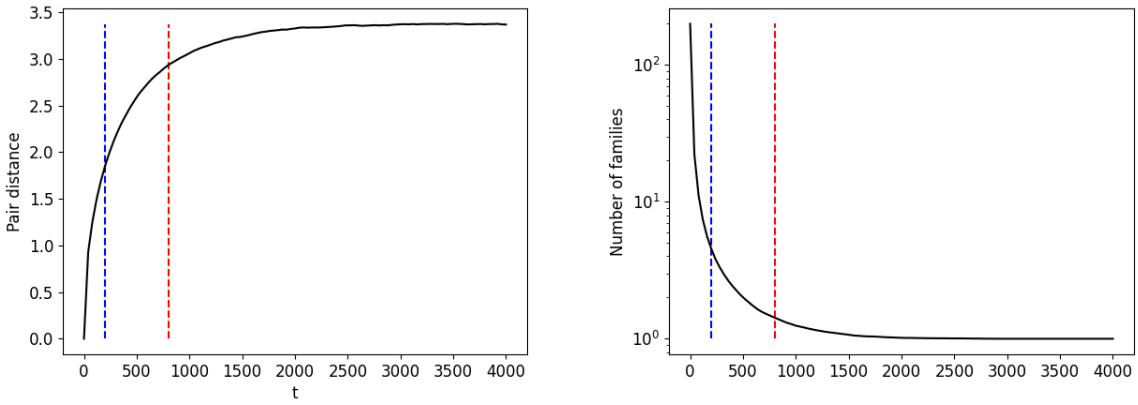

Figure 4.8 : Pair distance (left) and number of surviving families (right), as calculated by Monte Carlo simulation ; the average fixation time is represented by red dashed lines, and the estimated renewal time is represented by blue dashed lines. Parameters are those of Fig. 4.7.

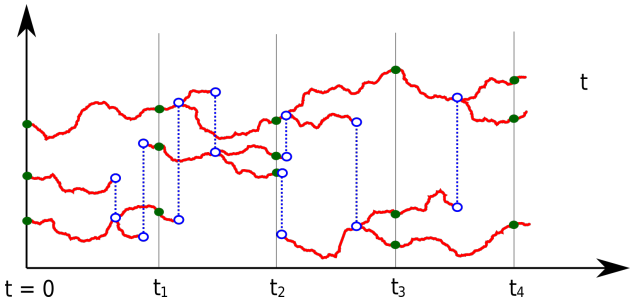

Figure 4.9 : A typical history for a system with 3 neutrons at $t = 0$, in the immigration model. Neutrons diffuse (in red) until they branch or are killed by another neutron branching somewhere else (vertical blue dashed lines show these correlated events). They can also be produced by the source, thus killing another randomly chosen neutron.

4.4.1 . Derivation of the spatial master equation

In addition to diffusion, the transitions involved in this model are

- A neutron capture in bin i and a fission in bin j $(i \neq j)$. The corresponding transition is $a_i^\dagger a_j \mathbf{n} \to \mathbf{n}$ with rate

$$\beta_1 = \frac{\beta(n_i + 1)(n_j - 1)}{N(N-1)},$$

- A neutron capture in bin i and an emission by the Poisson source in a different bin j $(i \neq j)$. The corresponding transition is $a_i^\dagger a_j \mathbf{n} \to \mathbf{n}$ with rate

$$\beta_2 = \frac{\lambda M Q_j (n_i + 1)}{N},$$

where Q_j is the probability that the emission happens in bin j.

Following the usual derivation method, we obtain first the master equation associated to this stochastic process

$$\frac{\partial}{\partial t}\mathcal{P}(\mathbf{n},t) = \sum_i \Bigg[\xi(n_{i+1}+1)\mathcal{P}(a_{i+1}^\dagger a_i \mathbf{n},t) + \xi(n_{i-1}+1)\mathcal{P}(a_{i-1}^\dagger a_i \mathbf{n},t) - 2\xi n_i \mathcal{P}(\mathbf{n},t) + \frac{\beta}{N-1}\sum_{j\neq i}\Big((n_i+1)(n_j-1)\mathcal{P}(a_i^\dagger a_j \mathbf{n},t) - n_i n_j \mathcal{P}(\mathbf{n},t)\Big) + \frac{\lambda M}{N}\sum_{j\neq i}\mathcal{Q}_j\Big((n_i+1)\mathcal{P}(a_i^\dagger a_j \mathbf{n},t) - n_i \mathcal{P}(\mathbf{n},t)\Big)\Bigg]. \tag{4.80}$$

4.4.2 . Derivation and analysis of spatial moments

The equation for the discrete average neutron density is again obtained by summation from Eq. (4.80), namely

$$\frac{\partial}{\partial t}\mathbb{E}[n_i](t) = \xi\Delta\mathbb{E}[n_i](t) - \frac{\lambda M}{N}\mathbb{E}[n_i](t) + \lambda M \mathcal{Q}_i, \tag{4.81}$$

which, by taking the continuous limit, becomes

$$\frac{\partial}{\partial t}n(x,t) = \mathcal{D}\nabla^2 n(x,t) - \frac{\lambda}{\theta}n(x,t) + \mathcal{Q}_I(x). \tag{4.82}$$

Taking $\mathcal{Q}_I(x)$ as given by Eq. (4.79), the last two terms asymptotically cancel out and the dynamics of the average is driven only by diffusion, similarly to what happens in the anarchic model when the system is critical.

The equation for the discrete pair correlation function reads

$$\begin{aligned}\frac{\partial}{\partial t}\mathbb{E}[n_i n_j](t) = {} & \xi\left(\mathbb{E}[n_i\Delta n_j](t) + \mathbb{E}[\Delta n_i n_j](t)\right) - \left(\frac{2\beta}{N-1} + \frac{2\lambda M}{N}\right)\mathbb{E}[n_i n_j](t) + \delta_{i,j}\frac{2N\beta}{N-1}\mathbb{E}[n_i](t) \\ & + \lambda M\delta_{i,j}\left(\mathcal{Q}_i + \frac{\mathbb{E}[n_i](t)}{N}\right) + \lambda M\frac{N-1}{N}\left(\mathcal{Q}_j\mathbb{E}[n_i](t) + \mathcal{Q}_i\mathbb{E}[n_j](t)\right) \\ & + \delta_{i,j}\xi\left(\mathbb{E}[n_{i+1}](t) + \mathbb{E}[n_{i-1}](t) + 2\mathbb{E}[n_i](t)\right) - \delta_{i+1,j}\xi\left(\mathbb{E}[n_{i+1}](t) + \mathbb{E}[n_i](t)\right) \\ & - \delta_{i-1,j}\xi\left(\mathbb{E}[n_i](t) + \mathbb{E}[n_{i-1}](t)\right).\end{aligned} \tag{4.83}$$

which, under the continuous limit and after defining $\tilde{u}(x,y,t) = u(x,y,t) - \delta(x-y)n(x,t)$, becomes

$$\begin{aligned}\frac{\partial}{\partial t}\tilde{u}(x,y,t) = {} & \mathcal{D}\left(\nabla_x^2 + \nabla_y^2\right)\tilde{u}(x,y,t) - \tau_n^{-1}\tilde{u}(x,y,t) + C_N\left(n(x,t)\mathcal{Q}_I(y) + n(y,t)\mathcal{Q}_I(x)\right) \\ & + 2\beta\delta(x-y)n(x,t),\end{aligned} \tag{4.84}$$

where we recognize τ_n from Eq. (4.59a). Thus, in this model, neutron pair correlations relax with a time constant governed by τ_n.

Equations (4.82) and (4.84) have the same form as Eqs. (4.53a) and (4.58a), provided that one replaces $\mathcal{Q}_I(x)$ by its expression, Eq. (4.79). These equations can be solved analytically. In particular, taking a uniform initial condition for $n(x,t)$, we obtain

$$n(x,t) = \frac{N}{2L} \tag{4.85}$$

for the average neutron density, and

$$\begin{aligned}\tilde{u}(x,y,t) = {} & \frac{N(N-1)}{4L^2}\exp\left(-\frac{t}{\tau_n}\right) + \frac{2\tau_n\lambda M(N-1)}{4L^2}\left[1 - \exp\left(-\frac{t}{\tau_n}\right)\right] \\ & + \frac{2\beta N}{2L}\int dx' \int_0^t dt' \mathcal{G}'(x,t|x',t')\mathcal{G}'(y,t|x',t')\exp\left(-\frac{t-t'}{\tau_n}\right)\end{aligned} \tag{4.86}$$

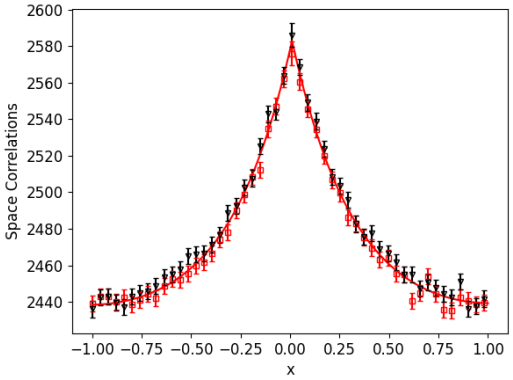

(a) Asymptotic pair correlation function for $\theta = 0.001$ and $y = 0$.

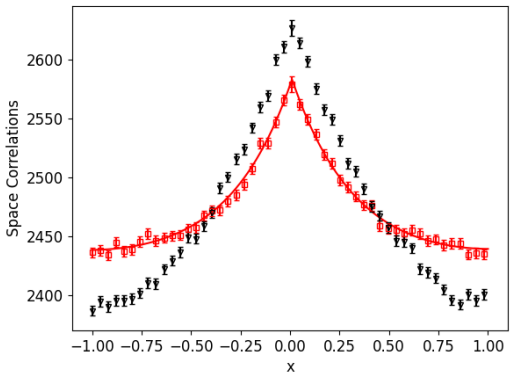

(b) Asymptotic pair correlation function for $\theta = 1$ and $y = 0$.

Figure 4.10 : Asymptotic pair correlation function for different values of θ, with parameters taken from Table 3.1. Red solid line : analytical solution of the immigration model. Red squares : Monte Carlo simulations of the immigration model. For reference, the results of the N-control scheme are plotted in black triangles.

for the pair correlation function, where $\mathcal{G}'$ is the Green's function associated to Eq. (4.82). As a side note, taking the $\lambda \to 0$ limit in this equation we recover the pair correlation function for a system of prompt neutrons under population control [46, 47, 79].

Comparison with Monte Carlo simulations (see Fig. 4.10a) shows that, for systems where $\theta \ll 1$, the immigration model closely matches the N-control model ; the remarks made about Fig. 4.4 also apply to the immigration model. Figure 4.10b provides the same comparison for a larger value of θ. Comparing Fig. 4.10b and Fig. 4.6b, it is clear that the N-control model is better approximated by the NM-control model than by the immigration model. This is unsurprising, in view of the crudeness of the treatment of neutron-precursor correlations in the immigration model.

4.5 . Mean squared pair distance functions

We now discuss the mean-squared pair distance for our population control models, and we compare it to the case of an anarchic population.

For the N-control scheme, we do not have access to an analytical expression for the mean-squared pair distance, because the moment equations, Eqs. (4.46), are not closed. However, we do have an asymptotic correlation function for the NM-control scheme, given by Eqs. (4.73), from which we can deduce an asymptotic mean-squared pair distance. For reflection boundary conditions, it is given by

$$\langle r_{NM}^2 \rangle = \frac{8L^4 \tilde{u}_{0,0}}{3N^2} - \left(\frac{16L^2}{\pi^2 N}\right)^2 \sum_{k=1}^{+\infty} \frac{\tilde{u}_{k,k}}{k^4}, \tag{4.87}$$

where $\tilde{u}_{k,k}$ is the Fourier coefficient for the neutron-neutron correlations asymptotic solution of Eq. (4.58a). On physical grounds, we expect the asymptotic pair distance in the NM-control scheme to be always smaller than the uncorrelated value, Eq. (3.61).

As for the immigration model, an analytical expression for the mean-squared pair distance can be obtained by applying the definition of the mean-squared pair distance function, Eq. (3.10), to the solution, Eq. (4.86). For reflection boundary conditions, straightforward calculations hence yield

$$\langle r_I^2 \rangle(t) = C_N \frac{2L^2}{3} - \frac{128L^2\beta}{N} \sum_{k=1}^{+\infty} \frac{1 - e^{-\left(\tau_n^{-1} - 2\alpha_k\right)t}}{(k\pi)^4 \left(\tau_n^{-1} - 2\alpha_k\right)} \tag{4.88}$$

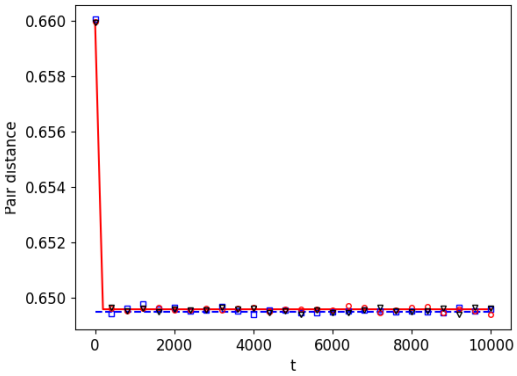

(a) Mean-squared pair distance for $\theta = 10^{-3}$.

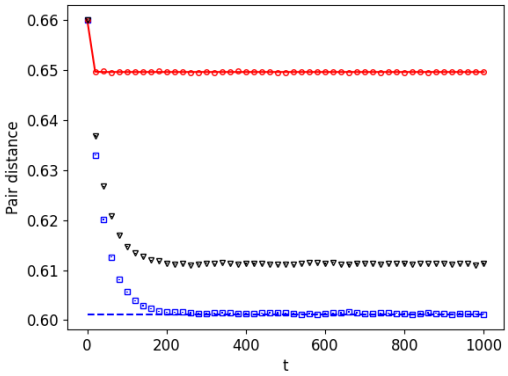

(b) Mean-squared pair distance for $\theta = 1$.

Figure 4.11 : Mean-squared pair distance for different values of θ, with parameters taken from Table 3.1. Blue dashed line : NM-control model analytical asymptotic value; blue squares : Monte Carlo result; red solid line : immigration model analytical solution; red circles : immigration model Monte Carlo result; black triangles : N-control model Monte Carlo result. All simulation results are obtained with 10^6 replicas. Error bars are plotted but barely visible.

The sum can be computed analytically in the asymptotic limit and reads

$$\langle r_I^2 \rangle_\infty = C_N \frac{2L^2}{3} + \frac{16\beta\tau_n}{N} \times \left(\left(\frac{D\tau_n}{L} \right)^2 - \frac{2D\tau_n}{3} - \frac{4L^2}{45} - \frac{\sqrt{2}(D\tau_n)^{\frac{3}{2}}}{L} \cot \sqrt{\frac{2\tau_n}{D}} L \right) \tag{4.89}$$

If we take the mean-squared pair distance as an indicator of clustering, Fig. 4.11a clearly illustrates that the three models have very similar clustering behaviour for $\theta \ll 1$, even for very long times. For $\theta \sim 1$, on the other hand, the models behave differently, as shown in Fig. 4.11b. In particular, we note that the immigration model yields the largest mean-squared pair distance of all the considered control schemes. This is easily explained by the fact that the 'decay source' of the immigration model is assumed to be uniformly distributed in space and completely uncorrelated with the neutrons, an assumption that is bound to reduce clustering. The NM-control scheme yields a smaller mean-squared pair distance than the N-control scheme, indicating that clustering is more prominent in the former. This behavior can be explained by observing that a precursor may in fact produce several neutrons at the same position before being destroyed, which tends to increase clustering. It is interesting to note that for all control models the squared pair distance asymptotically converges to $\langle r^2 \rangle_\infty < \langle r^2 \rangle_{\text{iid}}$, because the critical catastrophe is avoided, contrary to what happens in the anarchic case. However, Eqs. (4.87) and (4.89) show that $\langle r^2 \rangle_\infty$ tends to the uncorrelated value as N tends to infinity.

4.6 . Conclusions and perspectives

In an attempt to take into account population control effects, we introduced several idealized sampling strategies. These models break the statistical independence of the neutron fission chains, which forced us to abandon the Pál and Bell backward formalism in favour of the forward formalism. We derived the master equations for four different population-control models :

- in the prompt model without precursors, the neutron population is kept constant. We provided a formal derivation for the spatial moment equations instead of the previous derivation relying on heuristic arguments;
- in the N-control model, the neutron population is kept constant, but no constraint is applied to the precursor population. This model yields a non-closed hierarchy of moment equations;

- in the NM-control model, both the neutron and precursor populations are controlled. This model yields a closed hierarchy of moment equations. We identified the dominant timescales of the model and presented asymptotic solutions for the first two spatial moments.

- in the immigration model, precursors are modelled as a uniform Poisson neutron source whose intensity is equal to the asymptotic precursor decay rate at equilibrium.

For each model, we obtained two-point, one-time pair correlation functions by analytical means when possible, and compared them to analog kinetic Monte Carlo simulations. Such comparisons showed that all the models including precursors yield very close results when $\theta \ll 1$, which is the main regime of interest for nuclear reactors. We also showed that the introduction of population control prevents the occurrence of the critical catastrophe and thus quenches clustering.

Within the same theoretical framework, we also investigated family fixation, i.e. the eventual survival of a single particle family. In the case where precursors are neglected, we derived and analytically solved the equations for the first two moments of the fixation time starting with any number of neutrons. In particular, when there is a single initial neutron in each family, we showed that the average fixation time is given by $\mathbb{E}[\tau_p|A](1) = (N-1)^2/\beta N$. Furthermore, we discussed the relation between fixation and clustering. For the case of unbounded media, $\langle r^2(t)\rangle$ has an exponential saturation with a typical timescale $\tau_{R,p} = N/2\beta$, which suggests that clustering and fixation are intimately related, their respective timescales being similar when $N \gg 1$.

In the NM-control model, which includes precursors, we derived the equations for the first two moments of the fixation time, and we solved them numerically. We determined that, in this case, the average fixation time scales as $\tau_1 \sim N/\beta\nu_d\theta^2$ when $\theta = N/M \ll 1$. The solutions were verified against Monte Carlo simulations. Similarly as in the prompt case, we found that for the case of unbounded media the typical saturation time of the square pair distance $\langle r^2(t)\rangle$ has almost the same scaling as the average fixation time τ_1 when $N \gg 1$.

In Part I we investigated the behaviour of space-time correlations in analog Monte Carlo simulations of diffusion-based stochastic models including neutrons and precursors. We developed an analytical framework for the characterization of space-time correlations by making several assumptions : the energy dependency was neglected ; particle displacements were replaced with Brownian Motion ; the system was assumed to be spatially homogeneous with mass-preserving boundary conditions ; only the following events were considered : fission, capture, and precursor decay. This model can be treated analytically, at the expense of being considerably simplified.

The results obtained in Part I provide a clear setting for the investigation of kinetic Monte Carlo simulations, but are by construction restricted to the case of analog sampling, without any variance-reduction method, and only apply to single-speed diffusion in spatially homogeneous systems. To overcome these imitations, and broaden the domain of validity of our findings, in Part II, we will relax many of the assumptions we made so far. In particular, while some simplifications will be retained for the ease of computation (use of multi-group formalism, with a set of collision events including only fission, sterile capture, isotropic scattering and precursor decay), we will now move to fully non-analog Monte Carlo simulations, covering a large spectrum of variance-reduction and population-control strategies. Our main goal for Part II will be to assess the impact of such techniques on the behaviour of the fluctuations and correlations in kinetic simulations.

Deuxième partie

Correlations in time-dependent transport problems solved by non-analog Monte Carlo methods

5 -Spatial and generational correlations in Monte Carlo eigenvalue calculations

As shown in Chapter 2, the critical source for kinetic problems depends on the fundamental eigenmode of the k-eigenvalue formulation of the Boltzmann equation. Within the framework of Monte Carlo simulation, the fundamental eigenmode and the associated dominant eigenvalue can be obtained using the well-known power iteration method, which relies on the iteration of the fission source : neutrons starting a given 'generation' are chosen amongst the neutrons born from fission in the previous generation [2, 10]. After a sufficient number of generations, the phase-space distribution of fission neutrons eventually becomes stationary, and so do the related tallies, such as neutron flux and reaction rates.

Once the fission source has converged to a stationary state, the sought tallies are averaged using an ergodic average over successive generations in order to reduce the statistical uncertainty on the estimated values. For the purpose of estimating confidence intervals on the ergodic averages, for the sake of simplicity most production-level Monte Carlo codes ignore correlations between successive generations, although some statistical tests are becoming progressively available [89], fostered by the increased awareness of Monte Carlo practitioners. Ground-breaking investigations concerning the impact of correlations on the estimation of variance in Monte Carlo power iteration have been carried out by Brissenden and Garlick, who noted that inference techniques based on an assumption of independent and identically distributed samples led to an underestimation of the sample variance of the average multiplication factor k_{eff} [29]. The severity of the underestimation was later related to the value of the dominance ratio (i.e. the ratio of the second over the first eigenvalue of the Boltzmann equation) by Ueki et al. [30], and since then several authors have tried to predict and correct the estimates of the variance [31, 34–37].

More recently, Dumonteil et al. have pointed out that fission-induced correlations may lead to a strong spatial patchiness (i.e. non-Poisson spatial fluctuations) in the fission source, which was dubbed *neutron clustering* [27]. A characterization of spatial correlations relying on moment equations was derived in a time-dependent context in simplified nuclear reactor models [28, 46, 47, 77], and the key findings were shown to apply also to power iteration [38, 41] and to production-level Monte Carlo simulations of realistic configurations [90]. Several methods have been proposed in order to detect and possibly quench the effects of clustering. Nowak et al. suggested to use Shannon entropy for neutron clustering detection [38], by pointing out that entropy is systematically decreased by the presence of neutron clustering. Inspired by pioneering work in population dynamics by Zhang et al. [81], Sutton introduced the concept of neutron lineage in power iteration and outlined the relation between neutron clustering and fixation (i.e. the number of generations at which all neutrons in the Monte Carlo simulation share the same common ancestor) [41, 42]. Equations for the moments of the fixation time in kinetic simulations have been derived by us in Ref. 84, which might be used to establish a more rigorous theoretical framework for fixation in power iteration.

Over the last few years, the issue of spatial correlations has led to a collection of novel, albeit partially contradictory, results. Cosgrove et al. pointed out the impact of clustering, suggesting that it might induce spurious xenon oscillations in depletion calculations coupling Monte Carlo neutronics solvers and Bateman solvers [40]. Fröhlicher et al. suggested that neutron clustering could lead to an apparent bias on the average Monte Carlo tallies, in addition to affecting the estimation of the variance [44]. In contrast, Mickus and Dufek stated that neutron clustering should not be detrimental to criticality Monte Carlo simulations, in that the estimate of the variance is asymptotically not altered [45].

Given the lack of consensus on these matters, which are highly relevant for both conceptual and practical questions related to power iteration, we have decided to explore in more depth the emergence of spatial correlations and how they are affected by the key mechanisms at play in Monte Carlo simulations, namely the collision sampling strategies and the population-control and variance-reduction methods. Since the statistical behaviour of the Monte Carlo estimate of the fundamental mode has a direct impact on the

sampling of the critical source for kinetic problems, the quantification of the correlations affecting particle transport in the course of the power iteration algorithm is of utmost importance for the investigations carried out in this thesis work. In the following we will therefore briefly recall the main ideas behind the Monte Carlo power iteration, provide a thorough examination of the interplay between *generational* and *spatial* correlations, and show how they are affected by several variance-reduction and population-control techniques. We will focus in particular on the use of branchless collisions, which has been independently introduced in the context of power iteration calculations by Fröhlicher et al. in Ref. 44 and Belanger et al. in Ref. 91. Our analysis will rely on a broad class of global (i.e., integrated) and local (i.e., space-dependent) tallies, encompassing the Shannon entropy, the pair distance, the normalized variance and the Feynman moments, aimed at detecting the presence of correlations, whose advantages, drawbacks and relative performances will be assessed by resorting to a set of benchmark problems.

The material presented here is taken mostly from Ref. 92 and from the joint work with H. Belanger in Ref. 91.

5.1 . Power iteration in Monte Carlo simulation

As recalled in Sec. 2.1.4, the k-eigenvalue formulation of the Boltzmann equation is :

$$\begin{aligned}\mathbf{\Omega}\cdot\nabla\varphi_k(\mathbf{r},\mathbf{\Omega},E)+\Sigma_t(\mathbf{r},E)\varphi_k(\mathbf{r},\mathbf{\Omega},E) &= \iint \Sigma_s(\mathbf{r},\mathbf{\Omega}'\to\mathbf{\Omega},E'\to E)\varphi_k(\mathbf{r},\mathbf{\Omega}',E')d\mathbf{\Omega}'dE' \\ &+ \frac{1}{k}\frac{\chi_p(\mathbf{r},E)}{4\pi}\iint_{4\pi}\nu_p(\mathbf{r},E')\Sigma_f(\mathbf{r},E')\varphi_k(\mathbf{r},\mathbf{\Omega}',E')\,d\mathbf{\Omega}'\,dE', \qquad (5.1)\\ &+ \frac{1}{k}\sum_j\frac{\chi_d^j(\mathbf{r},E)}{4\pi}\iint\nu_d^j(\mathbf{r},E')\Sigma_f(\mathbf{r},E')\varphi_k(\mathbf{r},\mathbf{\Omega}',E')d\mathbf{\Omega}'dE' \qquad (5.2)\end{aligned}$$

where k is the eigenvalue and φ_k the corresponding eigenfunction. Notation is the same as in Sec. 2.1.4. The dominant eigenpair $\{k_0,\varphi_{k_0}\}$ of Eq. (5.2) can be estimated using a stochastic equivalent of the power iteration method, as described in Sec. 2.1.4. In the following, we shall present the specific aspects of our implementation.

5.1.1 . Variance reduction and population control methods

In order to prevent the population size from growing out of control or dying out over the course of many generations, the total statistical weight of the fission source is kept constant. Fixing the total statistical weight of the source is also crucial for normalizing the scores to one fission neutron. The statistical dispersion of neutron weights can be further reduced by using *optional* population control algorithms : *i)* local population control may be applied in the course of a generation on individual neutrons (e.g. Russian roulette and splitting are applied to neutrons emerging from collision events [10]), and *ii)* global population control can be applied to the fission bank, before neutrons are promoted to source neutrons for the following generation (e.g. weight combing is applied to fission neutrons in order to select source neutrons [57]).

The sampling of neutron histories can be either analog or non-analog ; in the latter case, neutrons are assigned weight correction factors to keep the Monte Carlo game unbiased. Here, the sampling of the flight kernel will always be analog, whereas for collisions we will use various non-analog sampling methods, in order to probe their effectiveness as variance-reduction techniques. We shall use implicit capture and forced fission (see Sec. 2.2.3), which are customary in most production Monte Carlo codes [53, 93–95]. For convenience, we remind the formula to sample the number of fission neutrons :

$$n_f=\left\lfloor\xi+\frac{\nu(\mathbf{r},E)\Sigma_f(\mathbf{r},E)}{\Sigma_t(\mathbf{r},E)}\right\rfloor \qquad (5.3)$$

where $\xi\sim\mathcal{U}[0,1]$ and $\lfloor\cdot\rfloor$ denotes the integer part. This formula is used twice, to sample the number of prompt neutrons (with $\nu=\nu_p$), and the number of delayed neutrons (with $\nu=\nu_d$) ; the family of each

delayed neutron is then sampled in an analog manner, with probabilities ν_d^j/ν_d. The energy of the fission neutrons are sampled from the corresponding spectra (χ_p or χ_d^j) ; the direction is sampled isotropically. Fission neutrons are assigned the weight w of their parent, regardless of their nature. Finally, the parent neutron is forced to undergo scattering, and the effect of absorption is taken into account by correcting the statistical weight by the survival probability, namely,

$$w' = w\frac{\Sigma_s(\mathbf{r}, E)}{\Sigma_t(\mathbf{r}, E)}. \tag{5.4}$$

In this non-analog scheme, particles never disappear by absorption ; histories can be terminated by either leakage or Russian roulette after collision events [10].

The sampling strategy described so far belongs to the class of 'branching' algorithms, in the sense that new particles (hence new branches of the particle histories) can be created at collision events through the sampling of fission progeny. In what follows, we shall also use branchless collisions, that ensure that exactly one single neutron is sampled at collisions [10]. The idea and basic implementation of branchless collisions are exposed in Sec 2.2.3. Here, we shall recall the expression for the weight modifier :

$$w' = w\frac{\Sigma_s + \nu\Sigma_f}{\Sigma_t}. \tag{5.5}$$

The probabilities to select scattering or fission then read

$$P_s = \frac{\Sigma_s}{\nu\Sigma_f + \Sigma_s} \qquad \text{and} \qquad P_f = \frac{\nu\Sigma_f}{\nu\Sigma_f + \Sigma_s}, \tag{5.6}$$

respectively. The use of branchless collisions in power iteration calculation was proposed independently by us in Ref. 91 and by Frohlicher et al. in Ref. 44, and requires some adjustments compared to its usual application in kinetic simulations : if scattering is chosen, energy and direction are sampled as customary, and the emitted neutron performs a new flight within the same history. Otherwise, if fission is chosen, the emitted neutron is sent to the fission bank and the current history is terminated : each neutron undergoes at most one fission event during a generation, producing at most one descendant per generation[1].

With the branchless sampling strategy, population control is mandatory : the number of neutrons would otherwise decrease over generations, since neutrons disappearing by leakage or Russian roulette would not be replaced. In practice, applying splitting to particles emerging from collision events suffices to counteract this limitation, provided that the number of particles per generation is sufficiently large. Note that splitting may reintroduce correlations between neutrons, which suggests that a trade-off must be found between keeping the population size large enough, and reducing the number of splitting events.

In this chapter, we will compare the performance of branchless collisions with a method proposed in Ref. 42, which relies on a last-event estimator for the fission source [96]. The sampling of the collision channel is kept analog (i.e. the statistical weight w of a given neutron is constant throughout a generation), although the statistical weight may vary from one neutron to another, and from one generation to the next generation. Upon sampling absorption (capture or fission), the neutron history is terminated, and an average weight of w_f fission neutrons is sent to the fission bank, where

$$w_f = w\frac{\nu(\overrightarrow{r}, E)\Sigma_f(\overrightarrow{r}, E)}{\Sigma_a(\overrightarrow{r}, E)}. \tag{5.7}$$

We chose to implement an unweighted strategy for populating the fission bank : $n_f = \lfloor \xi + w_f \rfloor$ neutrons of unit statistical weight are sent to the fission bank ("U method" ; here $\xi \sim \mathcal{U}([0,1])$)[42]. This method for populating the fission bank may be also applied to branching and branchless collisions, with an adequate choice of w_f : for branchless collisions, we simply have $w_f = w$, while for branching collisions we have

$$w_f = w\,\frac{\nu(\overrightarrow{r}, E)\Sigma_f(\overrightarrow{r}, E)}{\Sigma_t(\overrightarrow{r}, E)}. \tag{5.8}$$

[1]Observe that branchless collisions reduce to branching collisions with implicit capture in regions without fission.

Other population control mechanisms can be applied to power iteration. One such method is combing, originally proposed by Booth [57] and recently explored at length in the context of time-dependent simulations [49, 62] ; one can also refer to Section 2.2.3 above. As a reminder, the idea behind combing is essentially to enforce a constant number of particles in the source bank of each generation, while at the same time preserving the total weight. The source particles are sampled using a constant weight interval over the total weight, starting with a random offset that guarantees unbiasedness.

An alternative to combing relies on the sampling without replacement (WOR) method, proposed by Sutton [42], which is an improved version of the Duplicate-Discard strategy presented by Variansyah et McLarren [49]. In this method, N source neutrons for the next generation are sampled without replacement from the list of the N' fission sites that stem from the previous generation. In addition, when the size of the fission bank is smaller than the sought fission source size (i.e. $N' < N$), Sutton suggests a two-step procedure : first, each neutron in the fission bank is copied $\lfloor N/N' \rfloor$ times (with statistical weight), and the remaining $N - N'\lfloor N/N' \rfloor$ are then sampled without replacement. Thus, although this method is "without replacement", the same fission site can nonetheless be selected more than once when $N' < N$. This ensures that the number of neutrons at the beginning of each generation is constant.

The implementation of sampling WOR described in Ref. 42 applies to a simplified quasi-analog model where all particles share the same statistical weight, and the generalization to a more realistic framework including non-analog particle transport is straightforward : neutrons are sampled uniformly and without replacement from the list of (unweighted) fission sites, and are assigned the statistical weight of the fission site they originate from, which in our case is one. Finally, using the U method always leads to the same total weight, and all source neutrons will have a unit weight.

5.1.2 . Estimating the correlations of the sought observables

Most production simulation codes perform *ergodic* averages of the sought observables over successive 'active' generations, after convergence has been attained, and compute an *apparent* variance assuming (for ease of computation) that successive generations are independent. In practice, generational correlations cause the apparent variance to underestimate the *real* variance of the stochastic process. Several methods have been developed to recover the real variance from the apparent variance, for instance by block-averaging tallies over several generations in order to wash out correlations, or by modeling generational correlations in the system and applying suitable corrections to the apparent variance [34–36, 97]. Alternatively, one might take *ensemble* averages over fully independent power iteration replicas : in this case, the real variance of the stochastic process would be estimated, but this would come at the cost of an often intolerable increase in simulation time.

By construction, the collision sampling strategies and the variance-reduction and population-control methods described in Sec. 5.1.1 do not affect the estimate of the average, since these algorithms are precisely chosen to ensure a fair (i.e. unbiased) Monte Carlo game. Although Fröhlicher et al. suggested that spatial clustering may induce a bias in the estimation of the neutron flux, the number of inactive generations they had chosen for their system appears to be insufficient to ensure proper convergence to the fundamental eigenstate [44]. In spite of the unbiasedness of the variance-reduction techniques, the estimates of the critical flux and effective multiplication value in power-iteration calculations are affected by a well-known statistical bias, which is due to weight normalization at the beginning of each generation [29]. To first order, the bias is inversely proportional to the number of particles per generation. In Fröhlicher et al.'s case, the number of particles is arguably so small ($N = 10^3$) that the normalization bias cannot be excluded. Moreover, the bias does not necessarily manifest itself in the same way for branchless or branching collisions. Therefore, the bias observed in Ref. 44 cannot be confidently attributed to spatial clustering.

In any case, the non-analog methods presented above do have an impact on the generational and spatial correlations of the resulting simulation scheme, and therefore the apparent variance of the sought observables. Our goal is to characterize the effects of collision sampling strategies, variance reduction

and population control on correlations, using several kinds of *ad hoc* estimators, encompassing those that are commonly met for power iterations and some new ones that are hopefully more useful for the interpretation of the simulation results.

5.1.3 . Definition of estimators for correlation diagnostics

We introduce a few relevant estimators for correlation diagnostics. We require all such estimators to be 'non-Boltzmann', i.e. they must *not* be invariant under variance-reduction techniques, otherwise they would not be sensitive to correlations. Their significance in detecting correlations at the global or local spatial scale will be discussed in the following.

Shannon entropy

The Shannon entropy S of the fission source is commonly used as a tool for assessing the convergence of power iteration : the power iteration is assumed to have reached the stationary state when S reaches an asymptotic value S_∞. In view of the fact that the rate of convergence of the Shannon entropy depends on the dominance ratio, and that the dominance ratio also affects the behavior of correlations, the relation between the Shannon entropy of the fission source and the correlation-induced neutron clustering has been examined by Nowak et al. [38]. For this purpose, a Cartesian spatial mesh with B cells is superposed over the system geometry and the Shannon entropy S at generation g is computed as customary :

$$S(g) = -\sum_{i=1}^{B} p_i(g) \log_2(p_i(g)), \tag{5.9}$$

where $p_i(g)$ is the fraction of the total weight of the fission source particles in the spatial cell i at generation g. In our work, we compute $p_i(g)$ as the ratio of the weight of the fission source particles in cell i over the total weight after normalization. The spatial size of the cells follows from $\delta = L/B$, where L is the linear size of the system. In the simplified homogeneous reactor model tested in Ref. 38, the occurrence of spatial clustering was shown to lead to lower values of the asymptotic Shannon entropy S_∞ compared to the expected ideal value S_{id} that corresponds to the ideal assumption of N independently distributed particles of unit weight. The extended analysis performed in Ref. 91 shows that these findings also apply to continuous-energy transport.

Observe that entropy is just a single scalar for each generation : while it does convey information about the presence of spatial clustering, the fine details of the spatial distribution are lost through the coarse-graining in Eq. (5.9) : only the collective occupation statistics of the cells matters in computing $S(g)$.

Generally speaking, the ideal asymptotic value S_{id} of the entropy function is not known : thus, since the discrepancy between S_{id} and the asymptotic value S_∞ cannot be assessed in practice, the value $S(g)$ resulting from the power iteration cannot be directly used to detect the existence of spatial clustering [2]. Nonetheless, the values of Shannon entropy originating from different collision sampling strategies, variance-reduction and population-control methods can be compared relative to each other, which allows assessing the effectiveness of each technique.

Pair distance function

The pair correlation function $C(\mathbf{r}_i, \mathbf{r}_j, t_i, t_j)$ is a measure of the covariance between the occupation statistics of two spatial sites at positions $\mathbf{r}_i$ and $\mathbf{r}_j$, at time t_i and t_j, which may coincide. It reads

$$C(\mathbf{r}_i, \mathbf{r}_j, t_i, t_j) = \mathbb{E}[n_i(t_i) n_j(t_j)] \tag{5.10}$$

where $\mathbb{E}[\cdot]$ denotes the ensemble average, and $n_i(t_i)$ is the occupation number in space bin i at time t_i, that may be non-integer due to the use of statistical weights. Time can be either continuous (in

[2] To partially overcome this limitation, Nowak et al. have proposed to use the spatial moments of the Shannon entropy, weighted by Legendre polynomials along the Cartesian axes [38] : using spatial symmetries occurring in the simulated system, deviations of the moments of the Shannon entropy may help in revealing the emergence of clustering.

a time-dependent context) or discrete (i.e. generations). In the context of time-dependent diffusion-reproduction stochastic processes in infinite homogeneous media, Meyer et al. have shown that the pair correlation function of two spatial sites at a given time characterizes the evolution of particle clusters [79]. Similar conclusions have been later reached for generalized versions of Meyer's model, encompassing finite-size systems and two observation times [28, 47, 77], and also hold true with minor modifications for power iteration, where time t is replaced by discrete generations g [27, 41]. While being highly informative, the pair correlation function may be prohibitively expensive to compute for realistic three-dimensional configurations. A convenient alternative consists in collapsing the information content of the pair correlation function into the mean squared pair distance function (often shortened to pair distance function),

$$\langle r^2 \rangle(g) \propto \iint |\mathbf{r}_i - \mathbf{r}_j|^2 C(\mathbf{r}_i, \mathbf{r}_j, g) d\mathbf{r}_i d\mathbf{r}_j,$$

where $C(\mathbf{r}_i, \mathbf{r}_j, g)$ expresses the correlation function for particle pairs at two positions in the same generation, which provides a tool to estimate the typical cluster size [79]. The pair distance function is basically the mean squared distance between any two particles, and can be thus straightforwardly computed in Monte Carlo power iteration, e.g., at the beginning of each generation. Since the number of particle pairs scales quadratically with the number of particles present in the generation, the required computational cost might become an issue; however, this problem can be mitigated (without incurring any bias) by estimating the mean squared distance from a maximum number of randomly sampled pairs. Similarly to Shannon entropy, the pair distance function converges towards an asymptotic value $\langle r^2 \rangle_\infty$ for a sufficiently large number of generations, even in the presence of clustering. Departures of $\langle r^2 \rangle_\infty$ from the ideal value, corresponding to a simulation with no clustering, would suggest the presence of spatial clustering. If the distribution is uniform and the particles are independent, then it is easy to estimate the ideal value. In general, however, it is impossible to do so. Similarly to the case of the entropy function, the relative values of the mean squared distance can nonetheless be used to compare the effectiveness of different variance reduction and population control techniques in quenching the effects of correlations.

The statistics of neutron families

In the initial population at the beginning of the power iteration, one starts with N independent neutrons, each of which is assigned a different arbitrary numerical identifier. Each identifier represents an independent 'family'; the identifiers are transmitted to the descendant neutrons at fission events. Two neutrons sharing the same identifier are correlated because they share a common ancestor. During power iteration, the number of neutron families decreases along the generations, because neutrons die and family go extinct by capture or leakage. The intrinsic relationship between diffusion-reproduction processes and particle lineages has been explored by Zhang et al. [81] in the context of infinite, homogeneous, multiplying media : they showed that all the neutron histories become correlated after a characteristic time proportional to the population size, and they attributed the emergence of neutron clustering to this phenomenon. The effects of neutron lineage statistics on the average size and number of clusters has been recently revisited by Sutton et al. [41, 42] in the framework of a simplified power iteration model using the WOR sampling method, and in a more realistic multi-group and continuous-energy framework by Belanger et al. [91] and Frohlicher et al. [44].

For each independent realization of power iteration, there exists a *fixation generation* at which all the families but one have gone extinct : at the fixation generation, all the neutrons are correlated and the population is said to have reached fixation. All neutrons now share the same ancestor in the initial source. We derived an exact expression for the average fixation time in infinite, single-speed homogeneous media in Ref. 84 in the context of kinetic simulations; these findings can be straightforwardly extended to processes evolving in discrete generations. We define $\eta(g)$ to be the average number of surviving independent neutron families at generation g : the likeliness of occurrence of neutron clustering increases as η becomes much smaller than the initial number of families N.

While the statistics of neutron families does provide interesting insights about correlations, and for this reason it has been proposed as an estimator for clustering [41, 42, 91], it does not carry information

about the spatial and boundary effects (see the discussion in Chapter 4), and this may limit its usefulness, as shown in the following.

Feynman moments

The three previous estimators, although sensitive to correlations, are global and do not provide any information about the local distribution of the correlations within the system. As such, their application to the analysis of correlations occurring in systems exhibiting strong spatial heterogeneity is fraught with conceptual difficulties. Ideally, we would like indicators of spatial correlations to be *i)* local, i.e. space-dependent, and *ii)* having a known ideal behavior in the absence of correlations, which would make their interpretation easier. For this purpose, we introduce the *ensemble* Feynman moment

$$Y_{\mathcal{O}_i} = \frac{\mathbb{V}[\mathcal{O}_i]}{\mathbb{E}[\mathcal{O}_i]}, \tag{5.11}$$

where $\mathcal{O}_i$ is the value of observable $\mathcal{O}$ in spatial cell i. Here $\mathbb{E}[\cdot]$ denotes the *ensemble* average over M independent replicas of a given observable $\mathcal{O}$:

$$\mathbb{E}[\mathcal{O}_i] = \frac{1}{M}\sum_{m=1}^{M} \mathcal{O}_{i,m}, \tag{5.12}$$

$\mathcal{O}_{i,m}$ being the value of the estimator in cell i for replica m. The *ensemble* unbiased estimator of the variance of $\mathcal{O}$ is defined as

$$\mathbb{V}[\mathcal{O}_i] = \frac{1}{M-1}\sum_{m=1}^{M} (\mathcal{O}_{i,m} - \mathbb{E}[\mathcal{O}_i])^2, \tag{5.13}$$

We stress that $\mathbb{V}[\mathcal{O}_i]$ is the variance of the estimator and not the variance of the mean of the estimator. The variance of the mean is obtained by dividing the variance of the estimator by the number of realizations M over which the mean is performed. The Feynman moment has been originally conceived for the detection of fission-induced correlations in the time series of multiplying systems [80] : to the best of our knowledge, its application to the analysis of correlations occurring in power iteration has not been attempted before.

As mentioned in Sec. 5.1, to reduce the cost of power iteration, one generally uses ergodic averages over successive neutron generations. We therefore introduce the *ergodic* estimator of the expectation of $\mathcal{O}$ over G active generations, namely,

$$\mathcal{E}[\mathcal{O}_i] = \frac{1}{G}\sum_{g=1}^{G} \mathcal{O}_{i,g}, \tag{5.14}$$

where $\mathcal{O}_{i,g}$ is the value of the estimator in cell i at active generation g. Similarly, one can define the *ergodic* estimator of the variance of $\mathcal{O}$ by

$$\mathcal{V}[\mathcal{O}_i] = \frac{1}{G-1}\sum_{g=1}^{G} (\mathcal{O}_{i,g} - \mathcal{E}[\mathcal{O}_i])^2. \tag{5.15}$$

Because of positive correlations, we expect $\mathcal{V}[\mathcal{O}_i] < \mathbb{V}[\mathcal{O}_i]$ when the two estimators are taken over samples of the same size ($G = M$), i.e. when the number of active neutron histories in the single power iteration calculation used to compute the ergodic variance is the same as the sum of active neutron histories simulated throughout all power iteration replicas when computing the ensemble variance [29]. In order to have a better estimate of Eqs. (5.14) and (5.15), it is possible to perform ensemble averages over M independent replicas on $\mathcal{E}[\cdot]$ and $\mathcal{V}[\cdot]$. Finally, we define the *ergodic* Feynman moment of $\mathcal{O}$ by

$$Y^{\mathsf{G}}_{\mathcal{O}_i} = \frac{\mathbb{E}[\mathcal{V}[\mathcal{O}_i]]}{\mathbb{E}[\mathcal{E}[\mathcal{O}_i]]}, \tag{5.16}$$

which reduces to the ensemble Feynman moment defined in Eq. (5.11) when $G = 1$.

Since the Feynman moment for Poisson variates is equal to 1, it is possible to interpret its value as the deviation of a given observable (in a spatial cell) from a Poisson-like behavior. A process that generates Poisson-distributed counts is the following : consider N particles, independently and identically distributed into K bins following the probability distribution p. If p_k is the probability that a particle falls within bin k, then if $\forall k, p_k \ll 1$, the particle counts are approximately Poisson distributed in each cell, and the Feynman moment Y_k for cell k is approximately equal to 1, for all the bins and independently of the probability distribution p. However, when there are very few populated bins, then $p_k \sim 1$ for some k (i.e. the probability that a particle falls within bin k is large); in this situation, the counts actually follow a binomial distribution, and we expect $Y < 1$. Finally, suppose that the number of bins is high enough so that the number of particles in each bin is Poisson distributed. The particles are divided into groups of size α, and each group is independently tossed into a bin. In this situation, it is easy to check that the Feynman moment is equal to α, again for all the bins and independently of the probability distribution. This suggests that the value of the Feynman moment for a counting variable can be interpreted as the typical 'weight' of a particle cluster. This example also suggests that Feynman moments are most naturally applied to quantities that are akin to counts. Indeed, for counting variables, the Feynman moment is dimensionless and has a natural reference value to which it can be compared. It is less naturally applicable to commonly used quantities such as fluxes, which is why such quantities are not considered in the present work.

In this work, we apply the Feynman moments to the collision counts ψ, i.e. the average number of neutrons entering a collision in a space bin[3], and to the fission emission counts F, i.e. the average number of fission neutrons being emitted in a space bin. We will focus exclusively on energy-integrated Feynman moments.

Normalized variance

Another local estimator for correlations can be introduced using the *ensemble* estimator for the normalized variance

$$g_{\mathcal{O}_i} = \frac{\mathbb{V}[\mathcal{O}_i]}{\mathbb{E}[\mathcal{O}_i]^2}, \tag{5.17}$$

where $\mathbb{E}[\mathcal{O}_i]$ and $\mathbb{V}[\mathcal{O}_i]$ are defined as above. The normalized variance describes the amplitude of fluctuations relative to the average and is a simplified form of the centered normalized pair correlation function that is widely used in the context of spatial clustering analysis [47, 48, 79]. Observe that the normalized variance differs from the Feynman moment only in the normalization terms appearing at the denominator. However, this difference is crucial and conveys a distinct information content with respect to correlations, as illustrated in Sec. 5.4. The *ergodic* normalized variance $g^{\mathsf{G}}_{\mathcal{O}_i}$ can be defined similarly to that of the Feynman moments, namely

$$g^{\mathsf{G}}_{\mathcal{O}_i} = \frac{\mathbb{E}[\mathcal{V}[\mathcal{O}_i]]}{\mathbb{E}[\mathcal{E}[\mathcal{O}_i]]^2}. \tag{5.18}$$

In this work, we apply the normalized variance to the same observables as for the Feynman moments, i.e. the energy-integrated collision counts and fission emission counts.

5.2 . Analysis of a simple benchmark with single-speed particle transport

A previous study by Nowak et al. looked at the effects of particle clustering on the Shannon entropy of the fission source [38]. For a simple benchmark model of single-speed neutron transport in a uniform cubic reactor, with reflective boundary conditions, the fundamental eigenmode of the fission source is spatially uniform. In an analog simulation without clustering, the positions of the N fission neutrons at equilibrium would all be independent and uniformly distributed. Thus, we can decompose the cube into B elements of equal volume and measure the degree of clustering by comparing the entropy of the fission

[3] Given that reaction rates are akin to partial collision counts, one could also analyze their Feynman moments, which will not attempted here, for the sake of conciseness.

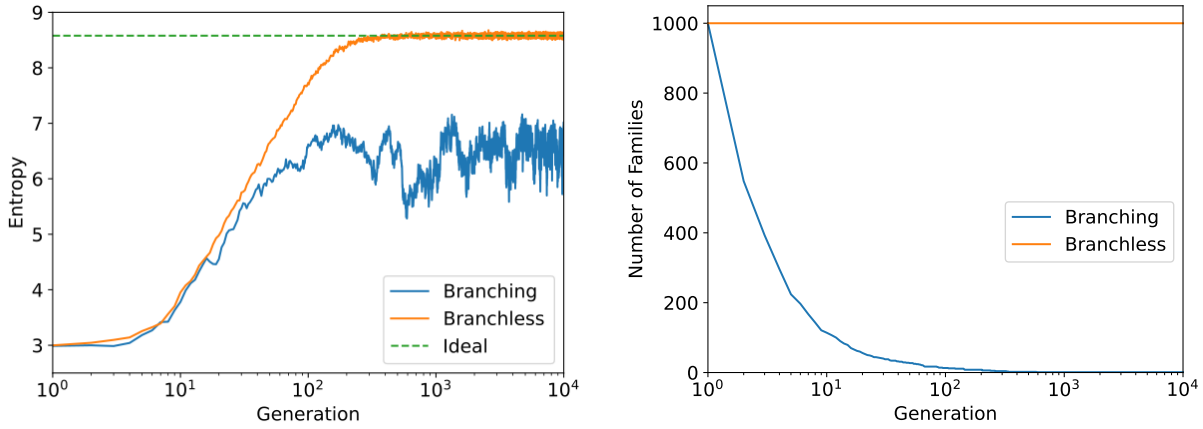

Figure 5.1 : Shannon entropy of the fission source, and the number of distinct families for a critical single-speed box, for both the branching and branchless simulation methods. The ideal value of the entropy for $N = 10^3$ and $B = 8^3$ is also provided.

source to the ideal entropy of a multinomial distribution of N particles into B categories, which reads

$$S_{\text{id}} = \log_2(N) - \frac{B}{N}\left(\frac{B-1}{B}\right)^N \sum_{k=1}^{N}(B-1)^{-k}\binom{N}{k} k\log_2(k). \tag{5.19}$$

From this comparison, Nowak et al. have demonstrated that clustering leads to a lower entropy in the fission source than the value of Eq. (5.19) [38][4].

To evaluate the possible benefits of using branchless collisions over the more traditional branching algorithm, we have replicated the study performed by Nowak et al., performing k-eigenvalue power iteration for single-speed neutron transport in a reflected, critical cubical reactor, with side lengths of 400 cm, and cross sections of $\Sigma_s = 0.27\,\text{cm}^{-1}$, $\Sigma_c = 0.02\,\text{cm}^{-1}$, $\nu_f = 2.5$, and $\Sigma_f = \frac{\Sigma_c}{\nu_f - 1}$. The total weight of the particles at the beginning of each generation is $N = 10^3$, and the initial source distribution is a point located at the center of the cube, with source particles having unit weight. The aim of this simulation is to provide a first indication of whether the branchless collision method can reduce the clustering of the particles in the simulation, compared to traditional branching transport. The simulations of three-dimensional configurations presented in this section were performed using Chenille, a mini-app also developed at CEA [98]. In Chenille, the formula used to determine the number of fission progeny when using branching collision is

$$n_f = \left\lfloor \frac{w}{k_{\text{eff}}^{(g-1)}} \cdot \frac{\nu(E)\Sigma_f(E)}{\Sigma_t(E)} + \xi \right\rfloor, \tag{5.20}$$

where k_{eff}^{g-1} denotes the estimate of the multiplication factor stemming from the previous generation ; in this scheme, fission particles are born with unit weight. For the remainder of the present section and for Sec. 5.5, we shall use this formula instead of Eq. (5.3).

The entropy of the fission source for single-speed transport in the critical cube is plotted in Fig. 5.1, as a function of the fission generations, for both branching and branchless simulations, along with the theoretical value for the ideal case of perfectly independent and homogeneously distributed particles. Clustering in the branching simulation leads to a fission source entropy which is much lower than the value associated with independent neutron histories, for the given number of particles, and entropy mesh. Using branchless collisions, however, the entropy of the fission source converges to the ideal value, and experiences much smaller fluctuations. This benchmark configuration is unique for several reasons.

[4]The derivation of Eq. (5.19) by Nowak et al. assumed analog transport ; its use for predicting the fission source entropy in a weighted game is perhaps inappropriate, but we use it here nonetheless, as an approximation.

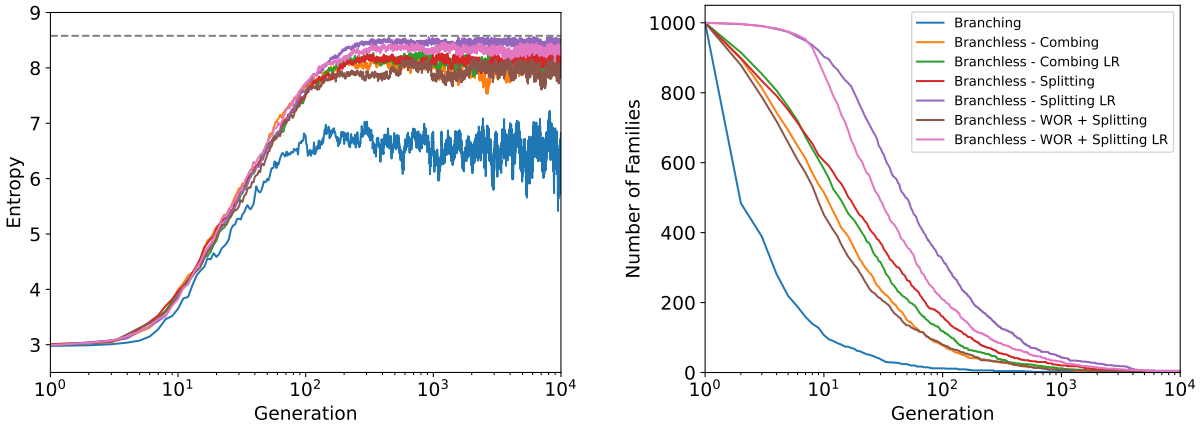

Figure 5.2 : Shannon entropy of the fission source, and the number of distinct families for single-speed transport in a subcritical reactor, for both the branching and branchless simulation methods. The ideal value of the entropy for $N = 10^3$ and $B = 8^3$ is given by the dashed line.

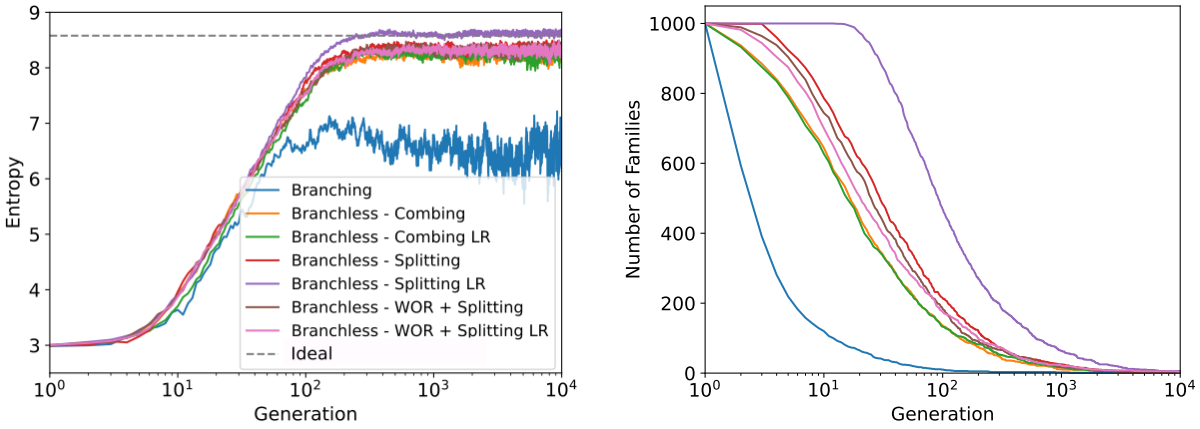

Figure 5.3 : Shannon entropy of the fission source, and the number of distinct families for single-speed transport in a supercritical reactor, for both the branching and branchless simulation methods. The ideal value of the entropy for $N = 10^3$ and $B = 8^3$ is given by the dashed line.

Single-speed transport in the critical cube leads to a branchless weight modifier of 1; thus, the weight of particles will never change, so no splitting or roulette will ever occur. This fact, combined with the reflective boundary conditions, means that no particles will ever be removed from the system, so the number of independent particle families will remain constant instead of decreasing as it would be the case otherwise. The decrease in the number of particle families has been shown to be one of the main causes of clustering in Monte Carlo simulations [42], and the fact that the number of families is constant, when using branchless collisions, explains the absence of clustering.

Thus, single-speed transport in a critical reactor is a somewhat pathological case that does not need any population control mechanism when using branchless collisions. We chose to also examine a subcritical and supercritical version of the reactor, where the fission yield was used to control k_{eff}. The respective parameters were $\nu = 2$, $k_{\text{eff}} = 0.8$ and $\nu = 3$, $k_{\text{eff}} = 1.2$. For these cases, we considered the use of combing, splitting, and sampling without replacement (WOR) with splitting. The entropy and number of families are presented in Fig. 5.2 for the subcritical case, and Fig. 5.3 for the supercritical case. In both the subcritical and supercritical configurations, all branchless collision variants yield larger numbers of families, larger values of the entropy and therefore seem to be much more effective at reducing clustering

Number	Type	Inactive generations	Lengths (cm)	Dominance ratio	k_{eff}
1	Homogeneous	100	50	0.9832	1.00003 ± 1 pcm
2	Homogeneous	200	100	0.9957	0.99986 ± 1 pcm
3	Heterogeneous	20	20/2/20	0.7908	0.99999 ± 3 pcm
4	Heterogeneous	1000	20/20/20	0.9971	0.99987 ± 5 pcm

Table 5.1 : Parameters for the four benchmark configurations. The dominance ratio and the value of the capture cross-sections are taken from Vitali et al. [1].

compared to the traditional branching algorithm. In contrast with the behaviour observed for the critical system, the source entropy of the branchless collision does not reach the ideal entropy (cf. Fig. 5.1). The reason for this is that, once the system is no longer exactly critical, population control mechanisms are required, which always causes the number of particle families in the simulation to decrease to 1 (fixation). The number of generations to fixation for the branching algorithm is much smaller than for branchless algorithms. Furthermore, for both the subcritical and supercritical cases, branchless collisions with splitting for population control and a low roulette threshold seem to give the longest fixation time. With branching transport, the fixation time is generally comparable to the time required for the fission source to converge, while the fixation time for the branchless algorithms is much longer than the time required for entropy convergence. Surprisingly, sampling WOR on its own had very poor performance when used with branchless collisions, in apparent contradiction with Sutton [42]. This discrepancy is likely attributed to the fact that, in Sutton's algorithm, each absorption site may contribute to populate the fission bank, which potentially induces less variation in the particle weights. Sampling WOR in conjunction with splitting had reasonable performance, but was still not as efficient as using splitting alone.

5.3 . Specifications for more complex benchmark problems

In order to gain a deeper insight, we have extended the simple system investigated in the previous section by introducing a set of benchmark problems, of which we provide the key specifications.

5.3.1 . Description of the chosen configurations

For the purpose of our analysis, we have chosen a total of four one-dimensional critical slab geometries taken from Vitali et al. [1]. The selected configurations have different values of dominance ratio R, and cover both homogeneous and heterogeneous systems, which are known to behave differently with respect to the parameter R. The geometrical data are listed in Tab. 5.1. All configurations have leakage boundary conditions at both sides of the slab. The first two configurations (1 and 2 in Tab. 5.1) are homogeneous, with different lengths. The material is a mixture of UO_2 and H_2O, whose parameters are provided in Tab. 5.2. Configurations 3 and 4 are heterogeneous, with a UO_2-H_2O-UO_2 sandwich structure, with lengths given in Tab. 5.1. The respective nuclear data are given in Tab. 5.3 for the fuel and in Tab. 5.4 for the moderator. The nuclear data for all the materials are intended to be realistic, and are represented using a three-group formalism, with thermal, epi-thermal and fast energy groups. In Ref. 1, prompt χ_p and delayed χ_d^j spectra for each precursor family j were provided separately. Here we collapsed them into an average fission spectrum χ, with $\chi = (\nu_p \chi_p + \sum_j \nu_d^j \chi_d^j)/\nu$.

Following Vitali et al., for all configurations we modify the capture cross section of the homogeneous material (for cases 1 and 2) and of UO_2 (for cases 3 and 4) so that the systems are critical. The system-dependent capture cross-sections are given in Table 5.5. The dominance ratios for each configuration have been computed by Vitali et al. and are also recalled in Tab. 5.1.

Parameters	$g = 1$ (fast)	$g = 2$ (epithermal)	$g = 3$ (thermal)
$\Sigma_{f,g}$ $[\mathrm{cm}^{-1}]$	3.0586×10^{-3}	2.1579×10^{-3}	5.6928×10^{-2}
$\Sigma_{s,1\to g}$ $[\mathrm{cm}^{-1}]$	4.48187×10^{-1}	1.78483×10^{-1}	0
$\Sigma_{s,2\to g}$ $[\mathrm{cm}^{-1}]$	0	1.8058111	1.41764×10^{-1}
$\Sigma_{s,3\to g}$ $[\mathrm{cm}^{-1}]$	0	0	4.31567
ν_g $[-]$	2.4	2.4	2.4
χ_g $[-]$	0.876304	0.123696	0

Table 5.2 : Nuclear data of the homogeneous fuel-moderator material. The three energy groups are indexed by g.

Parameters	$g = 1$ (fast)	$g = 2$ (epithermal)	$g = 3$ (thermal)
$\Sigma_{f,g}$ $[\mathrm{cm}^{-1}]$	3.0586×10^{-3}	2.1579×10^{-3}	5.6928×10^{-2}
$\Sigma_{s,1\to g}$ $[\mathrm{cm}^{-1}]$	2.21062×10^{-1}	7.3843×10^{-2}	0
$\Sigma_{s,2\to g}$ $[\mathrm{cm}^{-1}]$	0	7.77642×10^{-1}	4.3803×10^{-2}
$\Sigma_{s,3\to g}$ $[\mathrm{cm}^{-1}]$	0	0	1.55272
ν_g $[-]$	2.4	2.4	2.4
χ_g $[-]$	0.876304	0.123696	0

Table 5.3 : Nuclear data of the UO_2 material. The three energy groups are indexed by g.

5.3.2 . Description of the sampling strategies

Five algorithms (i.e. combinations of collision sampling strategies and population control algorithms) will be considered for each geometry : *i)* branching collisions; *ii)* last-event estimator with sampling WOR; *iii)* branchless collisions; *iv)* branchless collisions with weight combing; *v)* branchless collisions with sampling WOR. Russian roulette and splitting are always applied to the particles emerging from collision events, with roulette threshold $w_R = 0.8$ and unit target weight, and splitting threshold $w_S = 2$. A neutron of statistical weight w is split into $n_S = \lfloor w/w_S \rfloor$ particles with equal statistical weight w/n_S. The choice of these (somewhat arbitrary) thresholds is inspired by those used in the TRIPOLI-4® code developed at CEA [53]. It should be noted in particular that the choice of w_S can have a significant effect on the neutron correlations, especially if w_S is too small. Finally, when no population control algorithm is specified, the fission bank is wholly transmitted to the next generation ; in particular, no sampling with replacement is applied.

5.4 . Simulation results

In the following, we present numerical results for the benchmark configurations described in Sec. 5.3 and the five algorithms presented in Sec. 5.1, first for the global tallies (entropy, pair distance and family number), and then for the local tallies (Feynman moment and normalized variance). The aim of this investigation is to assess the impact of each algorithm on correlations, with the help of the diagnostics tools introduced in Sec. 5.1.3. All the power iteration simulations carried out here start with an initial neutron source belonging to the fast group and uniformly distributed in space (non-fissile media included). The number of inactive generations for each configuration is given in Tab. 5.1 and has been determined on the basis of Fig. 5.4, while the number of neutrons per generation will be detailed for each case separately.

Parameters	$g = 1$ (fast)	$g = 2$ (epithermal)	$g = 3$ (thermal)
$\Sigma_{c,g}$ $[\mathrm{cm}^{-1}]$	3.05×10^{-4}	3.699×10^{-4}	1.825×10^{-2}
$\Sigma_{s,1\to g}$ $[\mathrm{cm}^{-1}]$	2.27125×10^{-1}	1.0464×10^{-1}	0
$\Sigma_{s,2\to g}$ $[\mathrm{cm}^{-1}]$	0	1.02817	9.7961×10^{-2}
$\Sigma_{s,3\to g}$ $[\mathrm{cm}^{-1}]$	0	0	2.76295

Table 5.4 : Nuclear data for the H_2O material. The three energy groups are indexed by g.

System Number	$\Sigma_{c,1}[\mathrm{cm}^{-1}]$	$\Sigma_{c,2}[\mathrm{cm}^{-1}]$	$\Sigma_{c,3}[\mathrm{cm}^{-1}]$
1	9.3888852×10^{-4}	1.5003548×10^{-2}	6.9125769×10^{-2}
2	9.3920991×10^{-4}	1.5034394×10^{-2}	7.0670812×10^{-2}
3	3.8396068×10^{-4}	1.1656103×10^{-2}	4.8808556×10^{-2}
4	3.8089301×10^{-4}	1.1361681×10^{-2}	3.4061203×10^{-2}

Table 5.5 : Capture sections $\Sigma_{c,g}$ for each configuration. The three energy groups are indexed by g.

5.4.1 . Analysis of global estimators

We begin our analysis by considering global tallies. The evolution of the Shannon entropy $S(g)$ as a function of the generations in each of the benchmark configurations is illustrated in Fig. 5.4. As expected, all entropy curves converge towards an asymptotic value for a large number of generations. The asymptotic value of the entropy depends on the algorithm and the system, whereas the convergence rate (i.e. the number of generations needed to attain convergence) only depends on the system. For systems 1, 2, and 4, the asymptotic value of the entropy is smaller for the branching algorithm than for any of the other algorithms, suggesting stronger spatial correlations when using branching collisions. The method relying on the last-event estimator taken from Ref. 42 leads to an entropy lying between that of the branchless algorithms with and without population control. The typical spatial patchiness induced by spatial correlations is illustrated in Fig. 1.1 for the case of system 2 (homogeneous reactor with large dominance ratio). It is interesting to note that in system 3 all algorithms lead to similar asymptotic entropy ; additionally, the branching algorithm appears to lead to the higher entropy, and is thus expected to induce less spatial correlations. The behavior of system 3 can be probably explained by its small dominance ratio, cf. Tab. 5.1. Spatial clustering is the result of a competition between diffusion and multiplication : correlated branches induce spatial correlations when the neutrons cannot explore the whole system. When using branchless collisions, the only way for correlated branches to appear is through splitting or population control. In systems close to criticality such as ours, the weight correction factor in branchless algorithms is close to unity, which means that splitting seldom occurs during a generation. However, as stated previously, the number of neutrons decreases from one fission bank to the next. Thus, weight normalization increases the average weight of neutrons, ultimately leading to additional splitting. Alternatively, if population control such as combing or sampling WOR is applied, then the same neutron in the fission bank may be copied several times, introducing additional correlated branches.

Careful inspection of Fig. 5.4 will reveal that the difference between the asymptotic entropy of the branching algorithm, and of the four other algorithms increases with the dominance ratio. Conversely, if the dominance ratio is small enough, the entropy for branching collisions becomes slightly higher than for branchless collisions, as illustrated by Fig. 5.4c for system 3. In this case, correlated branches explore the whole viable phase space, and the effects of spatial clustering will be quenched. Said differently, neutrons produce more fission neutrons (i.e. correlated branches) when using branching collisions than branchless collisions, meaning that more random walkers are available to explore the phase space. Given that spatial correlations are weak, the increasing number of events leads to better estimates of scores. This behavior is not specific to heterogeneous systems (such as configuration 3) : we have found similar results for a homogeneous configuration with a dominance ratio close to that of system 3. Note however that, in

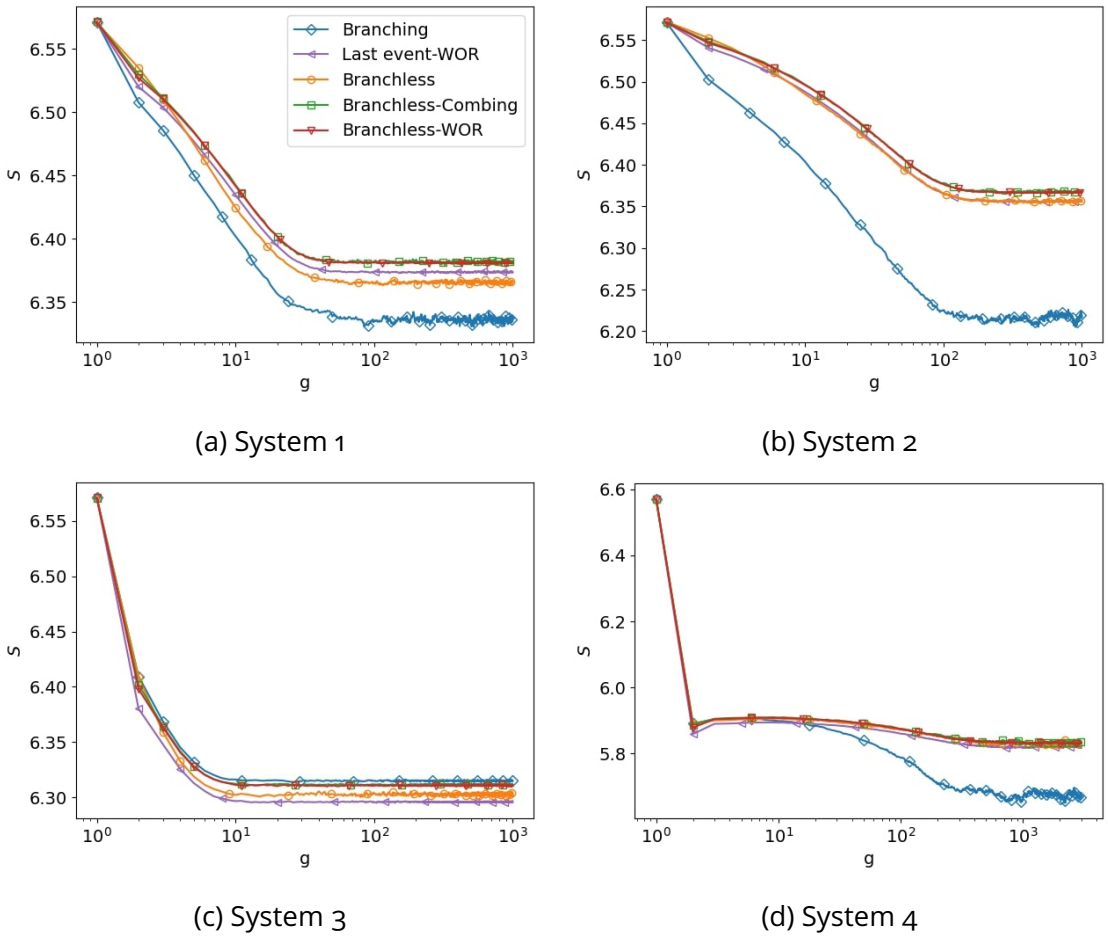

(a) System 1

(b) System 2

(c) System 3

(d) System 4

Figure 5.4 : Shannon entropy as a function of the generations in power iteration, computed for $N = 10^3$, $B = 10^2$, and for different systems, and averaged over 10^3 independent replicas.

systems with small dominance ratios, the difference among the asymptotic entropy values for the five algorithms is rather small, translating the fact that systems with small dominance ratio are anyway only weakly affected by spatial correlations and, thus, by clustering.

We conclude our analysis of Shannon entropy with a discussion on the dependence of the asymptotic entropy (i.e. the entropy reached after the inactive generations) on the spatial cell size, shown in Figs. 5.5. The dependence of S_∞ on the bin size is similar in both homogeneous and heterogeneous systems. As suggested by Fig. 5.4c, the Shannon entropy for the branching algorithm exceeds that of the other algorithms when the cell size is very small, while it is lower or equal for larger cell sizes. In addition, these trends appear to be strengthened in systems with large dominance ratio, suggesting that the effect of spatial correlations becomes irrelevant when the bin size becomes small enough. In this case, only the number of available random walkers matters, and using branching collisions might become advantageous. In any cases, the impact of the bin size on the value of the entropy is much stronger than the impact of the algorithm.

The indications that can be drawn from Fig. 5.6 for the pair distance function are consistent with those stemming from the entropy tally, with one significant exception : contrary to entropy, population control seems to have a weak influence on the pair correlation function. Moreover, Fig. 5.6c shows that the pair distance for the branching algorithm in system 3 is the lowest amongst the five algorithms considered here (the differences are nonetheless small). This is in contrast with the intuition that lower entropy values are the signature of enhanced spatial clustering. We showed above that, for system 3, the highest entropy (and thus, the situation with the smallest impact of neutron clustering) was also

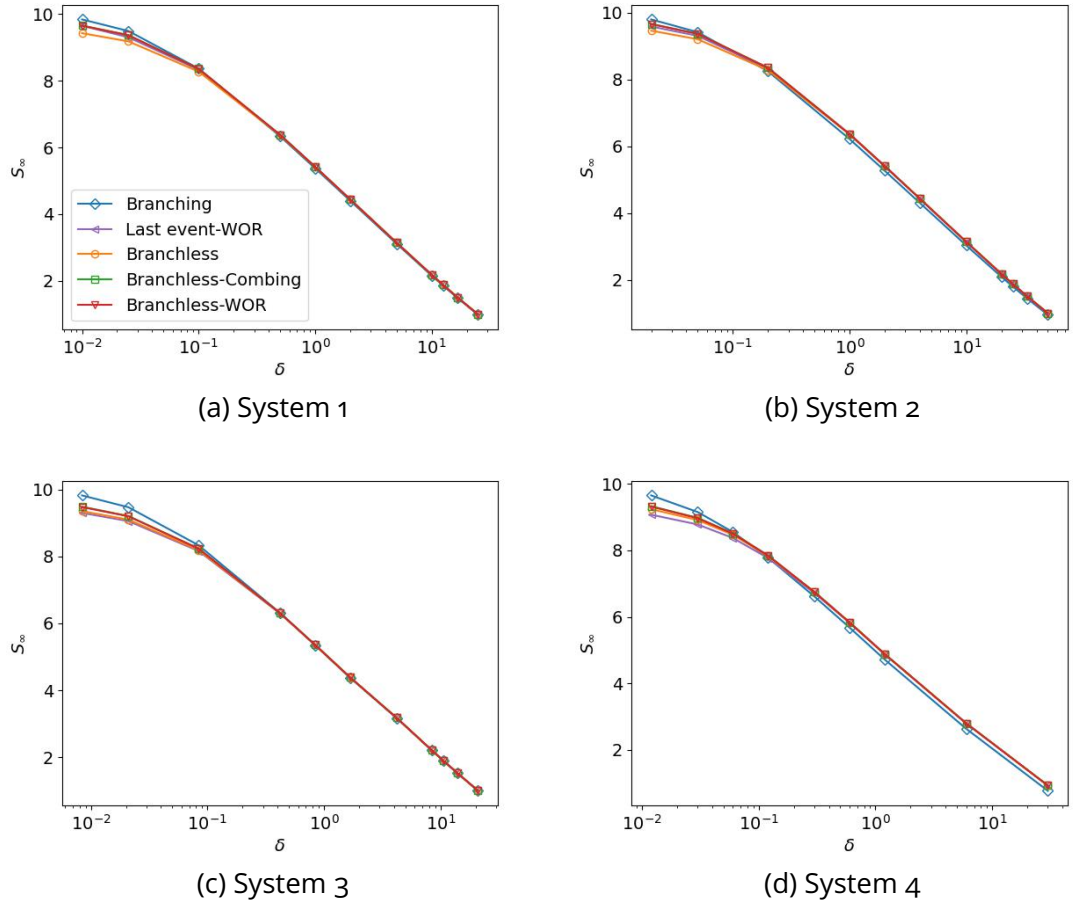

(a) System 1 (b) System 2

(c) System 3 (d) System 4

Figure 5.5 : Asymptotic Shannon entropy S_∞ as a function of the bin size δ after discarding an adequate number of generations (cf. 5.1). The values are averaged over 10^4 independent replicas.

achieved for the branching algorithm. Consequently, we would have expected that the largest pair distance function would be attained for the branching algorithm. Nonetheless, system 3 will not exhibit significant clustering for any reasonable number of particles, mostly because of its low dominance ratio.

For systems exhibiting strong heterogeneity, such as system 4, the use of the average pair distance tally to assess the impact of spatial correlations in the fission source becomes questionable, since the moderator region does not contain fission neutrons : if the pair distance is comparable to the linear size of the moderator region, then it is unclear whether the pair distance simply encodes the distance between the two fissile regions.

Figure 5.7 shows the average number of surviving families as a function of generations. At the fixation generation, all neutrons in the population are correlated : a larger fixation generation should imply weaker correlations. Figures 5.7a and 5.7b contradict this statement : in homogeneous media, branchless collisions without population control lead to the largest fixation generation, whereas the highest entropy and pair distance function (hence the weakest spatial correlations) are reached for branchless collisions with combing. Similarly, Fig. 5.7c shows that branching collisions lead to the smallest fixation generation, although the associated entropy is the highest amongst the algorithms considered here. This surprising finding is coherent with previous work : the statistics of families are unsuitable to detect correlations in systems of finite size [84]. In infinite media, the dynamics of spatial correlations is driven by the statistics of families, due to the lack of a spatial scale. On the contrary, in systems of finite size, the emergence of spatial clustering depends on the competition between the number of generations required to reach fixation and the number of generations required to reach mixing, i.e. to explore the whole

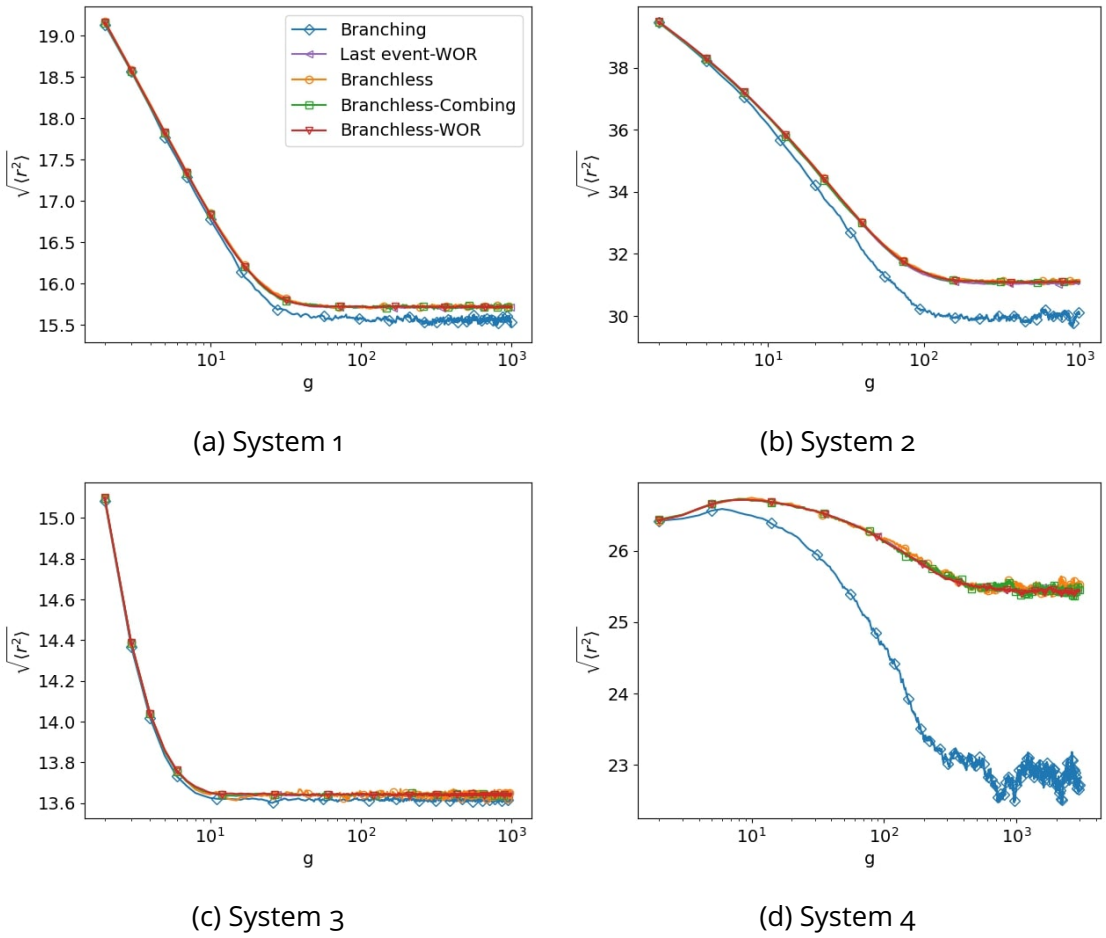

(a) System 1 (b) System 2

(c) System 3 (d) System 4

Figure 5.6 : Square root of pair distance as a function of the generations, computed for $N = 10^3$, for different systems, with 10^3 independent replicas.

space [28, 47, 77]. In this context, the statistics of families alone becomes insufficient to provide the full picture.

5.4.2 . Analysis of the fission source : Feynman moment

In view of the shortcomings of global tallies, we move now to the analysis of local tallies : the Feynman moment and the normalized variance. These tallies will be applied to the fission source and to the collision counts. We will investigate both the spatial shape of the local tallies and their dependence on the mesh cell size δ. Indeed, coarse-graining over a length δ influences the impact of correlations on the sought observables.

The Feynman moment of the fission source describes the correlations between fission neutrons. Figure 5.8 shows the ensemble Feynman moments for the fission source after the inactive generations, for each configuration and algorithm considered. Let us initially focus on the homogeneous cases, i.e. systems 1 and 2. In the ideal case where all particles are independent, we expect fission neutrons to be Poisson distributed, which is equivalent to a spatially flat Feynman moment $Y \simeq 1$ everywhere. Figures 5.8a and 5.8b show that the Feynman moment for the branching algorithm in a homogeneous configuration has a non-trivial shape, indicating that deviations from the ideal behavior do not develop uniformly. The same figures illustrate that for this particular choice of bin size δ, simulations using branchless collisions without additional population control introduce smaller and more evenly distributed fluctuations in the distribution of fission sites, as witnessed by the lower and spatially flatter Feynman moment. The discrepancy in the Feynman moment for branchless and branching collisions increases with increasing dominance ratio : for branching collisions Y increases with increasing dominance ratio, whereas it is fairly constant for branchless collisions when increasing the dominance ratio. Introducing

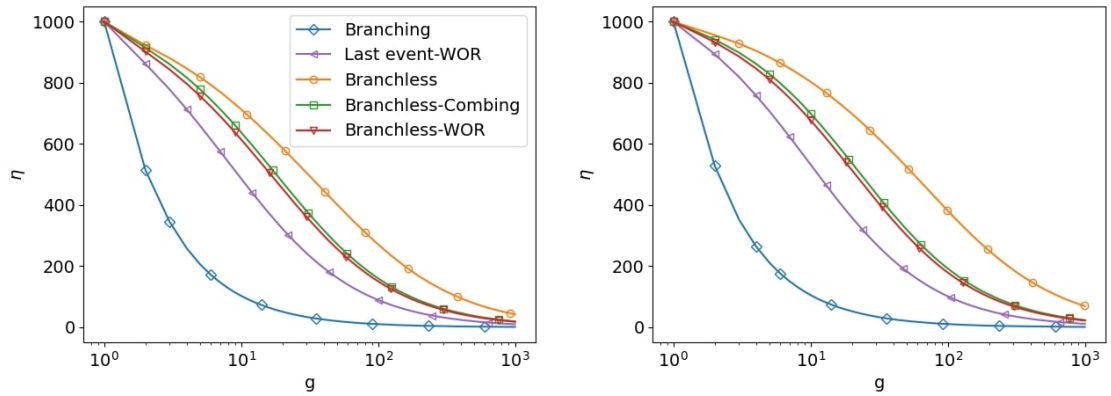

(a) System 1

(b) System 2

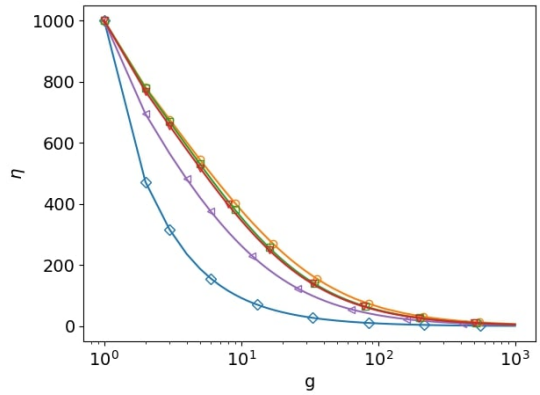

(c) System 3

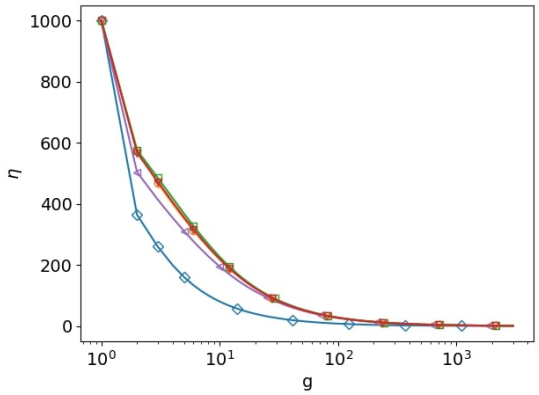

(d) System 4

Figure 5.7 : Average number of surviving families as a function of the generations, computed for $N = 10^3$, for different systems, with 10^3 independent replicas.

combing or sampling WOR in branchless algorithms further lowers the Feynman moments and introduces a slight spatial shape, which suggests that population control algorithms amplify the effects of leakage boundary conditions on spatial correlations. This is reminiscent of what happens with reflecting boundary conditions [34]. The last-event algorithm shares the same spatial shape as the branchless collisions with population control algorithms, with a slightly larger value, suggesting that it is slightly less effective in quenching spatial correlations.

Insight can be gained by examining how Y scales with respect to the cell size δ. We define l_{clust} as the typical size of the largest cluster in the system. In systems that are homogeneous or where the effects of heterogeneity on particle transport are mild, the typical cluster size can be estimated using $l_{\text{clust}} \sim \sqrt{\langle r^2 \rangle_\infty}$; this assumption fails for systems where the effects of heterogeneity are more pronounced, such as configuration 4. We thus have the following picture : if $\delta \simeq l_{\text{clust}}$, the observables will be strongly affected by correlations; on the contrary, if $\delta \ll l_{\text{clust}}$, the probability that two particles belonging to the same cluster fall into the same cell becomes small, and the effects of the correlations will be milder. Figures 5.9a and 5.9b show the Feynman moment for the spatially-averaged fission source defined by

$$Y_F^{av} = \frac{1}{B'} \sum_{i=1}^{B'} Y_{F_i}, \tag{5.21}$$

where B' is the number of spatial cells with fissile material. As we consider homogeneous systems, $l_{\text{clust}} \sim \sqrt{\langle r^2 \rangle_\infty}$. The Feynman moment for branching collisions has a power law increase for $\delta \lesssim \sqrt{\langle r^2 \rangle_\infty}$ and saturates when $\delta \sim \sqrt{\langle r^2 \rangle_\infty}$. This translates the fact that there exists clusters at all spatial scales up to $\sqrt{\langle r^2 \rangle_\infty}$. More strikingly, the Feynman moment for branchless collisions without population control

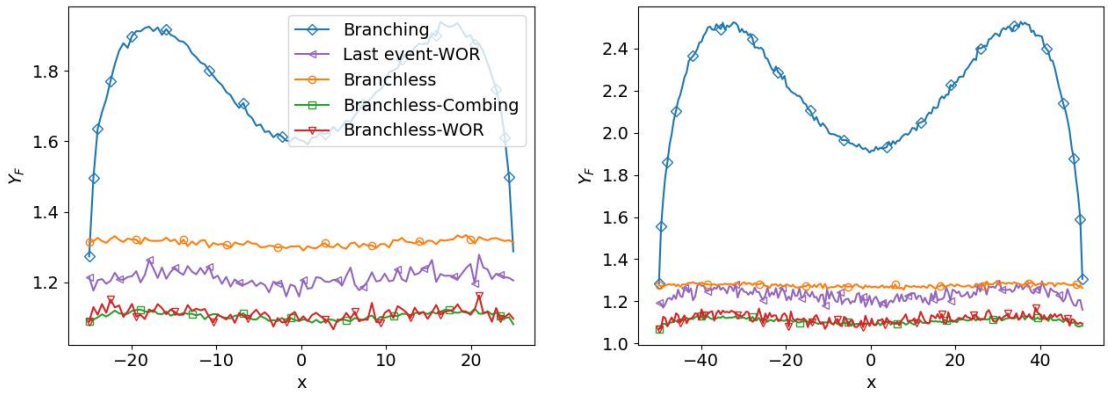

(a) Y_F in power iteration for system 1 with 10^5 independent replicas.

(b) Y_F in power iteration for system 2 with 10^5 independent replicas.

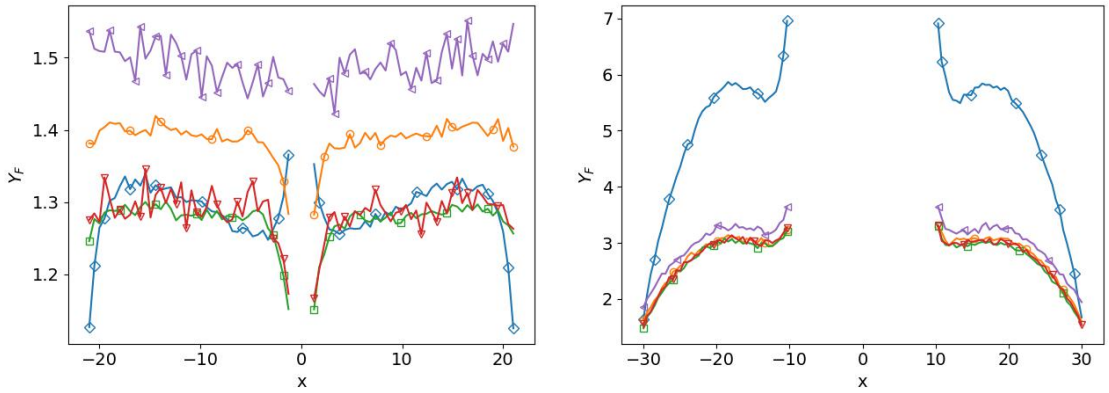

(c) Y_F in power iteration for system 3 with 10^4 independent replicas.

(d) Y_F in power iteration for system 4 with 10^4 independent replicas.

Figure 5.8 : Equilibrium Feynman moment for the fission source computed for $N = 1000$ and $\delta = 0.5$ for different systems.

is constant when $\delta \lesssim \sqrt{\langle r^2 \rangle_\infty}$ and decreases when $\delta \sim \sqrt{\langle r^2 \rangle_\infty}$, the latter being related to the counts following a binomial law instead of a Poisson law when the number of bins is small, as mentioned earlier. In this case, clustering is completely mitigated by the use of branchless collisions : if fission neutrons are Poisson distributed, the variance and the average of the distribution of fission neutrons scale similarly with respect to δ and the Feynman moment becomes constant. When adding combing or sampling WOR, the Feynman moment stays constant for $\delta \ll \sqrt{\langle r^2 \rangle_\infty}$ and start increasing when approaching $\delta \sim \sqrt{\langle r^2 \rangle_\infty}$, whereupon it saturates. We observe the same behaviour for the last-event algorithm, with larger values.

The shape of the curves in Fig. 5.9 can be given an interesting interpretation. When the average Feynman moment is constant for small values of δ, as for all algorithms except the branching algorithm, it translates the fact that clusters have some minimum spatial scale ; at scales finer than the minimum cluster size, clusters are essentially infinitely large, and the neutrons occupation statistics behaves as if the particles were independent. For very fine meshes, branching collisions appear to be more efficient than branchless collisions in quenching correlations. This could be explained by the fact that, as the cell size decreases, the probability that correlated particles fall within the same cell also decreases ; the fact that neutrons are strongly correlated when using branching collisions becomes irrelevant, but the fact that there are many more particles (thus, more sampling events) than when using branchless collisions or the last-event algorithm holds true. At the opposite extreme, the Feynman moment saturates at scales of the order of $\delta \sim \sqrt{\langle r^2 \rangle_\infty}$, which (at least in homogeneous systems) can be interpreted as the typical size of the largest clusters. Between the minimum and maximum scales, the Feynman moment follows a power law, which is the expected behavior for self-organized critical systems, as recently suggested by

Dechenaux et al. on the basis of the application of techniques borrowed from the renormalization group in particle physics [99]. The power-law exponents range between 0.5 and 1 for systems 1 and 2. The occurrence of power laws in the scale dependence of Feynman spectra is suggestive, but more careful analysis is required to confirm the existence of a deeper connection. Finally, at scales coarser than the typical cluster size, the occupation statistics of the space bins behaves as if the system were populated by independent macro-particles. In the limit $\delta \to L$, the Feynman moment decreases, as the counts follow binomial laws, and converges to zero because of the constraint on weight conservation of the fission source.

We move now to the case of heterogeneous systems 3 and 4. Figure 5.8c shows the Feynman moments for system 3, which has a small dominance ratio. For this case, all algorithms behave similarly. The main difference lies at the fuel-moderator interfaces. Here, branchless collisions lead to a dip in the Feynman moment near the material boundary, and a peak for branching collisions, while the last-event algorithm leads to an almost flat spatial shape. Figure 5.8d shows that for case 4, which has a larger dominance ratio, the Feynman moment is significantly smaller when using branchless collisions than when using branching collisions. In both systems the use of the last-event algorithm leads to a larger value of Feynman moments than when using any of the branchless variants. In system 4, this value is nonetheless much smaller than when using branching collisions. The spatial shape for all Feynman moments is similar in system 4, suggesting that spatial correlations are always at play, although they are the weakest for branchless collisions.

Again, interesting conclusions can be drawn from the dependence of the Feynman moment on δ. First, due to heterogeneity, l_{clust} cannot be identified with the pair distance. However, we still use the pair distance as a qualitative estimate of l_{clust}. Figure 5.9c shows that the *spatially-averaged* Feynman moment for all branchless variants in the heterogeneous configuration with a small dominance ratio is roughly constant for $\delta \lesssim \sqrt{\langle r^2 \rangle_\infty}$, and decreases for $\delta \gtrsim \sqrt{\langle r^2 \rangle_\infty}$. This suggests the absence of strong spatial correlations when using any of the five algorithms ; it also illustrates that the pair distance function is still a good approximation of the typical cluster size for systems with mild heterogeneity. On the other hand, Fig. 5.9d shows that $Y_F^{av} \propto \delta^{0.82}$ for $\delta \lesssim \sqrt{\langle r^2 \rangle_\infty}$ for all algorithms in the heterogeneous configuration with a large dominance ratio. Moreover, the power law scaling of the space-averaged Feynman moment as a function of δ is the same for each algorithm. By analogy with the three other cases, we expect the space-averaged Feynman moment in system 4 to reach a maximum for $\delta \gtrsim l_{\text{clust}}$; a direct confirmation is not possible, because $\sqrt{\langle r^2 \rangle_\infty}$ is essentially driven by the size of the moderator region, which means that it is not a good approximation of the (unknown) typical cluster size.

So far, we have investigated ensemble Feynman moments, which are not directly accessible by power iteration (unless one accepts to sample independent replicas). One may wonder how the ergodic Feynman moment relates to the ensemble Feynman moment. We consider then the dependence of the Feynman moment on the number of active generations G : based on Refs. 36 and 45, we expect that, when the number of active generations is large enough, the apparent variance converges towards the real variance. Therefore, we also expect the ergodic Feynman moments to converge towards the ensemble Feynman moments. In what follows, we want to characterize the relationship between the value of the dominance ratio and the ability of our algorithms to mitigate the bias on the variance induced by the use of ergodic averages instead of ensemble averages. We stress this bias is *not* related to discarding an insufficient number of inactive generations before tallying the observables.

Figures 5.10a-5.10d show the convergence of the spatially-averaged Feynman moments $Y_F^{G,av}$ obtained by ergodic average over G generations towards the ensemble spatially-averaged Feynman moments Y_F^{av}. For this purpose, we compute the relative bias defined by $|Y_F^{av} - Y_F^{G,av}|/Y_F^{av}$, as a function of the number of active generations. In all cases, it is clear that the underestimation of errors due to ergodic averages is significantly smaller when using branchless collisions than when using branching collisions, by about a factor 5 in homogeneous systems and up to a factor 3 in heterogeneous systems. Additionally, the slope of the relative bias as a function of active generations only weakly depends on the details of the sampling algorithm and population control, and is essentially driven by the value of the dominance

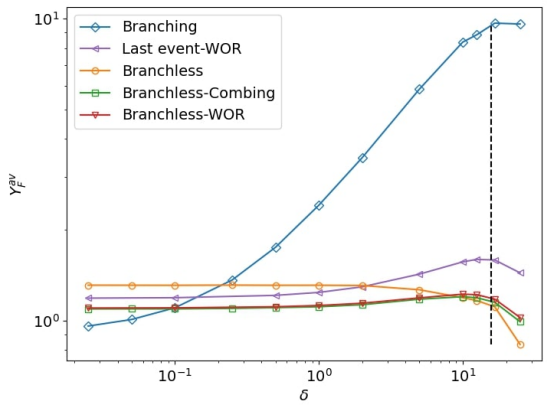

(a) System 1 with 10^5 realizations.

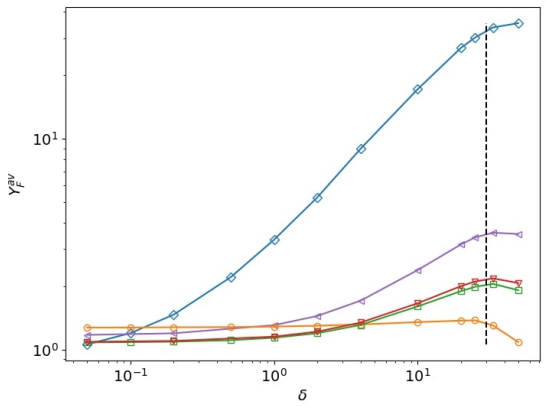

(b) System 2 with 10^5 realizations.

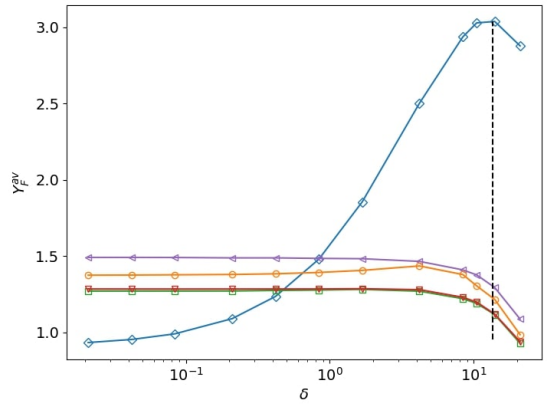

(c) System 3 with 10^5 realizations.

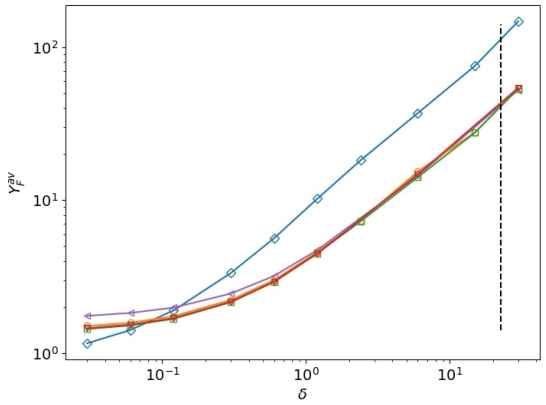

(d) System 4 with 10^4 realizations.

Figure 5.9 : Space-averaged Feynman moment of the fission source, as a function of the cell size δ, for $N = 10^3$. Dashed black line : square root of $\langle r^2 \rangle_\infty$ for branching algorithm. Given that the $\langle r^2 \rangle_\infty$ are relatively close to each other for all five algorithms, we only show the value for the branching algorithm.

ratio. However, the 'initial offset' depends on sampling and population control. This is reminiscent of the fact that, in power iteration, the speed of convergence of the dominant eigenvalue of k_0 only depends on the dominance ratio, but the initial value of k_0 (and so the number of inactive generations to discard) depends on the initial condition. In addition, the effect of population control algorithms appears to be milder compared to the effect of collision biasing.

We conclude our analysis by considering the effects of the neutron population size. Previous investigations have shown that the impact of spatial clustering becomes milder as the number of particles per generation increases [28]. Figures 5.11a-5.11b show the space-averaged ensemble Feynman moments for all five algorithms in system 2 (homogeneous case with higher dominance ratio), as a function of the population size. We observe that the Feynman moment for the branching algorithm converges towards an asymptotic value for large N. This scaling is consistent with similar findings in the context of time-dependent Monte Carlo simulations, for the case of spatially homogeneous branching-diffusion processes under population control [47]. Additionally, we verified that the shape of the Feynman moment also converges to an asymptotic shape for large N (not showed here for conciseness). We further observe that, using branchless collisions as well as using the last-event algorithm in systems 1-3, Feynman moments appear to be almost independent of N (only shown for system 2 in Fig. 5.11a). This behavior is presumably due to the absence of significant spatial correlations with these algorithms. Conversely, in

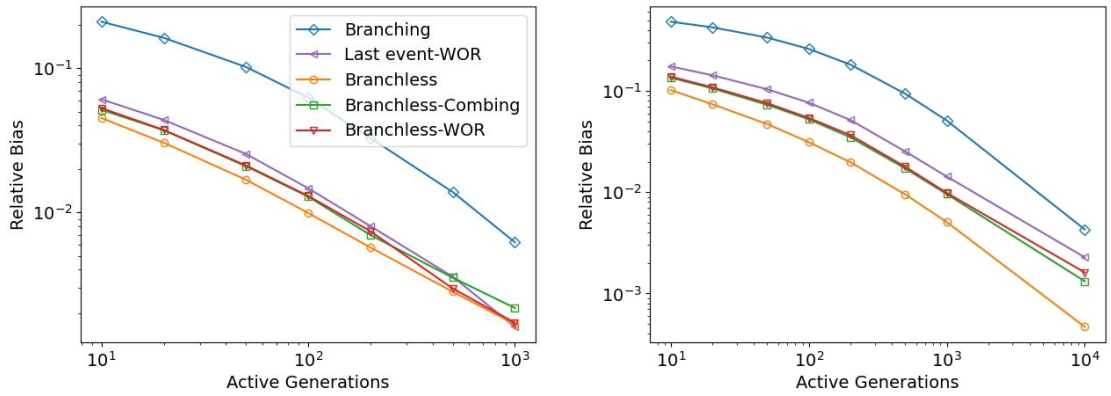

(a) System 1. (b) System 2.

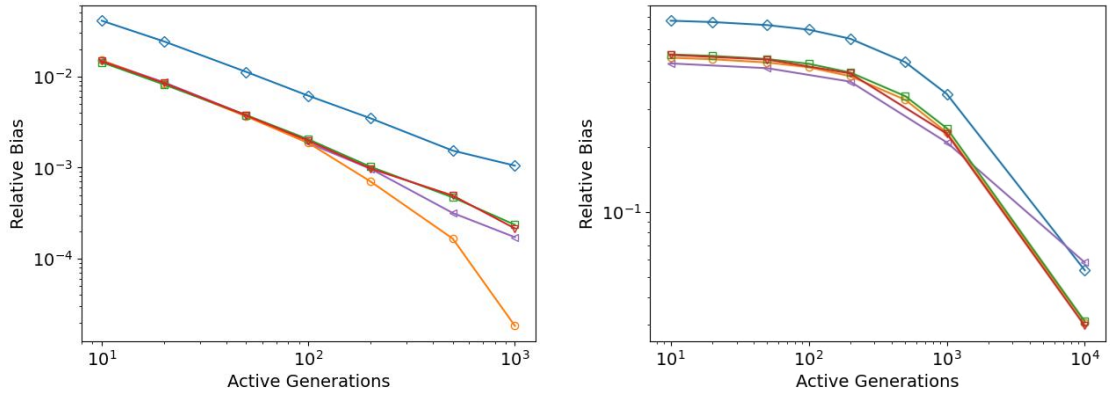

(c) System 3. (d) System 4.

Figure 5.10 : Convergence of the space averaged $Y_F^{G,av}$ with respect to the number of active generations G in terms of the relative bias $|Y_F^{av} - Y_F^{G,av}|/Y_F^{av}$. The population size is $N = 10^3$ and $B = 10^2$.

system 4, where strong spatial correlations exist for all algorithms, the Feynman moments depend on N and converge towards an asymptotic value for large N. It should be noted that, even then, the Feynman moment of branchless variants and of the last-event algorithm saturates at a smaller value of N than for the branching algorithm.

5.4.3 . Analysis of the fission source : normalized variance

Additional insight can be obtained by assessing the behavior of the *normalized variance* g_F of the fission source. As discussed above, $g \sim 0$ is a reasonable definition of 'weak correlations', similarly as for $Y \sim 1$. However, in the following we will show that the two tallies are not equivalent, and convey different pieces of information. The amplitude of fission-induced spatial fluctuations depends on the population size, and we will illustrate that this is captured by normalized variances.

All cases in Fig. 5.12 display a significant increase of g_F close to the leakage boundary conditions, even when using branchless collisions. This peak is explained by inspecting Fig. 5.8 : although Feynman moments are (almost) flat for branchless collisions, the average of the fission source is close to zero near leakage boundary conditions. Since $g_F = Y_F/\mathbb{E}[F]$, this explains the shape of g_F.

Let us analyze the homogeneous systems first. In Figs. 5.12a-5.12b we observe that the normalized variances of all algorithms except the branching algorithm are rather similar, and close to zero in the bulk of the geometry. On the other hand, the normalized variance using the branching algorithm can be close to 1 even far from the boundaries, which suggests that large fluctuations will occur. We observe that the shape of the normalized variance for all algorithms is almost independent of the dominance ratio. In the case of the heterogeneous media, Fig. 5.12c for case 3 shows that all the algorithms behave similarly

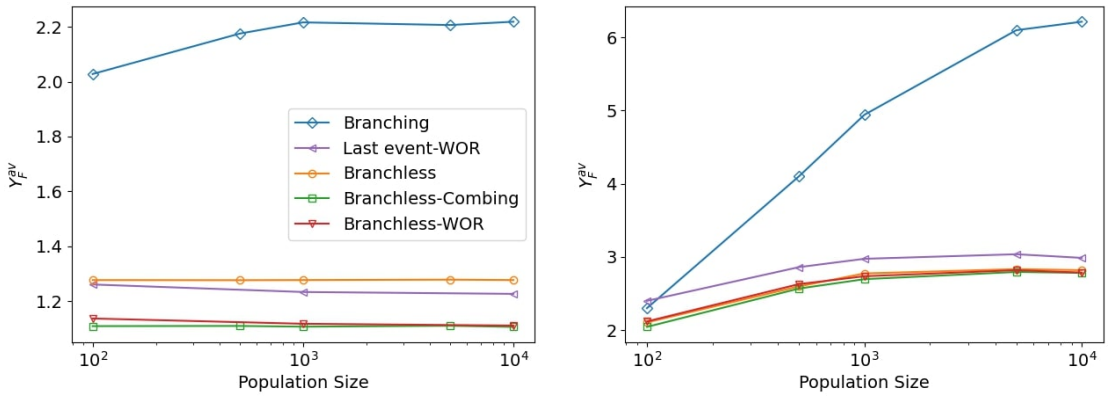

(a) For homogeneous configuration with large dominance ratio (system 2)

(b) For heterogeneous configuration with large dominance ratio (system 4)

Figure 5.11 : Space-averaged ensemble Feynman moments of the fission source Y_F^{av} as a function of the population size N, with bin size $\delta = 0.5$ cm.

in terms of normalized variances. Furthermore, Fig. 5.12d for case 4 confirms the hierarchy between the algorithms, and shows that, even in the bulk of the system, typical fluctuations are larger for the branching algorithm than for the other algorithms. Similarly to the homogeneous cases, the normalized variance is only weakly dependent on the dominance ratio when using branchless algorithms or the last-event algorithm.

Next, we examine the dependence of normalized variances on the population size N and the cell size δ. For the sake of conciseness, we will not consider the dependence on G, the number of active generations, because these effects are very similar to those occurring for Feynman moments of Sec. 5.4.2. As for the dependence on δ, previous findings suggest that $g_F \sim 1/\delta$ for small values of δ [47]. Figure 5.13 illustrates this scaling. We consider

$$g_F^{av}(B) = \frac{1}{B'} \sum_{i=1}^{B'} g_{F_i}, \tag{5.22}$$

where B' is the number of cells with fissile material. We note that $g_F^{av} \propto B$ for all algorithms, when $L/\delta = B \gg 1$. For large cell sizes, the normalized variance is smaller for branchless collisions than for branching collisions. The converse is true for small cell sizes. This can be explained by the fact that spatial correlations are weakened by decreasing the cell size. Branching sampling typically results in more fission neutrons than branchless sampling, because each collision site is a potential fission site in branching sampling. Due to the excess of fission neutrons, when spatial correlations are weak, the branching algorithm introduces less variance in the estimation of the fission source than branchless algorithms. There are essentially two ways to obtain weak spatial correlations : either the dominance ratio is small enough (cf. system 3) or the cell size is small enough (as clearly illustrated by Figs. 5.13b and 5.13d). Finally, additional numerical findings (not shown here for the sake of conciseness) suggest that the normalized variances scale as $1/N$ regardless of the algorithm, which is consistent with the literature [28].

5.4.4 . Analysis of the collision counts : Feynman moment

Most of the tallies of interest for reactor physics (such as reaction rates or energy deposition) are estimated by summing over all the collisions in a generation. In this respect, the Feynman moments of the collision counts can help to interpret the behavior of spatial correlations for such observables.

The Feynman moments of the collision counts, shown in Fig. 5.14, are significantly higher than those of the fission source. Scattering now contributes to the tally and there are several scattering events per generation ; in contrast, there is only one fission event per generation. Additionally, correlations between collision sites are stronger than correlations between fission sites. Figures 5.14c and 5.14d for

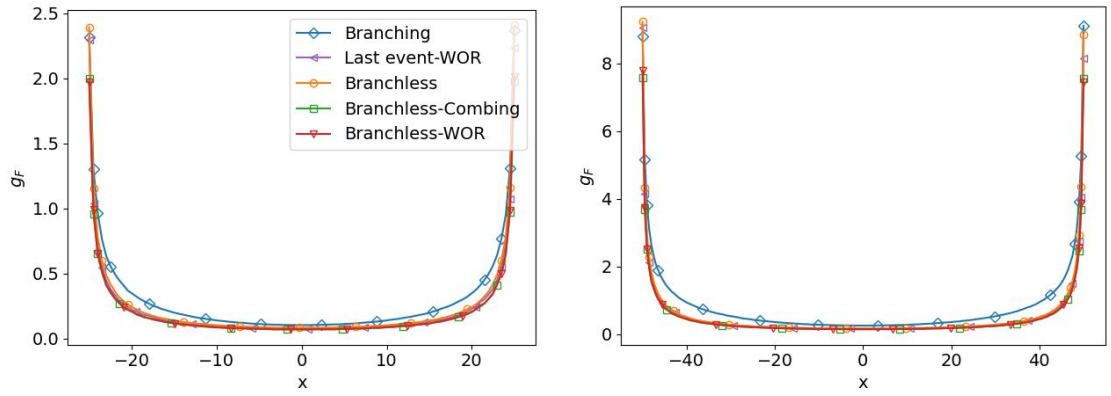

(a) System 1, with 10^5 independent replicas. (b) System 2, with 10^5 independent replicas.

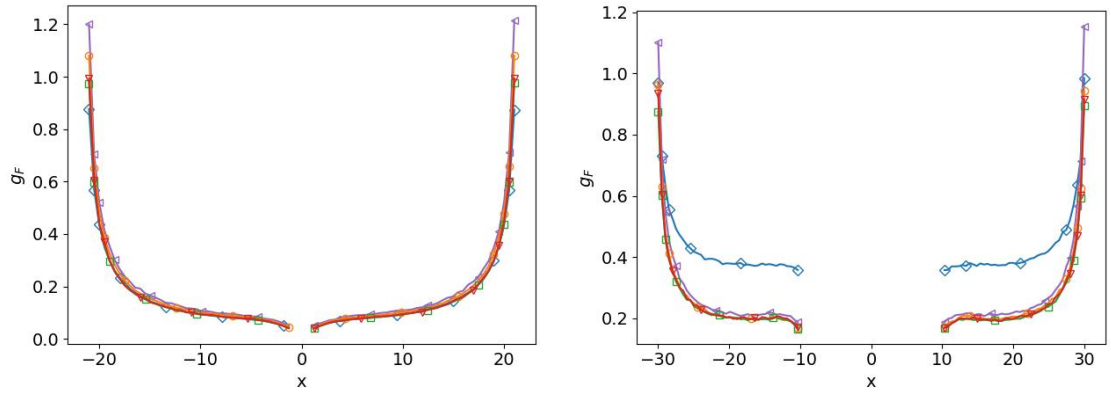

(c) System 3, with 10^5 independent replicas (d) System 4, with 10^4 independent replicas.

Figure 5.12 : Equilibrium ensemble normalized variances for the fission source computed over 10^5 independent replicas. $N = 1000$ and $\delta = 0.5$ for different systems.

the heterogeneous cases 3 and 4 indicate strong spatial correlations between collision sites near the fuel-moderator interfaces. Similar peaks in the spatial profile of the correlations were already observed in the fission source, but their amplitude is considerably amplified in the Feynman moments of the collision counts. Far from the fissile regions, all algorithms behave similarly, due to the fact that they all reduce to implicit capture in the moderator region. Note that sampling WOR has no significant effect on the Feynman moments of the collision counts.

Figures 5.15a and 5.15b show the dependence of the spatially-averaged Feynman moments of the collision counts with respect to the bin size δ, in homogeneous and heterogeneous systems, respectively. All the Feynman moments of the collision counts scale as a power law of δ, for $\delta \lesssim l_{\text{clust}}$. Additionally, Fig. 5.15a saturates around $\sqrt{\langle r^2 \rangle_\infty}$, similarly to the Feynman moment of the fission source. The latter remark does not hold for system 4 (see Fig. 5.15b), which is related to the discussion on Fig. 5.9d (in Section 5.4.2), where we observed the same trend for the dependency on δ of the Feynman moments for the fission source. In any case, branchless collisions lead to Feynman moments that are considerably smaller than those of branching collisions, and all population control algorithms seem to have little effect on the dependence on coarse-graining of the Feynman moments of the collision counts. The dependence on N and G of the Feynman moment of the collision counts is similar to that of the fission source, and for the sake of conciseness it will not be shown here.

5.4.5 . Analysis of the collision counts : normalized variance

In the homogeneous cases, the normalized variance of the collision counts behaves similarly to that of the fission source (not shown here for conciseness). The two heterogeneous configurations are shown in Fig. 5.16. In both cases 3 and 4, it is interesting to note that the peaks observed in the corresponding

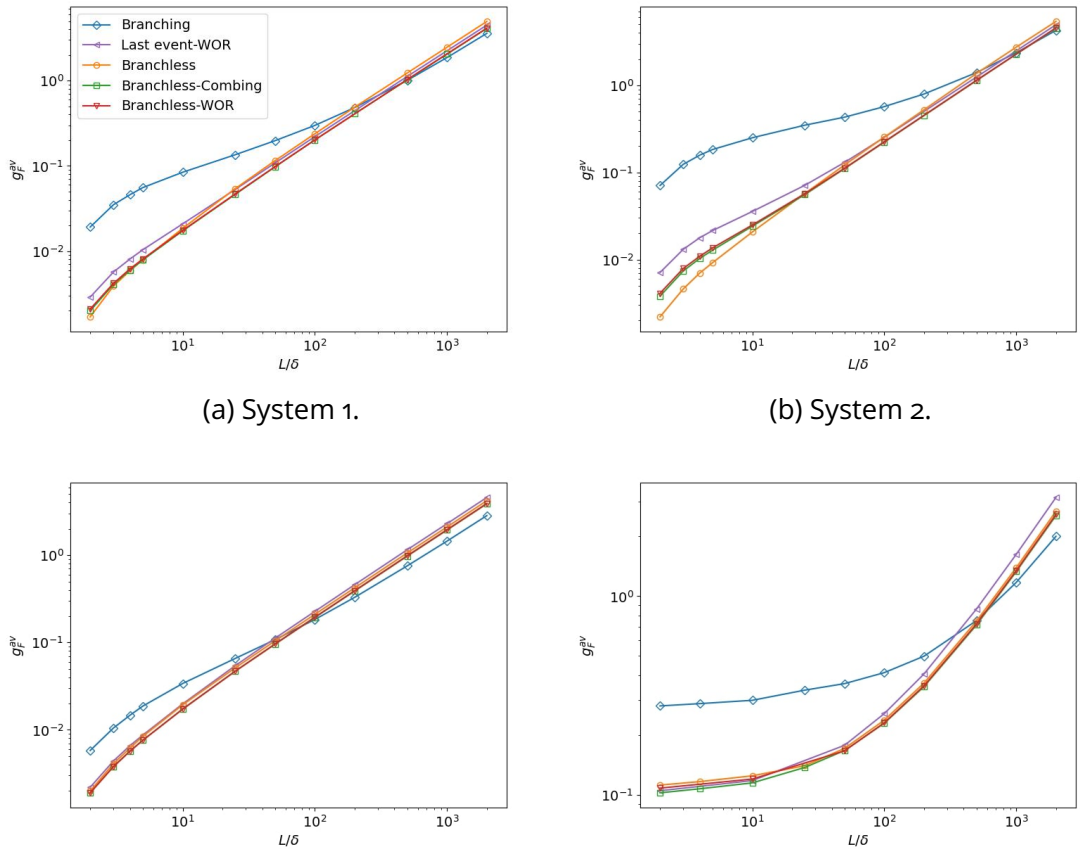

(a) System 1.

(b) System 2.

(c) System 3.

(d) System 4.

Figure 5.13 : Scaling of the space-averaged normalized variance g_F^{av} as a function of the number of cells $L/\delta = B$, for all 4 systems and algorithms, $N = 10^3$, and with 10^4 independent replicas.

Feynman moments do not occur in the normalized variance. This illustrates clearly the difference between Feynman moments and normalized variances.

Finally, we consider the dependence of normalized variance with the size of spatial cells, which is expected to scale as $1/\delta$ when δ is small enough [47]; indeed, Fig. 5.17 shows that the normalized variance behaves as $1/\delta$. When the dominance ratio is close to unity (see Fig. 5.17d), the normalized variance for the branching algorithm is significantly higher than for the other algorithms. Additionally, although all algorithms except from the branching algorithm yield similar normalized variances, branchless collisions in combination with either combing or sampling WOR appear to consistently yield the lowest normalized variance in our systems.

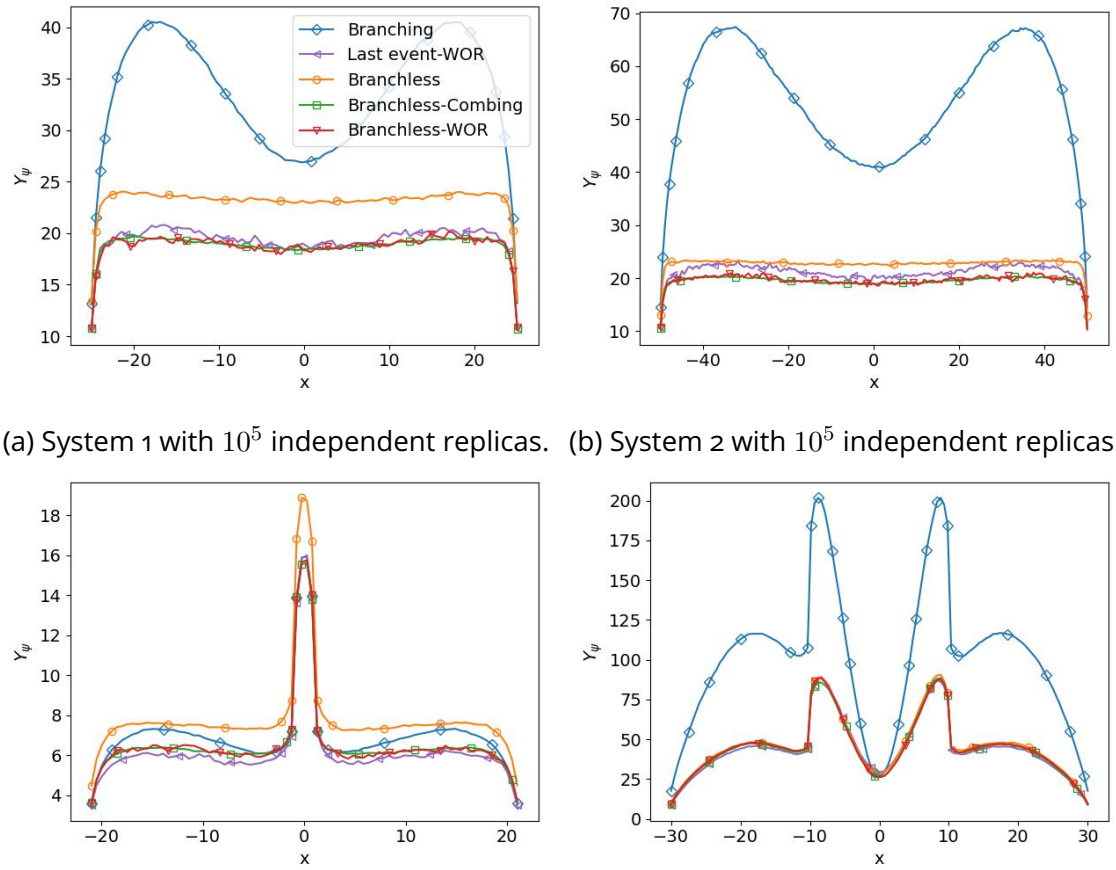

(a) System 1 with 10^5 independent replicas. (b) System 2 with 10^5 independent replicas.

(c) System 3 with 10^4 independent replicas. (d) System 4 with 10^4 independent replicas.

Figure 5.14 : Equilibrium Feynman moments for the collision counts of neutrons computed for $N = 1000$ and $B = 100$ for different systems.

5.5 . A digression on continuous-energy problems

Most investigations concerned with possible methods to reduce clustering typically consider simplified systems in a single-speed or multi-group framework [27, 42], such as those examined in Sec. 5.2 and 5.4. It is indeed easier to draw conclusions on the performance of these systems and methods when disregarding heterogeneity and continuous energy ; however, in realistic applications, the effects of these two aspects cannot be neglected. In Sec. 5.4, we discussed the effect of heterogeneity on spatial correlations. Now, we shall investigate how continuous energy affects the statistical behaviour of the neutron population. Interaction probabilities now depend on the isotopic concentration in materials, so one cannot indiscriminately use microscopic or macroscopic cross sections. In the original formulation of the branchless collision, however, it is somewhat ambiguous whether the cross sections are intended to be the macroscopic cross sections for the material, or the microscopic cross sections for the sampled isotope [18]. There are in fact several ways to sample branchless collisions. One can sample first the collision channel (fission, capture or scattering), whereupon the weight multiplier is independent of the chosen isotope, or one can first sample the collision isotope, whereupon the weight multiplier is independent of the collision channel. Additionally, one can also choose whether to use the cross section or the yield-weighted cross section for making the first sampling (be it for the isotope or channel). Here, we will briefly outline two options for this sampling procedure. Note that the distinction between these two methods only makes sense when considering continuous energy. In a single-speed (or multi-group) system, where there is effectively just one isotope per material, there is no difference between performing branchless collisions on the isotope, or on the material.

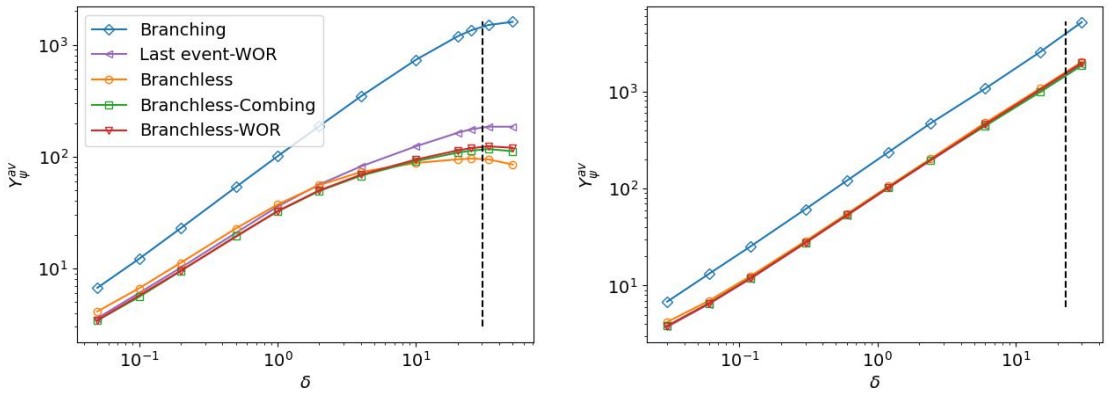

(a) System 2, with 10^4 replicas.

(b) System 4, with 10^3 replicas.

Figure 5.15 : Space-averaged Feynman moments of the collision counts for all five algorithms, as a function of the cell size δ, for $N = 10^3$. Dashed black line : square root of $\langle r^2 \rangle_\infty$ for the branching algorithm.

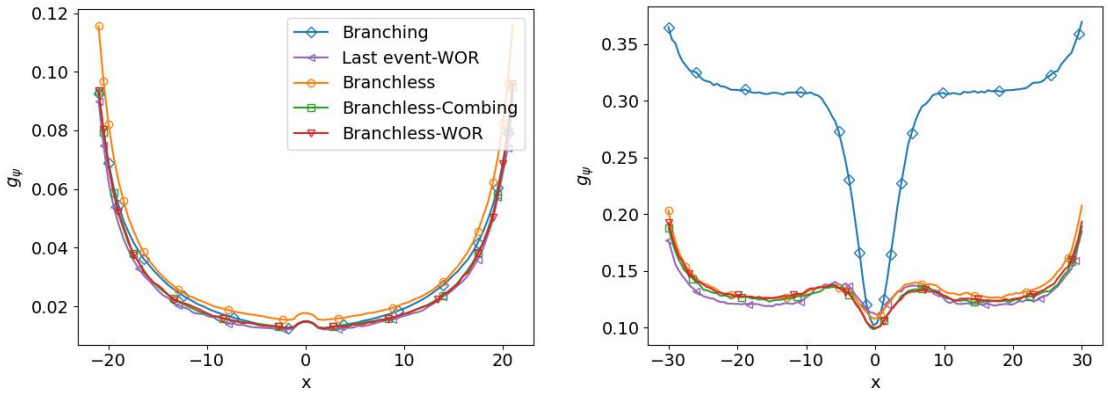

(a) System 3.

(b) System 4.

Figure 5.16 : Equilibrium normalized variance for the collision counts of neutrons, computed for $N = 1000$, $\delta = 0.5$, and with 10^4 independent replicas, for the two heterogeneous systems.

5.5.1 . Branchless collisions on the isotope

We begin by illustrating the branchless collision strategy applied to an isotope. In most continuous-energy Monte Carlo codes, the collision event begins with the sampling of isotope i, whose probability is given by

$$P_i(\mathbf{r}, E) = \frac{N_i(\mathbf{r})\ \sigma_{i,t}(E)}{\Sigma_t(\mathbf{r}, E)}, \tag{5.23}$$

where $N_i(\mathbf{r})$ is the concentration of isotope i at position $\mathbf{r}$, $\sigma_{i,t}(E)$ is the total microscopic cross section for isotope i at incident energy E (see Chapter 2 for details). Due to this simple fact, developers interested in adding branchless collisions to a pre-existing Monte Carlo code are likely to immediately consider this algorithm, which avoids a potentially large refactoring of source code. It is possible to keep the methods for sampling the isotope, and only change how the reaction channel is sampled. This is why the isotope-based branchless collision method was implemented in TRIPOLI-4®, when the reactor kinetics simulation was added to the code [62].

Isotope i is first sampled using Eq. (5.23). Knowing the isotope i, the scattering and fission proba-

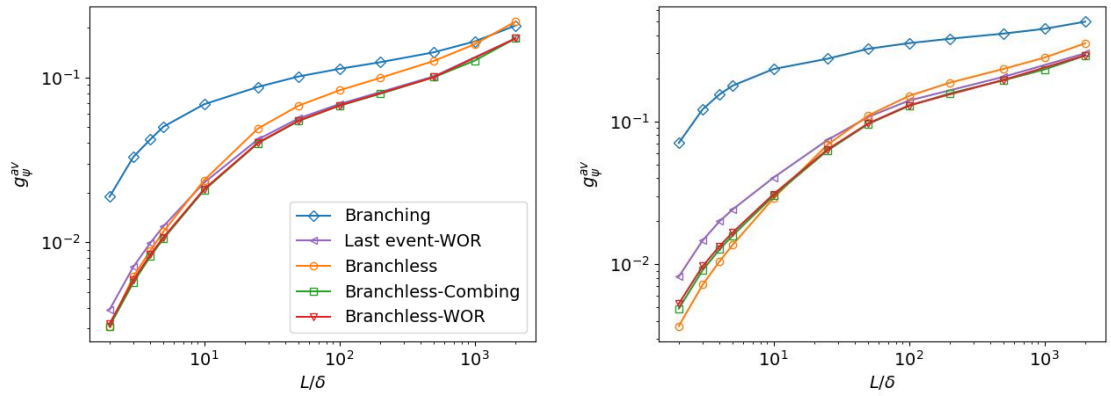

(a) System 1, with 10^5 independent replicas. (b) System 2, with 10^5 independent replicas.

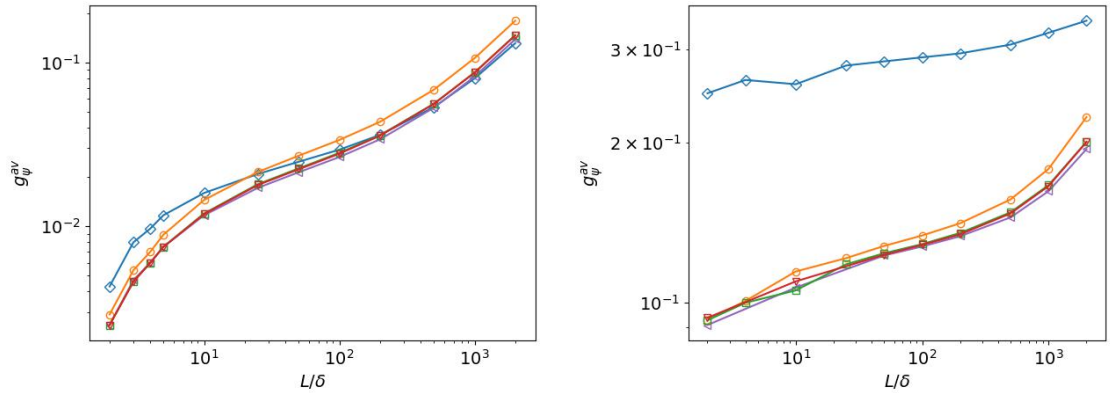

(c) System 3, with 10^5 independent replicas. (d) System 4, with 10^4 independent replicas.

Figure 5.17 : Space-averaged equilibrium normalized variance for the collision counts of neutrons as a function of bin size, computed for $N = 1000$ and $B = 100$ for different systems.

bilities follow from

$$P_{s|i} = \frac{\sigma_{i,s}(E)}{\nu_{i,f}(E)\sigma_{i,f}(E) + \sigma_{i,s}(E)} \quad \text{and} \quad P_{f|i} = \frac{\nu_{i,f}(E)\sigma_{i,f}(E)}{\nu_{i,f}(E)\sigma_{i,f}(E) + \sigma_{i,s}(E)}. \tag{5.24}$$

If scattering is chosen, the scattering channel α is then sampled in the standard manner, with probability

$$P_{s_\alpha|i} = \frac{\sigma_{i,s_\alpha}(E)}{\sigma_{i,s}(E)}. \tag{5.25}$$

After the final reaction state has been determined, the particle weight is modified by

$$w' = w\frac{\nu_{i,f}(E)\sigma_{i,f}(E) + \sigma_{i,s}(E)}{\sigma_{i,t}(E)}. \tag{5.26}$$

Note that this form implicitly assumes that the yield of all scattering reactions is exactly 1. Explicitly considering the yields of reactions such as (n, xn), which are somewhat rare, would add to the computational complexity when computing the scattering and fission probabilities, and change how scattering reaction channels are sampled. Instead, here we assume that the scattering yield is always 1 for the probabilities and weight modifier in Eqs. (5.24) and (5.26); if we sample a scattering reaction where $\nu_{i,s_\alpha}(E) \neq 1$, we also multiply the neutron weight by $\nu_{i,s_\alpha}(E)$. It should also be noted that while our weight modifier in Eq. (5.26) is independent of the reaction channel, it is dependent on the sampled isotope at the collisions site. Therefore, at the same position in phase space, this weight multiplier could exhibit a large variance; in the fuel for example, all the isotopes but one could have a null fission cross

Isotope	Concentration [$b^{-1}cm^{-1}$]
^{1}H	$6.6856 \cdot 10^{-2}$
^{16}O	$8.21578701 \cdot 10^{-2}$
^{17}O	$3.129604 \cdot 10^{-5}$
^{18}O	$1.688339 \cdot 10^{-4}$
^{235}U	$2.67228041 \cdot 10^{-4}$
^{238}U	$2.4197772 \cdot 10^{-2}$

Table 5.6 : Isotopic composition of the reflected continuous-energy cube reactor.

section. This variance in the weight multiplier will increase the variance in the length of fission chains, which will also increase the variance of scores [55].

5.5.2 . Branchless collisions on the material

An alternative approach is to first sample whether the reaction channel will be scattering or fission, and then sample the isotope given this information. The probability of scattering and fission are calculated following Eqs. (5.6) with the macroscopic material cross sections. If fission was sampled, then the probability of sampling isotope i is

$$P_{i|f} = \frac{N_i(\boldsymbol{r})\nu_{i,f}(E)\sigma_{i,f}(E)}{\nu_f(\boldsymbol{r},E)\Sigma_f(\boldsymbol{r},E)}. \tag{5.27}$$

If scattering was sampled, then the probability of sampling isotope i is

$$P_{i|s} = \frac{N_i(\boldsymbol{r})\sigma_{i,s}(E)}{\Sigma_s(\boldsymbol{r},E)}. \tag{5.28}$$

The scattering channel α is then sampled with the same probability used in Eq. (5.25). The particle weight is modified using Eq. (5.5), using the macroscopic cross sections. Thus, in this sampling scheme, the weight multiplier is independent of the reaction channel *and* of the selected isotope. Should the sampled scattering channel not have a yield of 1, then we again multiply the particle weight by $\nu_{i,s_\alpha}(E)$. Compared to the algorithm of the previous section, it is clear that this strategy requires larger modifications to the algorithms already present in an existing Monte Carlo code.

5.5.3 . Numerical results

To illustrate the differences between the two alternatives presented above, we shall now examine the case of a reflected reactor filled with a homogeneous mixture of light water and uranium, the isotopic composition of which is provided in Table 5.6. This mixture is not intended to be realistic, but simply provide a multiplying system which we can use for our clustering study. Using the ENDF/B-VIII.0 library (with the thermal scattering law for light water), a 400 cm $\times$ 400 cm $\times$ 400 cm box of this composition is nearly critical.

As the box remains completely homogeneous, we are able to continue using Eq. (5.19) to approximate the ideal entropy for the box, given the number of particles and partitions. Figure 5.18 presents the entropy and the number of families for simulations, using different forms of branchless collisions, with either combing or splitting. It is immediately evident that, despite the box being nearly critical, branchless collisions do little to increase the saturation value of the entropy to the ideal value, unlike the case of single-speed transport (Fig. 5.1). Branchless collisions do seem to lead to a slightly higher entropy, with branchless collisions on the material faring only slightly better than branchless collisions on the isotope. Looking at the number of particle families, we note that branchless collisions on the isotope lead to no significant change with respect to branching collisions. Branchless collisions on the material do however seem to produce a slower decrease in the number of particle families.

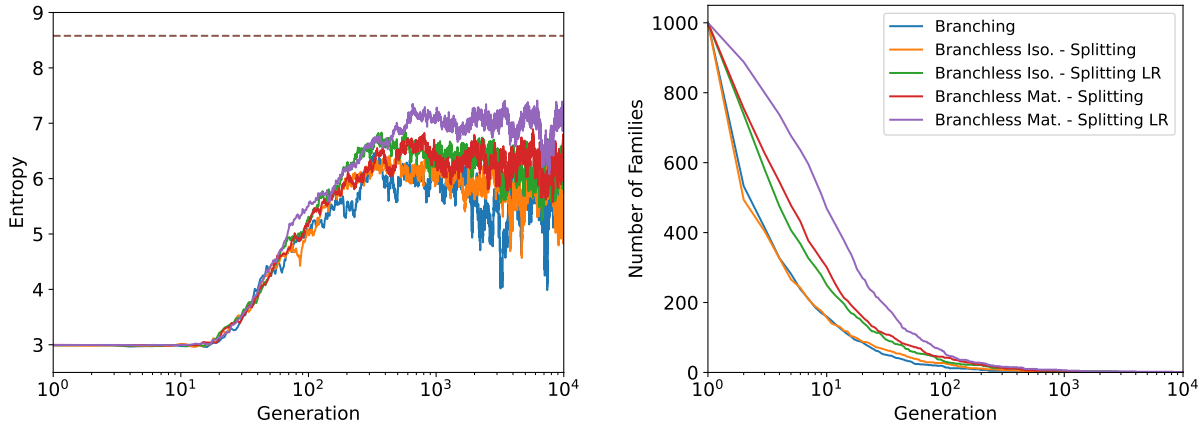

Figure 5.18 : Shannon entropy of the fission source, and the number of distinct families for a critical continuous energy box, for both the branching and branchless simulation methods. The ideal value of the entropy for $N = 10^3$ and $= 8^3$ is also provided.

As the weight modifier for the single-speed critical configuration is always equal to one, all the particles are able to remain truly independent, eliminating the possibility of clustering. While the continuous-energy case is nearly critical, the weight multiplier is never equal to one, and depends on the energy of the incident particle (for both the isotopic and material variants). This causes the weights of the particles to diverge from unity, and the use of population control mechanisms is then required. Combing and splitting both lead to the effective duplication of particles at a phase-space coordinate, and therefore contribute to clustering. Branchless collisions on the isotope can in fact exacerbate this situation, as the weight multiplier could vary greatly between different isotopes in a material. Branchless collisions on the material reduce the variance of the weight multiplier, because the latter is independent of the isotope *and* the reaction channel. Thus, the number of particle families decreases more slowly ; particle weights are less dispersed, and therefore less population control is needed.

5.6 . Conclusions

In this chapter we have investigated the impact of sampling strategies, variance-reduction and population-control methods on the correlations that occur in the Monte Carlo implementation of the power iteration algorithm, which is key to the sampling of the critical source for kinetic simulations. For this purpose, we have selected several distinct tallies : the Shannon entropy, the average pair distance squared, the average number of surviving families, the Feynman moments and the normalized variance. This analysis has been carried out on a set of simple, yet meaningful benchmark configurations encompassing homogeneous and heterogeneous geometries. In order to probe the effects of each technique, the power iteration was run with different combinations of branching and branchless collisions as well as the last-event estimator for the fission source, and combing or sampling WOR.

All the proposed tallies help in some way to detect the presence of anomalous fluctuations in the examined systems. However, each comes with specific advantages and drawbacks. Global (i.e., integrated) tallies such as the entropy and the average square pair distance, while being easy to use and interpret, have been shown to be inadequate for the investigation of heterogeneous systems, due to lack of information on the spatial details. Conversely, local (i.e. space dependent) tallies such as the Feynman moments and the normalized variance are inherently useful in extracting information on the spatial behavior of the correlations, at the expense of an increased complexity.

Our main finding is that, in all tested configurations, the use of branchless collisions (as opposed to regular branching collisions) is very effective at quenching correlations and thus lowering the ratio between the apparent (ergodic) and real (ensemble) variance. In addition, while population control is

generally advantageous in terms of weakening the effects of correlations, the impact of these methods is much milder than that of using branchless collisions. Using the last-event estimator in combination with sampling WOR was shown to be slightly less efficient than using branchless collisions for quenching spatial correlations.

In addition, we presented an exploratory work on the effects of branchless collisions in continuous-energy problems. Two different branchless sampling strategies were introduced : the reacting isotope is first sampled as usual, and the branchless algorithm is applied afterwards with the corresponding microscopic cross sections ; or the reaction channel is sampled using macroscopic cross sections, and the reacting isotope is then sampled with probability laws depending on the chosen collision channel. Using branchless collisions on the material was found to better quench clustering in the system, although the improvement in terms of entropy and average surviving independent families was less significant than in multi-group problems.

6 -Space-time correlations in time-dependent Monte Carlo simulations

In Chapter 5, we examined the correlations affecting the power iteration algorithm, in view of their relevance for the sampling of the equilibrium source for the time-dependent problem. In the following, we will focus on the space-time correlations affecting kinetic simulations, by relying on the insight gained in Part I of the thesis (Chapters 3 and 4), and in Chapter 5.

For the purpose of the analysis carried out here, we will relax most of the simplifying hypotheses introduced in the diffusion-based analog transport models of Chapters 3 and 4. In particular, we will consider homogeneous configurations in a multi-group setting, similarly as in Chapter 5. Furthermore, we will use non-analog Monte Carlo methods, with several variance-reduction and population-control techniques : our main goal will be to assess their impact on correlations due to the interplay of these strategies.

Our investigation will be based on the methods and diagnostic tools developed in Chapter 5 for eigenvalue problems, with fairly minor modifications. Some of the findings related to power iteration, such as the emergence of spatial correlations leading to a patchy neutron density, will be shown to apply also to kinetic simulations. The role played by the fission source distribution in the power iteration algorithm will be played by the neutron and precursor populations at the end of a time step in kinetic simulations. Similarly, observables related to generation-wise tallies in power iteration have a counterpart in tallies integrated over a time step in kinetic simulations. However, we will also illustrate some peculiar phenomena that are specific to kinetic simulations, without a direct counterpart in eigenvalue problems.

We will begin by adapting and extending the estimators that we have introduced in Chapter 5 for the correlations to the case of time-dependent problems. For this purpose, in Sec. 6.1 we will consider in particular the Shannon entropy and the Feynman moment of the neutron and precursor populations.

As a first step towards the analysis of correlations in kinetic simulations, in Sec. 6.2 we will revisit the homogeneous slab reactor benchmark introduced by Nowak et al. in Ref. 38, which we previously examined in Sec. 5.2 in the context of power iteration. For kinetic simulations, we will initially neglect precursors, we will model neutron transport as single-speed, and we will apply reflective boundary conditions. In order to probe the sensitivity of our results to these simplifying assumptions, we will introduce several modifications and assess their impact on correlations. To begin with, we will vary the reactor size, and we will also replace reflective boundary conditions by leakage boundary conditions. The most relevant change will be the introduction of precursors : unsurprisingly, we will show that they deeply affect the amplitude and the spatial behaviour of the correlations.

Next, in Section 6.3, we will revisit the more realistic case of the multi-group homogeneous slab-geometry benchmark configurations introduced in Chapter 5. We will assess the correlations of the equilibrium neutron and precursor populations, as determined by running the power iteration described in the previous chapter, and how the equilibrium source affects the spatial correlations within the time-dependent Monte Carlo simulations. Three different regimes will be explored : critical, subcritical and supercritical.

Conclusions for this chapter will be finally drawn in Sec. 6.4.

6.1 . Adapting the diagnostic tools to the time-dependent case

Based on the findings of Chapter 5, we are now aware of the limitations of the global diagnostic tools for correlations. Nonetheless, such global observables still retain the advantage of being easy to interpret, and easy to compute. In order to facilitate the investigation of space-time correlations performed in the following sections, here we briefly recall the definition of the main observables that we will use, namely the Shannon entropy and on Feynman moments. We refer the reader to Sec. 5.1.3 for a more thorough presentation.

6.1.1 . Neutron and precursor entropy

For time-dependent problems, we shall define the Shannon entropy separately for neutrons and precursors, as the statistical behaviour of the two populations is expected to considerably differ. The Shannon entropy for neutrons reads

$$S_n(t) = -\sum_{i=1}^{B} p_{n,i}(t) \log_2(p_{n,i}(t)), \tag{6.1}$$

where $p_{n,i}$ is the fraction of the total *neutron* statistical weight in the spatial cell i at time t. Similarly, we define the Shannon entropy for precursors as

$$S_c(t) = -\sum_{i=1}^{B} p_{c,i}(t) \log_2(p_{c,i}(t)), \tag{6.2}$$

where $p_{c,i}$ is the fraction of the total *precursor* statistical weight in the spatial cell i at time t. Although we may consider also the entropy of the total population, in realistic systems close to critical conditions the precursor population is much larger than the neutron population, so that the total entropy is entirely dominated by the precursor entropy. Therefore, we shall not include the total entropy in our investigation.

6.1.2 . Feynman moments

Contrary to Chapter 5, the question of ergodic vs. ensemble Feynman moment does not occur in pure time-dependent simulations. Nonetheless, it can still arise from the calculation of the equilibrium source using the power iteration. However, in the following we decided to simplify the study by looking at genuinely independent replicas, which are easier to interpret. By analogy with the time-independent case, we define the time-dependent ensemble Feynman moment (or simply, Feynman moment) for an observable $\mathcal{O}$ as

$$Y_{\mathcal{O}}(\mathbf{r}_i, t) = \frac{\mathbb{V}[\mathcal{O}](\mathbf{r}_i, t)}{\mathbb{E}[\mathcal{O}](\mathbf{r}_i, t)}, \tag{6.3}$$

where $\mathbf{r_i}$ is the center of the i-th spatial cell, $\mathbb{E}[\cdot]$ denotes the *ensemble* average over M independent replicas of the time-dependent observable $\mathcal{O}$, and $\mathbb{V}[\mathcal{O}]$ is the *ensemble* unbiased estimator of the variance of $\mathcal{O}$. The interpretation of the Feynman moment presented in Chapter 5 still holds.

In this chapter, we apply the Feynman moments separately to the neutron and precursor spatial distribution in the equilibrium source (namely, $Y_{S,n}$ and $Y_{S,c}$), to the neutron and precursor spatial distribution during the kinetic simulation (namely, Y_n and Y_c), and, when relevant, to the (neutron) collision counts (i.e. Y_ψ). Sometimes, for configurations where precursors are neglected, we will drop the n subscript.

6.2 . Analysis of a simplified homogeneous reactor benchmark

We begin our analysis by revisiting the simple benchmark problem proposed by Nowak et al. in Ref. 38 for the purpose of investigating particle clustering in power iteration, which we have previously introduced in Sec. 5.2. We consider a model of single-speed particle transport within a spatially homogeneous, reflected slab of varying length L, with scattering cross section $\Sigma_s = 0.27\,\mathrm{cm}^{-1}$, capture cross section $\Sigma_c = 0.002\,\mathrm{cm}^{-1}$, fission cross section $\Sigma_f = 0.002\,\mathrm{cm}^{-1}$; the fission multiplicity ν_p will be adjusted depending on the desired multiplication factor k_{eff}. The neutron speed is $v = 10^3\,\mathrm{cm}\cdot\mathrm{s}^{-1}$. Delayed neutron precursors are initially neglected.

For the purpose of running time-dependent Monte Carlo simulations, we will assume that the time interval $[0, T]$ is partitioned into $K_T = 100$ equal time steps. We shall investigate a 'large' system of length $L = 400\,\mathrm{cm}$ and a 'small' system of length $L = 100\,\mathrm{cm}$. By large system, we mean that $L \gg \sqrt{\mathcal{A}}$, i.e. the system size is large compared to the migration length; conversely, in the small system we have $L \sim \sqrt{\mathcal{A}}$. With the parameters described in the previous paragraph, we have $\sqrt{\mathcal{A}} = 42.71 \pm 0.02$ cm for the large system, and $\sqrt{\mathcal{A}} = 37.47 \pm 0.01$ cm . For spatial tallies, the slab is partitioned into $B = 100$ evenly spaced bins.

For a suitable choice of the fission multiplicity ν_p, the dominant eigenvalue of this configuration can be adjusted to any sought value; the corresponding equilibrium distribution (i.e. the fundamental mode) will be spatially uniform over the slab, independently of ν_p.

Neutron collisions are sampled using the branchless strategy, as described in Sec. 2.2.3. After collision events, neutrons undergo either Russian roulette, with threshold $w_R = 0.8$ and survival weight $w_{\mathsf{surv}} = 1$, or splitting, with threshold $w_S = 2$. At first, no population control algorithm (such as combing) is applied at the end of the time steps. The neutron flights are sampled in an analog fashion.

In the following sections, this model will be made incrementally more complex by adding weight combing, leakage boundary conditions, and a single delayed neutron precursor family with an analog or forced-decay strategy, and we will assess the effect of each contribution on space-time correlations.

6.2.1 . Russian roulette and splitting as drivers of entropy steps

Our first goal is to investigate the space-time correlations occurring in the time-dependent simulation of a critical, supercritical or subcritical configuration. We will characterize these correlations using the neutron and precursor Shannon entropy, and the Feynman moments. Occasionally, we will refer to other observables introduced in Chapter 5, such as the number of surviving neutron genealogical trees.

For this simple benchmark configuration, the equilibrium source can be sampled directly (the fundamental mode being spatially uniform), without resorting to the power iteration algorithm. The ideal Shannon entropy for the equilibrium source is therefore given by the expression given in Sec. 5.2, which is recalled here for convenience

$$S_{\mathsf{id}} = \log_2(N) - \frac{B}{N}\left(\frac{B-1}{B}\right)^N \sum_{k=1}^{N} (B-1)^{-k} \binom{N}{k} k \log_2(k), \tag{6.4}$$

where N is the number of particles (assuming unit statistical weights) and B is the number of spatial cells for the entropy tally.

About the absence of spatial correlations in the critical case

In the critical state, obtained by taking $\nu_p = 2$, the system presented in the previous section will lead to the same conclusions as in Section 5.2 : no spatial correlations arise and the neutron population behaves at any time like a collection of particles independently and identically distributed following a uniform spatial distribution in $[-L/2, L/2]$ (recall that here the source particles are sampled independently). The neutron entropy will thus reach the ideal value given by Eq. 6.4. The reason for this behaviour is the same as in the case of power iteration : *i)* there is no loss of neutrons, and *ii)* the weight multiplier for branchless collision is of unity. Thus, the statistical weight of each individual neutron and the number of neutrons in the simulation will be constant. It is worth stressing that this behaviour is somewhat

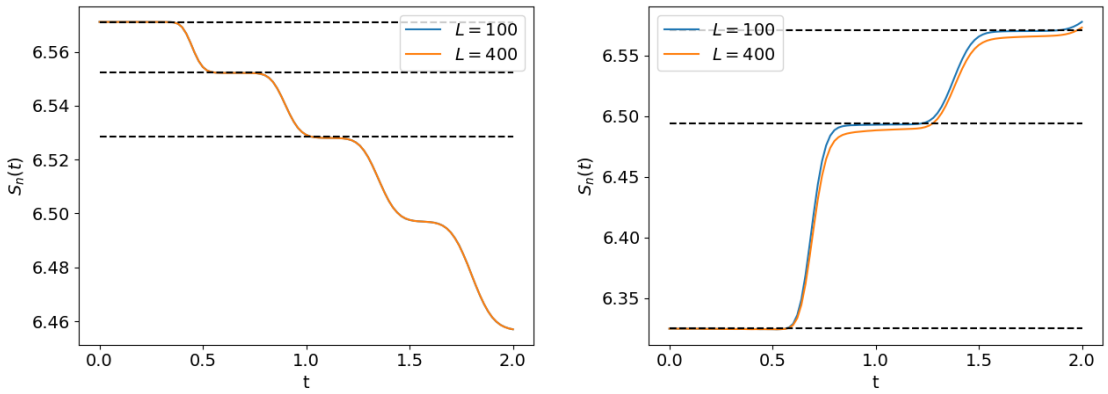

(a) Subcritical configuration with $k_{\text{eff}} = 0.875$ and $\nu_p = 1.75$, with initial population size $N_0 = 1000$.

(b) Supercritical configuration with $k_{\text{eff}} = 1.25$ and $\nu_p = 2.5$, with initial population size $N_0 = 250$

Figure 6.1 : Shannon entropy as a function of time. The solid lines represent Monte Carlo results, and dashed black lines the ideal Shannon entropy computed for different population sizes.

pathological, in the sense that it is due to the concurrence of several simplifying assumptions (branchless collisions ; lack of leakage ; homogeneous system ; criticality). If only one of these simplifying assumption is broken, non-trivial correlations will fatally develop.

Entropy steps in non-critical systems

More interesting situations arise when considering systems away from criticality. Non-stationary behaviour will be achieved by adjusting the fission multiplicity at $t = 0$; the supercritical state is achieved by taking $\nu_p = 2.5$, and the subcritical state is achieved by taking $\nu_p = 1.75$. The time-evolution of the neutron entropy is plotted in Figs. 6.1 for subcritical and supercritical systems. The step-like time-evolution of these two observables can be explained by the interaction of the evolution of statistical weights with either Russian roulette or splitting. Let us first analyze the supercritical case, and assume that we start with an initial population size $N_0 = 250$. In this case, the branchless weight multiplier is larger than unity, and the particle weight is strictly increasing with time ; on average, neutrons from the source will reach the splitting threshold at the same time, and consequently increase the number of particles in the system. In Fig. 6.1b, the splitting threshold will be reached on average at

$$\tau_{\text{th}} = \frac{\ln w_S}{\ln f} \frac{1}{v\Sigma_t}, \tag{6.5}$$

where f is the branchless weight multiplier. For this one-speed supercritical system, we have $\tau_{\text{th}} \simeq 0.6944$ s, which roughly coincides with the time interval between successive entropy steps in Fig. 6.1b. The number of Monte Carlo particles doubles upon reaching w_S (we have set $w_S = 2$), and the entropy correspondingly jumps to a new value. If the effect of the spatial correlations induced by splitting is negligible, the new value of the entropy coincides with the ideal Shannon entropy given by Eq. (6.4) and computed for $N_{new} = 2N_0$, as illustrated in Fig. 6.1b for the small system with $L = 100$; otherwise, when correlations have a stronger effect on the spatial distribution of neutrons, the entropy will temporarily converge towards a value smaller than the ideal entropy, as illustrated in Fig. 6.1b for the large system with $L = 400$. The subsequent entropy steps can be predicted in the same way, and the entropy converges to the asymptotic value $S_\infty = \log_2(B)$: for large time, spatial correlations are always quenched by the increasingly large population size.

In general, there will be particles that will reach the splitting (or roulette) threshold earlier or later than at time τ_{th}. Therefore, as such occurrences accumulate over time, the amplitude of the entropy oscillations will be dampened over time as the occurrence of roulette and splitting become distributed

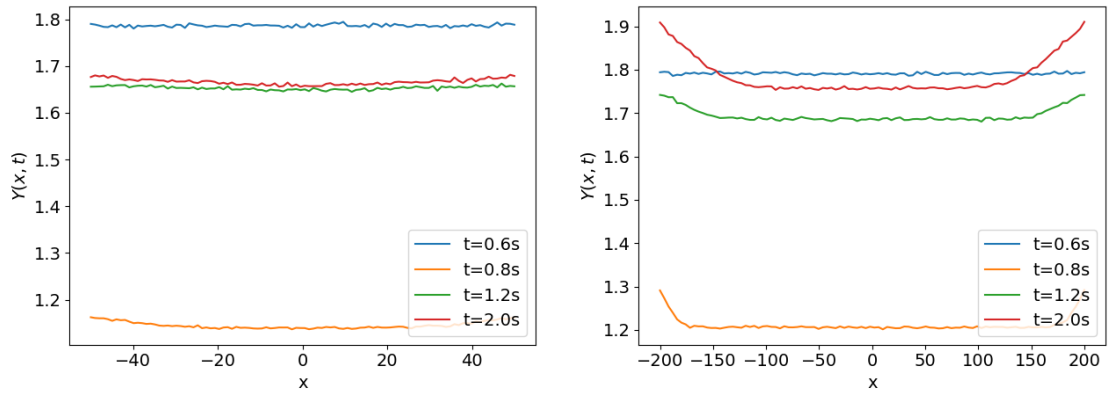

(a) For the system with $L = 100$ (b) For the system with $L = 400$

Figure 6.2 : Feynman moment for the neutron positions in the supercritical one-speed configuration, with initial population size $N_0 = 250$, at different times.

more uniformly over time : asymptotically, such oscillations disappear (not shown here for conciseness). In multi-group and even more strikingly in continuous-energy systems, the multiple values of the branchless weight modifier (which is energy-dependent) may prevent the observation of entropy oscillations.

Remark that in this system the statistics of family trees is trivial : neutrons cannot be destroyed, and the number of independent neutron trees is thus constant in time. This fact precisely illustrates that the analysis of the statistics of neutron genealogical trees may fail to catch the behaviour of spatial correlations. The neutron population in a non-analog Monte Carlo simulation may show spatial clustering even though fixation is forbidden, although it may be arguable that the system is approaching fixation because the number of families stays constant while the number of particles is increasing. However, we take this observation as a confirmation that the use of the statistics of family trees as a diagnostic tool for spatial correlations is questionable, as previously suggested by our analysis in Chapter 5.

A similar behaviour is detected in subcritical systems, as illustrated by Fig. 6.1a, this time driven by Russian roulette. The weight multiplier is now smaller than unity, and the statistical weight of neutrons is strictly decreasing. On average, neutrons reach the roulette threshold around the same time ; if the weight multiplier is sufficiently close to 1, on average $f_R = (w_{\text{surv}} - w_R)/w_{\text{surv}}$ neutrons are eliminated, while the rest is restored to unit weight. The new entropy then converges to the ideal value corresponding to a number of particles $N_{\text{new}} = f_R N_0$. In this case, the time step is again given by Eq. (6.5) with w_S replaced by w_R, leading to $\tau_{\text{th}} \simeq 0.4458$ s. The value of the entropy after each step is predicted by Eq. (6.4). Thus, in both subcritical and supercritical conditions, the Shannon entropy for this very simplified model is essentially driven by the total number of particles in the simulation, since all the particles have approximately the same weight (at least initially, for short times).

In the supercritical configuration, it is legitimate to ask whether the peculiar time-evolution of entropy leads to significant spatial correlations. The slight differences between the the entropy values for $L = 100$ and $L = 400$ in Fig. 6.1b faintly suggest so. To better characterize the effect of splitting on the spatial correlations, we rely on the Feynman moment of the neutron positions. The time evolution of the Feynman moment is plotted in Fig. 6.2. Figure 6.2a illustrates the absence of significant spatial correlations when $L = 100$. To be more precise, around $t = \tau_{\text{th}} \simeq 0.6944$ s, the average neutron weight approaches w_S for the first time, and the value of the Feynman moment simply encodes this fact. There are no spatial correlations between neutrons, which is indicated by the fact that the Feynman moment is flat. At $t = 0.8$ s, most neutrons just underwent splitting, and their average weight is close to one. Spatial correlations are introduced by splitting, leading to an increase of the Feynman moment near the reflective boundary conditions, which is reminiscent of the behaviour of the apparent-to-real variance ratio in the context of power iteration [34]. However, these correlations are washed away between each splitting event, and the Feynman moment before the next entropy step (at $t = 1.2$ s, which is close to $2\tau_{\text{th}} \simeq 1.4$ s) is

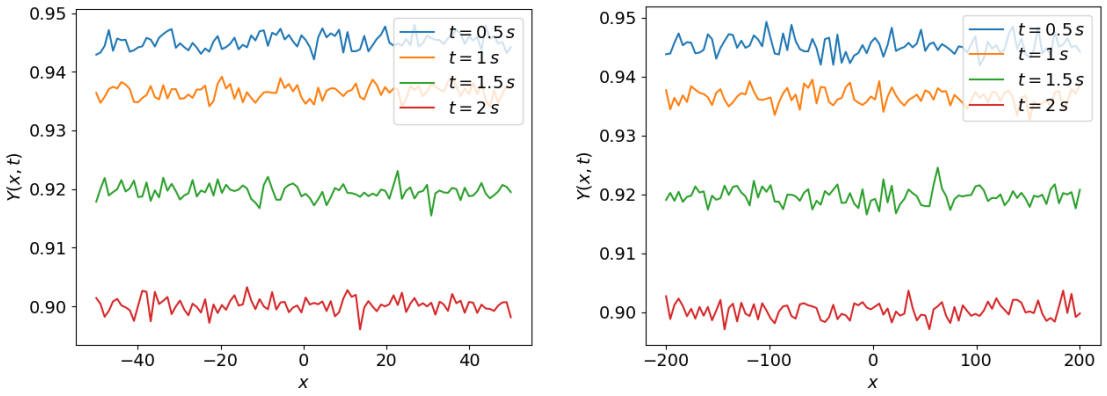

(a) For the system with $L = 100$

(b) For the system with $L = 400$

Figure 6.3 : Feynman moment for the neutron positions in the subcritical one-speed configuration, with initial population size $N_0 = 1000$, at different times.

flat.

On the contrary, it clearly appears that the system with $L = 400$ is strongly affected by spatial correlations. The convex shape arising from splitting events is amplified over time, and does not have time to relax between successive entropy steps. This behaviour can be further characterized by relying on previous insight gained on Brownian motion. The mixing time, as defined in Chapter 3 for a population of diffusing neutrons in a one-dimensional system with mass-preserving boundary conditions, is given by $\tau_{p,D} = 4L^2/\mathcal{D}\pi^2$. We can assume $\mathcal{D} = v/\Sigma_t$ to recast the diffusion-based parameters into a single-speed transport setting. For the system with $L = 100$, the mixing time is thus $\tau^{(1)}_{p,D} = 1.2178\,s$, while it is $\tau^{(2)}_{p,D} = 19.48\,s$ for the system with $L = 400$. By analogy with the analysis performed in Chapter 3 and 4, the ratio $\eta = \tau_{\text{th}}/\tau_{p,D}$ predicts the strength of spatial correlations in the system. When $\eta \gtrsim 1$, spatial correlations will be washed between each entropy step (like in the $L = 100$ case), and the effect of splitting will be negligible. Otherwise, when $\eta \ll 1$, spatial correlations will grow over successive entropy steps, and spatial clustering may occur (like in the $L = 400$ case).

In the subcritical system, the weight multiplier is smaller than one, and no splitting occurs. Spatial correlations cannot appear, and the Feynman moment will be flat, with a value driven by the average neutron weight which will decrease in time, as illustrated by Fig. 6.3. For long times, the value of the Feynman moment will saturate at w_R.

6.2.2 . The effect of combing on spatial correlations

Even in this simple system, the addition of weight combing has a drastic effect on the entropy, as illustrated in Fig. 6.4. It should be noted that our implementation of combing ensures that the number of Monte Carlo particles after combing is set to the integer closest to the total weight in the simulation, i.e. if the total weight of neutrons is $W = 10000$, then weight combing will comb the Monte Carlo particle population to $N = 10000$ neutrons of unit weight. Furthermore, neutron entropy and Feynman moments are computed just before combing is applied, i.e. they are affected by the weight fluctuations within a time step. The ideal entropy in Fig. 6.4 is computed for the total neutron weight at time t, rounded to the closest integer. Combing is applied on the same time grid as the one used to score time-dependent tallies, with $\delta t = 0.02\,s$.

In the supercritical configuration, the entropy steps disappear, but additional correlations occur in the simulation, as illustrated by the discrepancy between the neutron entropy and the ideal entropy for the corresponding (now strictly increasing) number of Monte Carlo particles. In the system with $L = 100$, the Monte Carlo entropy appears to converge towards the ideal entropy for large times, whereas the discrepancy between the Monte Carlo and ideal entropy remains for the system with $L = 400$; for longer times, we checked that the discrepancy disappears even in the large system, albeit slowly. For both

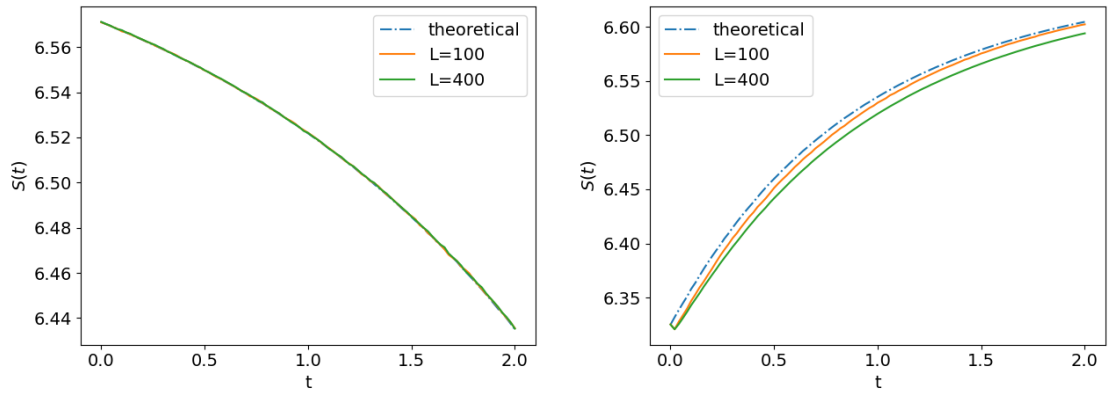

(a) Subcritical configuration with $k_{\text{eff}} = 0.875$ and initial population size $N_0 = 1000$.

(b) Supercritical configuration with $k_{\text{eff}} = 1.25$ and initial population size $N_0 = 250$

Figure 6.4 : Shannon entropy as a function of time when applying weight combing at each time step. The solid lines represent Monte Carlo results, and the pointed lines the ideal Shannon entropy computed for the total neutron population at a given time.

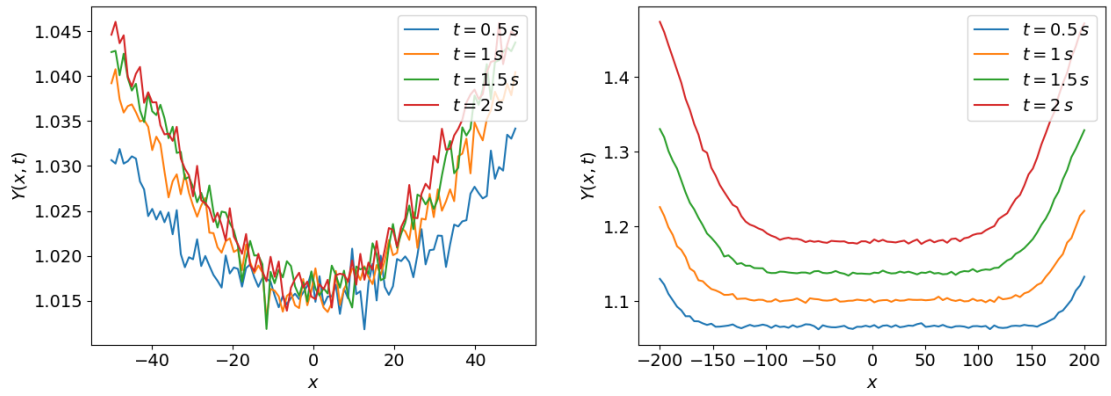

(a) For the system with $L = 100$

(b) For the system with $L = 400$

Figure 6.5 : Feynman moment for the neutron positions in the supercritical one-speed configuration, with initial population size $N_0 = 250$, at different times.

systems, there is a small entropy dip after the first time step, corresponding to the first application of combing on an otherwise uncorrelated neutron population.

The analysis of Feynman moments in Fig. 6.5 shows a spatial shape at all times for both small and large systems, indicating the existence of spatial correlations. For the small system, the value of the Feynman moment is close to unity everywhere, suggesting that the effect of spatial correlations is in fact negligible. For the large system, however, the value of the Feynman moments significantly differs from 1; at this point, it is unclear whether it only encodes the average weight of the neutron population (recall that the Feynman moment is sensitive to the weight increase within a time step) or if it is an indicator of spatial correlations. The average weight after a single time step δt for a neutron of unit initial weight is given by $w_{\delta t} = f^{\delta t \, v \Sigma_t}$, leading to $w_{\delta t} \simeq 1.02$. After combing, the average particle weight goes back to approximately 1. Therefore, the increase in weight during the time step is insufficient to explain the value of the Feynman moment in Fig. 6.5b, which suggests the occurrence of significant non-Poisson fluctuations in the spatial distribution.

In the subcritical configuration (not shown here for conciseness), combing also suppresses the entropy steps induced by Russian roulette and leads to a convex entropy function. However, contrary to the supercritical case, the Monte Carlo entropy coincides with the ideal entropy, suggesting that, in this case,

System	ν_p	k_{eff}	Leakage probability	τ_{th}[s]
$L = 100$ (sup)	3.2	1.25925 ± 8 pcm	0.21291 ± 5 pcm	0.2900
$L = 100$ (sub)	2.2	0.86576 ± 5 pcm	0.21294 ± 5 pcm	1.7341
$L = 100$ (crit)	2.54103	1.00007 ± 7 pcm	0.21286 ± 5 pcm	0.6418
$L = 400$ (sup)	2.5	1.22759 ± 13 pcm	0.01795 ± 5 pcm	0.6944
$L = 400$ (sub)	1.75	0.85932 ± 7 pcm	0.01797 ± 5 pcm	0.4458
$L = 400$ (crit)	2.03655	0.99993 ± 5 pcm	0.01802 ± 5 pcm	9.4834

Table 6.1 : Parameters for the one-speed problem with vacuum boundary conditions

combing does not introduce spatial correlations. This conclusion is further substantiated by remarking that the Feynman moments of the neutron positions (not plotted here for conciseness) are flat, with a value dictated by the average weight of the neutron population. This is coherent with the fact that, in our implementation of combing, the length of the comb tooth is always very close to 1 (i.e. it is the average weight after combing), whereas the weight of neutrons before combing is always smaller than one (due to $f < 1$), and a single neutron cannot be selected twice by the combing procedure.

6.2.3 . The effect of vacuum boundary conditions on spatial correlations

If vacuum boundary conditions are used, the equilibrium source is not spatially uniform anymore, and must be sampled via the procedure described in Sec. 2.4.1 based on power iteration. The advantage of using combing in the power iteration is minimal : it increases the computation time without a significant improvement in the quenching of spatial correlations ; therefore we simply use branchless collisions in the power iteration calculation. The size of the system now affects the multiplication factor k_{eff}, which complicates the comparison between systems of varying lengths : in order to ensure multiplication factors similar to the ones encountered in the previous example, the multiplication factor will be modified by adjusting the fission multiplicity. The new parameters and multiplication factors are given by Tab. 6.1. We also give the expected τ_{th} for each system. We checked that 100 inactive generations were enough to reach statistical equilibrium in the preliminary power iteration calculation for each of these systems.

Analysis of correlations in the supercritical case

We first focus on the supercritical case. The Feynman moments of the equilibrium source before and after combing are presented in Fig. 6.6. For both systems, the Feynman moment of the equilibrium source before combing is lower than one, which is directly related to the average weight of neutrons in the equilibrium source. In turn, this quantity is driven by the number of collisions in one generation of the power iteration, which is typically larger than the number of neutrons introduced in the power iteration (each neutron in the power iteration undergoes several collisions during one generation). After the equilibrium source has been sampled, it is re-normalized so that new statistical weight of each particle starting the kinetic simulation is given by

$$w' = \frac{N_0}{W} w, \tag{6.6}$$

where W is the total weight of the equilibrium source before normalization, and w is the individual weight of the particle before normalization. The total weight of the equilibrium source is thus set to N_0, which leads to an average weight significantly smaller than 1. The fact that the shape of the Feynman moment does not really change after combing suggests that here combing is not effective in quenching spatial correlations. Only the value of the Feynman moment is changed. Given that the average neutron weight after combing is very close to 1, the value of the Feynman moments in Fig. 6.6 indicates that the spatial distribution of neutrons in the equilibrium source deviates from a locally Poisson distribution. The spatial shape is close to the one of the Feynman moments of the fission source and collision counts in Chapter 5, with two maxima near the vacuum boundaries.

The time evolution of the entropy is given by Fig. 6.7. In the simulations without combing, the initial entropy jump stems from the fact that the average weight of neutrons in the equilibrium source

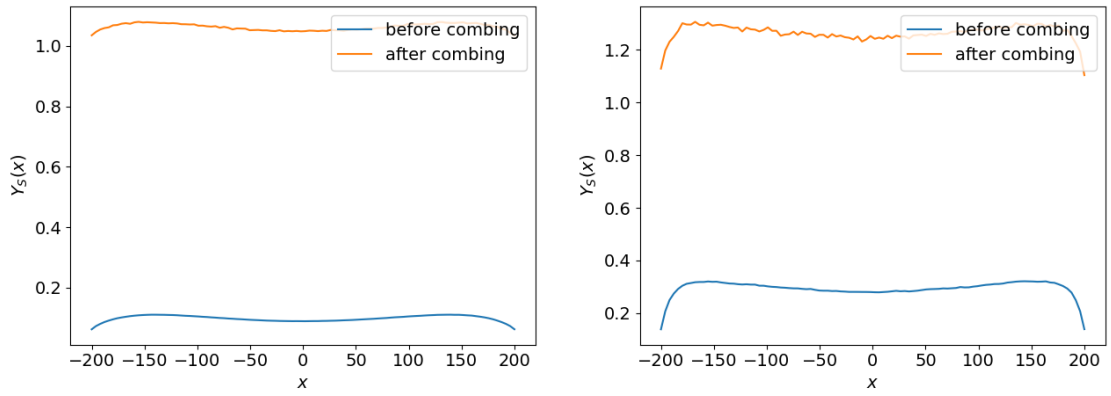

(a) For the system with $L = 100$ (b) For the system with $L = 400$

Figure 6.6 : Feynman moment for the equilibrium source in the supercritical one-speed configuration, with $L = 400$, with initial population size $N_0 = 250$, at different times.

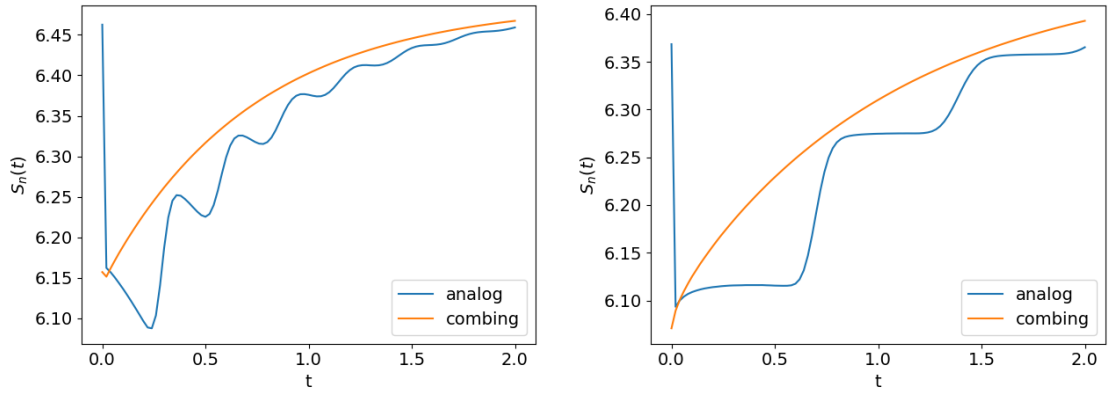

(a) Entropy for the small system with $N_0 = 250$ (b) Entropy for the large system with $N_0 = 250$

Figure 6.7 : Entropy of the neutron positions as a function of time. Blue line : without combing; orange line : with combing at each time step and on the equilibrium source.

is considerably smaller than the Russian roulette threshold, as remarked in the previous paragraph, and a significant number of Monte Carlo particles are immediately killed upon starting the time-dependent simulation ; the expected entropy of the neutron positions is consequently lower. For the small system, entropy oscillations occur. This is explained by the large leakage rate of this system (see Tab. 6.1) : leakage significantly reduces the number of neutrons in the system, thus reducing the expected entropy. After time $\tau_{\text{th}} \simeq 0.29\,s$, surviving neutrons reach the splitting threshold : the number of Monte Carlo particles increases, and so does the entropy. Since the system is supercritical, the average number of Monte Carlo particles created by splitting over a time step is larger than the average number of particles lost by leakage, and the entropy will globally increase. As time goes on, the amplitude of oscillations decreases. For the large system, the rate of leakage is small enough that it does not significantly alter the entropy, and the system behaves similarly as the case with reflective boundary conditions ; however, it is no longer possible to use Eq. (6.4) to interpret the values of the entropy at the intermediate steps, since the number of surviving particles is not known. Applying combing to the system effectively suppresses the initial jump, the entropy steps, and the entropy oscillations : the number of Monte Carlo particles closely follows the total neutron weight, and so does the entropy.

Figure 6.8 shows the Feynman moment of the neutron positions for the small supercritical system. The spatial shape of the Feynman moment without combing (see Fig. 6.8a) inherited from the shape

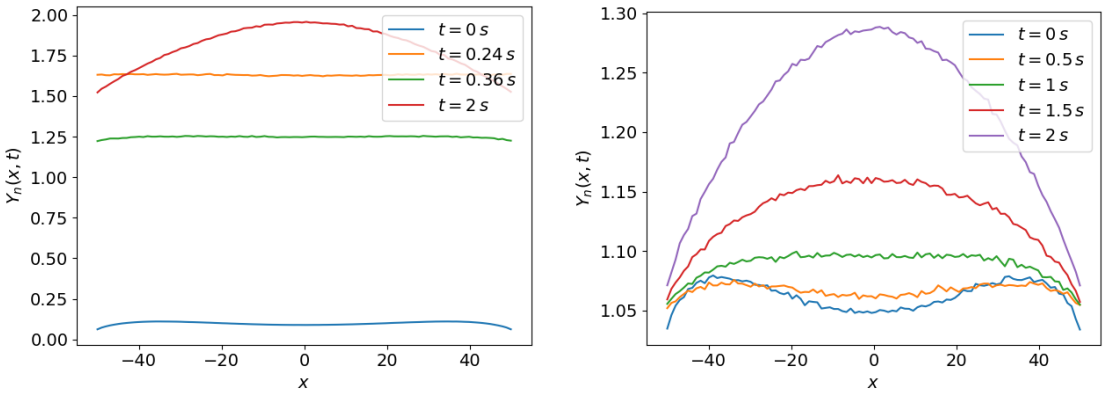

(a) Feynman moments of the neutron positions when not applying combing.

(b) Feynman moments of the neutron positions when applying combing.

Figure 6.8 : Feynman moment of the neutron positions in the supercritical small system with leakage, for different times.

of the Feynman moment for the equilibrium source is quickly forgotten, as illustrated by the curve for $t = 0.24$ s, which corresponds approximately to the time of the first entropy oscillation. The spatial Feynman moment is flat, indicating the absence of strong spatial correlations. At $t = 0.36$ s, the first oscillation has just finished, and the Feynman moment now takes a non-uniform spatial shape, indicating that spatial correlations were introduced by splitting. The final time illustrates how spatial correlations grow over successive entropy oscillations. For longer times, the Feynman moment of the neutron positions then takes a single maximum at the centre of the system. The value of the Feynman moment is related to the oscillations of the average neutron weight (and thus to the extrema of the entropy), and also increases with time due to the build-up of spatial correlations. When combing is applied (see Fig. 6.8b) the spatial shape inherited from the power iteration calculation of the equilibrium source survives longer, for the small system, although for larger times the spatial shape of the Feynman moment has again a single maximum at the centre of the system. The expected weight after a time step here is still $w_{\delta t} \simeq 1.02$, as in Sec. 6.2.2, which is smaller than the value of the Feynman moment and thus indicates slightly non-Poisson fluctuations in the spatial distribution of neutrons. In addition, the analysis of the Feynman moments clearly illustrates that the spatial correlations of the fission source in power iteration (see e.g. Fig. 5.8a) are qualitatively different from the spatial correlations arising from the time-dependent simulations.

Figure 6.9 presents the Feynman moments for the large system with $L = 400$. The analysis of this figure raises some questions. First, it appears that the spatial shape of Feynman moment of the equilibrium source deeply influences the shape of the Feynman moment of the neutron positions. Contrary to the previous paragraph, the Feynman moment takes two maxima near the boundaries of the system, for all times. This behaviour occurs both in the case with combing and the case without combing. Note that the time evolution of entropy, especially when applying combing, is insufficient to discriminate between the case of the small system, whose spatial correlations have a peak at the centre, and the large system, whose spatial correlations have a peak near the boundaries. Finally, the value of the Feynman moment again overshoots the value of the average neutron weight, indicating non-Poisson fluctuations of the spatial distribution.

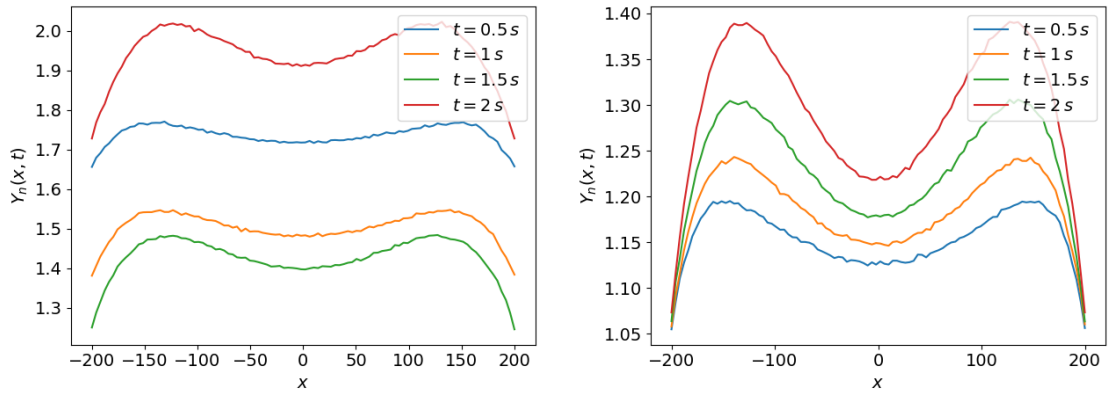

(a) Feynman moments of the neutron positions when not applying combing

(b) Feynman moments of the neutron positions when applying combing

Figure 6.9 : Feynman moment of the neutron positions in the supercritical large system with leakage, for different times

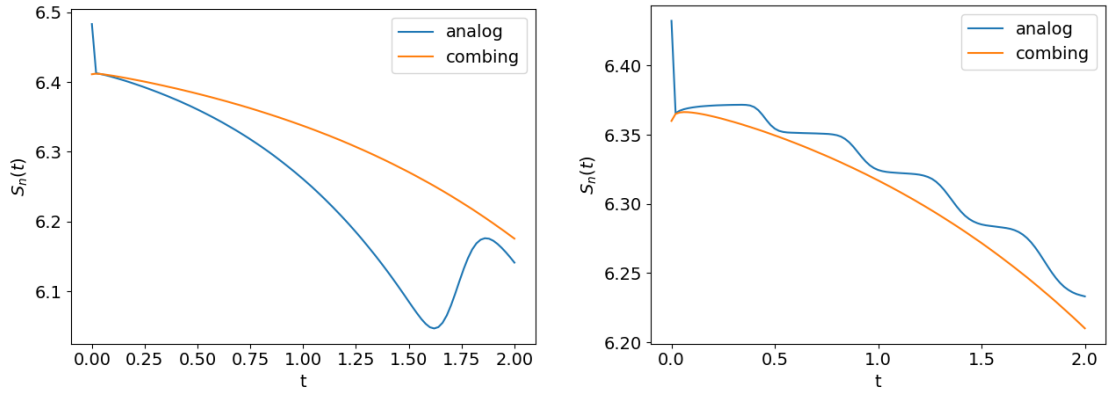

(a) Entropy for the small system.

(b) Entropy for the large system.

Figure 6.10 : Entropy of the neutron positions as a function of time in the subcritical configurations with leakage boundary conditions. $N_0 = 1000$. Blue line : without combing; orange line : with combing at each time step and on the equilibrium source.

Analysis of correlations in the subcritical case

The time evolution of the entropy for the subcritical case is given by Fig. 6.10. We observe again entropy oscillations, which evolve as described in the supercritical case, with different τ_{th} due to the different physical parameters. The system is however subcritical : the number of Monte Carlo particles killed by Russian roulette or leakage exceeds the number of Monte Carlo particles created by splitting ; the total number of Monte Carlo particles will on average decrease with time, and so will entropy. Applying combing again removes the initial entropy jump and the oscillations. Analysis of the Feynman moments for these subcritical systems (not shown here for conciseness) leads to the following conclusions : for the small system, we have $f > 1$, thus the behaviour of the Feynman moment follows closely the one of the supercritical configuration investigated before ; for the large system, $f < 1$ and leakage is small, so that the behaviour of the Feynman moment is close to the one in Fig. 6.3 ; however, the spatial shape inherited from the equilibrium source survives for a time of the order of the mixing time $\tau_{p,D}$.

Analysis of correlations in the critical case

To conclude, the critical case formally corresponds to a situation with $f > 1$ and the increase of neutron weight exactly compensates the loss by leakage. Figure 6.11 shows the neutron entropy in the small and large systems. For the large system, given that $\tau_{\text{th}} \simeq 9.4834$s, we had to extend the time

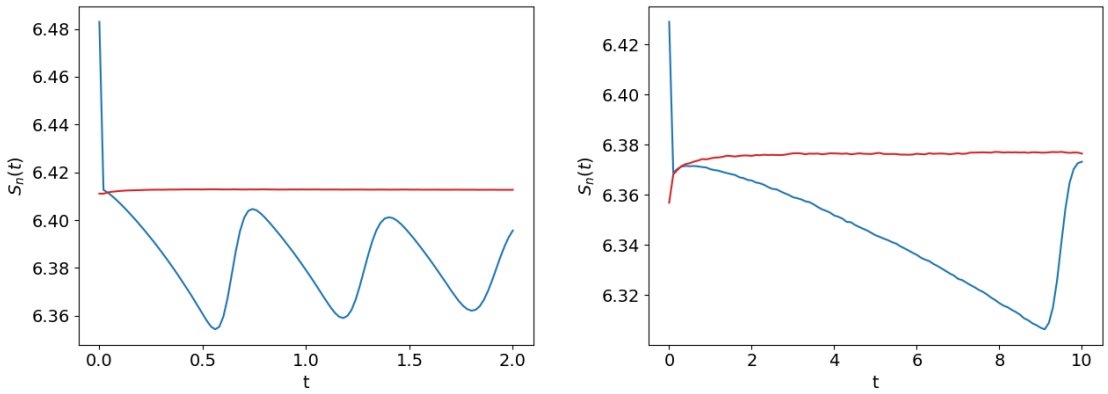

(a) Entropy for the small system.

(b) Entropy for the large system.

Figure 6.11 : Entropy of the neutron positions as a function of time in the critical configurations with leakage boundary conditions. $N_0 = 1000$. Blue line : without combing; orange line : with combing at each time step and on the equilibrium source.

boundary to $T = 10$ s (and $\delta t = 0.1$ s) in order to observe at least one oscillation. In the absence of combing, we observe the usual jump at short times, as in the supercritical and subcritical cases; we also observe the oscillations, which suggests that the critical regime is not 'special'. We verified that, for (very) long times, the entropy oscillations are dampened, and the entropy converges towards an asymptotic value. When applying combing, the only difference with respect to the non-stationary states is that the entropy converges more rapidly towards an asymptotic value. We also verified that the behaviour of the Feynman moments is qualitatively similar to the one of the supercritical system (not shown here for conciseness).

6.2.4 . The effect of precursors on spatial correlations

We illustrate now the effect of adding precursors to the neutron model of the previous section on spatial correlations, using either analog or forced decay, which are described in Sec. 2.4.2. For this purpose, we introduce a delayed-neutron precursor family in the system with leakage, assuming that we apply combing at each time step. Let the single precursor family be characterized by a delayed fraction $\beta = 0.1$ and a decay constant $\lambda = 0.01$ s^{-1}. The parameters of the precursor family are not realistic, but they are chosen to speed up the simulation times, yet retaining a sufficient separation between the time scales of neutrons and precursors. The introduction of the combined precursor (which requires several precursor families) is left for Sec. 6.3.

When using forced decay, the weight of the delayed neutrons produced in each time step is proportional to the time step size; a small time step allows investigating the fast dynamics of prompt neutrons, but leads to a large number of neutrons of small weight. In contrast, a larger time step makes it harder to follow the time evolution of the prompt neutron population. Note that this last remark could be mitigated using the relative importance introduced by Faucher et al., and increasing the importance of neutrons compared to precursors [62]. If a neutron is produced through forced decay with a statistical weight $w < w_R$, it is immediately tested for Russian roulette (i.e. we do not wait for the first collision).

We will investigate supercritical, subcritical and critical configurations. We take the final time to be $T = 200$ s, which is of the order of $1/\lambda$; with such a long final time, the simulations of the prompt-supercritical systems of Tab. 6.1 would be prohibitively costly. Therefore, we use instead the fission yields given in Tab. 6.2, which yield prompt-subcritical systems.

Analysis of correlations in the equilibrium source

The sampling of the equilibrium source is independent of the choice of the decay algorithm in the time-dependent simulation. The Feynman moments of the equilibrium source, before and after combing, are presented in Fig. 6.12 for the supercritical configurations. We notice that the Feynman moment of

System	ν	k_{eff}	Leakage probability
$L = 100$ (sup)	2.6	1.02310 ± 6 pcm	0.21302 ± 5 pcm
$L = 100$ (sub)	2.4	0.94446 ± 5 pcm	0.21292 ± 5 pcm
$L = 100$ (crit)	2.54103	1.00007 ± 7 pcm	0.21286 ± 5 pcm
$L = 400$ (sup)	2.1	1.03111 ± 2 pcm	0.01800 ± 2 pcm
$L = 400$ (sub)	1.9	0.93295 ± 2 pcm	0.01796 ± 2 pcm
$L = 400$ (crit)	2.03655	0.99993 ± 5 pcm	0.01802 ± 5 pcm

Table 6.2 : Fission yields for the configurations with delayed neutrons, and corresponding multiplication factors and leakage probability.

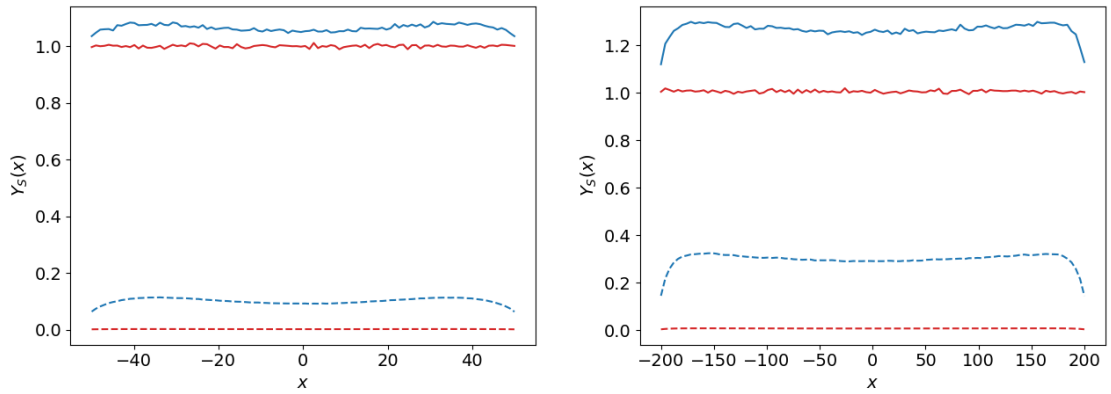

(a) For the small system.

(b) For the large system

Figure 6.12 : Feynman moment of the equilibrium source in the supercritical case, for $N_0 = 1000$. Dotted lines gives the Feynman moments before combing, and the solid lines gives the Feynman moments after combing. Red is for neutrons, and blue is for precursors.

neutrons is very small before combing, and flat with unit value after combing. Due to the ratio between neutrons and precursors, the total weight for precursor is much larger than for neutrons ; when normalizing the equilibrium source obtained at the end of the power iteration (as described in Sec. 2.4.1), neutrons are therefore assigned much smaller weights than precursors, leading to small values of the Feynman moment. This explains our first comment. Moreover, the number of neutrons in the equilibrium source is much larger than the number of neutrons targeted by combing. This means that the spatial correlations induced by power iteration are carried only by the precursor population, and will typically take a time of the order of $t \sim 1/\lambda$ to relax, as it will be illustrated in the following paragraphs. This explains our second comment. Note that this behaviour should qualitatively carry over to Monte Carlo simulations with realistic parameters. In addition, the comments on the equilibrium source apply straightforwardly to the subcritical and critical systems.

It may seem wasteful to sample a large number of neutrons for the equilibrium source and throw away most of them in the combing phase. Actually, it is possible to control the number of particles in the equilibrium source before combing by defining a probability p_{acc} to accept a collision as a valid sampling event of the equilibrium source. Upon a collision, particles for the equilibrium source are sampled the usual way with probability p_{acc}, or the collision is ignored with complementary probability. To keep the sampling of the equilibrium source unbiased, the statistical weight w of any particle sampled following this procedure is divided by p_{acc}. The benefit of this algorithm is that it gives control of the memory footprint of the equilibrium source, and prevents sampling particles only to discard them immediately afterwards. On the other hand, this procedure may have two negative effects. First, $p_{\text{acc}} \ll 1$ may lead to very large weights. Second, if p_{acc} is such that the number of particles in the equilibrium source before combing is smaller than the number of particles targeted by combing, then the combing procedure

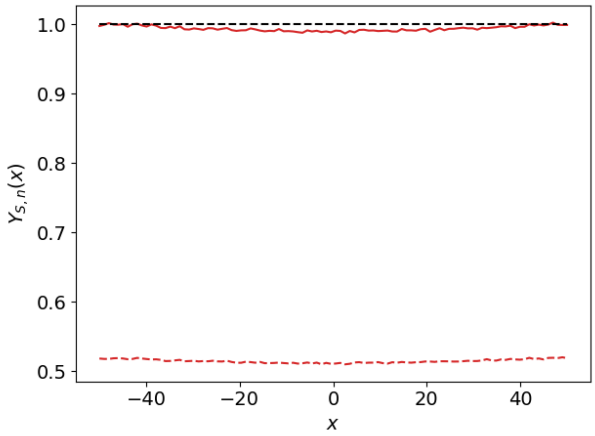

Figure 6.13 : Example of the Feynman moment of the neutron source when $p_{\text{acc}} = 10^{-}3$. Dashed red line for $Y_{S,n}$ before combing, solid red line for $Y_{S,n}$ after combing. The dashed black line simply illustrates the deviation from the flat spatial shape.

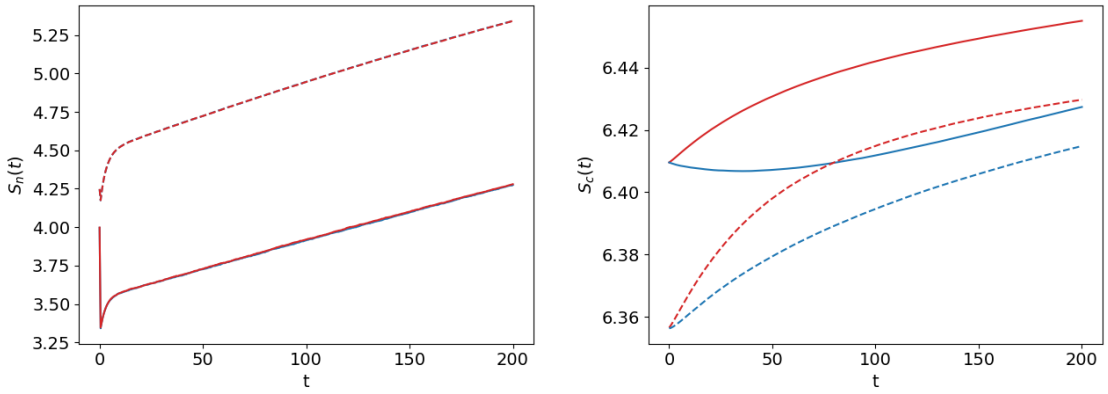

(a) Neutron entropy.

(b) Precursor entropy

Figure 6.14 : Time evolution of the entropy for neutrons and precursors in the supercritical systems, with $N_0 = 10^3$. Dashed lines : large system; solid lines : small system; blue for analog decay and red for forced decay.

may introduce additional spatial correlations. This is illustrated in particular for the neutron population in Fig. 6.13 for $p_{\text{acc}} = 10^{-3}$. Note that in our context (i.e. the dynamics of neutrons is much faster than the dynamics of precursors), spatial correlations within the neutron population stemming from the sampling of the equilibrium source quickly disappear during the time-dependent process, as illustrated in the following section.

Analysis of correlations in the supercritical case

The time evolution of the entropy of the neutron and precursor populations in the supercritical case is plotted in Fig. 6.14. The neutron entropy (in Fig. 6.14a) is unaffected by the decay strategy (forced or analog). The initial jump in the neutron entropy translates the fact that the neutron population is initially Poisson distributed (as mentioned in the previous paragraph), but some correlations quickly grow in the initial neutron fission chains. The linear behaviour occurring after the first few seconds corresponds to the exponential increase of the neutron population, due to the system being supercritical. This interpretation is supported by the analysis of the Feynman moments for neutrons in Fig. 6.15a and 6.15b : after a few seconds, the Feynman moment of neutrons saturates at an average value larger than one. To decide whether this is an indicator of spatial clustering, we need to assess the expected weight of a neutron. Within a time step, a neutron can increase its weight only through collisions; if it is transformed in a

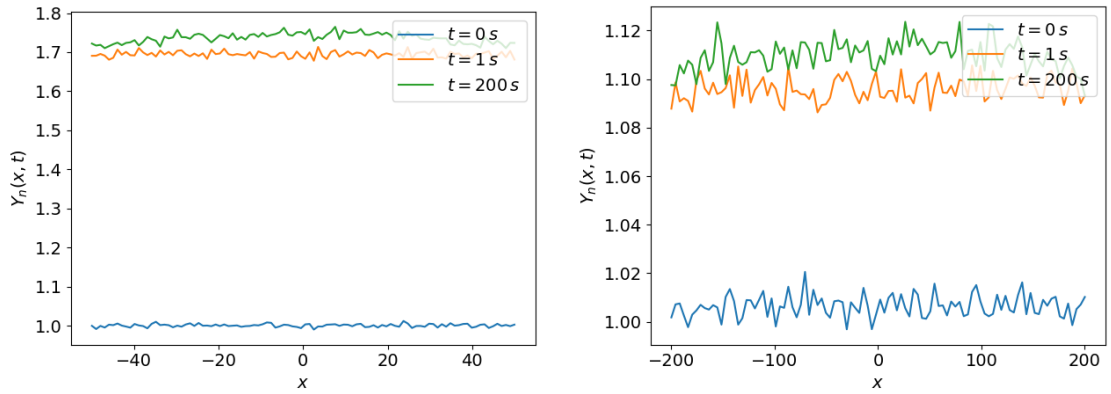

(a) Feynman moment of the neutron population for the small system.

(b) Feynman moments of the neutron population for the large system

Figure 6.15 : Feynman moment of the neutron population in the supercritical case for $N_0 = 1000$, for different times. We use forced decay.

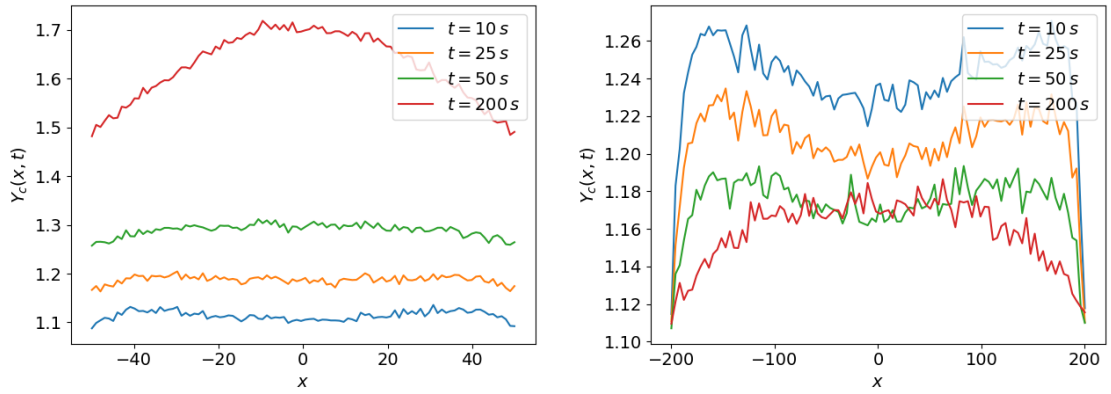

(a) For the small system.

(b) For the large system

Figure 6.16 : Feynman moment of the precursor population in the supercritical case for $N_0 = 1000$, for different times. We use analog decay.

precursor, its statistical weight can only decrease (in the case of forced decay) or be constant (in the case of analog decay). Thus, assuming that a neutron started with unit weight (i.e., from combing at the end of the previous time step), the maximum expected weight for a neutron at the end of the time step is again given by $w_{\delta t} = f^{\delta t v \Sigma_t}$; this leads to $w_{\delta t} = 1.82$ in the small system, and $w_{\delta t} = 1.11$ in the large system. The value observed in Figs. 6.15a and 6.15b are relatively close to the expected neutron weight at the end of a time step, and we can conclude the spatial fluctuations of the neutron population are close to being Poisson distributed. The Feynman moments for the neutron population behave similarly when using either forced or analog decay ; therefore, we only show the Feynman moments with forced decay. Note that, for long times, the spatial shape of the Feynman moment for neutrons becomes slightly convex.

Figure 6.14b for the small system indicates a qualitatively different behaviour for the precursor entropy when using forced or analog decay. In the analog case, entropy first decreases, suggesting that spatial correlations originating from the equilibrium source first favour spatial clustering in the time-dependent process. However, when approaching $t = 1/\lambda$, most of the initial precursor population has decayed, and the spatial correlations in the precursor population start to be driven by the time-dependent process. The ensuing linear growth corresponds to the exponential increase of the precursor population. This is illustrated by Fig. 6.16a representing the Feynman moment for the precursor population when using

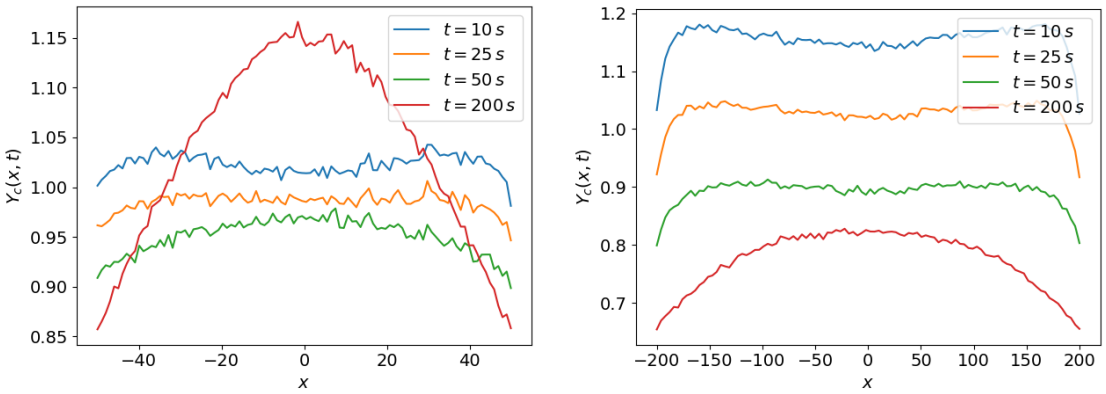

(a) For the small system.

(b) For the large system

Figure 6.17 : Feynman moment of the precursor population in the supercritical case for $N_0 = 1000$, for different times. We use forced decay.

analog decay : around $t = 50\,s$, the Feynman moment forgets the spatial shape inherited from the equilibrium source. On the other hand, it is less clear why we do not observe such behaviour when using forced decay ; we conjecture that it is due to the entropy being related to the number of Monte Carlo particles. With forced decay, the number of precursor particles is increasing within a time step. Since we compute entropy before combing is applied, a higher number of precursors induces a higher entropy. While the time needed for the precursor population to forget the correlations of the equilibrium source is similar using forced decay or analog decay (as illustrated in Fig. 6.17a), the behaviour of the entropy is mainly driven by the number of Monte Carlo particles. It is interesting to note that the value of the Feynman moment appears to decrease with time when using forced decay. The decrease of the average precursor weight within a time step is given by $w_{\delta t} \sim e^{-\lambda \delta t} \simeq 0.995$ for this system. This value does not explain the ones observed in Fig. 6.17a, and we have not explanation of why the Feynman moment of the precursor population decreases with time.

On the other hand, Fig 6.14b indicates that, in the large system, the precursor entropy behaves similarly for forced and analog decay. The entropy when using forced decay is larger, due to the fact that precursor particles are not destroyed upon decay. However, the analysis of the Feynman moment of the precursor population in the large system indicates a significant difference between using forced or analog decay. Figure 6.16b shows that the value of the Feynman moment for analog decay is close to the expected precursor weight at the end of the time step, indicating that spatial fluctuations are almost Poisson distributed. However, Fig. 6.17b shows that the value of the Feynman moment steadily decreases with time, until it cannot be related to the average precursor weight anymore ; this suggests that spatial fluctuations in the precursor population are quenched over time. We did not find a plausible argument to explain this behaviour.

Analysis of correlations in the subcritical case

The time-evolution of the entropy in the subcritical case is presented in Fig. 6.18. For the neutron entropy, the comments in the supercritical cases hold true. The behaviour of the precursor entropy, however, differs significantly. When using analog decay, the precursor entropy decreases with time, which encodes the fact that the neutron population is decreasing over time. However, when using forced decay, the entropy first increases until around $t \sim 1/\lambda$, before it starts decreasing, which is reminiscent of Fig. 6.14b ; the reason is, again, that $1/\lambda$ is the typical time it takes for precursors stemming from the equilibrium source to decay, and thus it is also the typical time it takes for precursors to forget the correlations of the initial distribution.

Again, the Feynman moments of the neutron population are independent of the use of forced or analog decay ; therefore, we only show those with forced decay. In the small system (see Fig. 6.19a), the

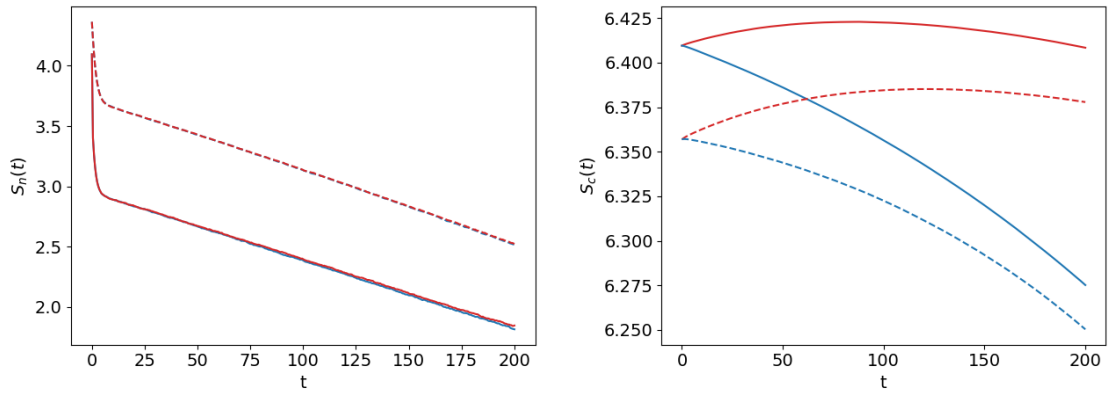

(a) Neutron entropy. (b) Precursor entropy

Figure 6.18 : Time evolution of the entropy for neutrons and precursors in the subcritical systems, with $N_0 = 10^3$. Dashed lines : large system; solid lines : small system; blue for analog decay and red for forced decay.

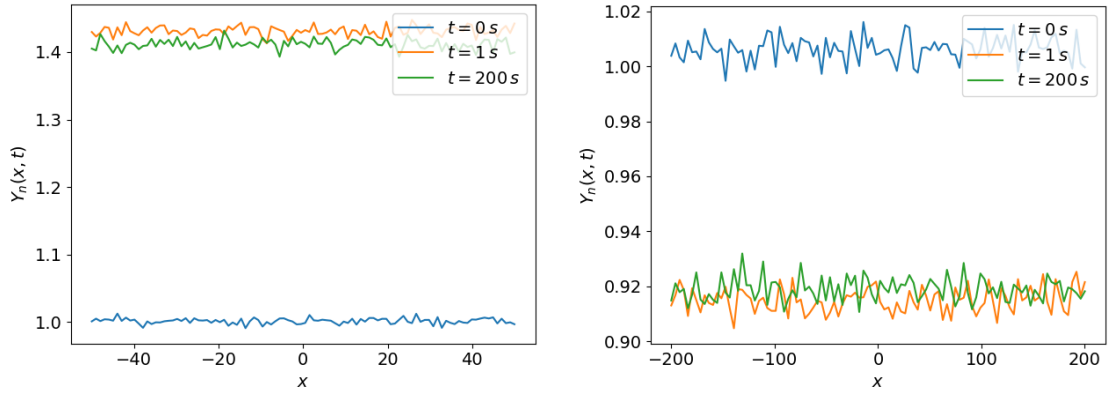

(a) Case of the small system. (b) Case of the large system

Figure 6.19 : Feynman moment of the neutron population in the subcritical case for $N_0 = 1000$, for different times. We use forced decay.

behaviour is qualitatively the same as for the supercritical case, because the weight multiplier $f > 1$: the value of the Feynman moment increases until it saturates around $w_{\delta t} \simeq 1.49$, i.e. the expected weight of a neutron of unit initial weight at the end of a time step. On the other hand, in the large system (see Fig. 6.19b), we have $f < 1$ and the Feynman moment for neutrons is flat. The value of the Feynman moment will decrease until it saturates at around $w_{\delta t} = 0.90$.

The analysis of the Feynman moment of the precursor population is illustrated by Fig. 6.20 and Fig. 6.21. When using forced decay, the Feynman moment of the precursor population decreases with time in both systems, to a value that is much smaller than the expected precursor weight at the end of a time step (which, assuming unit initial weight, is $w_{\delta t} = 0.995$). This is to be related to Fig. 6.17, and is similarly unexplained. When using analog decay, the Feynman moment becomes flat.

Analysis of correlations in the critical case

Finally, the time evolution of the entropy in the critical system is shown in Fig. 6.22. Again, the neutron entropy has an initial jump, corresponding to the equilibrium source after combing being Poisson distributed (as illustrated in Sec. 6.2.4), while the neutron distribution during the time-dependent process is not. Once the jump ends, the entropy is constant for forced decay, and slightly decreasing for the analog decay, suggesting that the latter has a weak tendency to spatial clustering. This can be explained by the fact that forced decay leads to the production of more neutrons, which makes the neutron distribution

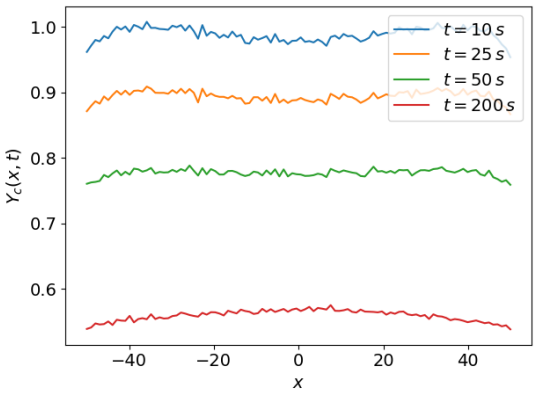

(a) Case of the small system.

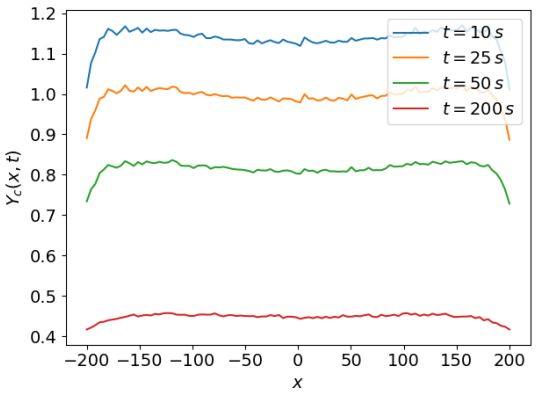

(b) Case of the large system

Figure 6.20 : Feynman moment of the precursor population in the subcritical case for $N_0 = 1000$, for different times. We use forced decay.

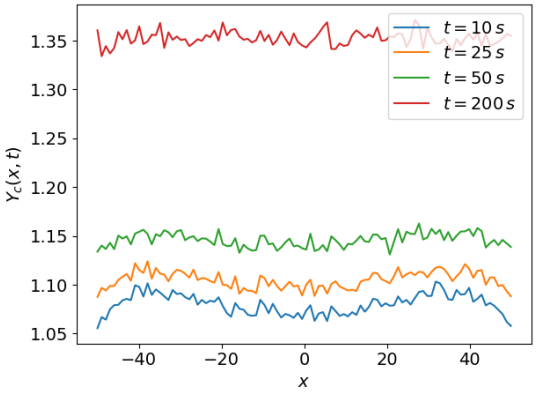

(a) Case of the small system.

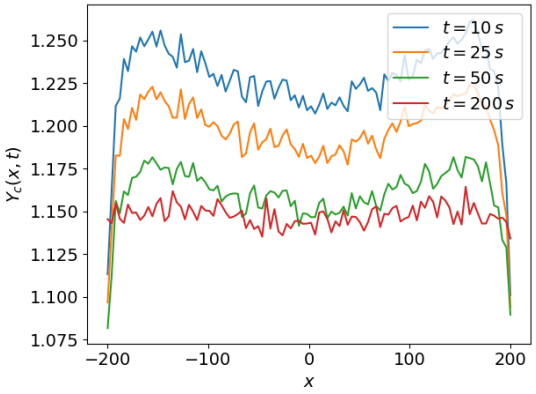

(b) Case of the large system

Figure 6.21 : Feynman moment of the precursor population in the subcritical case for $N_0 = 1000$, for different times. We use analog decay.

slightly less sensitive to statistical fluctuations, and thus to clustering. On the other hand, Fig. 6.22b resembles Fig. 6.14b for the supercritical case, where the linear increase for long times (which corresponds to the exponential population growth) is replaced by an asymptotic convergence to a constant value (which corresponds to the constant population).

The Feynman moments of the neutron population lead to the same conclusions as in the supercritical case (see Fig. 6.15), and are not shown here for conciseness. The Feynman moment of the neutron population is increasing with time and saturates at a value around $w_{\delta t} \simeq 1.72$ for the small system, and $w_{\delta t} \simeq 1.04$ for the large system. The Feynman moment of the precursor population is given in Figs. 6.23 and 6.24, and qualitatively resembles that of the supercritical population in Figs. 6.16 and 6.17.

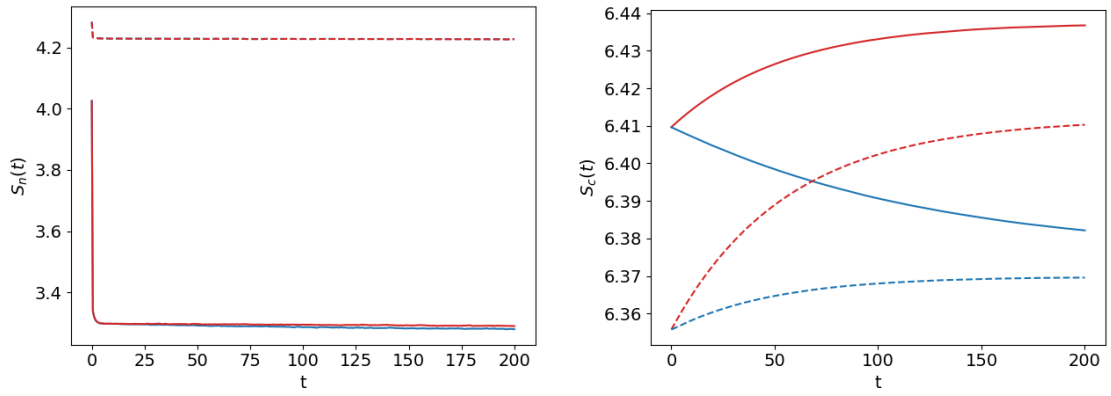

(a) Neutron entropy.

(b) Precursor entropy

Figure 6.22 : Time evolution of the entropy for neutrons and precursors in the critical systems, with $N_0 = 10^3$. Dashed lines : large system ; solid lines : small system ; blue for analog decay and red for forced decay.

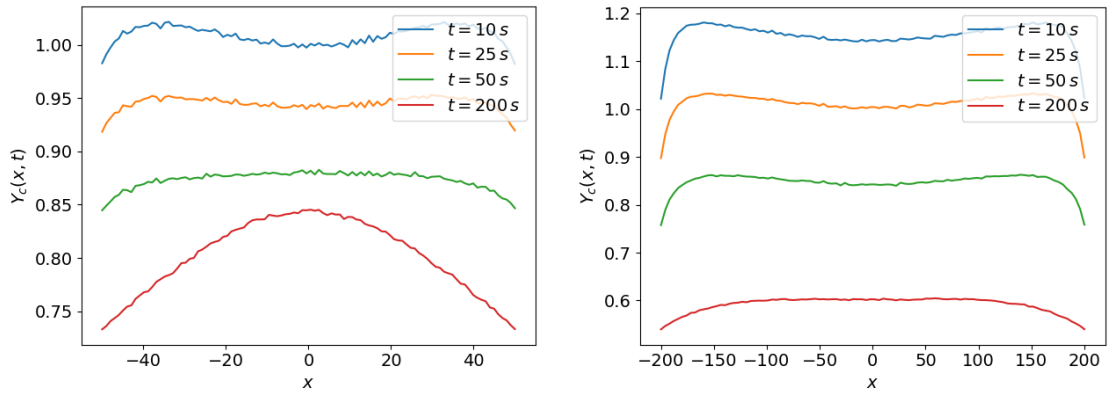

(a) Case of the small system.

(b) Case of the large system

Figure 6.23 : Feynman moment of the precursor population in the critical case for $N_0 = 1000$, for different times. We use forced decay.

6.3 . Analysis of space-time correlations in multi-group systems

Relying on the insights regarding the effect of non-analog methods and precursors on the space-time correlations of the time-dependent simulations obtained for the simple system in Sec. 6.2, we shall now revisit the slab benchmarks introduced in Chapter 5. Due to the large number of possible permutations of variance-reduction techniques, simulation parameters and benchmark configurations, and in view of the fact that each simulation involves an extremely high computational cost, we decided to restrict our analysis to homogeneous media, with a single set of variance-reduction techniques and space-time discretization.

The equilibrium source for the systems presented in Sec. 6.3.1 needs to be computed using a preliminary power iteration calculation, and we choose to use branchless collisions without combing, as detailed in Chapter 5. In addition, in order to limit the memory occupation, we use the alternative sampling procedure presented in Sec. 6.2.4, with an acceptance probability $p_{\text{acc}} = 10^{-3}$. The time-dependent calculations adopt branchless collisions for neutrons ; a single comb is applied on the total population at each time step, and on the equilibrium source. For precursors, we use the combined precursor particle (presented in Sec. 2.4.2), and we apply forced decay. If a neutron is produced through forced decay with a statistical weight $w < w_R$, it is immediately tested for Russian roulette (i.e. we do not wait for the first

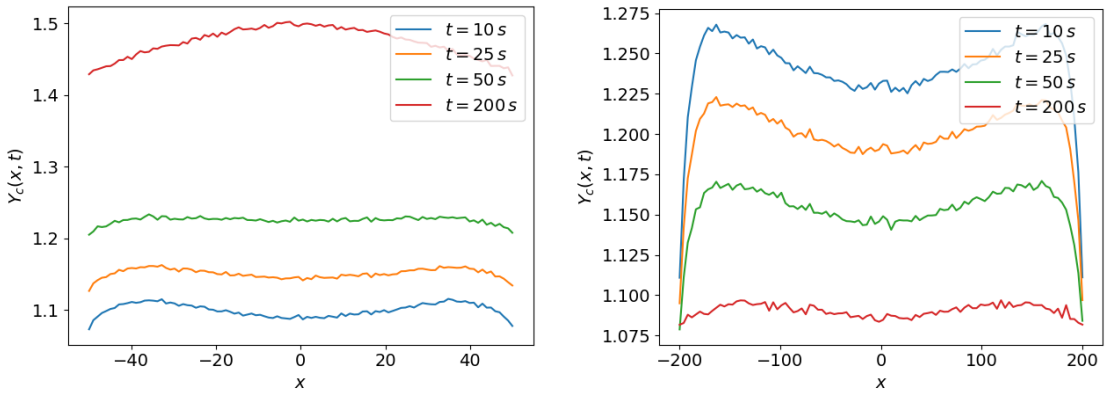

(a) Case of the small system.

(b) Case of the large system

Figure 6.24 : Feynman moment of the precursor population in the critical case for $N_0 = 1000$, for different times. We use analog decay.

parameters	family 1	family 2	family 3	family 4	family 5	family 6
$\beta_j[pcm]$	2.275×10^2	1.17455×10^2	1.12138×10^2	2.51407×10^2	1.03077×10^2	4.3173×10^1
$\lambda[s^{-1}]$	1.3336×10^{-2}	3.2739×10^{-2}	1.2078×10^{-1}	3.0278×10^{-1}	8.4949×10^{-1}	2.8530
$\xi_d(1)[-]$	0.52296	0.56487	0.54697	0.61504	0.59265	0.60533
$\xi_d(2)[-]$	0.47704	0.43513	0.45303	0.38496	0.40735	0.39467

Table 6.3 : Nuclear data for the precursors in the homogeneous material.

collision). Neutron flights are sampled in an analog fashion. After a collision, neutrons undergo either Russian roulette with threshold $w_R = 0.8$ and survival weight $w_{\text{surv}} = 1$, or splitting with threshold $w_S = 2$.

The reactor is assumed to be critical at the initial state $(t = 0)$; for the time-dependent simulations, we will consider the case where the reactor stays critical, and the case where a certain amount of reactivity is introduced at $t = 0$: this latter configuration is achieved by modifying the capture cross sections. The behaviour of space-time correlations in the critical and non-critical regimes will be investigated by using the Shannon entropy and the Feynman moments for the neutron and precursor populations as defined in Sec. 6.1. We refer the reader to Chapter 5 for a thorough description of these observables.

6.3.1 . Simulation parameters for the homogeneous benchmark

We briefly recall the features of the homogeneous benchmark introduced in Chapter 5. We consider two system sizes, $L = 50$ (system 1) and $L = 100$ (system 2) of a homogeneous slab geometry with leakage boundary conditions. The nuclear data are represented in a three-group formalism for neutrons, as recalled in Tabs. 5.2 and 5.5. The nuclear data for the reactivity insertions and withdrawals is given in Tabs. 6.4 and 6.5. The reactivity insertions $\delta\rho = 1/k_{\text{eff}} - 1/k_{t\geq 0}$ are provided in Tab. 6.6, where k_{eff} is the multiplication factor in the critical cases[1]. Note that our choice of reactivity insertion does not make the system prompt-supercritical. Since we now explicitly consider precursors, the fission spectrum given in Tab. 5.2 needs to be adjusted, and is given in Tab. 6.4. The six-family nuclear data for precursors are taken from Vitali et al. [1] (inspired by those of ^{235}U), and are provided in Tab. 6.2. Space is partitioned into intervals of equal length $\delta x = 0.5\,\text{cm}$, and we chose a time step $\delta t = 1\,\text{ms}$. Note that the slowest precursor decay typical time is $1/\lambda_1 \sim 100$ s : transients on the space-time correlations within the precursor population might thus last well beyond $100\,\text{s}$; due to the involved computational burden, for our simulations will nonetheless set a final time $T = 10\,\text{s}$.

[1]The multiplication factor k_{eff} of the critical cases is as close as possible to 1, within 1σ uncertainties.

Parameters	$g = 1$ (fast)	$g = 2$ (epithermal)	$g = 3$ (thermal)
$\xi_p(g)[-]$	0.878198	0.121802	0
$\Sigma_{c,g}$ (super)	9.300000×10^{-4}	1.490355×10^{-2}	6.906277×10^{-2}
$\Sigma_{c,g}$ (sub)	9.460000×10^{-4}	1.510355×10^{-2}	6.919277×10^{-2}

Table 6.4 : Capture cross sections for the reactivity insertions in system 1, along with the new prompt fission spectrum. The energy groups are indexed by g.

Parameters	$g = 1$ (fast)	$g = 2$ (epithermal)	$g = 3$ (thermal)
$\Sigma_{c,g}$ (super)	9.302099×10^{-4}	1.493439×10^{-2}	7.0600812×10^{-2}
$\Sigma_{c,g}$ (sub)	9.4820991×10^{-4}	1.5134394×10^{-2}	7.0720812×10^{-2}

Table 6.5 : Capture cross sections for the reactivity insertions in system 2. The energy groups are indexed by g.

6.3.2 . Investigating the spatial correlations in the equilibrium source

We start our investigation by considering the kinetic source for system 1 and 2. Based on our previous investigations in Sec. 6.2.4, we expect spatial correlations stemming from the equilibrium source to be carried mostly by the precursor population. The Feynman moments of the neutron and precursor populations after combing are shown in Fig. 6.25 for system 1 and in Fig. 6.26 for system 2. For the sake of simplicity, in the following we refer to them as 'neutron source' and 'precursor source'.

As suggested in Sec. 6.2.4, the choice of the acceptance probability leads to fluctuations in the Feynman moment for the neutron source, indicated by the noisy behaviour of the Feynman moment of the (thermal) neutron source in Figs. 6.25a and 6.26a. Spatial correlations are induced by combing, which manifests itself through the convex shape similar to the one observed in Fig. 6.13.

The behaviour of the Feynman moments of the precursor source is induced by the use of the combined precursor particle ; the value of the Feynman moment for each family is driven by the fractional weight for family j, which (for a particle stemming from the equilibrium source) is given by

$$w_j^{\text{eq}} = \frac{\bar{\lambda}}{\lambda_j} \frac{\beta_j}{\beta}, \tag{6.7}$$

with definitions as in Sec. 2.4.1. This distribution is a consequence of Eq. (2.34). The expected weight after combing is very close to 1. Thus, the expected fractional weight for each precursor family in the equilibrium source is only driven by the delayed nuclear data in Tab. 6.3 ; numerical values are given in Tab. 6.7. The values of the Feynman moments are proportional to the values of the expected fractional weights. However, the absolute values of the Feynman moments are different from the expected fractional weights, which indicates deviations from a locally Poisson distribution. Even in situations where the dominance ratio is large (for system 2, we recall that the dominance ratio is $R = 0.9957$), the use of branchless collisions in the power iteration effectively suppresses the spatial correlations that usually arise from the sampling of the kinetic source. This is revealed by the absence of spatial shape for the Feynman moment of the precursor populations (except close to the boundaries). Finally, because of the use of the combined precursor particle, the shape of the spatial correlations in the precursor source is independent of the precursor family.

6.3.3 . Analysis of space-time correlations in the critical case

The Shannon entropy for the neutron and precursor populations is represented in Fig. 6.27. The neutron entropy follows the same trend as in the simplified systems investigated in Sec. 6.2.4 : the initial jump happens on a very short timescale, suggesting that the spatial correlations within the neutron source are almost instantaneously forgotten. The long-time behaviour of the neutron entropy in system 1 appears to converge to a constant value, whereas the neutron entropy in system 2 seems to decrease, suggesting a build-up of spatial correlations within the neutron population. However, the decrease could also be

System number	k_{eff}	$\delta\rho$ (super)	$\delta\rho$ (sub)
1	1.00003 ± 1 pcm	1.08875×10^{-3}	-1.1219×10^{-3}
2	0.99986 ± 1 pcm	1.13902×10^{-3}	-9.61192×10^{-4}

Table 6.6 : Amplitude of the reactivity insertions for each case.

	family 1	family 2	family 3	family 4	family 5	family 6
w_j^{eq}	0.2373	0.4991	0.1292	0.1155	0.0169	0.0021

Table 6.7 : Expected fractional weight in the precursor source. The families are indexed by j.

related to the value of the multiplication factor, which is slightly subcritical, and additional investigations relying on the Feynman moments will be necessary. In system 1, the precursor entropy appears to reach saturation for large times, whereas it reaches a maximum near $t \simeq 8$ s for system 2, before decreasing. This last remark could be either an indicator of spatial clustering within the precursor population, or the consequence of the slight subcriticality of system 2.

As for the Feynman moments, we first focus on the space-time correlations within the neutron population. For neutrons, whose population is small at any given time, the Feynman moment of the neutron positions is typically noisy, and a satisfactory statistical accuracy could not be achieved. This makes the interpretation of the Feynman moments more difficult : for illustration, Fig. 6.28 represents the Feynman moment of the position of neutrons in the thermal group at different times (the Feynman moments for the epithermal and fast group were too noisy). Figure 6.28 suggests that the Feynman moment saturates almost instantaneously in both systems. Note that with the current parameters, $\tau_{\text{th}} \simeq 2.215 \times 10^{-4}$ s for the thermal group, which is much smaller than a single time step. It is therefore difficult to compare the value of the Feynman moment to the expected neutron weight ; nonetheless, the existence of spatial correlations within the neutron population are suggested by the large value of the Feynman moment. A clearer picture can be obtained from the analysis of the Feynman moments of the collision counts, which are integrated over a time step, as illustrated in Fig. 6.29 : after a short time (less than 0.1 s), the Feynman moments saturate for each group, and are constant for long times, suggesting that the critical catastrophe is successfully averted.

As suggested in Sec. 6.2.4, we expect that long-term correlations arise within the precursor population. This is illustrated by Fig. 6.30 for the large system, at $t = 0.1$ s (i.e. when spatial correlations are still affected by the kinetic source), and at $t = T = 10$ s (i.e. the final simulation time). Figure 6.30 clearly illustrates that at $t = T$ not all the precursor families have forgotten the source correlations and relaxed to the time-dependent correlations : the families with the slowest decay (i.e. $1/\lambda_1 \gg T$) still exhibit the (almost) flat shape inherited from the sampling of the kinetic source, while the spatial correlations within families with faster decay are now peaked in the centre of the system. For families with faster decay, the Feynman moment significantly increases with time : at much longer times, we expect this remark to extend also to the families with slower decay. The same conclusions would apply to system 1, which we do not detail here for the sake of conciseness.

6.3.4 . Analysis of space-time correlations with reactivity insertions and withdrawals

We now consider the behavior of the clustering indicators in scenarios where the system is prepared on the critical state, but an amount of reactivity is inserted or withdrawn at $t = 0$. The reactivity changes are given in Tab. 6.6.

The corresponding Shannon entropy for the neutron and precursor populations is plotted in Fig. 6.31. In both cases, the neutron entropy undergoes a prompt jump at short times, which is again explained by the fact that spatial correlations within the kinetic source are somewhat different from those of the time-dependent process. In the supercritical case (i.e. reactivity insertion), the height of the jump is smaller than in the critical or subcritical case (i.e. reactivity withdrawal). After the prompt jump, the neutron

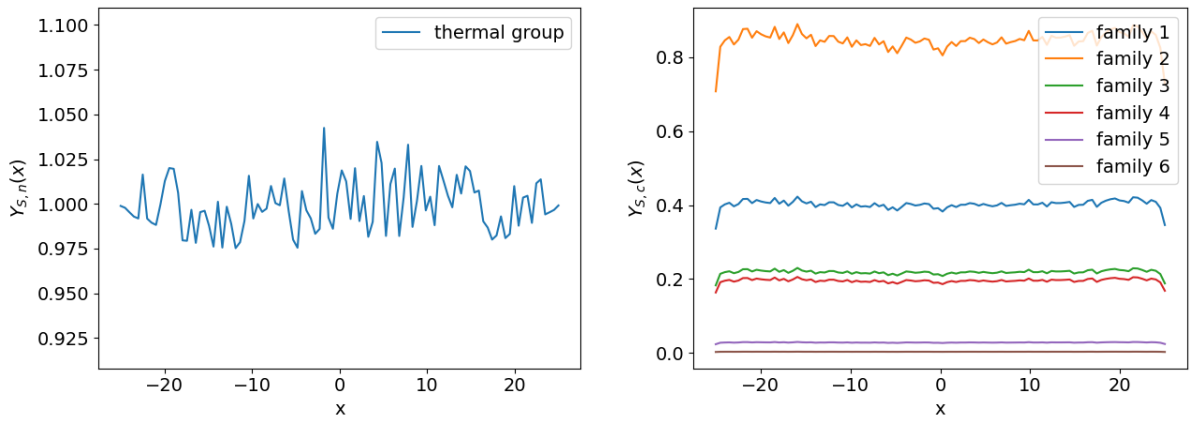

(a) Feynman moment of the neutron source. (b) Feynman moment of the precursor source

Figure 6.25 : Feynman moments of the equilibrium source for system 1, with a total population $N = 10^4$ and $M = 10^4$ independent replicas.

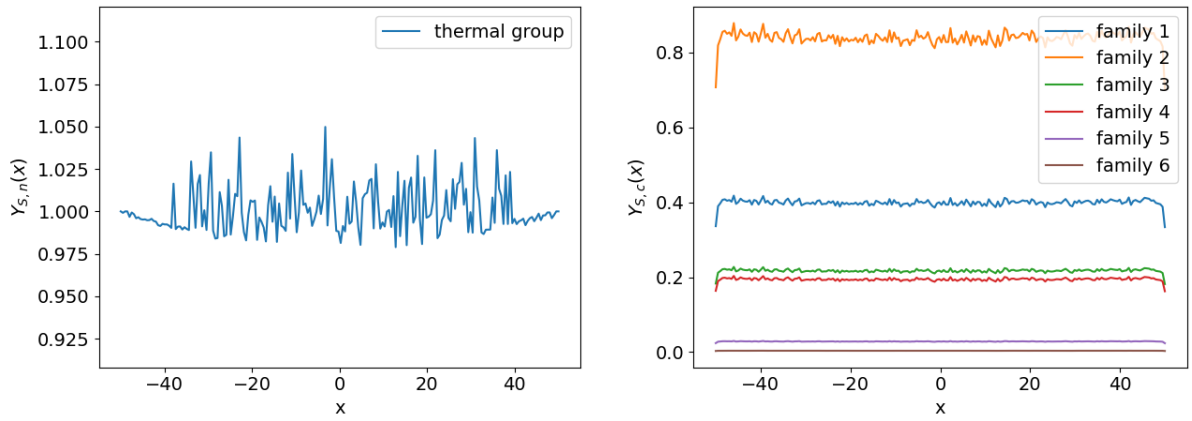

(a) Feynman moment of the neutron source. (b) Feynman moment of the precursor source

Figure 6.26 : Feynman moment of the equilibrium source for system 2, with a total population $N = 10^4$ and $M = 10^4$ independent replicas.

entropy increases in the supercritical case, which is related to the increasing population size. Conversely, the neutron entropy decreases in the subcritical case, which is related to decreasing population size. In this case, the long-time variations of the neutron entropy cannot be used to infer the emergence of spatial correlations in these systems.

We turn to the precursor entropy in Fig. 6.31b. The behaviour of the precursor entropy in the supercritical cases is very similar in both systems, with a monotonic increase with time. In the subcritical case, although both systems still behave similarly, we observe that a maximum is attained near $t \simeq 4.5$ s, and then the entropy decreases. The maximum can safely be associated to the fact that spatial correlations stemming from the kinetic sources progressively relax, while the subsequent decreases can be associated to the decreasing population size. In any case, the interpretation of the observed behaviour in terms of spatial correlations is not apparent.

We shall now rely on the Feynman moments to clarify our previous discussion. The Feynman moments of the neutron population lead to the same conclusions as in the critical case, and will therefore not be shown here. Figure 6.32 indicates that the prompt jump has a strong influence on the Feynman moments of the collision counts, which then saturate in the long-time behaviour. It is however unclear whether this conclusion would still hold if the final time of the simulation were longer. This behaviour is reminiscent of the fact that, in power iteration calculations, the Feynman moments are independent of the population

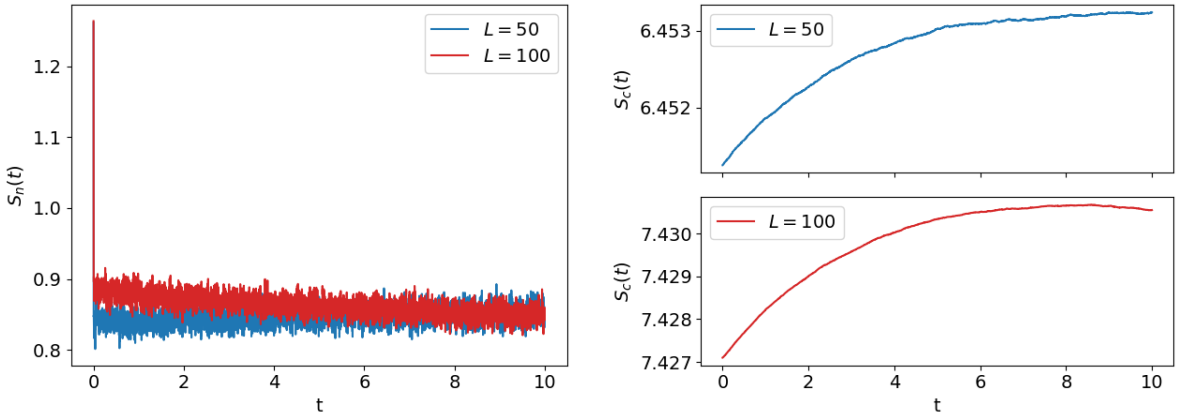

(a) Entropy of the total neutron population. (b) Entropy of the total precursor population.

Figure 6.27 : Shannon entropy of the neutron and precursor populations, with a total population $N = 10^4$ and $M = 10^4$ independent replicas.

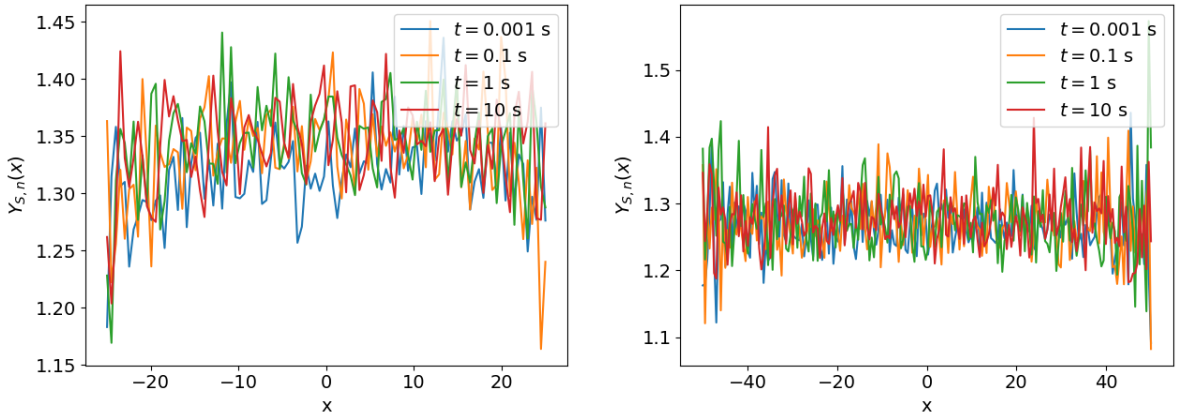

(a) Case of system 1. (b) Case of system 2.

Figure 6.28 : Feynman moment of the thermal neutron positions at different times, with a total population $N = 10^4$ and $M = 10^4$ independent replicas.

size for large enough population sizes (see Sec. 5.4.2). Combined with the remark in Sec. 6.3.3 regarding the saturation at large times of the Feynman moments in the critical configuration, this suggests that, in the supercritical case, the Feynman moment might also be independent of time. This reasoning should also hold true for the subcritical case for intermediate times, i.e. as long as the population size does not become too small. The Feynman moment in the subcritical case will eventually recover a time dependency for large times, as the population size vanishes. For the sake of conciseness, in Fig. 6.32 we only provide the curves for system 2, but the behaviour of system 1 is essentially the same.

To conclude, we present the Feynman moments of the precursor populations. The comparison of Figs. 6.33 and 6.34 for the non-stationary configurations of system 2 with respect to Fig. 6.30 for the stationary configuration indicates that spatial correlations grow similarly. This suggests that reactivity insertions and withdrawals only marginally affect the spatial correlations within the precursor population. The same conclusions hold true for system 1, which is not presented here.

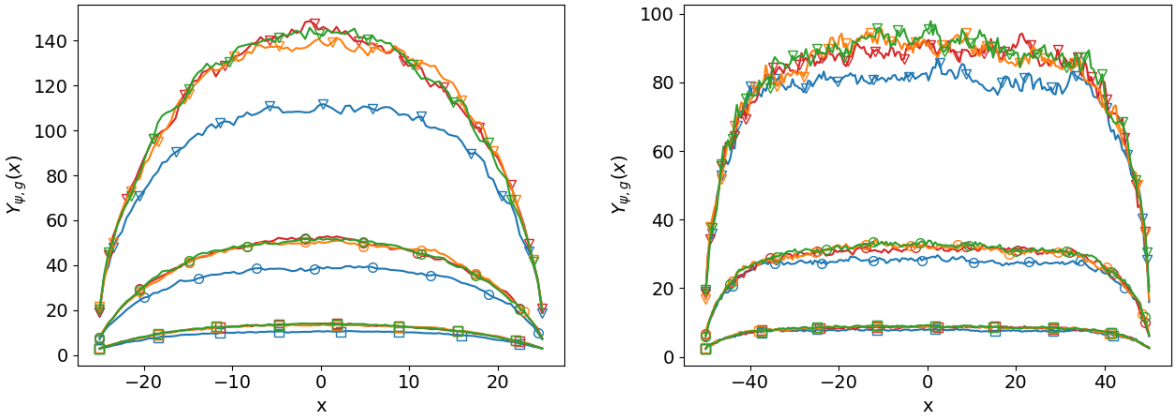

(a) Case of system 1. (b) Case of system 2.

Figure 6.29 : Feynman moments of the collision density at different times, with a total population $N = 10^4$ and $M = 10^4$ independent replicas. Squares are for the fast group, circles for the epithermal group, and triangles for the thermal group. Blue is for $t = 0.001$ s; red is for $t = 0.1$ s; orange is for $t = 1$ s, and green for $t = 10$ s.

6.4 . Conclusions

In this chapter, we investigated the effects of variance-reduction methods on the space-time correlations in time-dependent Monte Carlo simulations. Based on our discussion in Chapter 5 on estimators for spatial correlations, we focused on the analysis of the Shannon entropy (for an easy to compute, global observable), and of Feynman moments (for a local observable, leading to a more detailed analysis of spatial correlations). The impact of non-analog methods was first assessed in a simplified benchmark system, allowing for easier interpretation. We then revisited in a time-dependent setting the spatially homogeneous benchmark problems introduced in Chapter 5.

Based on a simple one-speed transport problem without precursors, in a slab with reflective boundary conditions, we showed that the combination of Russian roulette or splitting with branchless collisions lead to the occurrence of regularly spaced 'steps' in the time evolution of the Shannon entropy. The amplitude of the steps was shown to decrease with time. In supercritical systems, where splitting may occur, we showed how spatial correlations grow over successive entropy steps, and we discussed the conditions dictating whether significant spatial correlations will emerge. In subcritical systems, the entropy steps had no influence on spatial correlations. We have also shown that the use of weight combing suppresses the entropy steps, regardless of the reactivity of the system. In supercritical system, combing introduces additional spatial correlations; in subcritical system, we showed that combing was again not effective in quenching possible spatial correlations. Replacing reflective by leakage boundary conditions led to a shape of spatial correlations within the equilibrium source (computed using power iteration) that was qualitatively different from the shape of spatial correlations arising in the time-dependent process. We showed that spatial correlations within the equilibrium source may have a long-lasting effect on the spatial correlations of the time-dependent simulations. We also illustrated that the interaction of splitting with leakage boundary conditions leads to oscillations in the neutron entropy, which are also related to the build-up of spatial correlations. The introduction of 'realistic' precursors shows that spatial correlations within the equilibrium source carry over in the time-dependent simulation through precursors. The key findings of the case without precursors extend to the case with precursors.

Finally, we investigated the space-time correlations emerging in the spatially homogeneous multi-group transport benchmarks introduced in Chapter 5. In this case, precursors were taken into account. Relying on the results obtained in Sec. 6.2, we characterized the evolution in time and in space of the correlations. Our findings suggest that the effect of reactivity insertions or withdrawals on spatial

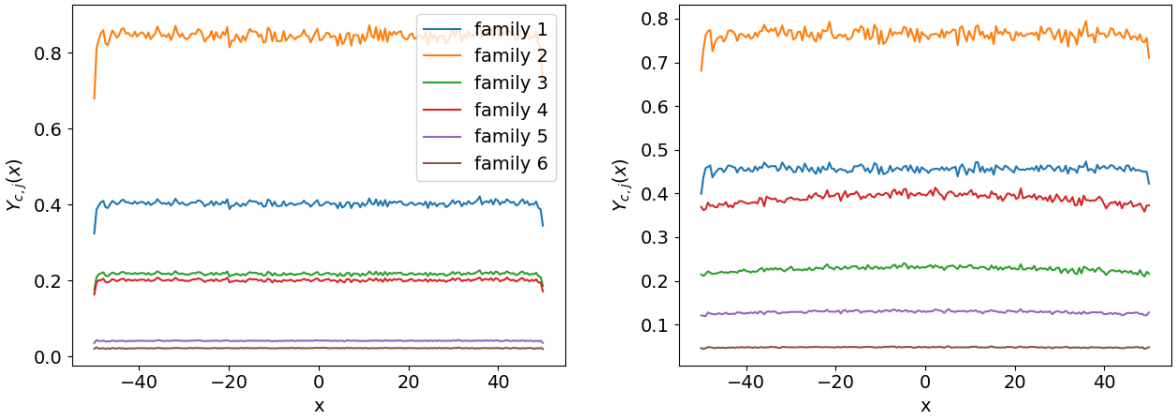

(a) Feynman moments of the precursor positions at $t = 0.1$ s.

(b) Feynman moments of the precursor positions at $t = 10$ s.

Figure 6.30 : Feynman moments of the precursor positions at different times for system 2 in stationary conditions. The total population is $N = 10^4$ and the number of independent replicas is $M = 10^4$.

correlations is marginal. Notably, the critical catastrophe is effectively averted by the use of non-analog methods.

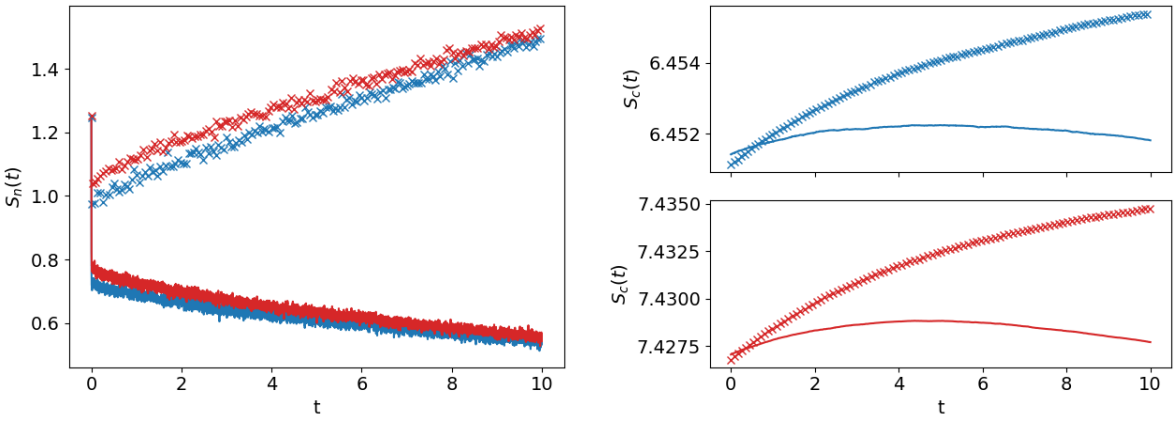

(a) Entropy of the total neutron population.

(b) Entropy of the total precursor population.

Figure 6.31 : Shannon entropy of the neutron and precursor populations when changing reactivity at $t = 0$, with a total population $N = 10^4$ and $M = 10^4$ independent replicas. Blue for system 1 and red for system 2; solid lines for the reactivity removal, and cross markers for the reactivity insertion.

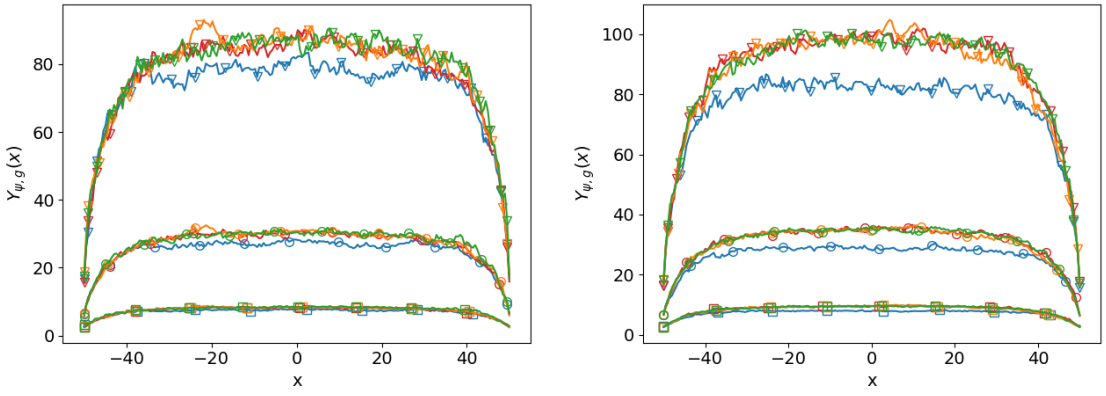

(a) Subcritical transient.

(b) Supercritical transient.

Figure 6.32 : Feynman moments of the collision density at different times, with a total population $N = 10^4$ and $M = 10^4$ independent replicas. We consider system 2 for the supercritical and for the subcritical transients. Squares are for the fast group, circles for the epithermal group, and triangles for the thermal group. Blue is for $t = 0.001$ s; red is for $t = 0.1$ s; orange is for $t = 1$ s, and green for $t = 10$ s.

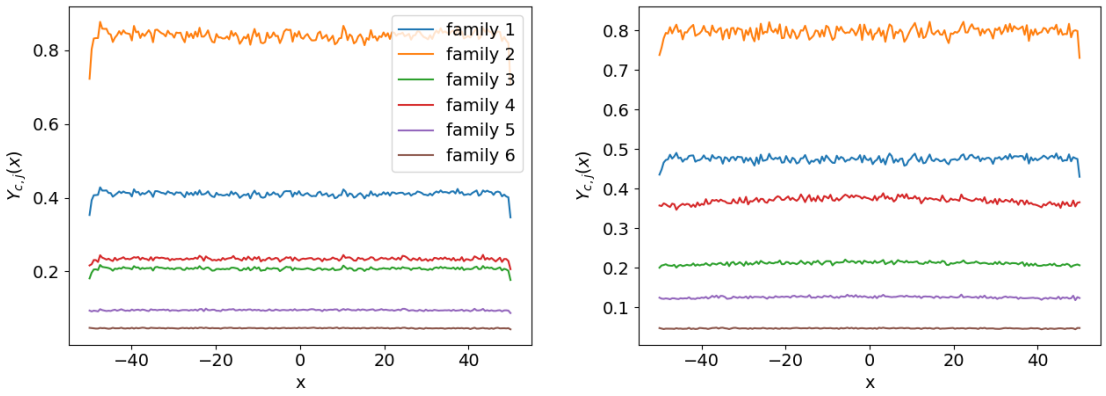

(a) Feynman moments of the precursor population at $t = 1$ s.

(b) Feynman moments of the precursor population at $t = 10$ s.

Figure 6.33 : Feynman moments of the precursor population at different times, with a total population $N = 10^4$ and $M = 10^4$ independent replicas. We consider system 2 for the subcritical transient.

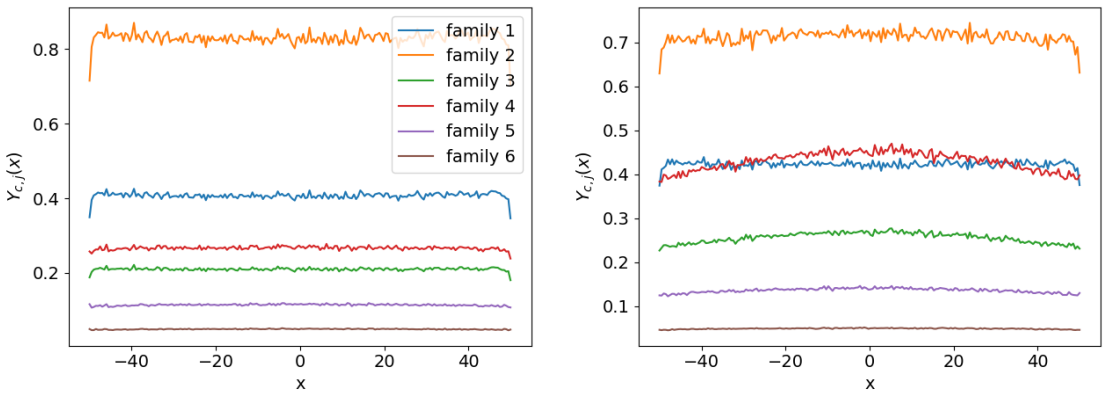

(a) Feynman moments of the precursor population at $t = 1$ s.

(b) Feynman moments of the precursor population at $t = 10$ s.

Figure 6.34 : Feynman moments of the precursor population at different times, with a total population $N = 10^4$ and $M = 10^4$ independent replicas. We consider system 2 for the supercritical transient.

7 -Conclusions and perspectives

Thanks to the combined benefits of the improvements in the algorithms and of the increased computer power, it becomes possible today to address non-stationary problems in reactor physics by Monte Carlo simulation, which allows for an 'exact' treatment of the geometry and of the nuclear data of the simulated system, introducing virtually no approximation nor discretization effects. In view of the intrinsically stochastic nature of the sampled events along each particle history, Monte Carlo tallies fluctuate, and the estimates of the average quantities of interest come with a statistical uncertainty that is asymptotically inversely proportional to the square root of the number of histories. The almost complete absence of approximations is thus thwarted by the very high calculation cost required to achieve the target accuracy, especially in kinetic (i.e. time-dependent) simulations. Furthermore, the simulated particle histories in kinetic problems are correlated, due to fission events, which makes the behaviour of the statistical uncertainty rather complex : the effects of correlations might for instance manifest themselves in the form of particle clustering, the spatial distribution of the simulated particles being extremely 'patchy', instead of uniform as expected. Since in most cases Monte Carlo simulations involve some forms of non-analog sampling, usually in combination with variance-reduction and population-control techniques, the evolution of fluctuations and correlations in kinetic Monte Carlo simulations depends on the non-trivial interplay between the way the sampling strategies are conceived, and the effects inherent to the physics-inspired underlying stochastic processes. An overview of these issues has been presented in Chapter 1.

Prompted by these considerations, in this thesis we have developed a unified and coherent framework for the analysis of fluctuations and correlations in kinetic Monte Carlo simulations, for the purpose of ensuring the reliability of the statistical uncertainty estimates in this class of calculations. In particular, we have focused on the interplay between the behaviour of fluctuations and correlations and the application of variance-reduction and population-control techniques, as well as sampling strategies used for non-analog Monte Carlo simulations. Our investigation has covered both algorithms devoted specifically to time-dependent problems and algorithms devoted to (stationary) eigenvalue problems, which are key for the sampling of the equilibrium neutron and precursor population.

Before presenting our novel contributions, in Chapter 2 we have recalled the general framework for both the eigenvalue and time-dependent formulation of the Boltzmann equation. For the time-dependent formulation, we have emphasized the crucial role of the delayed neutron precursor contributions. Correspondingly, we have then summarized the state-of-the-art of non-analog Monte Carlo strategies for reactor physics problems, with special emphasis on the methods used for kinetic problems. Monte Carlo simulations produce unbiased estimates of the first moments of the sought observables, which are precisely the solutions of the Boltzmann equation. We have discussed the main sampling algorithms for particle transport, and illustrated a few estimators that can be used in order to estimate the observables of interest. Furthermore, we have presented an overview of the most important variance-reduction and population-control schemes that can help reduce the statistical uncertainty and prevent the size of the particle population from becoming too large or too small. In addition, we have introduced simplified formulations of the Boltzmann equations, encompassing the multi-group formalism and the diffusion approximation, and we have shown how these equations can be also solved by Monte Carlo methods, by sampling the random walks of neutrons and precursors in the phase space.

For the investigations discussed in this thesis, we have developed two simplified Monte Carlo mini-apps, also presented in Chapter 2. The main argument behind this choice, as opposed to adding new functionalities and estimators to TRIPOLI-4®, the production-level Monte Carlo code developed at CEA, is that our analysis requires tools such as two-point correlation functions, which are typically very expensive to compute and memory-greedy. Furthermore, we often needed to extensively modify the tradi-

tional sampling strategies and implement unusual scores, which is cumbersome due to the complexity of production-level codes. The first Monte Carlo mini-app, named *JOFFREY*, is devoted to analog (i.e., without variance-reduction techniques) time-dependent transport simulations using the diffusion approximation, where particle displacements are sampled using Brownian motion, in one-dimensional geometries. The second Monte Carlo mini-app, named *COYOTE*, handles more realistic systems in a multi-group spatially heterogeneous framework, including power iteration to sample the stationary (critical) state of neutrons and precursors, and time-dependent transport.

In the first part of the thesis (Chapters 3 and 4), we have examined the behaviour of fluctuations and correlations in time-dependent Monte Carlo simulations for the simpler case where sampling is analog (which means that no variance-reduction techniques are used) and the diffusion approximation is used. These choices were made in order to set a framework amenable to exact solutions for the moment equations describing the two-point correlation functions, against which Monte Carlo simulations can be compared.

For this purpose, in Chapter 3 we have introduced a stochastic model where a collection of particles undergo diffusive displacements obeying a Brownian motion, coupled with a Galton-Watson birth-and-death process that mimics collision events where particles can be captured (and thus disappear) or fission (and thus give rise to a random number of descendants). The system is one-dimensional, with mass-preserving reflecting boundary conditions. Precursors have been modelled using an exponentially distributed delay between the fission events and the emission of further particles in the system at the collision sites. Despite some extremely strong simplifications, this model preserves the key ingredients of time-dependent particle transport in multiplying media, and provides thus meaningful insights on the behaviour of fluctuations and correlations in analog Monte Carlo simulations. Within this framework, using the Pál-Bell backward formalism we have derived the moment equations, which yield in particular the average particle number and the two-point correlation function. We have analytically solved these equations, and exact results have been compared to analog Monte Carlo simulations, used as a reference. Special emphasis has been given to the critical case, where births by fission are compensated by deaths by capture, which is crucial for reactor control. We identified the typical timescales over which correlations evolve : the time necessary for the prompt correlation dynamics to relax, the time necessary for correlations to achieve their asymptotic spatial shape, and the time required to observe catastrophic fluctuations of the total population size.

The model introduced in Chapter 3 has been refined in Chapter 4 by taking into account several idealized sampling strategies mimicking the effects of population control. These schemes break the statistical independence of the neutron fission chains, which forced us to abandon the Pál and Bell backward formalism in favour of the forward formalism. After discussing the derivation of the master equation for the simplified, yet instructive, case where precursors are neglected, we have developed three different population-control schemes : the N-control model, where the neutron population is kept constant, but no constraint is applied to the precursor population ; the NM-control model, both the neutron and precursor populations are controlled ; and the (approximate) immigration model, where precursors are described as a uniform Poisson neutron source whose intensity is equal to the asymptotic precursor decay rate at equilibrium. We have shown that the master equation related to the N-control model leads to an infinite hierarchy of moment equations ; nonetheless, the behavior of the average particle number and the pair correlation function can be determined using Monte Carlo simulation. For the NM-control model, the hierarchy of moment equation is closed : we have derived asymptotic solutions for the average particle number and the pair correlation function, and we have successfully compared them against Monte Carlo simulations. Finally, we have shown that the third model, although approximate, is in fairly good agreement with the N-control and NM-control model under reasonable assumptions on the values of the physical constants. In all cases, we showed that the introduction of population control prevents the occurrence of the critical catastrophe, and thus quenches clustering.

Within the same theoretical framework, we have also gained insight on the behaviour of kinetic

Monte Carlo simulations by investigating family fixation, i.e. the eventual survival of a single particle family, which provides a complementary point of view with respect to the pair correlation function. In particular, we have addressed the distribution of the fixation time, i.e. the time at which all the particles belong to the same family, and its relation to the typical time-scales leading to spatial clustering. We have shown that these quantities, although intimately related, have subtle differences : the fixation time is by construction insensitive to finite-size effects, whereas the evolution of clustering is deeply affected by the presence of boundaries.

The results obtained in the first part of the thesis provide a sound theoretical framework for the investigation of kinetic Monte Carlo simulations, but come with several restrictions : they apply only to the case of analog sampling, without any variance-reduction method, and to single-speed diffusion in spatially homogeneous systems. Population control can be taken into account, but only through highly simplified models where the population size is kept exactly constant. Practically all production Monte Carlo codes use some forms of non-analog sampling, involving variance-reduction and population-control methods : understanding the impact of such techniques on the behaviour of space-time correlations is thus crucial in order to increase the reliability of kinetic simulations.

To overcome the limitations of the models used in Chapters 3 and 4, in the second part of the thesis (Chapters 5 and 6) we have therefore examined the behaviour of fluctuations and correlations in a more realistic setting. The main generalizations have consisted in switching to fully non-analog Monte Carlo sampling, and in relaxing the diffusion approximation by considering multi-group transport processes.

In Chapter 5 we have investigated the impact of non-analog collision sampling, variance-reduction and population-control methods on the correlations that occur in the Monte Carlo implementation of the power iteration algorithm. Power iteration is the standard approach used to estimate the fundamental mode of the k-eigenvalue formulation of the Boltzmann equation, which are key to the sampling of the critical source, i.e., the equilibrium reactor configuration, for kinetic simulations. Our investigation has been carried out on a set of simple, yet meaningful benchmark problems encompassing homogeneous and heterogeneous geometries. Among the probed non-analog Monte Carlo methods, we have in particular focused on branchless collisions, which force the emergence of a single neutron at each collision and thus quench the correlations due to 'branches' in particle histories coming from common ancestors. Furthermore, we have focused on combing and sampling WOR (without replacement) as population-control techniques.

For the purpose of detecting the presence of strong correlations and assessing the relative benefits of various non-analog Monte Carlo methods in reducing their impact, we have selected several distinct tallies : the Shannon entropy, the average pair distance squared, the average number of surviving families, the Feynman moments and the normalized variance. We have shown that all the proposed tallies are useful to detect the presence of anomalous fluctuations in the examined systems. However, global tallies such as the entropy and the average square pair distance, while being easy to use and interpret, have been shown to be inadequate for the investigation of heterogeneous systems, due to lack of information on the spatial details. Conversely, local (i.e. space dependent) tallies such as the Feynman moments and the normalized variance are inherently useful in extracting information on the spatial behavior of the correlations, at the expense of an increased complexity.

Our main finding was that, in all tested configurations, the use of branchless collisions (as opposed to regular branching collisions) is very effective at quenching correlations. In addition, while population control is generally (but not always) advantageous in terms of weakening the effects of correlations, the impact of these methods is much milder than that of using branchless collisions.

After examining the case of power iteration, in Chapter 6 we have reverted to the case of time-dependent Monte Carlo simulations. Based on the analysis of Chapter 5, we have primarily focused on the Shannon entropy and on Feynman moments. The effect of non-analog methods was first characterized in a simplified system, allowing for easier interpretation. We have probed critical, sub-critical and super-critical configurations, with various combinations of system sizes and boundary conditions. Oscillations in

the neutron entropy were observed and related to the build-up of spatial correlations, whose shape depends on the interplay between the reactivity of the system, the specific variance-reduction and population-control method used, and the kind of boundary conditions. In some cases, the oscillations of the entropy function were shown to be persistent over long times.

Finally, we investigated the space-time correlations emerging in the more realistic homogeneous benchmarks introduced in Chapter 5. We detailed how spatial correlations grow over time. Our findings suggest that the effect of reactivity insertions on spatial correlations is marginal, at least in the regime where reactivity is small. Notably, the critical catastrophe is effectively averted by the use of non-analog methods.

The work carried out in this thesis has shed some light on the behaviour of fluctuations and correlations in time-dependent Monte Carlo simulations, starting from highly simplified settings and progressively making them more complex in order to broaden the domain of validity of our findings. In view of getting a deeper grasp of the interplay between sampling methods and correlations, we have kept even our most sophisticated benchmark problems much simpler than realistic applications that could be met in production Monte Carlo codes. On one hand, this has allowed estimating and analyzing tallies that would be generally out of reach due to computational issues, such as two-point correlation functions. On the other hand, we are aware that the conclusions drawn in one-dimensional configurations using multi-group nuclear data might not be representative of the behaviour observed in three-dimensional configurations using continuous-energy nuclear data. Furthermore, it is important to stress that kinetic Monte Carlo methods are a relatively young, thriving and still unsettled research field : novel variance-reduction or population control algorithms might appear in the near future, either conceived from scratch for time-dependent problems or adapted from strategies already existing for stationary problems. Such changes might force us to reconsider the outcomes of the analysis presented here, especially for the case of kinetic simulations discussed in Chapter 6.

Several paths for future work are quite naturally prompted by the findings of this thesis. As briefly illustrated in Chapter 5, replacing multi-group with *continuous-energy nuclear data* might have a significant impact on the behaviour of the variance-reduction techniques with respect to fluctuations and correlations. A more thorough investigation of realistic three-dimensional benchmarks with continuous-energy nuclear data is thus mandatory, which would simultaneously call for the development of improved diagnostic tools to detect correlations, in order to handle the increased computational complexity and memory footprint.

Another hint concerns the analysis of the *interplay between the spatial scale of correlations and the spatial scale of the Monte Carlo tallies*. Based on the Monte Carlo simulation results presented in Chapters 5 and 6, it is apparent that the emergence of spatial correlations is intimately related to the competition between the linear size of the particle clusters and the one of the regions over which the tallies are estimated. A similar interplay might occur also with respect to the time scales : the one of correlations and the one of the tallies in kinetic simulations ; this conjecture should be probed numerically. It would be also interesting to develop a theoretical framework enabling to adapt the tallying mesh in order to quench the effects of correlations.

Related to variance-reduction techniques, a further topic for future research would be the systematic exploration of *zero-variance schemes*, along the lines proposed in Ref. 100, to achieve a coherent framework for a time-dependent Consistent Adjoint-Driven Importance Sampling (CADIS) strategy. These methods would have the potential to become game-changers in kinetic Monte Carlo simulations, leading to considerable improvements in the figure of merit, similarly as what happens already for the case of stationary shielding problems, where CADIS is nowadays customarily employed.

Finally, although in this thesis for the sake of simplicity we have focused on kinetic simulations alone, in most applications the *effects of physical feedback* must be taken into account and deeply affects the evolution of the neutron and precursor population. If the overall feedback coefficient is negative, it will basically act as an average-restoring mechanism, preventing large excursions around the mean value of the

population density. Only the average values coming from the kinetic Monte Carlo simulations can be fed to the coupling codes, which are deterministic. Statistical uncertainty can be propagated by performing independent replicas, at the expense of an increased computational cost. In order to compensate for the extra computer time, one might be tempted to reduce the number of simulated histories per replica, but this would amplify the bias due to the fact of feeding a fluctuating quantity to the coupled solver, the coupling being non-linear. Theoretical and practical issues make therefore these problems non-trivial : an ambitious goal for future exploration would be the extension of the general framework presented in this thesis to the case where kinetics is coupled to thermal-hydraulics.

A -Résumé Détaillé en Français

A.1 . Introduction

Dans le contexte de la sureté des réacteurs nucléaires, le développement d'outils de simulations rapides et efficaces pour le couplage entre les solveurs pour le flux neutronique et les codes de thermo-hydraulique et de thermo-mécanique, dans des conditions stationnaires et transitoires, est le sujet de vastes programmes de recherche dans plusieurs institutions majeures[1].

La densité de neutrons, c'est-à-dire le nombre moyen de particules dans un volume élémentaire de l'espace des phases, obéit à l'équation de Boltzmann [2]. Les solutions analytiques de cette équation sont généralement inatteignables, à l'exception du cas de certains systèmes simplifiés, et l'usage de la simulation numérique est donc nécessaire. Grâce à la linéarité de l'équation de Boltzmann et à la dimension intermédiaire de l'espace des phases (qui n'est ni trop grande, ni trop petite), les méthodes Monte-Carlo et les méthodes déterministes sont toutes deux utilisables pour obtenir des solutions numériques, chacune de ces méthodes bénéficiant d'avantages et d'inconvénients propres.

L'équation de Boltzmann en conditions non stationnaires est traditionnellement résolue en utilisant les méthodes déterministes, dans lesquelles l'espace des phases est discrétisé. À cause du très grand nombre d'inconnues (de l'ordre de $\sim 10^{14}$) qui résulterait d'une discrétisation suffisamment fine de l'espace, de la direction et du temps, la plupart des codes déterministes modernes adoptent une approche en deux temps, lors de laquelle le résultat d'une simulation finement discrétisée à l'échelle d'un assemblage est utilisé afin de préparer les données nucléaires homogénéisées et condensées. Ces données sont ensuite injectées dans un solveur temporel simplifié, dont la discrétisation énergétique est assez grossière, afin d'effectuer une simulation à l'échelle du cœur complet [3–5]. De plus, il est courant de séparer la variable temporelle du reste des variables de l'espace des phases classique [4, 6, 7].

Les solveurs déterministes sont rapides, mais cette rapidité vient au prix de biais dus à la discrétisation et à l'usage de modèles dépendants du type de réacteur (par exemple, l'auto-protection). Ces biais impliquent que cette classe de méthodes numériques doit être validée par comparaison avec des méthodes de simulation de haute-fidélité ou bien avec des résultats expérimentaux [8]. Les données expérimentales sur les réacteurs en régime stationnaire sont généralement plutôt accessibles, bien que leur appartenance aux opérateurs exploitants des centrales nucléaires limitent cette accessibilité. Pour cette dernière raison, plusieurs initiatives ont récemment été promues afin d'établir des résultats de référence internationaux pour la validation des codes de calcul (y compris en incluant la déplétion du combustible et les couplages multi-physiques). On peut citer VERA (Virtual Environment for Reactor Applications)[2], BEAVRS (Benchmark for Evaluation And Validation of Reactor Simulations)[3], et Watts Bar (TVA Watts Bar Unit 1 Multi-Physics Benchmark)[4]. En revanche, dans les régimes non stationnaires tels que les transitoires opérationnels résultant de l'insertion des barres de contrôle ou bien les campagnes expérimentales destinées à évaluer le comportement du réacteur lors de sollicitations extérieures, la situation est bien plus problématique. De plus, les cas extrêmes, tels que les transitoires accidentels pouvant mener à la dégradation du combustible, sont dangereux et ne peuvent être explorés par les moyens expérimentaux, malgré leur importance pour la validation des codes de simulation numérique [9].

Dans le cadre de ces considérations, les simulations *Monte-Carlo* tiennent une place à part, car elles ne sont pas sujettes aux erreurs de discrétisation [10] et peuvent ainsi jouer le rôle de référence pour la validation des solveurs déterministes ; de plus, elles sont de fait inévitables pour évaluer les biais

[1] Voir par exemple les initiatives aux Etats-Unis, comme le projet CESAR (`cesar.mcs.anl.gov`),le consortium CASL (`www.casl.gov`), ou encore les projets européens FP7, HPMC, et McSAFE (`cordis.europa.eu/projects`).

[2] `https://world-nuclear-news.org/Articles/Federal-funding-for-reactor-modelling-initiative`.

[3] `http://crpg.mit.edu/sites/default/files/css_injector_images_image/BEAVRS_2.0.2_spec.pdf`.

[4] `https://www.oecd-nea.org/jcms/pl_32202/tva-watts-bar-unit-1-multi-physics-benchmark`.

déterministes dans les régimes non stationnaires.

A.1.1 . Simulations Monte-Carlo : du stationnaire au transitoire

Les simulations Monte-Carlo pour le transport de particules se basent sur l'échantillonnage aléatoire des trajectoires des particules dans l'espace des phases. Pour les applications intéressant la physique des réacteurs, les particules sont principalement des neutrons, des précurseurs de neutrons retardés, et des photons. Dans le cadre de cette thèse, nous nous concentrerons sur les neutrons et les précurseurs. Leurs interactions aléatoires avec le milieu environnant sont échantillonnées en accord avec les lois de probabilités données dans les librairies de données nucléaires ; le suivi des particules est effectué en calculant l'intersection des vols entre chaque collision avec les cellules constituants le système géométrique. Les trajectoires sont suivies jusqu'à ce que les particules disparaissent, par absorption ou bien en s'échappant des limites du système. Le long de chaque trajectoire, des observables physiques telles que les taux de réactions sont estimées en sélectionnant adéquatement des *scores* dont on calcule la moyenne et la variance. Grâce à la loi des grands nombres, la moyenne sur l'échantillon donne une estimation non biaisée de l'observable physique associée ; la variance de l'échantillon donne quant à elle une estimation de l'incertitude statistique sur la moyenne de l'échantillon, grâce au théorème central limite [10]. La variance de la moyenne de l'échantillon est inversement proportionnelle au nombre d'histoires échantillonnées, ce qui implique que les simulations Monte-Carlo sont généralement bien plus longues que les simulations déterministes. Cependant, cette limitation est compensée par l'absence d'approximations dans résultats ainsi obtenus : les codes Monte-Carlo et les codes déterministes se complètent les uns les autres et sont également nécessaires.

Principalement en raison du temps de calcul nécessaire et des limitations en puissance de calcul, en physique des réacteurs les codes Monte-Carlo ont longtemps été cantonnés exclusivement à l'étude des problèmes stationnaires à température fixée. Cependant, les avancées récentes tant en termes d'algorithmes qu'en termes de puissance de calcul ont permis de se diriger vers une nouvelle classe d'applications pour les simulations Monte-Carlo, et plus spécifiquement vers leur application aux problèmes multi-physiques. D'énormes progrès ont par exemple été effectués dans le domaine de la déplétion du combustible, lors de laquelle le comportement de la densité de neutrons est couplé avec la transmutation du matériau irradié, dont l'évolution est dictée par les équations généralisées de Bateman ; des codes Monte-Carlo ont été efficacement couplés avec des solveurs déterministes pour les équations de Bateman, et la stabilité des schémas de simulation correspondants a été largement étudiée [11–16].

Ces dernières années ont vu l'émergence d'un intérêt grandissant pour une nouvelle classe de méthodes Monte-Carlo dévolues aux simulations cinétiques (i.e dépendant du temps), dont le temps de calcul était bien trop élevé jusqu'à il y a peu. Encouragées par les travaux pionniers de Sjenitzer et Hoogenboom [17, 18], d'ingénieuses méthodes de réduction de variance et de contrôle de la population ont vu le jour, destinées à traiter efficacement les problèmes dépendant du temps. D'abord testées dans des modèles simplifiés, ces méthodes ont ensuite été introduites avec succès dans la simulation de réacteurs nucléaires réalistes prenant en compte l'effet des contre-réactions thermo-hydrauliques [19–26].

A.1.2 . Corrélations et fluctuations dans les simulations Monte-Carlo cinétiques

Étant donné l'apparition relativement récente de ces nouvelles méthodes, un cadre complet pour l'étude des simulations Monte-Carlo dépendantes du temps manque encore, malgré de prometteuses investigations préliminaires. Comme les simulations Monte-Carlo doivent servir de références auxquelles d'autres méthodes simplifiées seront comparées, la précision et l'exactitude des simulations Monte-Carlo sont cruciales. En particulier, la fiabilité des résultats dépend directement de la fiabilité des intervalles de confiance associés, qui sont typiquement estimés en utilisant des techniques d'inférence statistique (en estimant la variance des échantillons Monte-Carlo). La variance d'échantillon capture les fluctuations dans les scores dues à la nature stochastique des histoires. Si ces histoires sont indépendantes et si les fluctuations ne sont pas pathologiques, la quantification de la variance de l'échantillon est directe. Cependant, les simulations cinétiques posent des défis bien particuliers.

La condition initiale pour la densité de neutrons et de précurseurs dans les problèmes dépendant du

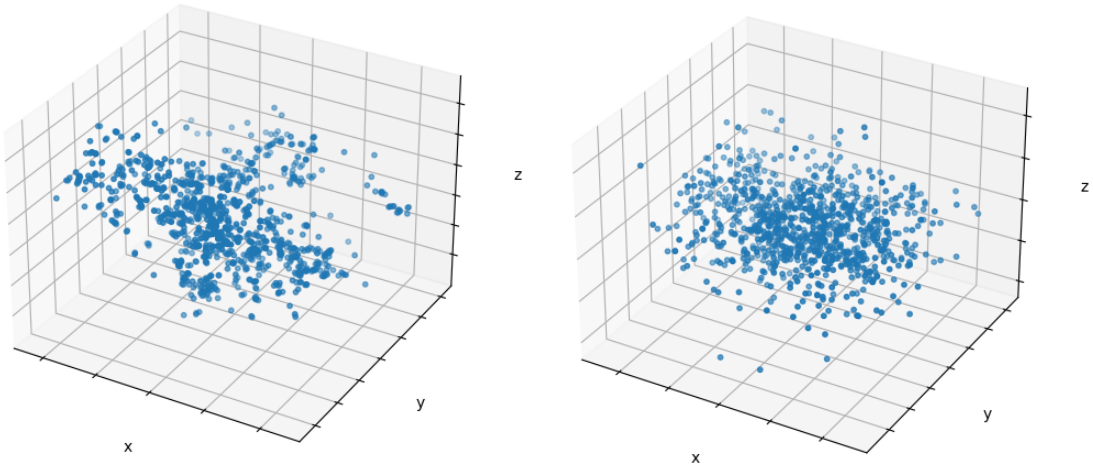

Figure A.1 : Photos de la distribution spatiale typique des neutrons dans un calcul aux valeurs propres Monte-Carlo. Gauche : les corrélations sont importantes, et les neutrons sont regroupés. Droite : les corrélations sont faibles, et les neutrons sont répartis uniformément dans l'espace.

temps correspond souvent à la condition d'équilibre (ou stationnaire) du réacteur, ce qui signifie que les particules commençant la simulation cinétique héritent des corrélations affectant le calcul aux valeurs propres nécessaire pour échantillonner la configuration à l'équilibre des particules [10]. Quand le nombre de particules est petit, l'effet de ces corrélations est amplifié, et se manifeste sous la forme de regroupements spontanés de particules ('clustering'), aboutissant à des distributions spatiales irrégulières [27] telles qu'illustré sur la Figure A.1. De plus, les simulations Monte-Carlo cinétiques sont affectées par des problèmes qui leur sont plus spécifiques : les histoires peuvent 'brancher' à cause des évènements de fission conduisant à l'apparition de neutrons secondaires, ce qui augmente la variance et se trouve être à l'origine des corrélations spatio-temporelles, même lorsque le réacteur est critique (stationnaire). Dans certains cas, ces effets peuvent mener à une croissance incontrôlée de la variance en fonction du temps, appelée la *catastrophe critique* [28].

Dans ce qui suit, nous donnons un rapide tour d'horizon des connaissances actuelles sur l'effet des corrélations dans les simulations Monte-Carlo, ainsi que les questions encore ouvertes et leur importance pour différentes applications.

Corrélations dans les calculs aux valeurs propres Monte-Carlo

Comme illustré dans cette thèse, la distribution à l'équilibre des neutrons et des précurseurs peut être déterminée par des méthodes Monte-Carlo simulant les chaines de fission sur plusieurs *générations* (une génération étant définie comme l'histoire d'un neutron depuis sa naissance jusqu'à sa mort par fuite ou par absorption), jusqu'à ce que le régime stationnaire soit atteint [10]. À chaque génération, la généalogie de n'importe quel neutron peut être retracée jusqu'à un ancêtre, et l'ensemble des neutrons partageant un même ancêtre commun forme une *famille* : des évènements issus d'une même famille seront corrélés. Ces corrélations vont affecter à la fois le comportement statistique d'un score au sein d'une même cellule spatiale au cours de générations successives, et le comportement des scores dans différentes cellules spatiales à une génération donnée : ces deux points de vue sont intimement reliés.

L'évaluation des corrélations *générationnelles* est un problème de longue date. Dans les calculs aux valeurs propres Monte-Carlo, la moyenne et la variance sont typiquement estimées au cours de générations successives, en faisant l'hypothèse que les scores collectés lors de chaque génération sont indépendamment et identiquement distribués. Cela correspond à une moyenne *ergodique*, par analogie avec l'hypothèse ergodique en physique statistique à l'équilibre. Bien que les scores soient effectivement identiquement distribués (une fois le système convergé vers l'état d'équilibre), ils sont aussi corrélés, comme discuté

précédemment, et cela affecte l'estimation de l'incertitude sur leur valeur moyenne.

Brissenden et Garlick ont les premiers remarqué que négliger les corrélations générationnelles en estimant la variance au moyen de la moyenne ergodique menait à une sous-estimation de la variance des scores [29] : pour cette raison, il est nécessaire de faire la distinction entre la variance *apparente* (sous-estimée) et la *vraie* variance obtenue par *moyenne d'ensemble* sur un ensemble de répliques totalement indépendantes[5]. Ueki et al. [30] ont montré que la différence entre la variance apparente et la vraie variance peut-être considérable pour des scores dépendant de l'espace. Ils ont aussi montré que le taux de convergence en fonction du nombre de particules simulées diffère de celui attendu pour des histoires indépendantes, bien que Herman ait montré plus tard que le comportement attendu est retrouvé asymptotiquement pour des populations de grande taille [31]. Min-Jae et al. ont découvert que le ratio de la variance apparente sur la vraie variance n'était pas uniforme dans l'espace [32].

Plusieurs méthodes visant à prédire la vraie variance en partant de la variance apparente ont été proposées, le plus souvent avec des hypothèses simplificatrices : Yamamoto et al. ont modélisé la sous-estimation de la variance des scores locaux (ou dépendant de l'espace) ainsi que sa dépendance sur la taille des cellules spatiales [33]. Sutton a appliqué une approche de discrétisation de l'espace des phases afin de comprendre l'hétérogénéité du ratio de la variance apparente sur la vraie variance [34]. Miao et al. ont calculé les coefficients d'auto-corrélation entre les cellules spatiales afin d'analyser le comportement des corrélations générationnelles [35–37].

L'impact des corrélations *spatiales* dans les calculs aux valeurs propres Monte-Carlo a été récemment remarqué par Dumonteil et al., qui les premiers ont noté l'émergence des regroupements de neutrons [27] ; des outils de diagnostic ont été développés plus tard par Nowak et al. [38] en approfondissant des recherches précédentes [28]. Bien que ces corrélations spatiales n'affectent pas affecter la moyenne des scores Monte-Carlo en eux-mêmes, Cosgrove et al. ont montré qu'elle pourrait avoir une influence lorsque des simulations Monte-Carlo sont couplées à un solveur pour la déplétion, et ainsi amplifier des instabilités numériques préexistantes [12, 39], aboutissant ainsi à l'apparition d'un biais sur la moyenne des observables [40]. Sutton a proposé d'étudier le comportement spatial des neutrons au moyen du comportement statistique des arbres généalogiques de neutrons, en notant que les corrélations étaient amplifiées lorsqu'il ne restait qu'un petit nombre de familles indépendantes (ou bien des familles plus grandes) dans la population de neutrons [41, 42]. Concernant la question du 'clustering', les résultats présents dans la littérature sont assez contradictoires, et il ne semble pas exister de véritable consensus. Certains auteurs ont suggéré que le 'clustering' des neutrons pourraient avoir un impact sur la moyenne des scores, en plus d'affecter l'estimation de la variance [43, 44]. Au contraire, d'autres ont suggéré que les corrélations spatiales n'avaient pas d'effets notables sur l'estimation des incertitudes statistiques [45].

Corrélations dans les simulations Monte-Carlo cinétiques

Les simulations Monte-Carlo dépendant du temps ont été introduites assez récemment dans le contexte de la physique des réacteurs, ce qui explique que l'étude du comportement des corrélations dans cette classe de problèmes en soit encore à ses balbutiements. De plus, malgré des avancées significatives concernant les méthodes de réductions de variance, le coût en calcul des problèmes cinétiques reste très élevé, et l'étude des corrélations est le plus souvent effectuée dans des modèles avec différents niveaux de simplification.

Dumonteil et al. ont évalué les corrélations spatiales à un temps d'observation donné en négligeant la contribution des précurseurs et en supposant que le milieu était infini [27]. L'effet du milieu fini sur les corrélations spatio-temporelles a plus tard été pris en compte [46, 47], menant finalement au développement d'un modèle plus raffiné dans lequel la taille de la population des neutrons est conservée constante, afin d'imiter l'effet des méthodes de contrôle de la population [28]. Une caractéristique intéressante de

[5] Il n'y a pas de restrictions de principe empêchant d'utiliser des répliques indépendantes dans l'itération de la puissance. La principale raison qui a mené les pratiquants du Monte-Carlo à adopter la moyenne ergodique vient du temps de calcul : utiliser des répliques indépendantes impliquerait un temps de calcul largement plus élevé qu'en utilisant la moyenne ergodique, ce qui était décourageant dans les premiers temps du Monte-Carlo.

ces modèles est que la plupart des résultats correspondants se généralisent aux problèmes aux valeurs propres résolus par des méthodes Monte-Carlo basées sur les générations, en remplaçant le temps par l'index discret de la génération [38] : cela signifie aussi que les questions ouvertes pour les modèles en temps continu ont leur contrepartie dans les modèles en générations discrètes. Le principal résultat de ces études est que le 'clustering' spatial émerge de la même manière pour les problèmes aux valeurs propres que pour les problèmes cinétiques, à cause des évènements de fission. En l'absence de contrôle de la population, la variance d'un système critique va diverger, menant possiblement à l'extinction prématurée de la simulation cinétique (catastrophe critique) ; l'application du contrôle de la population empêche l'arrivée de la catastrophe critique. L'impact des précurseurs (en milieu infini et sans contrôle de la population) a été examiné par Houchmandzadeh et al. [48], qui ont montré que l'amplitude des corrélations était largement réduite, et leur évolution temporelle ralentie pour des systèmes proches de la criticité.

Toutes ces investigations sont restreintes à des milieux homogènes et un modèle de transport simplifié, ce qui limite leur application à des systèmes plus réalistes, et ce bien que des tendances générales puissent être dégagées. La plus grande de ces limitations vient du fait que ces modèles sont définis pour des simulations Monte-Carlo analogues, ce qui exclut les méthodes de réduction de variance. Or, la plupart des calculs Monte-Carlo ont couramment recouru aux méthodes non-analogues ; il est donc nécessaire de caractériser précisément l'interaction entre les méthodes de réduction de variance, les méthodes de contrôle de la population et le comportement des corrélations dans les problèmes cinétiques.

A.1.3 . But et structure de la thèse

Inspirés par ces considérations, dans cette thèse nous avons développé un cadre cohérent et unifié pour l'analyse des fluctuations et des corrélations dans les simulations Monte-Carlo cinétiques, dans le but d'assurer la fiabilité des estimations de l'incertitude statistique dans cette classe de simulations. En particulier, nous nous sommes concentrés sur l'interaction entre le comportement des fluctuations et des corrélations, et l'application de méthodes de réduction de variance et de contrôle de la population, ainsi qu'avec les stratégies d'échantillonnage spécifiquement définies pour les problèmes cinétiques et stationnaires (ou aux valeurs propres), ces derniers étant essentiels pour l'échantillonnage de la source d'équilibre des neutrons et des précurseurs.

Ce travail est structuré de la manière suivante :

- Tout d'abord, dans les Chapitres 1 et 2, nous avons présenté l'état de l'art des simulations Monte-Carlo pour le transport des neutrons, et nous avons porté une attention particulière aux méthodes utilisées pour les simulations cinétiques.

- Dans la Partie I (Chapitres 3 et 4), nous avons présenté nos résultats dans le cadre d'un modèle simplifié de simulation Monte-Carlo analogue d'un processus de diffusion, dans lequel une population de neutrons et de précurseurs évolue en temps en suivant un mouvement Brownien branchant. Nous avons caractérisé les corrélations induites par la fission dans ce système, et nous avons dérivé des grandeurs caractéristiques afin de faciliter l'analyse de simulations plus réalistes. Nous avons aussi étudié l'effet d'un mécanisme idéalisé de contrôle de la population dans le cas de simulations analogues.

- Dans la Partie II (Chapitres 5 et 6), nous avons présenté nos résultats concernant les simulations Monte-Carlo cinétiques non-analogues, en utilisant un large panel de techniques de réduction de variance et de contrôle de la population. Nous avons proposé des estimateurs adéquats pour l'analyse des corrélations dans ces systèmes, et discuté de l'effet des méthodes de réduction de variance et de contrôle de la population sur les fluctuations et les corrélations.

A.2 . Conclusions et perspectives

Grâce à l'effet combiné des améliorations algorithmiques et de la puissance de calcul, il devient aujourd'hui possible d'aborder les problèmes non stationnaires en physique des réacteurs au moyen des simulations Monte-Carlo, ce qui permet un traitement 'exact' de la géométrie et des données nucléaires du système simulé, sans introduire d'approximations ou de biais de discrétisation. Au vu de la nature intrinsèquement stochastique des évènements échantillonnés le long de chaque trajectoire de particule, les scores Monte-Carlo fluctuent, et l'estimation des valeurs moyennes désirées est associée à une incertitude statistique qui est asymptotiquement inversement proportionnelle à la racine carrée du nombre d'histoires. L'absence presque totale d'approximations est ainsi contrebalancée par un coût de calcul très élevé dès lors que l'on veut une précision acceptable, particulièrement dans le cas des simulations cinétiques (dépendantes du temps). De plus, étant donné que les histoires simulées lors des simulations cinétiques sont corrélées à cause des évènements de fission, le comportement de l'incertitude statistique est complexe : par exemple, l'effet des corrélations peut se manifester sous la forme du 'clustering' spatial (la distribution spatiale des particules devient très hétérogène, au lieu d'être uniforme comme attendu). La plupart des simulations Monte-Carlo nécessitant l'usage de méthodes d'échantillonnage non-analogues, généralement en combinaison avec des méthodes de réduction de variance et de contrôle de la population, l'évolution des fluctuations et corrélations dans les simulations Monte-Carlo cinétiques dépend de l'interaction non triviale entre les méthodes d'échantillonnage et les effets inhérents aux processus stochastiques sous-jacents, qui sont inspirés par la physique. Nous avons donné une vue d'ensemble de ces questions dans le Chapitre 1.

Avant de présenter nos nouvelles contributions, dans le Chapitre 2 nous avons rappelé le cadre général des formulations de l'équation de Boltzmann dans le contexte dépendant du temps et dans le cas d'un problème aux valeurs propres. Pour la formulation dépendante du temps, nous avons mis en avant le rôle crucial joué par les contributions des précurseurs de neutrons retardés. Par la suite, nous avons résumé l'état de l'art des méthodes non-analogues couramment utilisées en physique des réacteurs, en particulier celles utilisées pour les problèmes dépendant du temps. Les simulations Monte-Carlo donnent des estimations non biaisées des premiers moments des grandeurs d'intérêt, qui sont précisément les solutions de l'équation de Boltzmann. Nous avons présenté les principaux algorithmes pour le transport de particules, ainsi que quelques estimateurs pouvant être utilisés afin d'estimer les observables d'intérêt. De plus, nous avons donné une vue d'ensemble des méthodes de réduction de variance et de contrôle de la population les plus importantes. Ces méthodes peuvent être utilisées afin de réduire l'incertitude statistique sur la moyenne et d'empêcher que la taille de la population ne devienne trop grande ou trop petite. De plus, nous avons introduit des formulations simplifiées de l'équation de Boltzmann, comprenant le formalisme multi-groupe ainsi que l'approximation de la diffusion, et nous avons montré que ces équations simplifiées pouvaient être résolues grâce aux méthodes Monte-Carlo, en échantillonnant les marches aléatoires des neutrons et des précurseurs dans l'espace des phases.

Pour les investigations discutées dans cette thèse, nous avons développé deux mini-applications Monte-Carlo, aussi présentées dans le Chapitre 2. Le principal argument derrière ce choix (au lieu d'ajouter de nouvelles fonctionnalités et estimateurs à TRIPOLI-4®, le code officiel du CEA), c'est que notre analyse nécessite des outils tels que la fonction de corrélation à deux points, qui sont typiquement très couteux à calculer et à stocker. De plus, nous avons souvent eu besoin de modifier largement les méthodes traditionnelles d'échantillonnage ou bien d'implémenter des scores inhabituels, ce qui est considérablement complexifié dans des codes industriels. La première mini-application, appelée *JOFFREY*, est dédiée à la simulation analogue (c'est-à-dire, sans méthodes de réduction de variance) du transport dépendant du temps en utilisant l'approximation de la diffusion, dans laquelle le déplacement des particules est échantillonné en utilisant un mouvement Brownien unidimensionnel. La seconde mini-application, appelée *COYOTE*, permet de simuler des systèmes plus réalistes dans un cadre multi-groupe en milieu hétérogène, incluant à la fois l'itération de la puissance pour l'échantillonnage de la source stationnaire (critique) de neutrons et de précurseurs, et le transport dépendant du temps.

Dans la première partie de la thèse (Chapitres 3 et 4), nous avons examiné le comportement des fluctuations et des corrélations dans les simulations Monte-Carlo cinétiques dans le cas simplifié où l'échantillonnage est analogue (ce qui signifie que nous n'utilisions pas de réduction de variance) et en utilisant l'approximation de la diffusion. Ces choix ont été effectués de manière à proposer un cadre permettant de calculer des solutions analytiques exactes pour les équations des moments décrivant la fonction de corrélation à deux points, et de les comparer à des simulations Monte-Carlo.

Dans ce but, dans le Chapitre 3 nous avons introduit un modèle stochastique dans lequel une collection de particules suit un mouvement Brownien couplé à un processus de vie et de mort de Galton-Watson imitant les évènements de collisions. Lors de ces évènements, les particules peuvent être capturées (et disparaissent), ou induire une fission (et donnent naissance à un nombre aléatoire de descendants). Le système est unidimensionnel avec des conditions de bord de réflexion préservant la masse. Les précurseurs sont modélisés en utilisant un retard exponentiellement distribué entre l'évènement de fission dont ils sont issus et l'émission de neutrons supplémentaires depuis le point de collision. Malgré ces approximations extrêmement fortes, ce modèle préserve les éléments clés du transport dépendant du temps dans un milieu multiplicatif, et offre ainsi d'importantes informations sur le comportement des fluctuations et des corrélations dans les simulations Monte-Carlo analogues. Dans ce contexte, nous avons utilisé le formalisme rétrograde de Pál-Bell pour dériver les équations des moments, en particulier pour la densité moyenne de particules et la fonction de corrélation à deux points. Nous avons résolu analytiquement ces équations, et nous avons comparé ces résultats à des simulations Monte-Carlo analogues, utilisées comme référence. Une attention particulière a été portée au cas critique, dans lequel les naissances par fission sont compensées (en moyenne) par les morts dues à la capture, ce qui est crucial pour le contrôle des réacteurs. Nous avons identifié les échelles de temps typiques selon lesquelles évoluent les corrélations : le temps pour que les corrélations issues de la dynamique prompte se stabilisent, le temps nécessaire pour que les corrélations atteignent leur forme spatiale asymptotique, et le temps nécessaire pour observer des fluctuations catastrophiques de la taille de la population.

Le modèle introduit dans le Chapitre 3 a été raffiné dans le Chapitre 4 en prenant en compte des stratégies idéalisées de contrôle de la population imitant l'effet du contrôle de la population dans les simulations non-analogues. Ces schémas brisent l'indépendance statistique entre différentes chaînes de fission, forçant l'abandon du formalisme de Pál-Bell au profit du formalisme direct. Après avoir présenté la dérivation de l'équation maîtresse pour le cas simplifié dans lequel les précurseurs sont négligés, nous avons développé trois modèles différents de contrôle de la population : le modèle avec contrôle de N, dans lequel la population de neutrons est maintenue constante tandis que les précurseurs évoluent librement ; le contrôle de N et M, dans lequel une contrainte est appliquée séparément sur les neutrons et les précurseurs ; et un modèle d'immigration dans lequel les précurseurs sont modélisés comme une source Poissonnienne uniforme dont l'intensité est égale au taux asymptotique de décroissance des précurseurs à l'équilibre. Nous avons montré que l'équation maîtresse du modèle de contrôle de N menait à une hiérarchie infinie d'équations des moments ; néanmoins, le comportement du nombre moyen de particules et de la fonction de corrélation de paires peut toujours être déterminé en utilisant les simulations Monte-Carlo. Pour le modèle de contrôle de N et M, la hiérarchie d'équations des moments est fermée : nous avons déterminé des solutions asymptotiques pour la fonction de corrélation de paires, qui ont été comparées avec succès aux simulations Monte-Carlo. Finalement, nous avons montré que le troisième modèle, quoiqu'approché, est en relativement bon accord avec les deux autres modèles pour certaines valeurs (raisonnables) des paramètres physiques. Dans tous les cas, nous avons montré que l'introduction du contrôle de la population empêche la catastrophe critique, et donc limite l'apparition du 'clustering'.

Dans le même cadre théorique, nous avons aussi caractérisé le comportement des simulations Monte-Carlo en étudiant le processus de fixation, c'est-à-dire la survivance d'une seule famille de particules à un temps donné, offrant ainsi un point de vue complémentaire à la fonction de corrélation de paires. En particulier, nous avons étudié la distribution du temps de fixation, c'est-à-dire le temps auquel toutes les particules appartiennent à la même famille, et ses liens avec les grandeurs caractéristiques du 'clustering'. Nous avons montré que ces quantités, quoiqu'intimement connectées, ont de subtiles différences : le

temps de fixation est par construction insensible aux effets de bord (en l'absence de fuites), tandis que l'évolution du 'clustering' est profondément affectée par la présence de conditions de bord.

Les résultats obtenus dans la première partie de la thèse offrent un cadre théorique robuste pour l'étude des simulations Monte-Carlo cinétiques, mais viennent avec plusieurs limitations : ils ne s'appliquent que pour l'échantillonnage analogue, sans aucune méthode de réduction de variance, et au cas de la diffusion en milieu homogène. Le contrôle de la population peut être pris en compte, mais seulement au moyen de modèles très simplifiés dans lesquels la taille de la population est fixée. Pratiquement tous les codes Monte-Carlo industriels utilisent des échantillonnages non-analogues, impliquant des méthodes de réduction de variance et de contrôle de la population : comprendre l'impact de ces techniques sur le comportement des corrélations spatio-temporelles est crucial pour améliorer la fiabilité des simulations cinétiques.

Pour surpasser les limitations des modèles utilisés dans les Chapitres 3 et 4, dans la seconde partie de la thèse (Chapitres 5 et 6), nous avons donc étudié le comportement des fluctuations et des corrélations dans un contexte plus réaliste. Les principales généralisations ont consisté à utiliser un échantillonnage non-analogue, et à passer de l'approximation de la diffusion au transport multi-groupe.

Dans le Chapitre 5, nous avons étudié l'effet de la stratégie de collision, de la réduction de variance et du contrôle de la population sur les corrélations apparaissant dans l'implémentation Monte-Carlo de l'itération de la puissance. L'itération de la puissance est l'approche standard utilisée pour estimer l'état fondamental de la formulation en problème aux valeurs propres k de l'équation de Boltzmann, ce qui est capital pour bien échantillonner la source critique (à l'équilibre) du problème cinétique. Notre étude a porté sur un ensemble de cas tests simples, mais physiquement intéressants comprenant des géométries homogènes et hétérogènes. Parmi les méthodes non-analogues étudiées, nous nous sommes concentrés en particulier sur les collisions non-branchantes, qui forcent l'émergence d'un seul neutron au sortir de chaque collision et donc réduit les corrélations dues à la présence de "branches" dans les histoires. De plus, nous avons considéré l'effet sur les corrélations du 'combing' et de l'échantillonnage sans remplacement en tant que techniques de contrôle de la population.

Dans le but de détecter la présence de fortes corrélations, et d'évaluer les avantages respectifs de ces différentes méthodes non-analogues, nous avons choisi différentes observables : l'entropie de Shannon, la distance de paire moyenne (au carré), le nombre moyen de familles survivantes, les moments de Feynman et la variance normalisée. Nous avons montré que toutes ces observables sont utiles pour détecter la présence de fluctuations anormales dans les systèmes examinés. Cependant, les observables globales telles que l'entropie et la distance de paire, bien qu'elles soient faciles à calculer et à interpréter, ne sont pas adaptées à l'étude des systèmes hétérogènes, en raison du manque d'information sur la distribution spatiale des corrélations. À l'inverse, les observables locales (dépendant de l'espace), telles que les moments de Feynman et la variance normalisée, sont par construction utiles pour extraire de l'information sur le comportement spatial des corrélations, au prix d'une complexité augmentée.

Notre résultat principal est que, dans toutes les configurations, l'utilisation de collisions non-branchantes (en opposition avec les collisions branchantes habituelles) est très efficace pour réduire les corrélations. De plus, bien que les méthodes de contrôle de la population soient généralement (mais pas toujours) efficaces pour réduire les corrélations, l'impact de ces dernières est bien plus limité que celui des collisions non-branchantes.

Après avoir étudié le cas de l'itération de la puissance, dans le Chapitre 6 nous nous sommes tournés vers le cas des simulations Monte-Carlo dépendantes du temps. En nous basant sur l'analyse effectuée dans le Chapitre 5, nous nous sommes concentrés sur l'entropie de Shannon et sur les moments de Feynman. Nous avons tout d'abord caractérisé l'effet des méthodes non-analogues dans un système simplifié, afin de faciliter l'interprétation des résultats. Nous avons considéré des configurations critiques, sous-critiques et sur-critiques, pour différentes tailles de systèmes et conditions de bord. Des oscillations de l'entropie ont été observées, et reliées à l'établissement des corrélations spatiales, dont la forme dépendait de l'interaction entre la réactivité du système, les méthodes de réduction de variance et de

contrôle de population utilisées, et la nature des conditions aux bords. Dans certains cas, les oscillations de l'entropie pouvaient perdurer sur de longues échelles de temps.

Enfin, nous avons étudié les corrélations spatio-temporelles apparaissant dans les cas tests homogènes plus réalistes introduits dans le Chapitre 5. Nous avons détaillé comment les corrélations spatiales se développent avec le temps. Nos résultats suggèrent que l'effet des insertions de réactivité sur les corrélations spatiales est marginal, au moins dans le régime des petites perturbations. De plus, la catastrophe critique est effectivement évitée grâce à l'usage de méthodes non-analogues.

Le travail effectué lors de cette thèse a permis de clarifier le comportement des fluctuations et des corrélations dans les simulations Monte-Carlo dépendantes du temps, en commençant par des modèles très simplifiés que nous avons progressivement rendu plus complexes afin d'agrandir le domaine de validité de nos résultats. Afin d'obtenir une compréhension plus précise de l'interaction entre les méthodes d'échantillonnage et les corrélations, nous avons conservé nos cas tests bien plus simples que pour des applications réalistes typiquement traitées par des codes Monte-Carlo industriels. D'un côté, cela nous a permis d'estimer et d'analyser des observables qui auraient autrement été hors de notre portée, en raison du coût de calcul, telles que la fonction de corrélations à deux points. De l'autre côté, nous sommes conscients que les conclusions obtenues à partir de configurations uni-dimensionnelles en utilisant des sections multi-groupes peut ne pas être représentatif du comportement observé dans des systèmes tridimensionnels utilisant des données nucléaires en énergie continue. De plus, il est important de noter que les méthodes Monte-Carlo cinétiques sont encore relativement jeunes et incomprises : de nouvelles méthodes de réduction de variance ou de contrôle de la population pourraient apparaître, soit spécifiquement conçues pour les méthodes dépendantes du temps, soit adaptées des simulations stationnaires. De tels changements pourraient nous obliger à réviser les conclusions présentées ici, particulièrement pour le cas des simulations cinétiques discuté dans le Chapitre 6.

Plusieurs chemins sont naturellement ouverts par les résultats de cette thèse. Comme brièvement noté dans le Chapitre 5, remplacer les sections multi-groupes par des données nucléaires en énergie continue pourrait avoir un effet significatif sur le comportement des méthodes de réduction de variance et les corrélations et fluctuations induites par celles-ci. Une étude plus vaste en trois dimensions et en énergie continue est donc nécessaire, ainsi que le développement d'outils de diagnostic adaptés à la détection des corrélations, afin de mieux contrôler l'augmentation du coût en temps de calcul et en mémoire.

Une autre possibilité concerne l'analyse de l'interaction entre l'échelle spatiale des corrélations et l'échelle spatiale des observables Monte-Carlo. En se basant sur les résultats présentés dans les Chapitres 5 et 6, il apparaît que l'émergence des corrélations spatiales est intimement reliée à la compétition entre la taille linéaire des regroupements de particules et celle des régions dans lesquelles les observables sont estimées. Une interaction similaire pourrait aussi exister pour les échelles temporelles : celles des corrélations et celles des observables dans les simulations cinétiques ; cette conjecture devrait être étudiée numériquement. Il serait aussi intéressant de développer un cadre théorique permettant d'adapter la taille des cellules (spatiales ou temporelles) pour les observables Monte-Carlo afin de réduire l'effet des corrélations.

En rapport avec les méthodes de réduction de variance, il serait intéressant d'effectuer une étude systématique des schémas à variance zéro telle que celle entamée dans la Ref. 100, afin d'obtenir un cadre cohérent pour une stratégie CADIS (Consistent Adjoint-Driven Importance Sampling). Ces méthodes pourraient avoir un immense potentiel dans le cadre des simulations Monte-Carlo cinétiques, de la même manière que pour les problèmes stationnaires de radioprotection, dans lesquels les méthodes CADIS sont maintenant couramment utilisée.

Enfin, bien que dans cette thèse nous nous soyons limités aux simulations cinétiques seules, dans la plupart des applications il est important de prendre en compte l'effet des contre-réactions physiques qui affectent profondément l'évolution des populations de neutrons et de précurseurs. Si le coefficient global de contre-réaction est négatif, elles agiront essentiellement comme un mécanisme ramenant le système vers la moyenne, et empêcheront de trop grandes fluctuations autour des moyennes. Seules les

valeurs moyennes peuvent être injectées dans les codes de couplages, qui sont déterministes. L'incertitude statistique peut être obtenue en effectuant des répliques indépendantes, au prix d'une augmentation du coût de calcul. Afin de compenser celle-ci, il est tentant de réduire le nombre d'histoires par réplique, mais cela viendrait augmenter le biais dû au fait de donner une quantité fluctuante au solveur couplé, sachant que le couplage est non-linéaire. Des questions théoriques et pratiques rendent donc ces problèmes complexes : un objectif ambitieux pour des explorations futures seraient d'étendre le cadre proposé dans cette thèse au cas où la simulation cinétique serait couplée à la thermo-hydraulique.

A.3 . Travaux publiés

Une partie des résultats présentés dans cette thèse ont déjà été publiés ou acceptés pour publication dans des journaux scientifiques :

- T. Bonnet, D. Mancusi, and A. Zoia, "Space and time correlations for diffusion models with prompt and delayed birth-and-death events", Phys. Rev. E, vol. 105, no. 6, p. 064105, Jun. 2022.[Online]. Disponible : `https://link.aps.org/doi/10.1103/PhysRevE.105.064105`
- T. Bonnet, D. Mancusi, and A. Zoia, "The Statistics of Family Histories in Kinetic Monte Carlo Simulations," in Proceedings of M&C 2023 International Conference on Mathematics and Computational Methods Applied to Nuclear Science and Engineering, Niagara Falls, Canada, Aug. 13-17th, 2023.
- H. Belanger, T. Bonnet, D. Mancusi, and A. Zoia, "The Effects of Branchless Collisions on Neutron Clustering" in Proceedings of M&C 2023 International Conference on Mathematics and Computational Methods Applied to Nuclear Science and Engineering, Niagara Falls, Canada, Aug. 13-17th, 2023.
- T. Bonnet, H. Belanger, D. Mancusi, and A. Zoia, "The effect of branchless collisions and population control on correlations in Monte Carlo power iteration", accepté par Nuclear Science and Engineering. Preprint disponible : `https://arxiv.org/abs/2309.03767`

De plus, certains résultats ont été présentés en conférence sous la forme de présentations orales :

- International Conference on Transport Theory (ICTT), Bertinoro, Italy, Jul. 10-16th, 2022.
- M&C 2023 International Conference on Mathematics and Computational Methods Applied to Nuclear Science and Engineering, Niagara Falls, Canada, Aug. 13-17th, 2023.
- Quatrième workshop "Mathématiques pour la neutronique", GdR MaNu, INSTN/Saclay, France, Dec. 7th, 2022.
- Présentation orale invitée à la première conférence du GdR Branchement, Institut de Mathématiques de Toulouse, France, Nov. 8-10th, 2023.

Bibliography

[1] V. Vitali, F. Chevallier, A. Jinaphanh, P. Blaise, and A. Zoia, "Eigenvalue separation and eigenmode analysis by matrix-filling Monte Carlo methods," *Ann. Nucl. Energy*, vol. 164, p. 108563, Dec. 2021.

[2] G. I. Bell and S. Glasstone, *Nuclear Reactor Theory*. Van Nostrand Reinhold Company, Oct. 1970.

[3] F. D'Auria *et al.*, "Neutronics and thermal-hydraulic coupling in LWR technology," OECD/NEA, Tech. Rep. 5434, 2004.

[4] S. Dulla, E. H. Mund, and P. P. Ravetto, "The quasi-static method revisited," *Prog. Nucl. Energ.*, vol. 50, pp. 908–920, 2008.

[5] E. W. Larsen, "Fundamentals, progress and limitations," in *Proceedings of the Frédéric Joliot / Otto Hahn summer school*, Karlsruhe, Germany, 2011.

[6] D. Caron, S. Dulla, and P. Ravetto, "New aspects in the implementation of the quasi-static method for the solution of neutron diffusion problems in the framework of a nodal method," *Ann. Nucl. Energy*, vol. 87, p. 34–48, 2016.

[7] S. Dulla, P. Ravetto, and P. Saracco, "Some new thoughts on the multipoint method for reactor physics applications," in *M&C 2017 International Conference on Mathematics and Computational Methods Applied to Nuclear Science and Engineering*, Jeju, South Korea, Apr. 2017.

[8] IAEA, *Safety Margins of Operating Reactors - Analysis of Uncertainties and Implications for Decision Making*. IAEA, 2003.

[9] ——, "Research reactor benchmarking database: Facility specification and experimental data," IAEA, Tech. Rep. 480, 2015.

[10] I. Lux and L. Koblinger, *Monte Carlo particle transport methods: neutron and photon calculations*. Boca Raton: CRC Press, 1991.

[11] J. Dufek and J. E. Hoogenboom, "Numerical stability of existing Monte Carlo burnup codes in cycle calculations of critical reactors," *Nucl. Sci. Eng.*, vol. 162, no. 3, pp. 307–311, Jul. 2009.

[12] A. Isotalo, J. Leppänen, and J. Dufek, "Preventing xenon oscillations in Monte Carlo burnup calculations by enforcing equilibrium xenon distribution," *Ann. Nucl. Energy*, vol. 60, pp. 78–85, Oct. 2013.

[13] D. Kotlyar and E. Shwageraus, "Numerically stable Monte Carlo-burnup-thermal hydraulic coupling schemes," *Ann. Nucl. Energy*, vol. 63, pp. 371–381, Jan. 2014.

[14] G. Kępisty and J. Cetnar, "Instabilities of Monte-Carlo burnup calculations for nuclear reactors—Demonstration and dependence from time step model," *Nucl. Eng. Des.*, vol. 286, pp. 49–59, May 2015.

[15] D. Ferraro, M. Garcia, L. Mercatali, V. H. Sanchez Espinoza, J. Leppänen, and V. Valtavirta, "Foreseen capabilities, bottlenecks identification and potential limitations of Serpent MC transport code in large-scale full 3-D burnup calculations," in *International Conference on Nuclear Engineering*, vol. 51456. American Society of Mechanical Engineers, 2018, p. V003T02A049.

[16] R. Tuominen, V. Valtavirta, M. García, D. Ferraro, and J. Leppänen, "Effect of energy deposition modelling in coupled steady state Monte Carlo neutronics/thermal hydraulics calculations," *EPJ Web Conf.*, vol. 247, p. 06001, 2021.

[17] B. L. Sjenitzer and J. E. Hoogenboom, "A Monte Carlo method for calculation of the dynamic behaviour of nuclear reactors," *Prog. Nucl. Energy*, vol. 2, no. 0, pp. 716–721, Oct. 2011.

[18] ——, "Dynamic Monte Carlo Method for Nuclear Reactor Kinetics Calculations," *Nucl. Sci. Eng.*, vol. 175, no. 1, pp. 94–107, Sep. 2013.

[19] B. L. Sjenitzer, J. E. Hoogenboom, J. Jiménez Escalante, and V. Sanchez Espinoza, "Coupling of dynamic Monte Carlo with thermal-hydraulic feedback," *Ann. Nucl. Energy*, vol. 76, pp. 27–39, Feb. 2015.

[20] M. Faucher, "Coupling between Monte Carlo neutron transport and thermal-hydraulics for the simulation of transients due to reactivity insertions," Ph.D. dissertation, Université Paris-Saclay, France, Oct. 2019.

[21] M. Faucher, D. Mancusi, and A. Zoia, "Variance-reduction methods for Monte Carlo kinetic simulations," in *M&C2019, Portland (USA)*, 2019.

[22] D. Ferraro, M. Faucher, D. Mancusi, A. Zoia, V. Valtavirta, J. Leppänen, and V. H. Sanchez-Espinoza, "Serpent and TRIPOLI-4 transient calculations comparisons for several reactivity insertion scenarios in a 3D PWR minicore benchmark," in *International Conference on Mathematics and Computational Methods applied to Nucl. Sci. Eng.* American Nuclear Society (ANS), 2019, pp. 1734–1743.

[23] A. Levinsky, V. Valtavirta, F. P. Adams, and V. N. Anghel, "Modeling of the SPERT transients using Serpent 2 with time-dependent capabilities," *Ann. Nucl. Energy*, vol. 125, pp. 80–98, Mar. 2019.

[24] D. Ferraro, M. García, V. Valtavirta, U. Imke, R. Tuominen, J. Leppänen, and V. Sanchez-Espinoza, "Serpent/SUBCHANFLOW pin-by-pin coupled transient calculations for the SPERT-IIIE hot full power tests," *Ann. Nucl. Energy*, vol. 142, p. 107387, 2020.

[25] D. Mancusi, M. Faucher, and A. Zoia, "Monte Carlo simulations of the SPERT III E-core transient experiments," *Eur. Phys. J. Plus*, vol. 137, no. 1, p. 127, Jan. 2022.

[26] D. Legrady, G. Tolnai, T. Hajas, E. Pazman, T. Parko, and I. Pos, "Full core pin-level VVER-440 simulation of a rod drop experiment with the GPU-based Monte Carlo code GUARDYAN," *Energies*, vol. 15, no. 8, p. 2712, Apr. 2022.

[27] E. Dumonteil, F. Malvagi, A. Zoia, A. Mazzolo, D. Artusio, C. Dieudonné, and C. De Mulatier, "Particle clustering in Monte Carlo criticality simulations," *Ann. Nucl. Energy*, vol. 63, pp. 612–618, Jan. 2014.

[28] C. de Mulatier, E. Dumonteil, A. Rosso, and A. Zoia, "The critical catastrophe revisited," *J. Stat. Mech.*, vol. 2015, no. 8, p. P08021, Aug. 2015, publisher: IOP Publishing.

[29] R. Brissenden and A. Garlick, "Biases in the estimation of k_{eff} and its error by Monte Carlo methods," *Ann. Nucl. Energy*, vol. 13, no. 2, pp. 63–83, 1986.

[30] T. Ueki, F. B. Brown, D. K. Parsons, and D. E. Kornreich, "Autocorrelation and dominance ratio in Monte Carlo criticality calculations," *Nucl. Sci. Eng.*, vol. 145, no. 3, pp. 279–290, Nov. 2003.

[31] B. R. Herman, "Monte Carlo and thermal hydraulic coupling using low-order nonlinear diffusion acceleration," Ph.D. dissertation, Massachusetts Institute of Technology, 2014.

[32] M.-J. Lee, H. Joo, D. Lee, and K. Smith, "Multigroup monte carlo reactor calculation with coarse mesh finite difference formulation for real variance reduction," in *PHYSOR 2010: Advances in Reactor physics to Power the Nuclear Renaissance*, 01 2010.

[33] A. Yamamoto, K. Sakata, and T. Endo, "Prediction on underestimation of variance for fission rate distribution in monte-carlo calculation," *Transactions of the American Nuclear Society*, vol. 110, pp. 515–518, 06 2014.

[34] T. M. Sutton, "Application of a discretized phase-space approach to the analysis of Monte Carlo uncertainties," *Nucl. Sci. Eng.*, vol. 185, no. 1, pp. 174–183, Jan. 2017.

[35] J. Miao, B. Forget, and K. Smith, "Analysis of correlations and their impact on convergence rates in Monte Carlo eigenvalue simulations," *Ann. Nucl. Energy*, vol. 92, pp. 81–95, Jun. 2016.

[36] ——, "Predicting correlation coefficients for Monte Carlo eigenvalue simulations with multitype branching process," *Ann. Nucl. Energy*, vol. 112, pp. 307–321, Feb. 2018.

[37] ——, "Correlation diagnosis method for heterogeneous Monte Carlo eigenvalue simulations based on a diffusion approximation," *Ann. Nucl. Energy*, vol. 130, pp. 301–318, Aug. 2019.

[38] M. Nowak, J. Miao, E. Dumonteil, B. Forget, A. Onillon, K. S. Smith, and A. Zoia, "Monte Carlo power iteration: Entropy and spatial correlations," *Ann. Nucl. Energy*, vol. 94, pp. 856–868, Aug. 2016.

[39] J. Dufek, D. Kotlyar, E. Shwageraus, and J. Leppänen, "Numerical stability of the predictor–corrector method in Monte Carlo burnup calculations of critical reactors," *Ann. Nucl. Energy*, vol. 56, pp. 34–38, Jun. 2013.

[40] P. Cosgrove, E. Shwageraus, and G. Parks, "Neutron clustering as a driver of Monte Carlo burn-up instability," *Ann. Nucl. Energy*, vol. 137, p. 106991, Mar. 2020.

[41] T. M. Sutton and A. Mittal, "Neutron clustering in Monte Carlo iterated-source calculations," *Nucl. Eng. Technol.*, vol. 49, no. 6, pp. 1211–1218, Sep. 2017.

[42] T. M. Sutton, "Toward a More Realistic Analysis of Neutron Clustering," *Nucl. Sci. Eng.*, pp. 1–12, May 2022.

[43] E. Dumonteil, G. Bruna, F. Malvagi, A. Onillon, and Y. Richet, "Clustering and traveling waves in the Monte Carlo criticality simulation of decoupled and confined media," *Nucl. Eng. Technol.*, vol. 49, no. 6, pp. 1157–1164, Sep. 2017.

[44] K. Fröhlicher, E. Dumonteil, L. Thulliez, J. Taforeau, and M. Brovchenko, "Generational variance reduction in monte carlo criticality simulations as a way of mitigating unwanted correlations," *Nucl. Sci. Eng.*, pp. 1–18, 2023.

[45] I. Mickus and J. Dufek, "Does neutron clustering affect tally errors in Monte Carlo criticality calculations?" *Ann. Nucl. Energy*, vol. 155, p. 108130, Jun. 2021.

[46] A. Zoia, E. Dumonteil, A. Mazzolo, C. de Mulatier, and A. Rosso, "Clustering of branching Brownian motions in confined geometries," *Phys. Rev. E*, vol. 90, no. 4, p. 042118, Oct. 2014, publisher: American Physical Society.

[47] A. Zoia and E. Dumonteil, "Neutron clustering: spatial fluctuations in multiplying systems at the critical point," in *M&C 2017 International Conference on Mathematics and Computational Methods Applied to Nuclear Science and Engineering*, Jeju, South Korea, Apr. 2017.

[48] B. Houchmandzadeh, E. Dumonteil, A. Mazzolo, and A. Zoia, "Neutron fluctuations: The importance of being delayed," *Phys. Rev. E*, vol. 92, no. 5, p. 052114, Nov. 2015, publisher: American Physical Society.

[49] I. Variansyah and R. G. McClarren, "Analysis of population control techniques for time-dependent and eigenvalue Monte Carlo neutron transport calculations," *Nucl. Sci. Eng.*, pp. 1–26, Sep. 2022.

[50] B. Watt, "Energy spectrum of neutrons from thermal fission of U235," *Phys. Rev.*, vol. 87, no. 6, p. 1037, 1952.

[51] "Using the PCG C++ implementation," https://www.pcg-random.org/using-pcg-cpp.html, accessed: 2023-08-29.

[52] M. Matsumoto and T. Nishimura, "Mersenne twister: A 623-dimensionally equidistributed uniform pseudo-random number generator," *ACM Trans. Model. Comput. Simul.*, vol. 8, no. 1, p. 3–30, jan 1998.

[53] E. Brun, F. Damian, C. M. Diop, E. Dumonteil, F.-X. Hugot, C. Jouanne, Y. K. Lee, F. Malvagi, A. Mazzolo, O. Petit, J. Trama, T. Visonneau, and A. Zoia, "TRIPOLI-4®, CEA, EDF and AREVA reference Monte Carlo code," *Ann. Nucl. Energy*, vol. 82, pp. 151-160, Aug. 2015.

[54] X-5 Monte Carlo Team, "MCNP-A General Monte Carlo N-Particle Transport Code, Version 5," Los Alamos National Laboratory, Tech. Rep. LA-UR-03-1987, 2003.

[55] B. L. Sjenitzer and J. E. Hoogenboom, "Variance reduction for fixed-source Monte Carlo calculations in multiplying systems by improving chain-length statistics," *Ann. Nucl. Eng.*, vol. 38, no. 10, pp. 2195–2203, Oct. 2011.

[56] B. Molnar, G. Tolnai, and D. Legrady, "A GPU-based direct Monte Carlo simulation of time dependence in nuclear reactors," *Ann. Nucl. Energy*, vol. 132, pp. 46–63, Oct. 2019.

[57] T. E. Booth, "A weight (charge) conserving importance-weighted comb for Monte Carlo," *Radiation Protection & Shielding Topical Meeting*, Apr. 1996.

[58] J. Eduard Hoogenboom and B. L. Sjenitzer, "Extensions of the MCNP5 and TRIPOLI4 Monte Carlo Codes for Transient Reactor Analysis," in *SNA + MC 2013 - Joint International Conference on Supercomputing in Nuclear Applications + Monte Carlo*, D. Caruge, C. Calvin, C. Diop, F. Malvagi, and J.-C. Trama, Eds. Paris, France: EDP Sciences, 2014, p. 03507.

[59] D. Legrady and J. E. Hoogenboom, "Scouting the feasibility of Monte Carlo reactor dynamics simulations," Jul 2008.

[60] J. Leppänen, M. Pusa, T. Viitanen, V. Valtavirta, and T. Kaltiaisenaho, "The Serpent Monte Carlo code: Status, development and applications in 2013," *Ann. Nucl. Energy*, vol. 82, pp. 142–150, Aug. 2015.

[61] A. G. Mylonakis, M. Varvayanni, D. Grigoriadis, and N. Catsaros, "Developing and investigating a pure Monte-Carlo module for transient neutron transport analysis," *Ann. Nucl. Energy*, vol. 104, pp. 103–112, Jun. 2017.

[62] M. Faucher, D. Mancusi, and A. Zoia, "New kinetic simulation capabilities for Tripoli-4®: Methods and applications," *Ann. Nucl. Energy*, vol. 120, pp. 74–88, Oct. 2018.

[63] C. Demazière, V. H. Sanchez-Espinoza, and B. Chanaron, "Advanced numerical simulation and modelling for reactor safety - contributions from the CORTEX, HPMC, McSAFE and NURESAFE projects," *EPJ Nucl. Sci. Technol.*, vol. 6, p. 42, 2020.

[64] D. Ferraro, M. García, V. Valtavirta, U. Imke, R. Tuominen, J. Leppänen, and V. Sanchez-Espinoza, "Serpent/SUBCHANFLOW pin-by-pin coupled transient calculations for a PWR minicore," *Ann. Nucl. Energy*, vol. 137, p. 107090, Mar. 2020.

[65] M. Coste-Delclaux, "Modélisation du phénomène d'autoprotection dans le code de transport multigroupe APOLLO2," Ph.D. dissertation, Paris CNAM, 2006.

[66] A. Hébert, "Advances in the development of a subgroup method for the self-shielding of resonant isotopes in arbitrary geometries," *Nucl. Sci. Eng.*, vol. 126, no. 3, pp. 245–263, 1997.

[67] D. E. Cullen, "Application of the probability table method to multigroup calculations of neutron transport," *Nucl. Sci. Eng.*, vol. 55, no. 4, pp. 387–400, 1974.

[68] R. Sanchez, J. Mondot, Ž. Stankovski, A. Cossic, and I. Zmijarevic, "APOLLO II: A user-oriented, portable, modular code for multigroup transport assembly calculations," *Nucl. Sci. Eng.*, vol. 100, no. 3, pp. 352–362, 1988.

[69] L. Mao, I. Zmijarevic, and R. Sanchez, "Resonance self-shielding methods for fast reactor calculations—comparison of a new Tone's method with the subgroup method in APOLLO3," *Nucl. Sci. Eng.*, vol. 188, no. 1, pp. 15–32, 2017.

[70] E. Fridman and J. Leppänen, "On the use of the Serpent Monte Carlo code for few-group cross section generation," *Ann. Nucl. Energy*, vol. 38, no. 6, pp. 1399–1405, 2011.

[71] E. Fridman and J. Leppänen, "Revised methods for few-group cross section generation in the Serpent Monte Carlo code," *Proceeding of the PHYSOR 2012*, 2012.

[72] W. Boyd, A. Nelson, P. K. Romano, S. Shaner, B. Forget, and K. Smith, "Multigroup cross-section generation with the OpenMC Monte Carlo particle transport code," *Nucl. Technol.*, vol. 205, no. 7, pp. 928–944, 2019.

[73] C.-S. Lin and W. S. Yang, "An assessment of the applicability of multigroup cross sections generated with Monte Carlo method for fast reactor analysis," *Nucl. Eng. Technol.*, vol. 52, no. 12, pp. 2733–2742, 2020.

[74] M. Kac, "On some connections between probability theory and differential and integral equations," in *Proc. Sec. Berkeley Symp. on Math. Stat. and Prob.*, 1957, pp. 189–215.

[75] H. Kesten, "Branching brownian motion with absorption," *Stoch. Process. their Appl.*, vol. 7, no. 1, pp. 9–47, March 1978.

[76] T. E. Harris, *The Theory of Branching Processes*. Springer Verlag OHG, 1963.

[77] T. Bonnet, D. Mancusi, and A. Zoia, "Space and time correlations for diffusion models with prompt and delayed birth-and-death events," *Phys. Rev. E*, vol. 105, no. 6, p. 064105, Jun. 2022.

[78] M. M. R. Williams, *Random processes in nuclear reactors*, 1st ed. Oxford, New York: Pergamon Press, 1974.

[79] M. Meyer, S. Havlin, and A. Bunde, "Clustering of independently diffusing individuals by birth and death processes," *Phys. Rev. E*, vol. 54, no. 5, pp. 5567–5570, Nov. 1996, publisher: American Physical Society.

[80] I. Pazsit and L. Pal, *Neutron Fluctuations: A Treatise on the Physics of Branching Processes*. Elsevier, Oct. 2007.

[81] Y. C. Zhang, M. Serva, and M. Polikarpov, "Diffusion reproduction processes," *J. Stat. Phys.*, vol. 58, no. 5, pp. 849–861, Mar. 1990.

[82] L. Pál and I. Pázsit, "Neutron fluctuations in a multiplying medium randomly varying in time," *Phys. Scr.*, vol. 74, no. 1, pp. 62–70, Jun. 2006.

[83] M. Serva, "On the genealogy of populations: trees, branches and offspring," *J. Stat. Mech.*, vol. 2005, no. 07, p. P07011, Jul. 2005.

[84] T. Bonnet, D. Mancusi, and A. Zoia, "The statistics of family histories in kinetic Monte-Carlo simulations," in *M&C 2023 International Conference on Mathematics and Computational Methods Applied to Nuclear Science and Engineering*, Niagara Falls, 2023.

[85] J. F. C. Kingman, "On the genealogy of large populations," *J. Appl. Probab.*, vol. 19, no. A, pp. 27–43, 1982.

[86] G. Bell, "Neutral Macroecology," *Science*, vol. 293, pp. 2413–2418, Sep. 2001.

[87] B. Houchmandzadeh, "Neutral Clustering in a Simple Experimental Ecological Community," *Phys. Rev. Lett.*, vol. 101, no. 7, p. 078103, Aug. 2008.

[88] N. A. Weiss and P. T. Holmes, *A course in probability*, 1st ed. Boston, Mass.: Pearson/Addison-Wesley, 2006.

[89] F. B. Brown and C. J. Josey, "Diagnostics for undersampling and clustering in Monte Carlo criticality calculations," Los Alamos National Laboratory, USA, Tech. Rep., 2018, LA-UR-18-27656.

[90] E. Dumonteil, R. Bahran, T. Cutler, B. Dechenaux, T. Grove, J. Hutchinson, G. McKenzie, A. McSpaden, W. Monange, M. Nelson, N. Thompson, and A. Zoia, "Patchy nuclear chain reactions," *Commun. Phys.*, vol. 4, no. 1, pp. 1–10, 2021.

[91] H. Belanger, T. Bonnet, D. Mancusi, and A. Zoia, "The effect of branchless collisions on neutron clustering," in *M&C23 International Conference on Mathematics and Computational Methods Applied to Nuclear Science and Engineering*, Niagara Falls, Ontario, Canada, 2023.

[92] T. Bonnet, H. Belanger, D. Mancusi, and A. Zoia, "The effect of branchless collisions and population control on correlations in Monte Carlo power iteration," Sep. 2023, arXiv:2309.03767 [physics]; submitted to Nucl. Sci. Eng.

[93] J. A. Kulesza *et al.*, "MCNP® code version 6.3.0 theory & user manual," Los Alamos National Laboratory, Los Alamos, NM, USA, Tech. Rep. LA-UR-22-30006, Rev. 1, September 2022.

[94] J. Leppänen, M. Pusa, T. Viitanen, V. Valtavirta, and T. Kaltiaisenaho, "The Serpent Monte Carlo code: Status, development and applications in 2013," *Ann. Nucl. Energy*, vol. 82, pp. 142–150, Aug. 2015.

[95] P. K. Romano, N. E. Horelik, B. R. Herman, A. G. Nelson, B. Forget, and K. Smith, "OpenMC: A state-of-the-art Monte Carlo code for research and development," *Ann. Nucl. Energy*, vol. 82, pp. 90–97, Aug. 2015.

[96] J. Spanier and E. M. Gelbard, *Monte Carlo principles and neutron transport problems*, dover ed ed. Mineola, N.Y: Dover Publications, 2008.

[97] L. Demaret, "Accurate determination of confidence intervals in Monte Carlo eigenvalue calculations," in *ICNC'99, Sixth Int. Conf. on Nuclear Criticality Safety, Versailles, France, Sep. 20-24, 1999*, vol. 1, 1999, pp. 66–80.

[98] H. Belanger, "Development of numerical methods for neutronics in continuous media," Ph.D. dissertation, Université Paris-Saclay, France, 2022.

[99] B. Dechenaux, T. Delcambre, and E. Dumonteil, "Percolation properties of the neutron population in nuclear reactors," *Phys. Rev. E*, vol. 106, p. 064126, Dec 2022.

[100] D. Mancusi and A. Zoia, "Zero-variance schemes for kinetic Monte-Carlo simulations," *Eur. Phys. J. Plus*, vol. 135, no. 5, p. 401, 2020.